Citation: Kahwash, Fadi (2017) Element-free galerkin modelling for cutting of fibre reinforced plastics. Doctoral thesis, Northumbria University.

ELEMENT-FREE GALERKIN MODELLING FOR CUTTING OF FIBRE REINFORCED PLASTICS

Fadi Kahwash

PhD

2017

ELEMENT-FREE GALERKIN MODELLING FOR CUTTING OF FIBRE REINFORCED PLASTICS

Fadi Kahwash

A thesis submitted in partial fulfilment of the
requirements of the University of Northumbria at
Newcastle for the degree of Doctor of Philosophy

Research undertaken in the Faculty of Engineering
and Environment

November 2017

Abstract

The utilisation of composite materials is increasing across many industries, spurred by the need for weight reduction and improved mechanical properties. This has led to an increase in their machining requirements. Although composites are laid in near-net shape, machining processes such as drilling and edge trimming are required to give the composites parts their final geometry and functionality. Machining of composites is challenging due to their low machinability and high cost. Numerical modelling presents a valuable tool for cost reduction and better understanding of the machining processes. Most modelling of machining is carried out using the Finite Element Method, which requires significant time in generating the mesh. Meshfree methods present an attractive choice for machining simulations due to their capabilities in modelling large deformations without the need to construct a mesh.

This work aims at developing an efficient meshfree model to simulate orthogonal cutting of unidirectional composites. The Element-Free Galerkin (EFG), which is a prominent meshfree method, is used to construct the model using MATLAB. Steady-state and dynamic models are developed and validated against experimental evidence. The models include several novel features in constitutive relations, composites failure and contact modelling. The main outputs of the simulations are cutting forces and chip formation. Good agreement with experiments is achieved in predicting cutting force. However, thrust force is significantly under-estimated, which is noticed in most of the relevant literature. Three phases of orthogonal cutting experiments are carried out to gain better understanding of the cutting process and generate model validation data. Statistical significance of fibre orientation angle, depth of cut, rake angle and cutting speed on cutting forces and surface integrity is established. Furthermore, the effect of fibre volume fraction on cutting forces is investigated. This work showed that the EFG is a viable numerical method to simulate orthogonal cutting. The simple and automated preprocessing and high quality of approximation are the most advantageous features of the developed model.

List of Publications

- F. Kahwash, I. Shyha, and A. Maheri, “Dynamic Simulation of Machining Composites Using Explicit Element-Free Galerkin Method”, submitted to: *Composite Structures*, October 2017
- F. Kahwash, I. Shyha, and A. Maheri, “Meshfree formulation for modelling of orthogonal cutting of composites”, *Composite Structures*, vol 166, pp. 193 - 201, Elsevier, 2017
- F. Kahwash, I. Shyha, and A. Maheri, “An Investigation into the Dependency of Cutting Forces on the Volume Fraction and Fibre Orientation during Machining Composite Materials”, *Materials Science Forum*, vol 882, pp. 61 - 65, Trans Tech Publications, 2017
- F. Kahwash, I. Shyha, and A. Maheri, “Machining unidirectional composites using single-point tools: analysis of cutting forces, chip formation and surface integrity”, *Procedia Engineering*, vol 132, pp. 569 - 576, Elsevier, 2015
- F. Kahwash, I. Shyha, and A. Maheri, “Modelling of cutting fibrous composite materials: current practice”, *Procedia CIRP*, vol 28, pp. 52 - 57, Elsevier, 2015

Declaration

I declare that the work contained in this thesis has not been submitted for any other award and that it is all my own work. I also confirm that this work fully acknowledges opinions, ideas and contributions from the work of others.

Any ethical clearance for the research presented in this thesis has been approved. Approval has been sought and granted by the Faculty Ethics Committee on 01/05/2014.

I declare that the Word Count of this Thesis is 40,756 words

Name:

Signature:

Acknowledgement

First and foremost, massive thanks to my supervisory team, Principle supervisor Dr. Islam Shyha and Co-supervisor Dr. Alireza Maheri. Their trust, knowledge and support have been indispensable in completing this work.

A special thanks to my loving family: Mom, Dad, Mai, Saleem, Rouba and Anthony. I would not have reached this milestone without their love, patience and encouragement.

I would like to thank my friends in Newcastle and beyond. Life through the PhD was more meaningful when sharing the ups and downs with friends. Credit is due to Balaji for proofreading my thesis and to Luan for his help in solid mechanics.

Finally, acknowledgement is due to the person who tolerated me the most in the final leg of the PhD journey; my dearest *Inga!*

Contents

List of Figures

List of Tables

List of Algorithms

Nomenclature

Abbreviations

BC	Boundary Conditions
ANOVA	ANalysis Of VAriance
CCW	Counter Clockwise
CDM	Central Difference Method
CFRP	Carbon Fibre-reinforced Plastic
CW	Clockwise
CZE	Cohesive Zone Elements
DoI	Domain of Influence
EFGM	Element-free Galerkin Method
EHM	Equivalent Homogeneous Material
FEM	Finite Element Method
FRP	Fibre-reinforced Plastic
GFRP	Glass Fibre-reinforced Plastic
HSS	High-Speed Steel
MLS	Moving Least Squares
MM	Meshfree Methods
PCR	Percentage Contribution Ratio
PDE	Partial Differential Equation
SPH	Smoothed Particle Hydrodynamics
UD	Uni-directional
UL	Updated Lagrangian

Numerical Modelling Symbols

α_u	Displacement penalty parameter
$\ddot{\mathbf{u}}$	Acceleration of the body
Δt_{cr}	Critical timestep
$\mathbf{A}$	MLS moment matrix

$\mathbf{F}^{con}$	Contact force vector
$\mathbf{F}^{ext}$	External force vector
$\mathbf{F}^{int}$	Internal force vector
$\mathbf{H}$	Deformation gradient
$\mathbf{N}_I$	Lagrnage multiplier shape function
$\mathbf{p}$	Complete polynomial basis
$\mathbf{S}$	Second Piola Kirchhoff stress
$\mathbf{T}$	Traction vector
$\mathbf{x}^M$	Master node position
μ	Friction coefficient
g_t	Tangential gap
K_f	Stress concentration factor
P_u	Penalty functional for displacement BCs
Q	External load
W	Width of domain
$\mathbf{b}$	Body force vector
$\mathbf{w}(\mathbf{r}_I)$	Weight function at I
n_I	Number of nodes in support domain of I
α_n	Penalty parameter for normal contact
α_t	Penalty parameter for tangential contact
β	DoI scaling parameter
$\delta\varepsilon$	Virtual strain
Δt	Finite time increment
$\delta\mathbf{u}$	Virtual displacement field
λ	Lagrange multipliers vector
ε	strain vector
$\mathbf{B}_I$	Strain matrix at point I
$\mathbf{C}(\mathbf{u})$	Set of constraints
$\mathbf{I}$	Identity matrix
$\mathbf{K}$	Global stiffness matrix
$\mathbf{K}^c$	Stiffness matrix due to contact imposition
$\mathbf{K}^u$	Stiffness matrix due to BC impsition
$\mathbf{L}$	Differential Operator

$\mathbf{M}$	Global mass matrix
$\mathbf{r}_I(\mathbf{x})$	Radial distance between $\mathbf{x}$ and $\mathbf{x}_I$
$\mathbf{u}$	Displacement vector
$\mathbf{v}$	Velocity vector
$\mathbf{x}$	Postion vector
$\mathbf{x}^S$	Slave node position
∇	divergence operator
Ω	Computational domain
ρ	Density of the solid
τ_{12}	In-plane shear stress
Θ	Angular polar coordinate
d_m	Size of DoI
g_n	Normal gap
I_m	Moment of inertia
L	Length of domain
N	Number of nodes in the domain
P_c	Penalty contact functional
$\bar{\mathbf{t}}$	Prescribed traction
$\bar{\mathbf{u}}$	Prescribed displacement
Γ_t	Traction boundary
Γ_u	Displacement boundary
$\hat{w}$	Gauss integration weight
$\mathbf{\Phi}(\mathbf{x})$	MLS shape function vector
$\mathbf{a}(\mathbf{x})$	Matrix of unknown MLS coefficients
$\mathbf{E}$	Green-Lagrange strain vector
σ	stress vector
n_j	outward normal on traction boundary

Machining Symbols

γ	Rake angle
F_c	Main cutting force
F_t	Thrust force
R_t	Maximum peak-to-valley roughness
W_t	Total waviness

φ	Shear plane angle
a_c	Depth of Cut
R_a	Average roughness
r_c	The cutting ratio
V_c	Cutting speed
V_f	Fibre volume fraction
W_a	Average waviness

Composite Materials Symbols

ν_{ij}	Poisson ratio acting on i and j planes
Υ	Fracture plane angle of lamina
E	Young modulus
E_i	Young modulus in the i direction
X^c	Compression strength in local x direction
S^l	In-plane shear strength
η^L	Coefficient of longitudinal influence
η^T	Coefficient of transverse influence
$\mathbf{D}$	Material coefficients matrix
$\mathbf{D}_k$	Coefficients matrix for Kirchhoff material model
ν	Poisson ratio
ψ	misalignment angle due to fibre compression
θ	Fibre orientation angle
Υ_0	Fracture plane angle in pure transverse compressive loading
FI	Failure index
G_{12}	In-plane shear modulus
S^T	Transverse shear strength
S_σ	Interface strength in the normal direction
S_τ	Interface shear strength
X^t	Tension strength in local x direction
Y^c	Compression strength in local y direction
Y^t	Tension strength in local y direction

Chapter 1

Introduction

1.1 Background

Composite materials utilisation is steadily growing worldwide. This is due to their favourable mechanical properties, such as light weight, high stiffness and the ability to tailor the material properties to fit a specific application. Industries that have witnessed expansion in composites market share include: aeronautics and aerospace, construction, consumer goods and wind turbines to name a few. There are several types of composite materials. The most common type is made from long fibres embedded in plastic layers and are called Fibre Reinforced Plastics (FRP). Glass and Carbon are the most common types of fibres used in FRPs. Multiple FRP layers (each is called lamina) are usually stacked to form a laminate. If the direction of the fibres is the same in all the stacked lamina, the composite is called Unidirectional (UD). UD-FRP will be the focus of this research work.

The increased utilisation of composites led to increase in demand for their machining. Although composites are fabricated to *near-net* shape, some machining processes such as drilling and edge trimming are required to give the composite part the final functionality and dimensional tolerances. Given the anisotropic and inhomogeneous nature of composites, obtaining high quality machined surfaces is a challenge. Poor quality of machined surfaces lead to performance degradation and often to parts rejection. Furthermore, with ever increasing parts sizes (e.g. aircraft fuselage and wind turbine blades), errors in machining can incur high cost. Improving machinability of composites requires deep understanding of material removal mechanisms. This is still developing area of research. A major obstacle is lack of fundamental understanding of composites failure. An illuminating example in this regard is the *World-Wide Failure Exercise* [9–16]. During its first phase, simple 2D loading cases were examined using most prominent failure theories and found significant discrepancies in their predictions. These cases assumed static loading and standard environmental conditions. Given the nature of loading and conditions during machining, the gap in composites failure prediction becomes more evident.

Improving fundamental understanding of material removal mechanisms can be done using two main approaches: experimental and modelling-based. The two approaches complement each other and are used in this study. Experimentally, *Orthogonal Cutting* process is widely used in research on material removal mechanisms due to its 2D nature and simplicity. Measurements of cutting forces are usually carried out using force dynamometer. Analysis of chip formation is most commonly performed by in-situ analysis using high speed videos and also by microscopic inspection of chips and machined surface.

Modelling-based approach can be either analytical or numerical. Analytical modelling relies on application of mechanics relations combined with simplification of the cutting conditions to reach a closed-form solution. The attained solution is used to predict fundamental outputs of the cutting process. Numerical modelling relies on finding an approximate solution to the governing equations/boundary conditions of the computational domain. The model is constructed using a numerical solution method such as: Finite Element Method (FEM), Meshfree Methods (MM), Finite Volume Method (FVM) and Boundary Element Method (BEM). *Meshfree Methods* have recently gained a lot of attention in the modelling community due to their potential in modelling challenging problems. One of these MMs (the Element-Free Galerkin Method) will be used in developing numerical model for orthogonal cutting of composites. In addition to its use in research, modelling of machining (analytical or numerical) can be a valuable practical tool to help meet industrial needs such as cost and effort reduction. Cost reduction can be achieved by using models to optimise machining parameters and therefore reduce the need for trial and error approach on shop floor. Other benefits include, cutting tool design, production planning and cutting energy estimates.

1.2 Problem Statement

Given the increasing use of composites and the increasing criticality of machining composites parts, modelling of machining is a valuable tool to reduce cost and mitigate risk of using inappropriate tools/machining parameters. Despite the maturity of FEM, significant development time is spent on meshing the computational domain. Furthermore, meshing requires highly skilled engineers to ensure the accuracy of the results. Using alternative numerical methods could address these shortcomings.

1.3 Aim and Objectives

This research aims to develop an efficient meshfree model for orthogonal cutting of unidirectional FRPs with emphasis on prediction of cutting forces and chip formation. This aim will be realised through achieving the following objectives:

1. Conduct a systematic survey of the literature to identify the most suitable cutting process to model and the best meshfree method to implement the model.
2. Develop the essential model components based on the chosen meshfree method in Objective 1. Starting with the mathematical model, followed by discretisation procedure and finally numerical implementation in MATLAB code. Each component is checked separately using numerical examples where an accurate solution is known

from literature. The model components will be used to achieve the next two objectives.

3. Develop and validate a steady state cutting model suitable for low-speed simulations.
4. Develop and validate a dynamic cutting model capable of predicting cutting forces and chip formation.
5. Conduct cutting experiments on uni-directional FRP samples. The purpose of these experiments is twofold: Firstly, to gain better understanding of the cutting process including the effect of various parameters on the process outputs. Secondly, to generate validation data for the meshfree model.
6. Disseminate the findings of this research through various scholarly publications.

1.4 Contribution to Knowledge

At this early stage, it is worth highlighting the major accomplishments of this research work. They can be divided into two components: contribution in numerical modelling and in experimental work

- *Numerically:* Extension of the EFG to modelling of machining composites. To the author's best knowledge, EFG has not been used in modelling of machining of any material. It proved to be a viable tool in such simulations, despite some drawbacks that will be discussed later. Simulations were carried out using steady-state and dynamic models with several advanced and novel features, especially in material and contact modelling.
- *Experimentally:* Generating sizeable amount of orthogonal cutting data that could be used for model validation and to guide parameters selection in other experiments. Furthermore, the dependency of cutting forces on fibre volume fraction is established and put into an empirical model.

1.5 Structure of the Thesis

The thesis is organised as follows: In *chapter 2*, necessary background topics are introduced. State of the art in experimental composite machining is then presented and finally, modelling of machining composites literature is reviewed and critically analysed. *Chapter 3* presents the development of the meshfree model components (refer to objective 1). The weak forms for static and dynamic linear-elastic models are presented then meshfree approximation based on the EFG procedure is detailed. Numerical examples are solved to verify implementation of the essential model components: stress calculations, non-convex boundaries, temporal integration, contact force calculations and composite materials failure. *Chapter 4* presents the steady-state meshfree cutting model (refer to objective 2). Novel contact algorithm is presented followed by progressive failure of composites and numerical implementation issues. Finally, comparison of the cutting force results with experimental evidence and FEM simulations in literature are presented and discussed. Building on the the previous two chapters, in *Chapter 5*, dynamic model is developed incorporating several novel features (refer to objective 3). The discrete equations are developed from the virtual work principle using the Updated Lagrangian Formulation and finite stress/strain measures. Contact force algorithm suitable for dynamic models is presented. Material behaviour is modelled using non-linear elastic constitutive relation and advanced failure theories. Simulation results focused on cutting forces and chip formation and were compared with in-house experimental data. *Chapter 6* details the experimental efforts of this project (refer to objective 4). Three experimental campaigns are carried out. The first focuses on identifying the most relevant process parameters on cutting forces, chip formation and surface integrity. The second is concerned with understanding the effect of fibre content on the cutting forces. In the third campaign, validation data for the meshfree model are generated. *Chapter 7* presents the conclusions drawn from this research and provides some guidance on possible areas of improvements and future research.

Chapter 2

Literature Review

2.1 Introduction

In this chapter, the context of the current research project is outlined and state of the art in relevant research areas is critically reviewed. The current research project is positioned at the intersection of three main disciplines; namely, machining processes, composite materials and numerical modelling. Figure 2.1 illustrates this graphically. It is noted that out of each discipline, a sub-discipline reflecting the boundaries of this research is shown. Orthogonal cutting is the chosen *process* from the wider machining processes. Unidirectional fibre reinforced plastics laminates are the chosen *material system* from the wider composite materials. Meshfree methods are the chosen *method of analysis* out of the wider numerical modelling discipline. The rationale of these choices will become clear by the end of this chapter.

The chapter is organised as follows: a brief description of machining processes is presented followed by discussion about composite materials. In depth review of experimental research on composite machining is then detailed. Finally, numerical modelling and meshfree methods are discussed then state of the art in numerical modelling of composites machining.

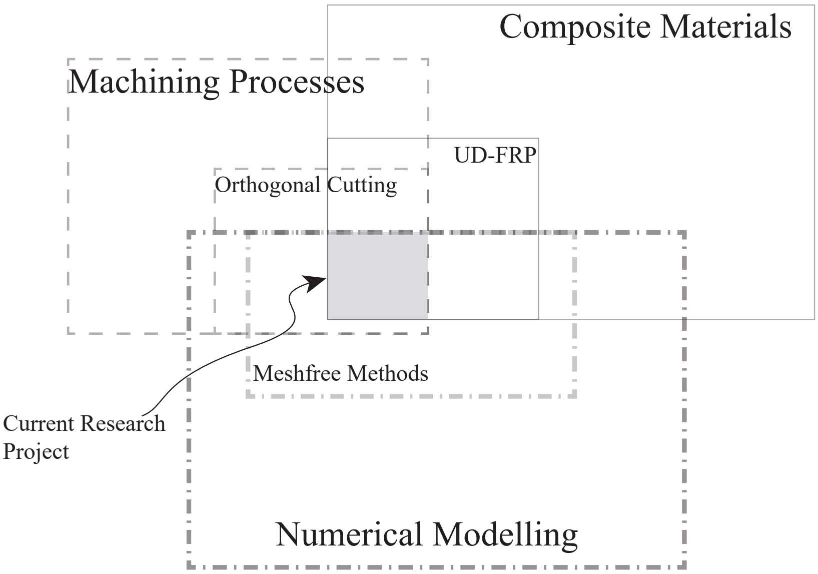

Figure 2.1: Position of the current research project in wider literature

2.2 An Overview of Machining Processes

Manufacturing techniques can be grouped into three main categories: machining, forming and joining [17]. In machining, unwanted material is removed from the workpiece to produce the required part [18]. In forming, the workpiece material is moved from one place to the other. In joining, the material volume is increased due to addition of material to the workpiece [17]. Machining processes can be further classified into: cutting, grinding and special techniques [17]. Cutting is characterised by the interaction and relative motion between a wedged-shaped tool and the workpiece to produce a chip [19]. Turning, milling, shaping and drilling are examples of cutting processes. Machining processes have a significant importance and economic value. Almost all engineering products have undergone some form of machining operations to bring them to the final geometry and accuracy. Furthermore, it is estimated that machining accounts for 15% of the value of all mechanical parts produced worldwide and that machining processes account for about 10% of the USA gross national product [17, 19].

In light of the above figures, understanding machining processes becomes of paramount importance to optimise them and reduce the operational costs. Even marginal gains in performance or cost reductions will have a large impact in mass production machining processes [17]. Understanding machining operations is challenging due to their complicated nature. Basic mechanics models were among the first tools to help in understanding cutting phenomena using orthogonal cutting models.

Orthogonal Cutting

Orthogonal cutting can be viewed as the simplest form of cutting processes. Its 2 dimensional nature lends itself well to research as the geometrical complexities associated with oblique cutting processes (e.g. drilling and milling) can be reduced to a minimum [1]. While it is idealised during analysis, some cutting operations such as turning, sawing and shaping are essentially 2D cutting processes [17]. This means that insights gained while studying orthogonal cutting could be readily extended to some real cutting processes. Orthogonal cutting models were developed in the context of metal cutting, specifically ductile metals in which continuous chip is produced by the cutting action. The first mechanics-based orthogonal cutting model was proposed by Merchant in 1940s [20], where the chip was subjected to mechanics analysis and forces balance concepts. Figure 2.2 shows an idealised orthogonal cutting process with the basic terminology and forces acting on the chip. The chip is in equilibrium state due to the opposing effect of the forces R and R'. These forces are decomposed either as horizontal and vertical components (cutting and thrust forces respectively) or parallel and perpendicular to the shear plane (frictional and normal forces respectively). The assumptions of the orthogonal cutting models are as follows [1, 17, 20]:

1. The tool edge is sharp (zero nose radius) and the clearance face of the tool does not contact the workpiece.
2. The shear surface is a plane extending from the cutting edge to the free surface.
3. The cutting edge is perpendicular to the direction of motion extending as straight

line across the width of the workpiece.

4. The chip only flows on the rake face of the tool and not on either sides.

5. The depth of cut is constant and relative velocity of workpiece and tool is constant.

6. A continuous chip is produced with no build-up edges.

The above assumptions and some vector treatments allow for easy estimation of the cutting forces, shear strains and other basic cutting quantities.

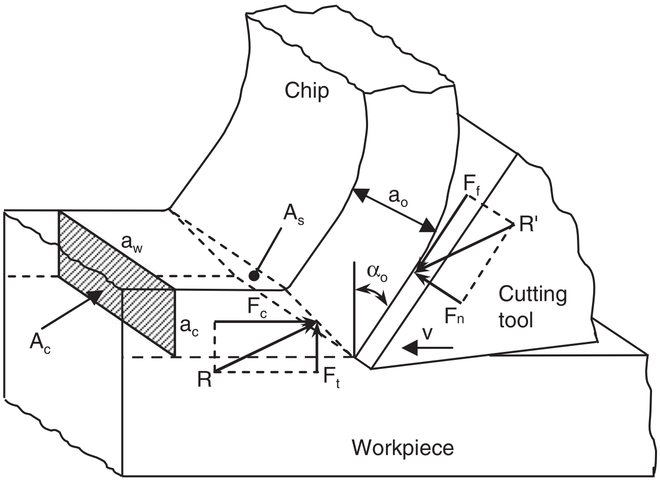

Figure 2.2: Schematic of Orthogonal cutting showing the forces acting on the chip [1]

2.3 Composite Materials

2.3.1 Definition and Classifications of Composites

Composite materials can be defined as “materials formed from two or more materials (constituents) producing properties that could not be obtained from any one of the materials” [21]. The constituents of composites are combined at macroscopic scale [22] and are not soluble in each other [23]. One constituent is called the reinforcement, which could be fibres, particles or flakes. The other is called the matrix, which maintains the geometric arrangement of the reinforcement and transmits load to the reinforcement [2].

Composites can be classified based on the geometry of the reinforcement or the type of matrix. Based on the geometry of the reinforcement they can be classified into [23]:

- fibre reinforced composites (FRC)
- particulate reinforced composite (PRC)
- flake reinforcement
- nano-composites

Composites also can be classified based on the matrix material into [21]:

- polymer matrix composites (PMC).
- metal matrix composites (MMC).
- ceramic matrix composites (CMC).

One of the most ubiquitous types of composites combine fibre reinforcement and plastic matrix (subset of polymers) and are called Fibre reinforced plastics (FRPs). Glass FRP (GFRP) and Carbon FRP (CFRP) constitute the bulk of composite materials production and will be the focus of this work.

2.3.2 Applications of Composites

GFRP and CFRP markets are steadily growing at an annual rate of 8.1% [24, 25] and total projected market worth of $B\$105.26$ by 2021. The market share of CFRP by application, in descending order is as follows: Aerospace and Defence, sport and leisure, wind turbines, moulding and compound, automotive and others [2]. As for GFRP the main sectors are (in descending order of total market share in Europe) transport, electro and electronic, construction, sports and leisure and others [25]. Figure 2.3 shows breakdown of the overall composites market share by application in terms of weight and total value. It is clear that aerospace industry constitutes large market share in terms of value rather than weight as the main driver of using composites in aerospace is weight reduction.

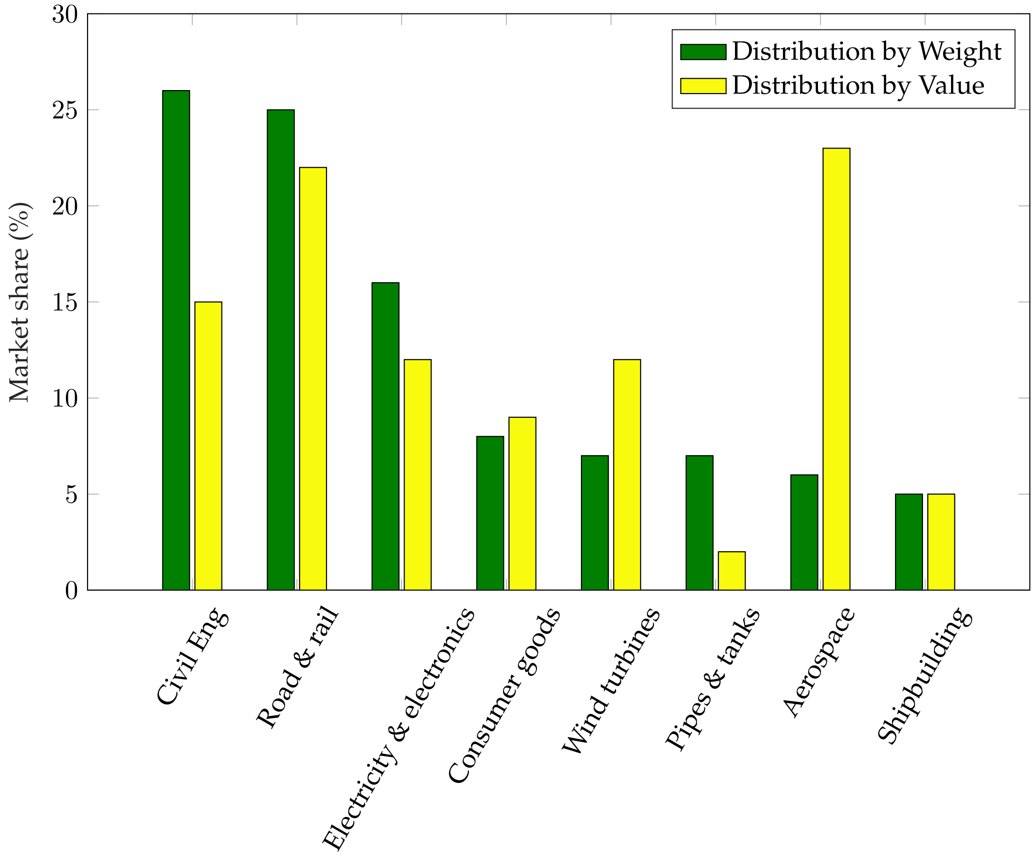

Figure 2.3: Composites market share per application in terms of weight and total value, adopted from [2]

There are many ways to manufacture composite parts. The choice of production method depends in part on the complexity of the part geometry, the available equipment and skilled workers and the required consistency of the manufactured parts. Common methods of FRP production include: tape or cloth laying or wrapping, filament winding, resin transfer moulding, sheet moulding compound, plutrusion and autoclave forming [22,23]. These production techniques produce composite parts in *near-net shape*. This means that further machining operations such as edge trimming and drilling are necessary to bring the composite part into the required functionality/accuracy and dimensional tolerances [21]. This will be discussed in details in Section 2.4.

2.3.3 Mechanics of Composites

This section will briefly introduce the basic mechanics of FRPs. A unidirectional composite laminate could be considered as orthotropic material and subject to linear elasticity condition. A generalised Hook's law for 3D orthotropic material is given as

$$\begin{bmatrix} \sigma_1 \\ \sigma_2 \\ \sigma_3 \\ \tau_{23} \\ \tau_{31} \\ \tau_{12} \end{bmatrix} = \begin{bmatrix} D_{11} & D_{12} & D_{13} & 0 & 0 & 0 \\ D_{21} & D_{22} & D_{23} & 0 & 0 & 0 \\ D_{31} & D_{32} & D_{33} & 0 & 0 & 0 \\ 0 & 0 & 0 & D_{44} & 0 & 0 \\ 0 & 0 & 0 & 0 & D_{55} & 0 \\ 0 & 0 & 0 & 0 & 0 & D_{66} \end{bmatrix} \begin{bmatrix} \varepsilon_1 \\ \varepsilon_2 \\ \varepsilon_3 \\ \gamma_{23} \\ \gamma_{31} \\ \gamma_{12} \end{bmatrix} \tag{2.1}$$

where, the D_{ij} are the independent material stiffness parameters. $\sigma_{ij},\ \tau_{ij}$ are the stress components and $\varepsilon_{ij},\ \gamma_{ij}$ are the strain components. A unidirectional lamina that is thin and not loaded in out-of-plane loads, could be considered in a state of plane stress [22, 23]. This reduces the problem from 3D to 2D and the number of independent material parameters from 12 to 4. Furthermore, the number of independent stress components is reduced from 6 to 3. Hooke's law for plane stress laminate is given as follows:

$$\begin{bmatrix} \sigma_1 \\ \sigma_2 \\ \tau_{12} \end{bmatrix} = \begin{bmatrix} Q_{11} & Q_{12} & 0 \\ Q_{12} & Q_{22} & 0 \\ 0 & 0 & Q_{66} \end{bmatrix} \begin{bmatrix} \varepsilon_1 \\ \varepsilon_2 \\ \gamma_{12} \end{bmatrix} \tag{2.2}$$

where, $Q_{11} = \frac{E_1}{1-\nu_{12}\nu_{21}}$, $Q_{12} = \frac{\nu_{12}E_2}{1-\nu_{12}\nu_{21}}$, $Q_{22} = \frac{E_2}{1-\nu_{12}\nu_{21}}$ and $Q_{66} = G_{12}$, E_i is the Young's modulus of the i^{th} direction and ν_{ij} is the Poisson ratio coupling the i and j planes.

When the lamina axes are not aligned with the global axes, certain rotation rules should be applied to transfer stresses and strains from local coordinates (lamina) to global coordinates. Assuming the fibre orientation angle of the lamina is (θ), the rotation matrix is given as

$$T = \begin{bmatrix} c^2 & s^2 & 2sc \\ s^2 & c^2 & -2sc \\ -sc & sc & c^2 - s^2 \end{bmatrix} \tag{2.3}$$

where, $c = cos(\theta)$ and $s = sin(\theta)$. In this work, positive orientation angle is defined from horizon and upwards in CW direction. The relation between the local and global stresses is given as

$$\begin{bmatrix} \sigma_x \\ \sigma_y \\ \tau_{xy} \end{bmatrix} = T^{-1} \begin{bmatrix} \sigma_1 \\ \sigma_2 \\ \tau_{12} \end{bmatrix} \tag{2.4}$$

Hooke's law for general 2D lamina in global coordinates is given as

$$\begin{bmatrix} \sigma_x \\ \sigma_y \\ \tau_{xy} \end{bmatrix} = \begin{bmatrix} \bar{Q}_{11} & \bar{Q}_{12} & \bar{Q}_{16} \\ \bar{Q}_{12} & \bar{Q}_{22} & \bar{Q}_{26} \\ \bar{Q}_{16} & \bar{Q}_{26} & \bar{Q}_{66} \end{bmatrix} \begin{bmatrix} \varepsilon_x \\ \varepsilon_y \\ \gamma_{xy} \end{bmatrix} \tag{2.5}$$

where,

$$\bar{Q}_{11} = Q_{11}c^4 + Q_{22}s^4 + 2(Q_{12} + 2Q_{66})s^2c^2$$

$$\bar{Q}_{12} = (Q_{11} + Q_{22} - 4Q_{66})s^2c^2 + Q_{12}(s^2 + c^4)$$

$$\bar{Q}_{22} = Q_{11}s^4 + Q_{22}c^4 + 2(Q_{12} + 2Q_{66})s^2c^2$$

$$\bar{Q}_{16} = (Q_{11} - Q_{12} - 2Q_{66})c^3s - (Q_{22} - Q_{12} - 2Q_{66})s^3c$$

$$\bar{Q}_{26} = (Q_{11} - Q_{12} - 2Q_{66})s^3c - (Q_{22} - Q_{12} - 2Q_{66})c^3s$$

$$\bar{Q}_{66} = (Q_{11} + Q_{22} - 2Q_{12} - 2Q_{66})s^2c^2 + Q_{66}(S^4 + c^4)$$

2.3.4 Failure of Composites

Failure of composites has been an active research field for over 50 years. Since the 1970s, numerous theories to predict composite failure have been proposed. The accepted practice in industry is to use theories that have been validated experimentally [26]. However, the difficulty in standardising test results has provided the context for what is known as "The World Wide Failure Exercise". The goal was to assess the predictive capability of the most prominent failure theories through carefully controlled case studies and then comparison with experimental evidence. The first exercise [9, 10, 12] was focused on predictions for in-plane failure cases. The second [13, 14] was concerned with 3D failure cases (e.g. delamination) and the third (which is still on-going) with progressive failure analysis [15,16].

In classical failure theories, *strength parameters* are used to predict the failure of lamina. For composite lamina in plane-stress condition, 5 independent strength parameters are usually needed: strength in fibre direction (tension and compression) ($X^t,\ X^c$), strength in transverse direction (tension and compression) ($Y^t,\ Y^c$) and in-plane shear (S^l). These parameters are obtained from standard mechanical testing of composites. These values provide the limit of strength of the lamina in principle stress directions. A complete description of failure can be achieved through failure envelopes. Failure envelope is a 3D plot of the combination of stresses that arises in a lamina at the onset of failure [23]. 2D plots are often used for simplicity where one stress component is assumed constant and the plot shows a slice in the 3D envelope. The material is considered safe if the stress state of the composite is within the envelope. The failure envelopes usually connect the strength parameters in principle directions so that the onset of failure could be estimated for arbitrary loading direction without the need for experimental data. This provides an easy tool for designers to assess the strength of composite components.

Failure theories of composites can be categorised into three main groups: (i) non-interactive theories (e.g. maximum stress, maximum strain); (ii) interactive theories (Tsai-Hill, Tsai-Wu); and (iii) failure mode-based theories (e.g. Hashin, Puck) [27]. The non-interactive theories do not account for the coupling of stress/strain component. The interactive theories do account for the coupling of stress components; however, they are not based on physical understanding of composites failure, rather it is a kind of curve fitting of experimental data. Failure mode-based theories distinguish between the different failure modes (e.g. fibre buckling, matrix cracking, etc.). This is expressed mathematically by deriving different expressions to generate corresponding parts of the failure envelope. A more detailed treatment of composites failure is presented in Section 3.8.1.

2.4 Machining of Composites

Composites are usually laid in near-net shape and some machining operations are usually required to bring the composite parts to the final geometry. Conventional and non-conventional machining methods are used. The most widely used conventional methods include edge trimming, drilling, milling and turning. Among the non-conventional machining processes are abrasive waterjet and laser beam cutting [1]. Obtaining high quality cut is more difficult in composites than in metals, due to their inhomogeneous, anisotropic nature and the complicated damage phenomena. Furthermore, cutting tools alternatively encounter the matrix and reinforcement, which have very different behaviour under cutting. This imposes special demands on tool geometry and tool wear [21] and can result in poor surface finish, dimensional inaccuracies and eventually rejected parts [28]. In this section, a description of the experimental findings in orthogonal cutting of composites is presented with emphasis on cutting forces and chip formation mechanisms.

2.4.1 Cutting Forces

Measurement of cutting forces[1] is among the fundamental outputs that shed light on the cutting process. A dynamometer is often employed in collecting the forces signal. The cutting force observations complement the chip formation mechanisms with the aim of gaining a better understanding of the cutting process. Many authors have measured the cutting forces during orthogonal cutting studies [3, 29–33].

The force signal is characterised by the existence of high frequency modes that indicate the discontinuous nature of the chips [28]. However, the extent of fluctuations is different

---

[1] In this work, cutting forces consist of the main cutting force F_c and thrust force F_t. For brevity, when discussed separately, F_c will be referred to as the cutting force.

for different fibre orientations as the force signal correlates well with the changing mode of chip formation with fibre orientations [1]. Fibre orientation is found to be the main factor affecting cutting force compared with cutting conditions and tool geometry. A direct comparison of the cutting forces reported in literature is difficult due to the variations in cutting conditions and materials used. Generally, it is noted that cutting force increases gradually between $\theta = 0^o$ and $\theta = 60^o$ or a local minima is observed in the range $15^o \leq \theta \leq 30^o$. Beyond 60^o, cutting force rises sharply to reach a maximum at 90^o. At orientations larger than 90^o, a decrease in the force magnitude is observed. A representative force values are shown in Figure 2.4 taken from the influential study of Wang et al. [3]. The fore mentioned trend in cutting forces is clear from the figure. The behaviour of thrust force is more complicated; at lower orientations, high magnitude (by comparison to cutting force) is observed. Beyond $\theta = 75^o$, the thrust force decreases. It is believed that the bouncing back effect has significant contribution to the high thrust force magnitude at lower orientations [1].

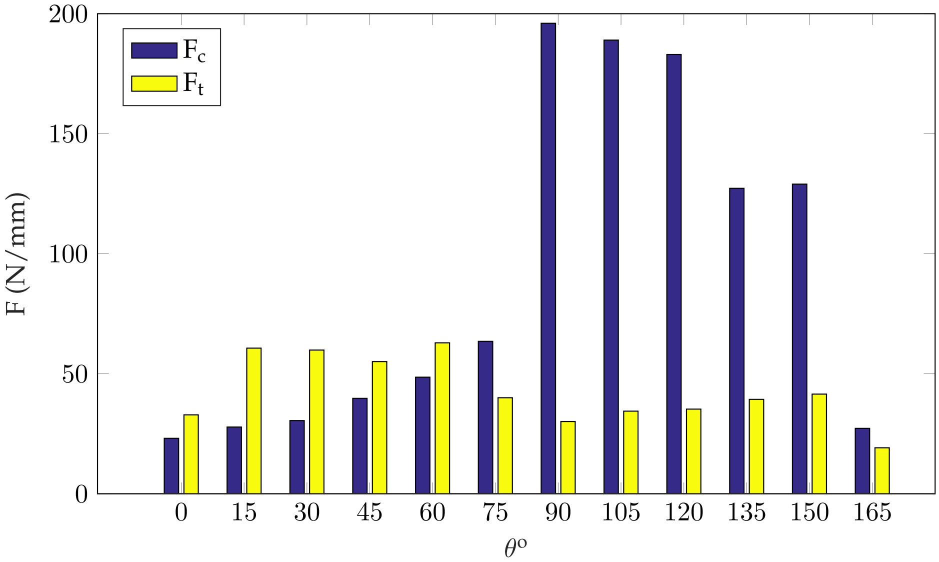

Figure 2.4: Mean cutting and thrust forces $V_c = 4m/min,\ a_c = 0.25mm,\ \alpha = 10^o$ [3]

The effect of rake angle was studied experimentally by Wang et al. [3] and found that at 0^o orientation, the cutting force decreased with increased rake angle, whereas at positive orientations $0 < \theta^o < 90$, increased rake angle caused a rise in the thrust force. The optimum rake angle to minimise the principle cutting force was found to be 30^o [28]. Several publications [3,29,31,34] have studied the effect of depth of cut on cutting forces; however, these studies investigated relatively small depth of cuts, between $0.08\ mm$ and $0.381\ mm$. It was found that the depth of cut causes an increase in the cutting force following a linear pattern. Quality of machined surface was closely related to the cutting mechanisms, which in turn was affected by fibre orientation. The best surface quality was obtained in the orientation range between 15^o and 60^o while at 0^o, roughness was marginally higher. Severe surface damage (delamination, matrix cracking) was observed beyond 60^o [3].

2.4.2 Chip Formation Mechanisms

Chip formation when cutting composites is very different than that when cutting metals. In metal cutting (especially ductile metals), cutting is assumed to happen due to plastic deformation along a shear plane extending from the cutting tool edge to the workpiece free surface. Composites on the other hand, exhibit very little plastic deformation and the chip formation is governed by fracture [1, 3]. Furthermore, due to the different failure mechanisms in unidirectional composites, fibre orientation plays a dominant role in chipping mechanisms. Several studies have investigated chip formation during orthogonal cutting of unidirectional composites [3, 31–33, 35–38]. Comprehensive discussion about chip formation mechanisms can be found in [1, 28].

There are several experimental techniques that were used to investigate the chip formation mechanisms. High speed camera was used to perform in-situ analysis of the chip formation in real time [3, 30, 35, 37, 38]. Macro-chip method was also used to collect the small and discontinuous chips resulting from cutting FRPs [3, 36]. In this method, a thin layer of glue is applied on the free surface of the workpiece. During the cutting process, the discontinuous chips are joined by the glue layer and can be inspected visually using visual microscope and/or scanning Electron Microscope (SEM). Quick stop method was also used to study the chip root and the contact between tool and workpiece [36]. Force signals have been used in previous work [35, 39] to infer the chipping process from the force signal, while Arola et al. [35] did not find clear correlation. However, Lopresto et al. [39] found a precise correlation between cutting force signal and the chipping action by performing the cutting experiments at very low speed (11mm/min). Other indirect methods include analysis of the roughness of the machined surface and then using some data processing techniques such as fast Fourier transforms or time series analysis [35].

In the following discussion, chip formation is divided into 4 categories. It is important to note that the last two categories are not entirely distinct. This is evident from the literature where chip formation is categorised into 5 groups in [1], 4 in [35] and 3 in [38]. The following discussion is summarised from [1, 3, 28, 35].

Chip formation when $\theta = 0^o$ and $\gamma \leq 0^o$

It is worth noting that tool geometry does not play a significant role in chip formation with the exception of cutting at $\theta = 0^o$. In this type of cutting, the tool applies intensive compressive stress on the workpiece at the rake face. The generated stress is in the same direction as the fibres, which leads to micro-buckling of fibres and failure due to mode II fracture loading. This is sometimes called “brooming failure”. As the tool advances into the workpiece, chips flow over the rake face and they fracture perpendicular to their direction near the cutting edge. A schematic of this mode is shown in Figure 2.5a.

Chip formation when $\theta = 0^o$ and $\gamma > 0^o$

When cutting with positive rake angle, the chipping mechanism changes. Mode I fracture becomes more prominent than mode II. A crack is formed at some distance ahead of the cutting tool along the fibre-matrix interface. As the cutting tool advances into the workpiece, chips are bent and are broken under cantilever loading, perpendicular to their direction. After separation, the bent chip flattens out due to the absence of plastic deformation. Chips surface is highly irregular indicating the bending fracture separation of the chip. A schematic is shown in Figure 2.5b.

Chip formation when $0^o < \theta \leq 90^o$

In this range, the chip is formed by two consecutive fractures, a primary fracture near the tool nose from compression-induced shear. This results in a process zone with crushed fibres and cracked matrix. The process zone extends to a small distance ahead of the cutting tool. A secondary fracture occurs along the fibre-matrix interface due to inter-laminar shear. It emanates from the primary fracture and propagates to the free surface. When mapping the cutting force signals on to the chipping mechanism, it was found that the maximum cutting force was recorded at the initiation of the primary fracture. The resulting chip can be seemingly continuous whereby the chips are loosely held together. This is noticed when cutting with positive rake angles and low orientations. With increased fibre orientations (60^o and above), the chip size decreases and the sub-surface damage becomes more severe. Bending-dominated failure of fibre replaces the shear fracture. Furthermore, out-of-plane displacement occurs at the un-supported edges leading to poor quality machined surface. The chips become dust-like ejecting at high speed ahead of the tool. This makes the collection of chips beyond 60^o orientations difficult. A schematic is shown in Figure 2.5c.

Chip formation when $\theta > 90^o$

This range of orientations is associated with the highest levels of subsurface damage and poorest quality. This is mainly due to the cutting action acting against the direction of the fibres. This causes extensive elastic bending in the fibres leading to delamination, interface failure and severe out-of-plane displacement at the unsupported edges. As the tool advances into the workpiece, the uncut fibres along the unsupported edges bounce back causing excessive rubbing against the clearance face. However, it was also noted that at the inner laminates, where macro-fracture is dominant, the depth of cut was often higher than the nominal depth of cut. This is caused by fibre fracture below the cutting plane and resulting in bulky discontinuous chips. A schematic illustrating this chipping mechanism is shown in Figure 2.5d.

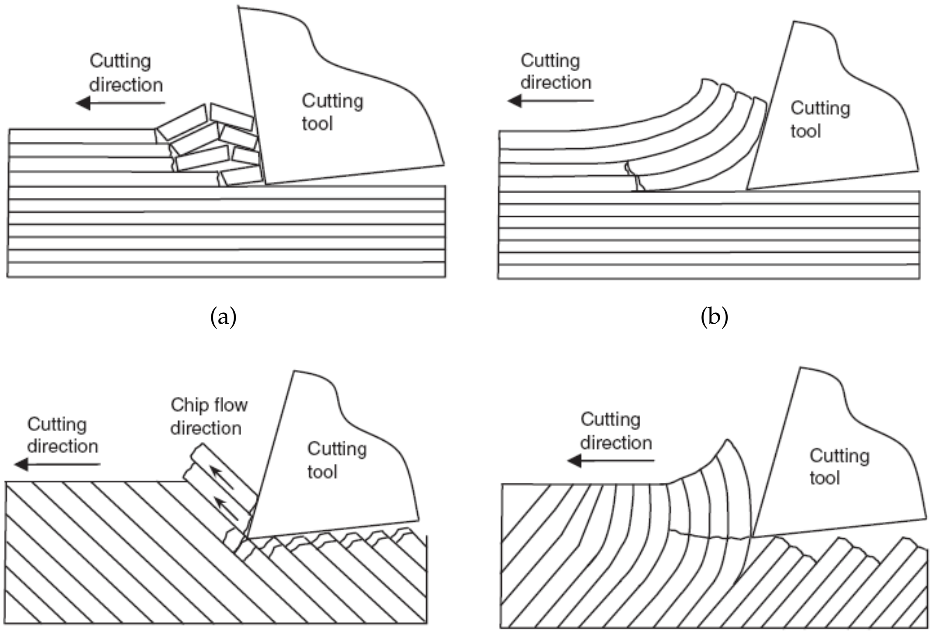

(a) (b)

(c) (d)

Figure 2.5: Chip formation modes as function of fibre orientation and tool rake angle [1]

2.5 Numerical Modelling

Numerical modelling of physical phenomena/systems is an essential feature of modern-day engineering activities. Its importance comes from the increasing complexity of engineering systems and the need to increase productivity and reduce costs. The term *digital prototyping* is now common place and refers to the complete system design and testing before any actual physical model is built. While there are many approaches used to construct a model, the focus in this work is on *numerical modelling*, in which the problem of interest is described in terms of partial differential equations with complicated geometries/boundary conditions that defy closed form (analytical) solutions. Numerical modelling of any physical problem has three main steps [40]: (i) problem definition (idealisation and simplification of the problem), (ii) mathematical model (representing the problem using governing equations) and (iii) computer simulation (solving the mathematical model using numerical methods). There are several numerical methods that could be used, such as

Finite Difference Method (FDM), Finite Element Method (FEM), Finite Volume Method (FVM), Boundary Element Method (BEM) and Meshfree Methods (MM).

FEM is the most used method in solid mechanics problems. It was proposed in the 1950s [41] and has undergone significant improvements to the point where it is currently the method of choice for modelling most of the engineering problems. In classical FEM, the problem domain is *discretised* into a set of finite connected elements. The field variable is approximated using interpolation functions over these elements and then assembled into sparse system equations. As such, the governing Partial Differential Equations (PDEs) are converted into a set of finite algebraic equations and an approximate solution is reached. Despite the success of FEM in many engineering applications, it is not without drawbacks. Many of these drawbacks are related to the existence of mesh [42]. Some of these shortcomings can be summarised as follows [4, 42–44]:

1. High cost in creating FEM mesh: mesh creation takes considerable amount of time. Man-labour costs are usually higher than that of computer, thus automatic discretisation of the domain becomes advantageous but not yet attainable for complex problems in FEM.

2. Low accuracy in stress: in models that study stress, the resulting stresses are often discontinuous at the interfaces of elements. Post processing is required to overcome this issue.

3. Difficulty in adaptive analysis: in adaptive analysis, remeshing is required which is expensive and complicated for 3D domains. Moreover, projections of field variables between successive meshes reduce the accuracy and add to computing time.

4. Limitation on analysis of some problems:

    4.1. Problems with large deformations

    4.2. Crack growth with arbitrary and complex paths

    4.3. It is very difficult to simulate the breakage of material with large number of fragments since FEM takes continuum mechanics approach and elements cannot be broken (element is either bonded or debonded)

5. FEM is not well suited for modelling discontinuities if the discontinuities do not coincide with elements' boundaries.

2.5.1 Meshfree Methods

Out of the above limitations and difficulties in FEM, meshfree methods were developed as an alternative for solving partial differential equations and boundary value problems. Meshfree methods can be defined as *"a method used to establish system algebraic equations for the whole problem domain without the use of a predefined mesh for the domain discretisation"* [42]. In meshfree methods, the construction of the shape function is done in terms of nodes rather than elements [45], thus eliminating the dependency on structured mesh. As seen in Figure 2.6, in MM, there is no connectivity between field nodes, which gives more freedom in moving, adding or removing nodes without worrying about their neighbouring points [42]. Review papers detailing state of the art in Meshfree methods can be found in [44–47].

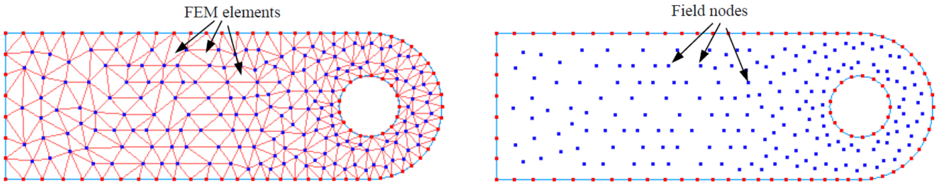

(a) FEM

(b) Meshfree

Figure 2.6: Difference in domain discretisation between FEM and Meshfree [4]

The first meshfree method, namely smoothed particle hydrodynamics, was developed in 1977 to solve boundless problems in astrophysics [44]. Later, substantial developments in MMs were made in the 1990s, where other methods and improvements were developed by influential researchers such as Belyteschko [48] , Liu [42], Daurte and Oden [49]. New methods and improvements to existing methods are still being proposed. Nonetheless, when compared with FEM, MMs are still under developed with large potential for improvement. Currently several meshfree methods exist; a non-exhaustive list include [50]:

- Smooth particle hydrodynamic (SPH)
- Element-free Galerkin (EFG)
- Reproducing kernel particle method
- Partition of unity
- Finite pointset method
- Discrete element method
- hp clouds
- Meshless finite element
- Finite sphere
- Natural element
- Non-structured finite differences
- Diffusive elements

These methods have been applied to solid mechanics problems [42,44,51,52], machining of metals [53–59], forming of metals [60] and fracture of composite materials [61–63]. EFG will be used in this research, a review of which will be presented in the next section. Derivation and implementation will be presented in Chapters 3, 4 and 5.

2.5.2 The Element-Free Galerkin Method

The EFG method was conceived in Belytschko's seminal paper in 1994 [48]. The method was an improvement of the diffuse element method proposed by Nayroles [64]. It utilised Moving Least Squares (MLS) approximation in constructing the shape functions. In the subsequent years, the EFG was extended and improved [8,65–72] with particular success in fracture mechanics applications. The lack of nodal connectivity is found to be especially helpful in modelling both static and dynamic fracture problems. As such the EFG became one of the most mature and widely used meshfree methods. The full extent of the EFG techniques that have been developed thus far are shown graphically in Appendix (B.1) and different applications of the EFG can be found in Appendix (B.2). Below is a summary of the state of the art in different aspects of the EFG:

Discontinuities

Dealing with continuous domains with embedded discontinuity gained a lot of attention in the context of EFG. Effective handling of discontinuities is essential for a robust and versatile method, since it allows the method to be applied in non-convex domains and to treat singularities such as the ones arising at the crack tip in fracture mechanics. Visibility criteria was the first of such methods, proposed by Belytschko et al. [48] and applied to static fracture. In this method, the domain of influence (DoI) of nodes in the vicinity of cracks are truncated to exclude nodes that are not “visible”from the point of interest. This has proven to be very powerful and simple technique, and was subsequently used in several publications. Other methods were also proposed such as the diffraction method [72] and the transparency method [8]. These were basically variations on the concept of visibility but rather than eliminating the non-visible nodes, the values of the shape function at these nodes were “filtered”due to the presence of cracks. These methods produced smoother shape functions resulting in better convergence. Another approach in handling crack problems is by using enrichment, in which the basis function is augmented with additional terms to improve the approximation accuracy near cracks. Several techniques were proposed and they can be categorised into two groups [8, 52]:

- Extrinsic enrichment: extrinsic MLS enrichment and extrinsic partition of unity enrichment
- Intrinsic enrichment: full basis enrichment and radial basis enrichment.

Shape Function

One of the most distinguishing features of the EFG method is the use of the MLS approximation to construct the shape functions. These shape functions are smooth and provide at least C^1 continuity. Detailed discussion on the construction of the shape function can be found in Section 3.3. A weight function is used to construct the shape function. The selection of the weight function is important to the resulting shape function. There are few criteria to select the weight function such as [4] :

1. Positive within the support domain
2. Vanishes outside the support domain
3. Monotonically decreasing from the point of interest
4. Sufficiently smooth, especially at the boundaries

Several weight functions have been proposed and use such as:

- Truncated Gaussian [48]
- Exponential [4]
- Cubic Spline [73]
- Quartic Spline [69]
- Higher order polynomial [74]

These weight functions all fulfil the above mentioned weight function criteria. Most and Butcher [75] proposed new weight function, which approximately fulfils the essential boundary conditions. This allows for the direct imposition of the essential boundary conditions, unlike the other weight functions, which result in shape functions that require special enforcement techniques at the essential boundaries. The lack of Kronecker-Delta property was also explored by Askes et al. [76], who found that MLS shape functions were generalisation of the finite element shape function which could be recovered from the MLS formulation by a certain choice of the domain of influence. Standard finite elements could be obtained if a C^0 weight function (e.g. piecewise constant) is used [48].

Improvements on the standard MLS formulation started with the work of Liew et al. [77], where they proposed an improved MLS approximation (IMLS) that utilises weighted orthogonal basis functions instead of a generic monomial basis functions. This formulation avoids the numerical efforts of inverting the moment matrix by developing an alternative diagonal moment matrix, thereby avoiding the possibility of ill-conditioning of the MLS equations. This formulation was later adopted in several subsequent publications such as [78–82]. Another improvement of the MLS approximation was proposed by Ren and Cheng [83] and applied to 2D potential problems. This implementation is called the Interpolating MLS (IMLS), whereby the shape function possesses the Kronecker-Delta property, which simplifies the implementation of the Dirichlet boundary conditions. Subsequently, this method was applied by Abbaszadeh and Dehghan [84] for solving fractional reaction sub-diffusion problem, by Cheng et al. [85] to solve 2D elasto-plasticity problems and by Dehghan et al. [86] to solve the regularised long wave equations. Local maximum entropy shape function was used in the context of EFG by Ullah et al. [87] for linear and nonlinear solid mechanics problems.

Domain of Influence

The domain of influence (DoI) is a local part of the domain that is constructed around a node where it has "influence", that is, it contributes to shape function and field variables calculations. Usually EFG calculations are performed at integration points, as such all the nodes that have integration point within their DoI will contribute to the calculations. Conventionally, a square or circular DoIs are constructed around the node. Another method of constructing the DoI is suggested by Zhang et al. [78], in which an arbitrary polygon is constructed around the node using neighbouring nodes and the polygon is used as DoI. It was found that this procedure is more computationally efficient and avoids the ill-conditioning of the moment matrix. The DoI construction is performed using the average nodal spacing and a non-dimensional quantity, namely β, controls the size of the DoI.

The size of the DoI has been studied extensively in many papers since it has a significant effect on the computational cost of the method and the recommended value depends on the application. The size of DoI in dynamic problems usually should be smaller than similar static ones due to the hyperbolic nature of the governing equations [65]. Large DoI values were found to be suitable in plates analysis [74], while Chung et al. [88] found that minimising the DoI while retaining the regularity of the moment matrix is the best option to minimise the errors associated with the meshfree interpolation.

Numerical Integration

Numerical integration of the weak form is a major concern since many meshless shape functions are non-polynomial, meaning that exact integration is very difficult/impossible for many meshfree methods [52]. The most widely used numerical integration techniques are [52]:

- direct nodal integration
- stabilised nodal integration
- stress point integration
- support-based integration
- background mesh integration (using Gauss quadrature)
- cell structure integration (using Gauss quadrature)

In problems of small and moderate deformations, integration using background mesh or cell structure is preferred because of their higher accuracy, while methods based on nodal and stress point integration are preferred in dynamics and large deformation problems [52] because it avoids remapping of the state variables that are required in other methods like the FEM [89].

In Puso et al. [89], the authors investigated three nodal integration schemes, namely nodal strain method, stabilised conforming nodal integration (SCNI) and nodal averaging. Recently, Li et al. [90] proposed a new integration scheme that employs the divergence-free condition combined with the truly mesh-free concepts and called it *support integration methods*. The new method was found to be efficient but aimed only at explicit or matrix-free implicit solvers. Methods that require stiffness matrices were not included [91]. In 2012, Racz and Bui [92] proposed two adaptive numerical integration schemes using mapping of complex integration domain into simpler ones. By using these methods, a truly meshfree implementation was achieved by eliminating the need for mesh-based integration schemes such as background mesh or cell structure that was employed in the standard EFGM and RIPM. Liu and Tu [93] proposed integrating the domain using background mesh by using triangular integration cells rather than the conventional quadrilateral cells. The field nodes are used as cell vertices. This approach can make the automatic mesh generation easier for complex shapes. In order to increase the efficiency of the nodal search during the construction of the domain of influence, bucket algorithm is used. In an earlier study, the same authors proposed a relay model for irregular domains containing arbitrary number of cracks, discontinuities and non-convex boundaries [93].

Liu et al. [91] proposed a new numerical integration technique based on the local support that takes advantage of the divergence-free condition. This method is developed mainly for explicit time integration or implicit integrators without explicit derivative calculations. The proposed nodal support integration scheme share similarities with the truly meshless methods but is much quicker since only n+1 integration points per particle is required (n is the number of dimensions of the problems) as opposed to dozens of points. The position of the quadrature point depends only on the nodal location and support domain. However, the weights of the quadrature points have to be calculated and cannot be evaluated explicitly, as such these are calculated at the beginning of the simulation using full Gaussian quadrature. Other integration methods include hierarchical cover construction coupled with decomposition quadrature [94].

2.6 Numerical Modelling of Machining Composites

This section presents state of the art in modelling of orthogonal cutting of unidirectional FRPs. Building a numerical model to simulate cutting of FRP requires several decisions from the engineer/researcher. The major ones can be summarised as:

- Choice of numerical method (e.g. FEM, MM)
- Type of mesh (e.g. Lagrangian, Eulerian)
- Number of dimensions (two or three)

- Inclusion of dynamic effects
- Constitutive model to be used (e.g. Elastic, Elasto-plastic)
- Failure modelling to be used (e.g. max stress, Hashin)
- Modelling contact between the tool and workpiece
- Required outputs from the model (e.g. cutting forces, temperature)

Below is a detailed explanation of each of the above points including how different studies compare to each other. Hopefully this would provide a clear guidance of the overall process beyond summarising what each study has done.

2.6.1 Numerical Method

This is the first basic choice that the engineer has to make. The majority of studies have used FEM due to its maturity and the availability of several commercial packages (ANSYS, Abaqus, Ls-Dyna, etc). It was noted however, that most of FEM studies have used Abaqus [5, 6, 34, 95–105]. Recently, meshfree methods have been used to investigate cutting composites. Iliescu et al. [106] used the discrete element method, Shchurov et al. [107] used SPH method, and most recently, Kahwash et al. [108] have used the Element-free Galerkin Method. There is limited availability of meshfree methods in commercial software with exception of the SPH. However, LS-Dyna is pioneering the integration of other methods (e.g. isogemetric analysis and smoothed particle Galerkin) into the software.

2.6.2 Type of Mesh

There are three basic types of meshes, namely, Lagrangian, Eulerian and Arbitrary Lagrangian-Eulerian (ALE). Lagrangian mesh is the most used type in solid mechanics codes. The mesh nodes are connected to material points in the domain and as the material points move, the nodes move similarly. In Eulerian meshes, the mesh is fixed in space and the materials move through the computational domain. It is mainly used in fluid mechanics although it was used in early modelling of machining of metals, where chip shape could be reasonably assumed. In ALE approach, the mesh is neither fixed in space nor fixed on material points, rather it can move in arbitrary manner (not random though, 1 to 1 mapping has to be maintained for every time step between the mesh and material points, although not necessarily the same point [72]). The ALE formulation can be used to combine the advantages of the Lagrangian and Eulerian types. However, it is difficult to implement numerically. An additional non-symmetric advective term appears in the discretised system equations and needs special solving techniques such as operator splitting to deal with the coupled system equations. Previous work [98, 109–111] have used ALE, but not all have explicitly stated which approach was used.

2.6.3 Number of Dimensions

One of the main reasons to choose orthogonal cutting is because it can be reasonably assumed as a 2D process. Indeed, most of past research have assumed this [5–7,95,98,99,110, 112]. However, recently several 3D models have been proposed. Mahdi and Zhang [109] were the earliest to propose such a model, later [97, 100, 103–105, 107, 113] have proposed 3D orthogonal cutting models. The most interesting approach was found in the work of Santiuste et al. [100]. They compared the damage of the 2D and 3D orthogonal cutting models. It was found outer lamina damage profile resembled that of the 2D case, whereas inner lamina had lesser damage. As such, it was concluded that thinner laminates are approximated better by 2D model than thicker ones.

2.6.4 Dynamic Effects

Machining simulation can be steady-state [5, 31, 95, 97, 110, 112] or dynamic [7, 99–103, 105, 111, 113, 114]. Steady-state simulation utilises implicit algorithms (e.g. Newton Methods), while the dynamic uses explicit algorithms (e.g. central differencing). By changing the simulation from steady-state to dynamic, the nature of the governing PDE changes and the solution methods requires more attention. Cutting speed and computational resources should be considered when making this choice as dynamic simulations are usually more time consuming. The dynamic approach is more suitable for high speed machining and for capturing chip formation mechanisms. Publications trend is moving toward the dynamic approach. This might be due to the highly transient nature of composites cutting and the increased availability of computational resources needed for dynamic studies.

2.6.5 Constitutive Model

Material modelling is a crucial aspect in modelling of machining. The material behaviour is modelled by an appropriate constitutive model. It is critical to appreciate that choosing a certain constitutive models is an *assumption* about the behaviour of the real material and has to be justified in light of the cutting conditions that the model is built to predict. Furthermore, the availability of reliable material data poses an obstacle in adopting more sophisticated constitutive models. For example, if a FRP laminate is assumed to be orthotropic in plane stress, 4 independent material parameters need to be known; whereas if it is assumed to be anisotropic in general stress state, 21 independent parameters should be known. Another assumption about the material is the uniformity of composite plates. Only one study in literature was found to address this issue; Calzada et al. [7] identified three main parameters: fibre angle deviation, fibre grouping number and matrix spacing. These parameters measure the variability of the composite from perfect unidirectional lamina. SEM imaging was used to scan the workpiece samples and estimate the values of these parameters, which were then used to generate the modelled workpiece.

Two main approaches are used in modelling composite workpieces, namely, single phase models and multi-phase models.

Single phase models

Single phase models are commonly known in literature as Equivalent Homogeneous Material models (EHM) or macro-mechanical models. In this approach, the composite plate is assumed to be one phase with mechanical properties obtained from testing the laminates.

In most studies that have adopted this approach [5,6,95,96,99,100,102,105,111,112,114], the material is assumed to be orthotropic and in plane stress condition. This method is widely used to date due to the significant simplification in solution it offers. Most of the studies have used a linear elastic up to failure constitutive model on the basis that composites are brittle material that show little or no plastic deformation before failure and the chip formation is discontinuous [115]. However, Zenia et al. [102,114] have developed elasto-plastic constitutive model with isotropic hardening and no plastic flow in the fibre direction. Good agreement between predicted cutting force and high speed machining experiments was obtained as a result.

Multi-phase models

Multi-phase models are commonly referred to as micro-mechanical models. Following this approach, the matrix, fibres and often an interface are modelled using distinct constitutive equations. Given the dimensions of fibres (usually in the order of $10\ \mu m$), the mesh used in this type of model is significantly smaller than that necessary in the single phase models. $1 \times 1\ \mu m$ element size is common in literature. In order to reduce the computational cost, some studies have used a combination of single and multi-phase models. The area of interest is modelled as multi-phase, while the surrounding areas are modelled as single phase. Multi-phase models are usually better than single phase in predicting the complex behaviour of composites under machining conditions. Most of the studies have assumed the fibres to be elastic up to failure materials. Glass fibres were modelled as isotropic linear elastic [34,116] with exception of Dandekar and Shin [98] who assumed it to be isotropic and strain rate dependent. Carbon fibres were modelled as anisotropic linear elastic materials in [7,98,103,105,117]. The matrix (epoxy) is often modelled as elasto-plastic with von Mises yield criterion and isotropic hardening [7,34,103,105,116,117] with the exception of Dandekar and Shin [98] who modelled the matrix as isotropic linear elastic.

Multi-phase material approach requires an auxiliary model to describe the interaction between the phases. This is physically equivalent to the adhesion bond between the matrix and the fibres or between adjacent lamina. Cohesive zone elements (CZE) are mostly used to achieve this end. Zero or finite thickness elements can be used. Separation-traction law is a widely used mechanism that govern the failure of these elements. It has been applied in [34, 98, 103]. Further discussion about CZE can be found in the work of Abena et al. [103].

2.6.6 Failure Modelling

Failure modelling is another critical aspect in machining simulations. It is also found in literature under the term "chip separation criteria". Failure modelling has two essential components: failure initiation and failure progression.

Failure Initiation

Failure initiation model controls the onset of failure in the workpiece material. This is calculated usually at the integration points of elements. Failure initiation model differs in single and multi-phase material models. Single phase models usually utilise one of the numerous composite failure criteria found in literature, such as Tsai-Hill [31, 95, 97, 110, 111], maximum stress [31,112], and Hashin [99,101,104,112,118]. Some studies [5,6,95,96] combined two failure models, that is a primary model for the onset of chip formation and a secondary for the progressive failure. This was justified based on experimental observations of chip formation mechanisms in the range $0^o < \theta < 90^o$ (refer to Section 2.4.2).

In multi-phase materials, failure of each constituent is modelled independently in addition to the interface failure (CZE elements failure). Rao et al. [34] used von Mises yield criterion to estimate the matrix failure. Rao et al. [116] assumed the fibres failed once the principle stresses at the Gauss points reached the critical value. Fibre failure in [98] was modelled using Marigo model for brittle materials.

Failure Progression

Failure progression is essentially a numerical technique used to simulate the behaviour of material point post initial failure. Two main approaches have been used, sudden stiffness degradation [112] or continuum damage mechanics approach [99–101, 118]. In the former, the stiffness parameters at the failed material point is multiplied by a small number (usually in the order of 0.01). Whereas in the latter, stiffness degradation occurs gradually between two critical values of strain. The former method is easier to implement and is less susceptible to mesh-sensitivity issues. However, Santiuste et al. [99] used the continuum damage model to distinguish between the failure of GFRP and CFRP. This was achieved by changing the energy level required to totally break an element after the initial failure. The approach seem to capture some of the different behaviour in failure between glass and carbon FRPs. However, the parameter that controls this behaviour was not measured experimentally.

2.6.7 Tool-Workpiece Contact

Contact is one of the most difficult phenomena to model using continuum mechanics approach. This is because of the inherent discontinuity at the moments of contact and separation of contacting bodies. Furthermore, it adds one more non-linearity to the problem as the contact boundary is part of the solution and requires special techniques to deal with it. In orthogonal cutting simulations, the tool contacts the chipped region at the rake face and possibly the machined surface at the clearance face. High levels of friction exist since most FRP machining is performed dry. All existing literature have used Coulomb friction law in orthogonal cutting models. Nayak et al. [6] conducted pin-on-disk experiments on composites and found that there is a strong influence of θ on the value of friction coefficient, which was incorporated in later studies [7, 111]. However, most studies used a constant friction coefficient, usually in the range 0.3 to 0.5. Clearly, this is an area in which significant improvement is yet to be made.

2.6.8 Studied Outputs

Arrazola et al. [43] have argued that the outputs in machining simulations can be grouped into two main categories. The first category consists of fundamental variables such as cutting forces, chip dimensions, temperature, etc. The second category is the "industry-relevant outcomes", such as tool wear, surface roughness, residual stresses, etc. Outcomes of the first category could be used to estimate the second category outcomes. The second category is deemed as the most important as it leads to improvements in productivity. Three outputs were mainly studied in the modelling of machining literature, namely, cutting forces, chip formation/chipping mechanisms and machined surface damage. The findings are detailed below:

Cutting Forces

Cutting forces were studied extensively with nearly all papers predicted them. Some popular experimental results have been used for validation of several models. A collection of predicted cutting force data compared with experiments are shown in Figures 2.7, 2.8 and 2.9. These studies cover different cutting conditions and material parameters. Generally, the trend of cutting force was predicted well in literature to more or lesser degree of accuracy.

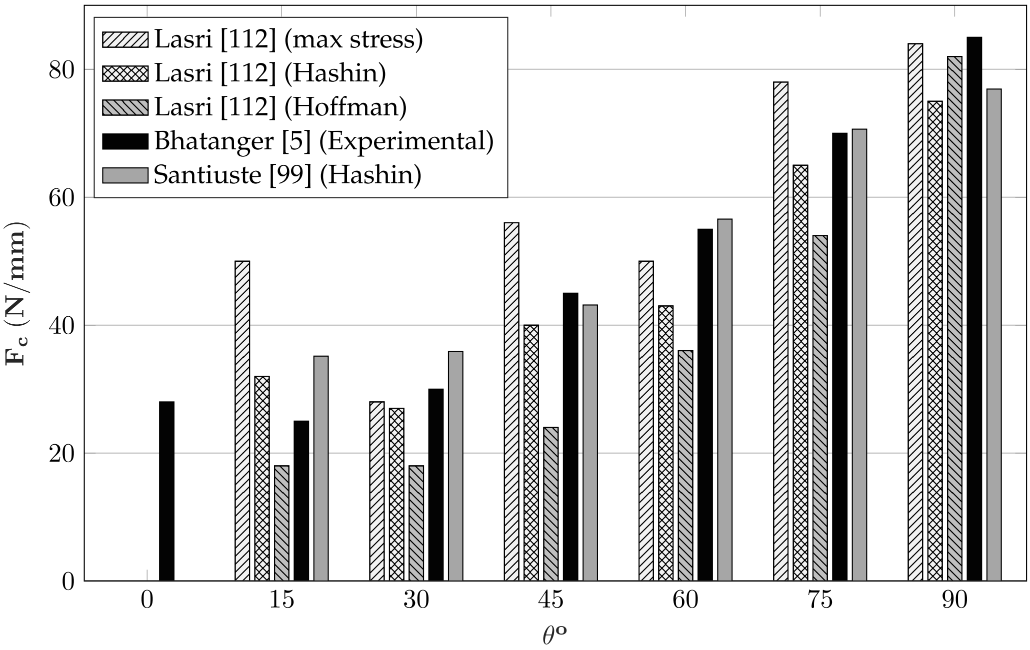

Figure 2.7: Comparison of cutting force predictions against experimental evidence of Bhatnagar et al. [5]. Cutting conditions: $V = 0.5\ m/min$, $a_c = 0.2\ mm$, $\gamma = 5^o$

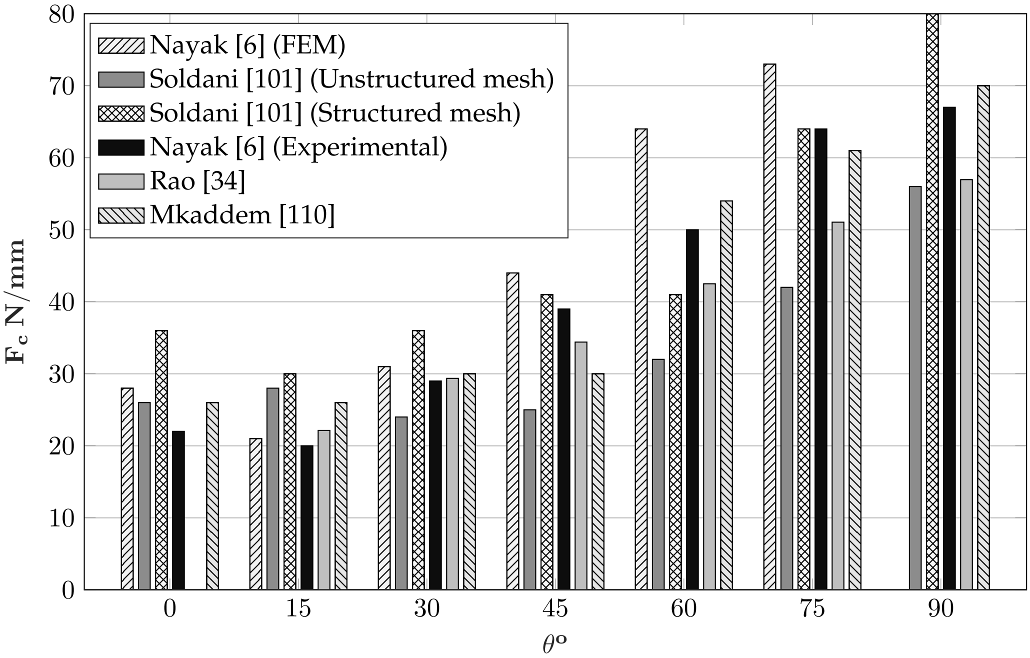

Figure 2.8: Comparison of cutting force predictions against experimental evidence of Nayak et al. [6]. Cutting conditions: $V = 0.5\ m/min$, $a_c = 0.2\ mm$, $\gamma = 10^o$

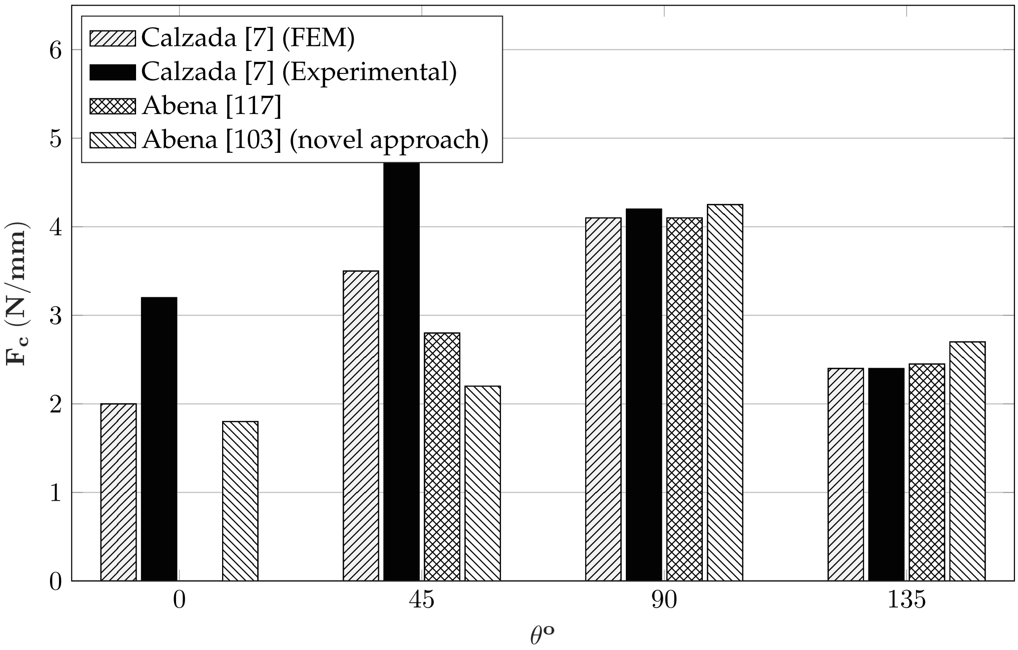

Figure 2.9: Comparison of cutting force predictions against experimental evidence of Calzada et al. [7]. Cutting conditions: $V = 500\ m/min$, $a_c = 0.015\ mm$, $\gamma = 25^o$

Predictions of thrust force proved to be much more challenging than that of cutting force as is clear from Figures 2.10, 2.11 and 2.12. In Figure 2.10, with the exception of Santiuste model [99], thrust values were an order of magnitude less than that of the experimental values. Several hypothesis were put to explain this, such as the inability to capture the *bouncing back effect*, which is a reaction of the machined surface on the clearance face of the tool. This was identified as one of the major reasons [112]. Another contributing factor was to start simulations at some distance inside the workpiece and not from the edge [6].

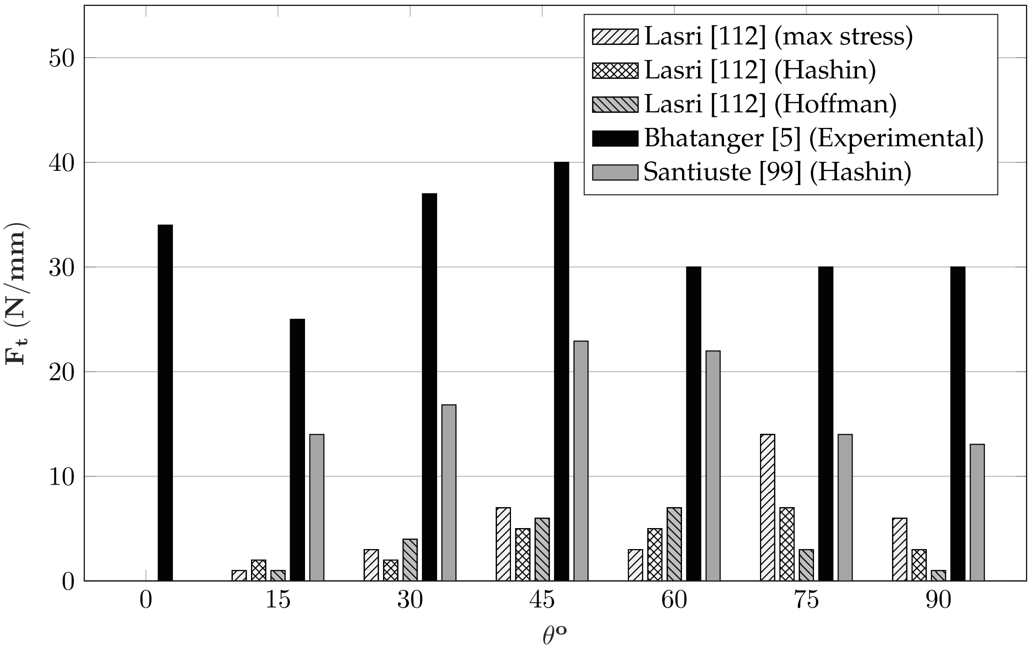

Figure 2.10: Comparison of thrust force predictions against experimental evidence of Bhatnagar et al. [5]. Cutting conditions: $V = 0.5\ m/min$, $a_c = 0.2\ mm$, $\gamma = 5^o$

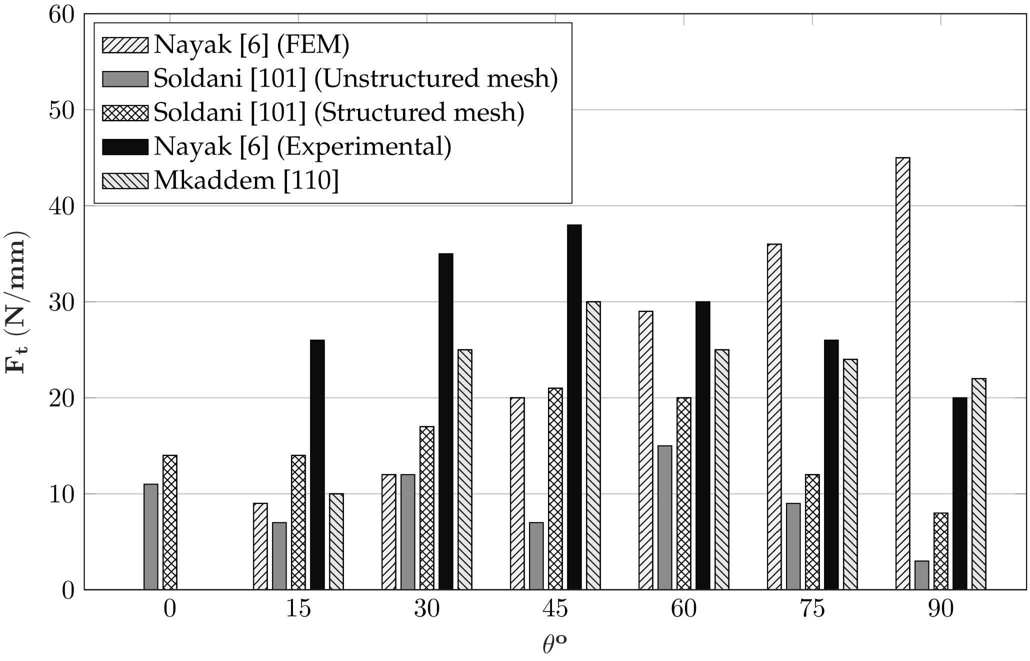

Figure 2.11: Comparison of thrust force predictions against experimental evidence of Nayak et al. [6]. Cutting conditions: $V = 0.5\ m/min$, $a_c = 0.2\ mm$, $\gamma = 10^o$

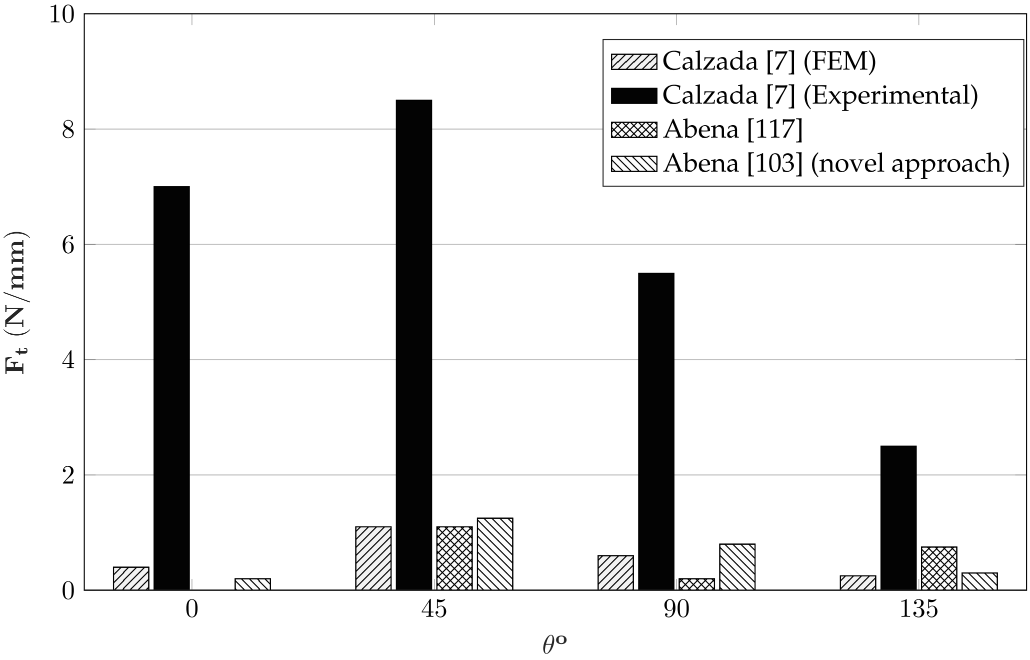

Figure 2.12: Comparison of thrust force predictions against experimental evidence of Calzada et al. [7]. Cutting conditions: $V = 500\,m/min$, $a_c = 0.015\,mm$, $\gamma = 25^o$

Chipped Region

The study of the chipped region is different for single and multi-phase models. In single phase models, the failure model is used to generate failure envelope in the workpiece (both in the chipping region and in the machined area) which is used to deduce the shape of the chip and the mode of failure. Failure in the local material system is often correlated with different modes of failure. For example, failure in the local x direction is usually interpreted as fibre failure; failure in the local y direction is interpreted as matrix failure and in local xy as interface failure. This is a powerful way to infer the type of the damage in the constituents of the composite without the need to use multi-phase models.

Lasri et al. [112] used three different failure criteria and found that interface failure is the first to initiate and propagate along the fibre direction. Fibre breakage was last to initiate above the nominal cutting plane. This was also observed by Santiuste et al. [99] who found negligible fibre failure at the completion of the chip. The variation in the size of the chip between CFRP and GFRP was found to be substantial. This was modelled through continuum damage mechanics approach (refer to Section 2.6.6). Mkaddem et al. [111] found the application of ALE mesh to be beneficial in studying chip formation mechanisms. The dimensions of the modelled chip were changed according to the fibre orientation and the size of the chip was reduced with increased θ as experimentally observed. Zenia et al. [102, 114] modelled the chip formation and cutting forces with single phase elasto-plastic material model. The chipping process for 45^o fibre orientations was found to follow the two fracture planes model which was observed experimentally. However, it was not shown for other studied orientations such as 90^o and 0^o.

Multi-phase modelling allows for deeper investigation of the chip formation process than single phase models. Nayak et al. [6] utilised a multi-phase FEM model to investigate the mode of chip breakage. It was noted that the modelled fibre in contact with the tool was subjected to compressive stress on the contact face and tensile stress on the opposite side due to the inferior strength of the supporting matrix. Failure initiation in the fibre was observed on the back side of the fibre. The stresses were mainly coincident with the fibre direction indicating the fibre breakage is likely to happen along the transverse plane. It was also found that the length of the chip is likely to decrease with increased fibre orientation, which correlated well with experimental evidence from Nayak et al. [31]. Failure initiation was found to start in the matrix behind the first row of fibres contacting the tool [116] then propagating to the adjacent fibres. One of the useful insights about the model by Rao et al. [116] was the prediction of loose or hanging chip for depth of cut larger than 0.1mm, as the matrix damage did not reach the free surface at the complete failure of fibres. Fibre failure was predicted on its front and back by the model proposed by Dandekar et al. [98]. The micro-machining model [7] was used for detailed simulation of chip formation at 0^o, 45^o, 90^o and 135^o fibre orientations. At 0^o, the phases were seen to separate at the interface and then followed by bending failure in the fibres at a distance ahead of the tool edge. At 90^o, the bending stress in fibres under cutting plane was less than usually observed in macro-machining, however, crushing-dominated failure was observed ahead of the cutting tool. For 135^o orientation, interfacial failure caused the fibre to be peeled from the rest of the workpiece and eventually failed under bending beneath the nominal cutting plane.

Machined Surface Damage

This is sometimes called sub-surface damage and is mainly caused by de-bonding failure and matrix cracking due to the pressure of the cutting tool on the workpiece, leading to a reduction in service life of the component [5]. One of the early studies in trying to quantify this is by Bhatnagar et al. [5]. Experimentally machined surface was cleaned and dyed then imaged with UV light to show the extent of the subsurface damage. Single phase FEM model was then proposed with Tsai-Hill failure criteria to estimate the sub-surface damage. The model was able to predict, with reasonable accuracy, the extent of damage for fibre orientations $\theta^o < 60$ but it was under-estimating the damage in higher orientations. The effect of cutting conditions on subsurface damage was carried out by Nayak et al. [6]. Tsai-Hill criteria was also used and found that fibre orientations and depth of cut had the largest effect on the sub-surface damage. The minimum damage is found at orientations 15^o to 30^o, this means that the cutting force correlates well with the sub-surface damage as opposed to thrust force. Lower cutting forces are likely to give better surface quality. The effect of rake angle was found to be less significant for small fibre orientations. With larger orientations, a reduction in damage was observed with higher rake angles up to 30^o. Multi-phase models were also used to estimate machined surface damage [34,116]. One of the main advantages is the ability to predict failure modes related to the damage. It was found that matrix damage is the main reason for the subsurface damage for all the studied cutting conditions.

2.7 Gaps in Literature

The need for modelling of machining composites is clear for several reasons:

- *Better understanding of the fundamentals of the cutting process*, especially where it is difficult to obtain experimental data (e.g. strain rates and temperature distribution inside the workpiece). Significant progress have been made by utilising numerical models. For example, better understanding of failure mechanisms in fibres was made in several publications [31,34,98].

- *Optimisation of cutting parameters in a cost effective way.* Once a reliable cutting model is developed, it can be used iteratively to choose cutting speed, depth of cut, rake angle, etc. This has the potential to save time and resources compared with the experimental approach; albeit, validation of modelling results through experiments is always recommended when possible. However, the number of the experiments can be reduced significantly if preceded by numerical simulations.
- *Guiding design of cutting tools.* By calculating the temperatures and forces acting on the cutting tools at different operating conditions, better tools can be designed for specific material/application. A good illustration of this is shown in the work of Calzada et al. [7], where the orthogonal cutting model was used to modify an existing cutting tool used in micro-machining of CFRP workpieces to yield lower cutting forces.

As shown in Section 2.6.1, the majority of the numerical models of machining composites utilised FEM. This is not surprising given the robustness and availability of FEM. However, mesh generation is still a bottleneck in the engineering analysis process, especially for complex systems. For example, it is estimated that mesh generation takes about 80% of the overall analysis time in aerospace and automotive industries. In automotive industry, creating a complete mesh for a vehicle could takes about four months [119]. The advent of novel numerical methods such as meshfree methods provides an opportunity to alleviate some of the burden of creating a mesh. As discussed in Section 2.5.1, meshfree methods are well suited to study problems with large deformation, fracture and arbitrary crack growth, all of which make them good candidate to simulate the cutting process. Furthermore, meshfree methods could improve some limitations in modelling composites using FEM. As seen in Soldani et al. [101], the direction of mesh affected the chip formation predictions. It is usually recommended to align element edges with fibre orientation [120]. This means that a separate mesh should be created for each fibre orientation under investigation.

2.8 Concluding Remarks

This chapter aimed at providing context for the research effort presented in later chapters. To achieve this, necessary background in the relevant areas of research was presented first, namely, machining operations and composite materials. Later, state of the art in experimental research of composites machining was discussed. Finally, numerical modelling methods and their application to composite machining was presented.

Referring back to Figure 2.1, the choices of process, material and method can be summarised as follows: Orthogonal cutting process is chosen since the interest of this study lies in fundamental understanding of the cutting process. Furthermore, it is the simplest machining process to model. Unidirectional composites are chosen as they are the building blocks of multi-directional laminates, which constitute significant share of the total composites market. EFG is chosen since it is a promising alternative to FEM that can address some of the issues discussed in the previous sections.

Chapter 3

Meshfree Model Development

3.1 Introduction

As discussed in Section 2.5.1, meshfree methods are still in the development stage with large potential for improvement. For this reason, few commercial packages support meshfree implementations[1]. In light of this, and given the promising performance that these methods offer, it was decided to build a code in a bottom-up approach and not rely on any mechanics commercial software package such as ANSYS or ABAQUS. MATLAB was chosen to write the code as it offers a lot of capabilities in scientific computing. This allows more focus on the content of the code rather than on the implementation aspects, which could be daunting in other programming languages. MATLAB's large library of built-in functions, especially in geometrical calculations and system equations solving was particularly useful in this study. While it is true that runtime in MATLAB is usually longer than C++ or Fortran; however, coding and debugging times are considerably lower. The developer time is more valuable than the machine time.

This chapter aims at developing the essential components of the meshfree orthogonal cutting model. Rigorous bottom-up approach is adopted: starting with mathematical

---

[1] With exception of SPH, which might be the case since it is the oldest meshfree method; despite the well known issues with stability and spurious energy modes that SPH suffers from.

modelling (governing equations) followed by approximation procedure and then algorithmic implementation. The essential machining model components are depicted in Figure 3.1. The complexity of the model is evident from the various essential components required to build it. To ensure high accuracy, each model component was tested separately using appropriate verification examples, starting from the simplest elasto-static case and then building new capabilities based on the tested ones. This chapter presents the details of this model building effort. It should be noted however, that the complete orthogonal cutting model will be developed in Chapters 4 and 5. Furthermore, novel aspects of the model will be presented in those later chapters. For example, novel penalty formulation for contact calculation is presented in Chapter 4 and novel orthotropic constitutive model is presented in Chapter 5.

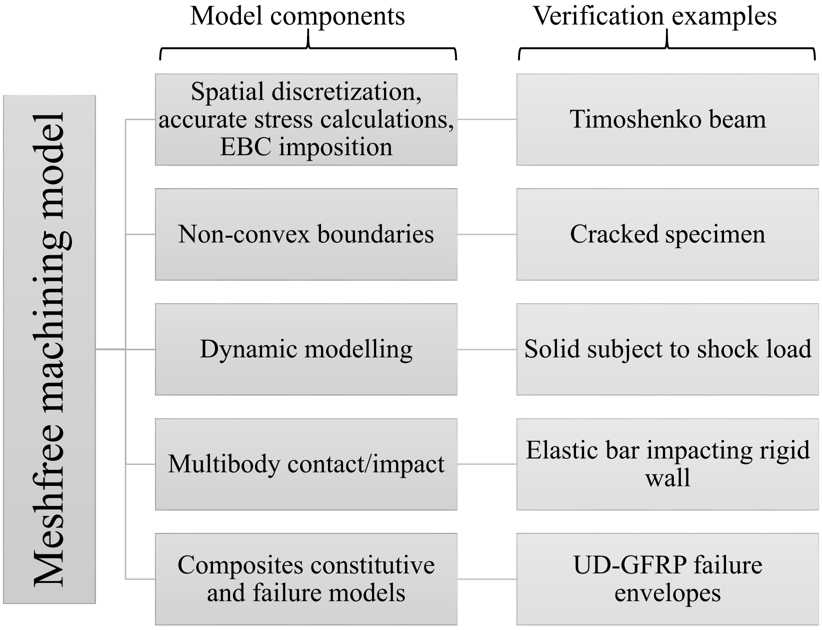

Figure 3.1: Main components of the meshfree model and the corresponding verification examples

This chapter is organised as follows: starting with presentation of the weak forms in static and dynamic cases, followed by derivation of the meshfree spatial approximation techniques and methods to impose constraints on the weak forms. The EFG formulation for elasto-statics is then developed followed by the elasto-dynamics, contact and finally composites failure. Verification examples are presented at the end of each section.

3.2 Governing Equations

In computational solid mechanics, a body is governed by the following equations [121]

- conservation of mass
- conservation of momentum
- conservation of energy
- displacement-strain relationship
- constitutive model

Assuming the density of the solid does not change, conservation of mass equation is no longer needed. Furthermore, assuming the domain is isothermal and adiabatic, the conservation of energy becomes no longer necessary. As such, in developing the model throughout this work, conservation of momentum, displacement-strain relations and constitutive equation will be used as the mathematical basis of the numerical model.

The strong form[2] of conservation of momentum equation is given as

$$\nabla \, . \, \sigma + \mathbf{b} = \rho \ddot{\mathbf{u}} \tag{3.1}$$

where, ∇ is the divergence operator, σ is the stress tensor, $\mathbf{b}$ is the body force tensor, ρ is the density of the material and $\ddot{\mathbf{u}}$ is the acceleration.

Introducing a differential operator $\mathbf{L}$, the above equation can be cast in matrix notation as follows

$$\mathbf{L} \, \sigma + \mathbf{b} = \rho \ddot{\mathbf{u}} \tag{3.2}$$

---

[2] Strong form refers to the strong continuity requirement on the solution field as compared with the weak form

For $2D$ problems,

$$\mathbf{L} = \begin{bmatrix} \frac{\partial}{\partial x} & 0 \\ 0 & \frac{\partial}{\partial y} \\ \frac{\partial}{\partial y} & \frac{\partial}{\partial x} \end{bmatrix} \tag{3.3}$$

The above differential equation is subject to the following *boundary conditions*

$$n_j\, \sigma = \bar{\mathbf{t}} \quad \text{on} \quad \Gamma_t \tag{3.4a}$$

$$\mathrm{u}_i = \bar{\mathrm{u}} \quad \text{on} \quad \Gamma_u \tag{3.4b}$$

where, $\bar{\mathbf{t}}$ is the prescribed traction on the traction boundary Γ_t, n_j is the outward normal on the Γ_t and $\bar{\mathbf{u}}$ is the prescribed displacement on the displacement boundary Γ_u. Since Equation 3.2 is a hyperbolic partial differential equation, it is subject to the following *initial conditions*

$$\mathrm{u}(\mathrm{x}, 0) = \mathrm{u}_0(\mathrm{x}) \tag{3.5a}$$

$$\sigma(\mathrm{x}, 0) = \sigma_0(\mathrm{x}) \tag{3.5b}$$

The term on the RHS of Equation 3.2 represents the inertial effects on the solid. In static cases, the inertial effects can be neglected and the strong form in static loading is obtained

$$\mathbf{L}\, \sigma + \mathbf{b} = \mathbf{0} \tag{3.6}$$

Equation 3.6 requires boundary conditions (i.e. Equations 3.4), but it does not require initial conditions (i.e. Equations 3.5) since the temporal derivative is absent.

The weak form of the dynamic and static momentum conservation can be obtained by multiplying with a kinematically admissible[3] virtual displacement field $\delta\mathbf{u}$, then integrating by parts and rearranging to obtain in the dynamic case

$$\int_\Omega (\mathbf{L}\ \delta\mathbf{u})^T \sigma \ \mathrm{d}\Omega - \int_\Omega \delta\mathbf{u}^T\mathbf{b}\ \mathrm{d}\Omega - \int_{\Gamma_t} \delta\mathbf{u}^T\bar{t}\ \mathrm{d}\Gamma + \int_\Omega \rho\delta\mathbf{u}^T\ddot{\mathbf{u}}\ \mathrm{d}\Omega = 0 \tag{3.7}$$

The term $(\mathbf{L}\ \delta\mathbf{u})$ refers to the virtual strain $\delta\varepsilon$ that results from subjecting the body to virtual displacement field $\delta\mathbf{u}$. The strain-displacement relation is given in matrix notation as follows

$$\varepsilon = \mathbf{L}\ \mathbf{u} \tag{3.8}$$

Similarly, the weak form for the static case is given as

$$\int_\Omega (\mathbf{L}\ \delta\mathbf{u})^T \sigma \ \mathrm{d}\Omega - \int_\Omega \delta\mathbf{u}^T\mathbf{b}\ \mathrm{d}\Omega - \int_{\Gamma_t} \delta\mathbf{u}^T\bar{t}\ \mathrm{d}\Gamma = 0 \tag{3.9}$$

3.3 Moving Least Squares Approximation

When attempting to solve Equations 3.7 and 3.9, the unknown field variable (i.e. displacement field in this case) need to be approximated using shape (trial) function [4]. In this section, the Moving Least Squares (MLS) is used to construct such shape functions. This is necessary for constructing the discretised system equations and obtaining an approximate solution.

The following development is taken from [45,48,122]. The goal here is to approximate a scalar function u by u^h. The MLS formulation states that

$$u^h(x) = \sum_j^m p_j(x)a_j(x) \equiv \mathbf{p}^T(\mathbf{x})\mathbf{a}(\mathbf{x}) \tag{3.10}$$

where, $\mathbf{p}$ is a complete polynomial basis function with m monomial terms, $\mathbf{a}(\mathbf{x})$ is the matrix of unknown coefficients. In Least squares approximation, these coefficients are constants, but in MLS, they are functions of spatial coordinates and should be computed.

---

[3] Kinematically admissible displacement field is the one that satisfies the boundary and initial conditions

A linear basis function in 2D is given as

$$\mathbf{p}^T(\mathbf{x}) = [1, x, y], \quad m = 3 \tag{3.11}$$

and a quadratic basis by

$$\mathbf{p}^T(\mathbf{x}) = [1, x, y, x^2, xy, y^2], \quad m = 6 \tag{3.12}$$

The unknown coefficients $a_j(x)$ in Equation 3.10 can be calculated by minimising the difference between the local approximation and the function through a weighted least-squares fit, which gives

$$\mathbf{J} = \sum_{I}^{n} w(x - x_I)[\mathbf{p}^T(\mathbf{x})(\mathbf{x}_I)\mathbf{a}(\mathbf{x}) - u_I]^2 \tag{3.13}$$

where n is the number of points in the neighbourhood of $\mathbf{x}$ for which the weight function $\mathbf{w}(\mathbf{x} - \mathbf{x}_I) \neq 0$, and u_I is the nodal value of $\mathbf{u}$ at $\mathbf{x} = \mathbf{x}_I$. The choice of weight function is an important aspect and will be explained further in Section 3.3.1. Equation 3.13 can be re-written as follows

$$\mathbf{J} = (\mathbf{p}\,\mathbf{a} - \mathbf{u})^T\mathbf{w}(\mathbf{x})(\mathbf{p}\,\mathbf{a} - \mathbf{u}) \tag{3.14}$$

where,

$$\mathbf{u}^T = \begin{Bmatrix} u_1 & u_2 & \cdots & u_n \end{Bmatrix}$$

$$\mathbf{p} = \begin{bmatrix} p_1(x_1) & p_2(x_1) & \cdots & p_n(x_1) \\ p_1(x_2) & p_2(x_2) & \cdots & p_n(x_2) \\ \vdots & \vdots & \ddots & \vdots \\ p_1(x_n) & p_2(x_n) & \cdots & p_n(x_n) \end{bmatrix}$$

$$\mathbf{w}(\mathbf{x}) = \begin{bmatrix} w(x-x_1) & 0 & \cdots & 0 \\ 0 & w(x-x_2) & \cdots & 0 \\ \vdots & \vdots & \ddots & \vdots \\ 0 & 0 & 0 & w(x-x_n) \end{bmatrix}$$

$a_j(x)$ is obtained by differentiating Equation 3.14 with respect to $\mathbf{a}$ and finding the stationary point

$$\frac{\partial \mathbf{J}}{\partial \mathbf{a}} = (\mathbf{p}\,\mathbf{a} - \mathbf{u})^T \mathbf{w}(\mathbf{x}) = \mathbf{0} \tag{3.15}$$

Therefore, $\mathbf{a}$ is given as

$$\mathbf{a} = \mathbf{A}^{-1}\,\mathbf{B}\,\mathbf{u} \tag{3.16}$$

where, $\mathbf{A} = \mathbf{p}^T\,\mathbf{w}(\mathbf{x})\,\mathbf{p}$ is called the moment matrix and $\mathbf{B} = \mathbf{p}^T\,\mathbf{w}(\mathbf{x})$. From the above, the final MLS approximation relationship is obtained

$$u^h(\mathbf{x}) = \sum_{I=1}^{n} \Phi_I(\mathbf{x}) u_I \quad = \mathbf{\Phi}(\mathbf{x})\mathbf{u} \tag{3.17}$$

The shape function $\mathbf{\Phi}(\mathbf{x})$ is defined by

$$\mathbf{\Phi}(\mathbf{x}) = \sum_{j=0}^{m} p_j(\mathbf{x})(\mathbf{A}^{-1}(\mathbf{x})\mathbf{B}(\mathbf{x}))_j = \mathbf{p}^T\mathbf{A^{-1}B} \tag{3.18}$$

where m is the order of the polynomial $p(\mathbf{x})$. The partial derivatives of $\Phi_I(\mathbf{x})$ can be obtained as follows

$$\mathbf{\Phi}_{,i} = \sum_{j}^{m} \{p_{j,i}(\mathbf{A^{-1}B})_j + p_j(\mathbf{A_{,i}^{-1}B}) + (\mathbf{A^{-1}B_{,j}})_j\} \tag{3.19}$$

where the index that follows a comma is a spatial derivative and $\mathbf{A_{,i}^{-1}} = -\mathbf{A^{-1}}\mathbf{A}_{,\mathbf{i}}\mathbf{A}^{-1}$.

The MLS procedure presented above have two main advantages [42]: (i) The desired order of consistency can be obtained by the proper choice of the basis function and (ii) The approximated field is continuous and smooth across the domain.

3.3.1 Weight Functions

The choice of weight function is important in constructing the shape function. Improper choice can lead to poorly conditioned moment matrix and loss of partition of unity of the shape function. The values of the weight function should be high near the point of interest and low towards the vicinity of the support domain [48]. As such the weight function is defined in terms of the normalised distance between the point of interest and the supporting nodes.

$$w(\mathbf{x} - \mathbf{x}_I) = w(r_I); \qquad r_I = \frac{\parallel \mathbf{x} - \mathbf{x}_I \parallel}{\mathbf{d}_m} \tag{3.20}$$

where, $\mathbf{d}_m$ is the size of the support domain. Several weight functions have been used in this work and are as follows Cubic spline weight function

$$w(r_I) = \begin{cases} \frac{2}{3} - 4r_I^2 + 4r_I^3 & \text{if} \quad 0 < r_I \leq 0.5 \\ \frac{4}{3} - 4r_I + 4r_I^2 - \frac{4}{3}r_I^3 & \text{if} \quad 0.5 < r_I \leq 1 \\ 0 & \text{if} \quad r_I > 1 \end{cases} \tag{3.21}$$

The derivative of the weight function are required in the calculation of shape function derivatives (Equation 3.19). The derivative of the cubic spline function is given as

$$\frac{\partial w(r_I)}{\partial x} = \frac{\partial w}{\partial r}\frac{\partial r}{\partial x} = \begin{cases} (-8r_I + 12r_I^2)\,\mathrm{sign}(r_I) & \text{if} \quad 0 < r_I \leq 0.5 \\ (-4 + 8r_I - 4r_I^2)\,\mathrm{sign}(r_I) & \text{if} \quad 0.5 < r_I \leq 1 \\ 0 & \text{if} \quad r_I > 1 \end{cases} \tag{3.22}$$

Quartic spline weight function is given as

$$w(r_I) = \begin{cases} 1 - 6r_I^2 + 8r_I^3 - 3r_I^4 & \text{if} \quad 0 < r_I \leq 1 \\ 0 & \text{if} \quad r_I > 1 \end{cases} \tag{3.23}$$

and its derivative as

$$\frac{\partial w(r_I)}{\partial x} = \frac{\partial w}{\partial r}\frac{\partial r}{\partial x} = \begin{cases} (-12r_I + 24r_I^2 - 12r_I^3)\,\mathrm{sign}(r_I) & \text{if} \quad 0 < r_I \leq 1 \\ 0 & \text{if} \quad r_I > 1 \end{cases} \tag{3.24}$$

An exponential weight function is also used

$$w(r_I) = \begin{cases} e^{-\left(\frac{r_I}{\zeta}\right)^2} & \text{if} \quad 0 < r_I \leq 1 \\ 0 & \text{if} \quad r_I > 1 \end{cases} \tag{3.25}$$

where, ζ is a constant. The derivative of the above function is given as

$$\frac{\partial w(r_I)}{\partial x} = \begin{cases} -2\frac{r_I}{\zeta^2} e^{-\left(\frac{r_I}{\zeta}\right)^2}\,\mathrm{sign}(r_I) & \text{if} \quad 0 < r_I \leq 1 \\ 0 & \text{if} \quad r_I > 1 \end{cases} \tag{3.26}$$

3.3.2 Domain of Influence

The domain of influence (DoI) or support domain is one of the key aspects in constructing meshfree shape functions. It refers to the area around a field node where it exerts *influence*, i.e. where it will be used in interpolation of field variable values. In traditional FEM, the domain of influence of nodes span over the elements they are part of. In EFG, as there are no elements, the size and shape of the DoI can be changed to suit each model requirements. Figure 3.2 shows an example of different types of DoI. The domain is said to be *local* as only nodes in the vicinity of the point of interest are used in the interpolation.

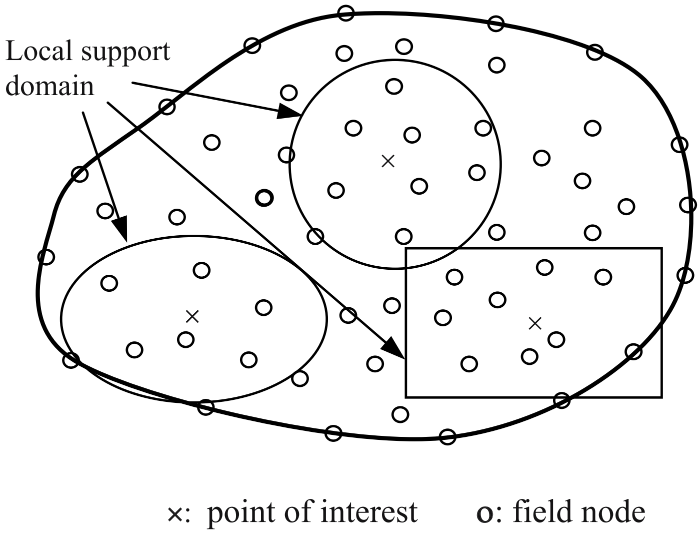

Figure 3.2: DoI representation [4]

The DoI is calculated using a scaling parameter β and a geometrical quantity $\mathbf{d}_I$ describing the nodal distribution near the point of interest. For uniform nodal distribution, $\mathbf{d}_I$ is usually the nodal spacing. The scaling parameter is set to $\beta \geq 1$ in order to ensure the invertibility of the moment matrix as shown in Equation 3.16. The DoI size is calculated as follows

$$\mathbf{d}_m = \beta \, \mathbf{d}_I \tag{3.27}$$

3.4 Constraints Imposition on the Weak Form

In many situations, the solution of Equations 3.7 and 3.9 should satisfy certain conditions in addition to the boundary and initial conditions. As such, the model has to be constrained. In the context of the EFG, displacement boundary conditions should be imposed using constraints when the shape function lacks Kronecker-delta property. For example, when using regularised weight function described in section 2.5.2, the resulting

MLS shape function approximately fulfils the Kronecker-delta and therefore, displacement boundary conditions can be imposed by direct substitution. Several methods could be used to impose constraints on the model. Two common methods will be presented and used, namely, Lagrange multiplier and penalty. These methods were originated in the context of optimisation theory to change the constrained optimisation problem into an unconstrained one. Let's consider a generic set of constraints that the solution field cannot fulfil

$$\mathbf{C}(\mathbf{u}) = \begin{Bmatrix} C_1(\mathbf{u}) & C_2(\mathbf{u}) & \cdots & C_k(\mathbf{u}) \end{Bmatrix}^T \tag{3.28}$$

In the context of this work, the fore-mentioned constraints include displacement boundary conditions and contact conditions. Generally, these constraints are fulfilled by adding the integral form of the constrained terms to the corresponding weak form of the problem.

3.4.1 Lagrange Multiplier

Lagrange multiplier method can be used to enforce constraints 3.28 as follows

$$\Lambda = \int_{\Omega} \lambda^{\mathbf{T}}\, \mathbf{C}(\mathbf{u}) \mathrm{d}\Omega \tag{3.29}$$

where, the vector of the unknown Lagrange multipliers is given as

$$\lambda^T = \begin{Bmatrix} \lambda_1 & \lambda_2 & \cdots & \lambda_k \end{Bmatrix} \tag{3.30}$$

The unknown multipliers could be thought of as smart forces used to enforce the constraints. This is achieved when Λ is differentiated with respect to the field variable, and the resulting terms added to the unconstrained weak form. This result in increasing the number of unknowns and loss of bandedness of the system matrices. On the other hand, the constraint is enforced exactly.

3.4.2 Penalty Method

Penalty is another commonly used constraint enforcement method. It *penalises* the terms in the solution field that violate the constraint. It is built as follow

$$P = \int_{\Omega} \mathbf{C}^T \alpha \mathbf{C} \mathrm{d}\Omega \tag{3.31}$$

where, α is a diagonal matrix of penalty parameters, usually large positive numbers. As in Lagrange multipliers, δP is added to the unconstrained weak form. Unlike Lagrange multiplier, using penalty method does not increase the number of unknowns in the system. Furthermore, if the unmodified system matrix is positive definite [4], it will remain as such after modification by the penalty functional P. On the other hand, enforcement of the constraint is only approximate and the choice of penalty parameter is not trivial but requires some numerical experiments.

3.5 The Element Free Galerkin for Elasto-statics

The MLS shape function generally does not posses the Kronecker-delta property, as such, in this section the discrete equations will be developed from the weak form with a penalty and Lagrange multiplier methods to enforce displacement boundary conditions. If the material behaviour is assumed to be linear elastic, further simplification for the weak form given in Equation 3.9 becomes possible. The constitutive equation for isotropic, linear-elastic body in plane stress is given as

$$\begin{Bmatrix} \sigma_x \\ \sigma_y \\ \sigma_{xy} \end{Bmatrix} = \frac{E}{1-\nu^2} \begin{bmatrix} 1 & \nu & 0 \\ \nu & 1 & 0 \\ 0 & 0 & \frac{1-\nu}{2} \end{bmatrix} \begin{Bmatrix} \varepsilon_x \\ \varepsilon_y \\ \varepsilon_{xy} \end{Bmatrix} \tag{3.32}$$

---

[4] Positive definite matrix is a symmetric matrix with all positive eigenvalues.

This can be put in a matrix notation as follows

$$\sigma = \mathbf{D}\,\varepsilon \tag{3.33}$$

Substituting Equations 3.33 and 3.8 into Equation 3.9, the following is obtained

$$\int_{\Omega} (\mathbf{L}\,\delta\mathbf{u})^T(\mathbf{L}\,\mathbf{D}\,\mathbf{u})\,\mathrm{d}\Omega - \int_{\Omega} \delta\mathbf{u}^T\mathbf{b}\,\mathrm{d}\Omega - \int_{\Gamma_t} \delta\mathbf{u}^T\bar{t}\,\mathrm{d}\Gamma = 0 \tag{3.34}$$

The displacement boundary conditions mentioned in Equation 3.4 can be rewritten as a constraint as

$$c(\mathbf{u}) = \mathbf{u} - \bar{\mathbf{u}} = 0 \quad \text{on} \quad \Gamma_u \tag{3.35}$$

Substituting Equation 3.35 into Equation 3.31 and applying the virtual displacement field, the following is obtained

$$\delta P_u(\mathbf{u}) = \int_{\Gamma_u} \delta(\mathbf{u} - \bar{\mathbf{u}})^T \alpha_u\,(\mathbf{u} - \bar{\mathbf{u}})\,\mathrm{d}\Gamma \tag{3.36}$$

This term is added to Equation 3.34 to yield the final form of the EFG using penalty method.

$$\int_{\Omega} (\mathbf{L}\,\delta\mathbf{u})^T(\mathbf{L}\,\mathbf{D}\,\mathbf{u})\,\mathrm{d}\Omega - \int_{\Omega} \delta\mathbf{u}^T\mathbf{b}\,\mathrm{d}\Omega - \int_{\Gamma_t} \delta\mathbf{u}^T\bar{t}\,\mathrm{d}\Gamma - \int_{\Gamma_u} \delta(\mathbf{u}-\bar{\mathbf{u}})^T \alpha_u\,(\mathbf{u}-\bar{\mathbf{u}})\,\mathrm{d}\Gamma = 0 \tag{3.37}$$

If Lagrange multiplier is used, the constraint terms become

$$\delta\Lambda = \int_{\Gamma_u} \delta\lambda^T(\mathbf{u} - \bar{\mathbf{u}})\mathrm{d}\Gamma + \int_{\Gamma_u} \delta\mathbf{u}^T\lambda\mathrm{d}\Gamma \tag{3.38}$$

Similarly to penalty, terms of Equation 3.38 are added to Equation 3.34 to yield the final form of the EFG using Lagrange multiplier

$$\int_{\Omega}(\mathbf{L}\,\delta\mathbf{u})^T(\mathbf{L}\,\mathbf{D}\,\mathbf{u})\,\mathrm{d}\Omega-\int_{\Omega}\delta\mathbf{u}^T\mathbf{b}\,\mathrm{d}\Omega-\int_{\Gamma_t}\delta\mathbf{u}^T\bar{t}\,\mathrm{d}\Gamma-\int_{\Gamma_u}\delta\lambda^T(\mathbf{u}-\bar{\mathbf{u}})\mathrm{d}\Gamma-\int_{\Gamma_u}\delta\mathbf{u}^T\lambda\mathrm{d}\Gamma=0 \tag{3.39}$$

3.5.1 Discrete Equations

Using the MLS approximation in constructing the shape functions and their derivatives, the weak form in Equation 3.37 can be discretised. First, the displacement and strain are approximated and then substituted into the each term in the weak form to obtain the algebraic system equations.

The 2D displacement field $\mathbf{u}^T = [u_x\ u_y]$ can be approximated at a point of interest using MLS shape functions as follows

$$\mathbf{u}=\sum_{I}^{n}\mathbf{\Phi}_I\,\mathbf{u}_I \tag{3.40}$$

where $\mathbf{\Phi}$ is the MLS shape function, n the number of nodes in the support domain of the point of interest. This leads to

$$\delta\mathbf{u}=\sum_{I}^{n}\mathbf{\Phi}_I\delta\mathbf{u}_I \tag{3.41}$$

The strain can be discretised as follows

$$\varepsilon=\sum_{I}^{n}\mathbf{L}\,\mathbf{\Phi}_I\,\mathbf{u}_I\ =\sum_{I}^{n}\mathbf{B}_I\,\mathbf{u}_I \tag{3.42}$$

where, $\mathbf{B}_I$ is called the strain matrix at the point I.

$$\mathbf{B}_I=\begin{bmatrix}\frac{\partial\Phi_1}{\partial x} & 0 & \cdots & \frac{\partial\Phi_n}{\partial x} & 0\\ 0 & \frac{\partial\Phi_1}{\partial y} & \cdots & 0 & \frac{\partial\Phi_n}{\partial y}\\ \frac{\partial\Phi_1}{\partial y} & \frac{\partial\Phi_1}{\partial x} & \cdots & \frac{\partial\Phi_n}{\partial y} & \frac{\partial\Phi_n}{\partial x}\end{bmatrix} \tag{3.43}$$

The first Term in Equation 3.34 is changed as follows

$$\begin{aligned}\int_{\Omega}(\mathbf{L}\,\delta\mathbf{u})^T(\mathbf{L}\,\mathbf{D}\,\mathbf{u})\,\mathrm{d}\Omega &= \int_{\Omega}\left(\sum_I^n \mathbf{B}_I\delta\mathbf{u}_I\right)^T\left(\sum_J^n \mathbf{D}\,\mathbf{B}_J\,\mathbf{u}_J\right)\mathrm{d}\Omega \\ &= \int_{\Omega}\sum_I^n\sum_J^n \delta\mathbf{u}_I^T(\mathbf{B}_I^T\,\mathbf{D}\,\mathbf{B}_J)\mathbf{u}_J\,\mathrm{d}\Omega\end{aligned} \tag{3.44}$$

The summation in the above equation is written in terms of local nodes (varies from $1 \to n$). The numbering can be changed to the global nodal numbering, whereby each node in the domain is uniquely numbered ($1 \to N$). This can be performed due to the local support property of the shape function, which ensures that the node I only contributes to the calculations of points that have it in their support domain [4]. Now, Equation 3.44 can be re-written as follows

$$\begin{aligned}\int_{\Omega}(\mathbf{L}\,\delta\mathbf{u})^T(\mathbf{L}\,\mathbf{D}\,\mathbf{u})\,\mathrm{d}\Omega &= \int_{\Omega}\sum_I^N\sum_J^N \delta\mathbf{u}_I^T(\mathbf{B}_I^T\,\mathbf{D}\,\mathbf{B}_J)\mathbf{u}_J\,\mathrm{d}\Omega \\ &= \sum_I^N\sum_J^N \delta\mathbf{u}_I^T\underbrace{\int_{\Omega}(\mathbf{B}_I^T\,\mathbf{D}\,\mathbf{B}_J\,\mathrm{d}\Omega)\,\mathbf{u}_J}_{\mathbf{K}_{IJ}}\end{aligned} \tag{3.45}$$

where, $\mathbf{K}_{IJ}$ is called the nodal stiffness matrix. Now the above formulation can be generalised for the entire domain by applying the summation over all the nodes in the domain and collecting the contributions in global matrices as follows

$$\delta\mathbf{U}^T = \sum_I^N \delta\mathbf{u}_I^T \tag{3.46}$$

$$\mathbf{K} = \sum_I^N\sum_J^N \mathbf{K}_{IJ} \tag{3.47}$$

The second and third terms in Equation 3.37 are discretised in a similar way as follows

$$\begin{aligned}\int_{\Omega}\delta\mathbf{u}^T\mathbf{b}\mathrm{d}\Omega + \int_{\Gamma_t}\delta\mathbf{u}^T\bar{\mathbf{t}}\mathrm{d}\Gamma &= \int_{\Omega}\sum_I^N \mathbf{\Phi}_I^T\delta\mathbf{u}_I^T\mathbf{b}\mathrm{d}\Omega + \int_{\Gamma_t}\sum_I^N \mathbf{\Phi}_I^T\delta\mathbf{u}_I^T\bar{\mathbf{t}}\,\mathrm{d}\Gamma \\ &= \sum_I^N \delta\mathbf{u}_I^T\underbrace{\left[\int_{\Omega}\mathbf{\Phi}_I^T\mathbf{b}\mathrm{d}\Omega + \int_{\Gamma_t}\mathbf{\Phi}_I^T\bar{\mathbf{t}}\,\mathrm{d}\Gamma\right]}_{\mathbf{F}_I^{ext}} = \delta\mathbf{U}^T\mathbf{F}^{ext}\end{aligned} \tag{3.48}$$

where $\mathbf{F}^{ext}$ is a vector representing the contribution of the body forces and prescribed traction on the solid, both of which are viewed as external forces. The final term in Equation 3.37 is discretised as follows

$$\begin{aligned} \delta P_u &= \int_{\Gamma_u} \delta \left(\sum_I^N \mathbf{\Phi}_I \mathbf{u}_I - \bar{\mathbf{u}} \right)^T \alpha_u \left(\sum_J^N \mathbf{\Phi}_J \mathbf{u}_J - \bar{\mathbf{u}} \right) \mathrm{d}\Gamma \\ &= \int_{\Gamma_u} \sum_I^N \sum_J^N \mathbf{\Phi}_I^T \delta \mathbf{u}_I^T \alpha_u \mathbf{\Phi}_J \mathbf{u}_J \mathrm{d}\Gamma - \int_{\Gamma_u} \sum_I^N \mathbf{\Phi}_I^T \delta \mathbf{u}_I^T \alpha_u \, \bar{\mathbf{u}} \, \mathrm{d}\Gamma \\ &= \sum_I^N \sum_J^N \delta \mathbf{u}_I^T \underbrace{\int_{\Gamma_u} \mathbf{\Phi}_I^T \alpha_u \mathbf{\Phi}_J \mathrm{d}\Gamma}_{\mathbf{K}_{IJ}^u} \mathbf{u}_J - \sum_I^N \delta \mathbf{u}_I^T \underbrace{\int_{\Gamma_u} \mathbf{\Phi}_I^T \alpha_u \bar{\mathbf{u}} \mathrm{d}\Gamma}_{\mathbf{F}_I^u} = \delta \mathbf{U}[\mathbf{K}^u \mathbf{U} - \mathbf{F}^u] \end{aligned} \tag{3.49}$$

By combining the resulting terms from Equations 3.46, 3.48 and 3.49 the following is obtained

$$\delta \mathbf{U}^T \left[(\mathbf{K} + \mathbf{K}^u)\mathbf{U} - \mathbf{F}^{ext} - \mathbf{F}^u \right] = 0 \tag{3.50}$$

Since $\delta \mathbf{U}$ is arbitrary, it follows that

$$(\mathbf{K} + \mathbf{K}^u)\mathbf{U} = \mathbf{F}^{ext} + \mathbf{F}^u \tag{3.51}$$

Equation 3.51 is the discretised equation using the penalty method, which now can be solved using a numerical solver to obtain a solution.

In case of using Lagrange multiplier, the discretisation is more involved due to the fact that the multipliers are unknowns in coordinates and need to be interpolated at the displacement boundaries

$$\lambda(\mathbf{x}) = \sum_I^{n_\lambda} \mathbf{N}_I \lambda_I \qquad \mathbf{x} \in \Gamma_u \tag{3.52}$$

where, n_λ is the number of nodes on the essential boundary.

The last two terms in Equation 3.39 are discretised to give in final form[5]

$$\int_{\Gamma_u} \delta \lambda^T (\mathbf{u} - \bar{\mathbf{u}}) \mathrm{d}\Gamma = -\delta \lambda^T \mathbf{G}^T \mathbf{U} + \delta \lambda \, \mathbf{q} \tag{3.53}$$

---

[5] The lengthy details of the discretisation can be found in reference works such as [123].

$$\int_{\Gamma_u} \delta \mathbf{u}^T \lambda \mathrm{d}\Gamma = \delta \mathbf{U}^T \mathbf{G}\ \lambda \tag{3.54}$$

where,

$$\mathbf{G} = \sum_{I}^{n} \sum_{J}^{n_\lambda} \mathbf{\Phi}_I^T \mathbf{N}_J \mathrm{d}\Gamma \tag{3.55}$$

$$\mathbf{q} = \sum_{I}^{n_\lambda} \mathbf{N}_I^T \bar{\mathbf{u}} \mathrm{d}\Gamma \tag{3.56}$$

The terms are added together to give

$$\delta \mathbf{U}^T \left[\mathbf{K}\mathbf{U} + \mathbf{G}\lambda - \mathbf{F}\right] + \delta \lambda^T \left[\mathbf{G}^{\mathbf{T}}\mathbf{U} - \mathbf{q}\right] = 0 \tag{3.57}$$

since $\delta \mathbf{U}$ and $\delta \lambda$ are arbitrary, the final discrete equation in compact matrix notation is obtained

$$\begin{bmatrix} \mathbf{K} & \mathbf{G} \\ \mathbf{G}^T & \mathbf{0} \end{bmatrix} \begin{bmatrix} \mathbf{U} \\ \lambda \end{bmatrix} = \begin{bmatrix} \mathbf{F} \\ \mathbf{q} \end{bmatrix} \tag{3.58}$$

3.5.2 Numerical Implementation

The terms in Equations 3.51 and 3.58 are integrated over the domain and boundaries. Numerical integration is carried out by Gauss quadrature method. This is done by dividing the domain into cells and then distributing gauss points in the cells. The construction of the cells can be dependent or independent of the field nodes. This method is found to be accurate and easy to implement [48]. As an example, given a generic integrand $\mathbf{Z}$ over domain Ω divided into n_Ω integration cells, $\mathbf{Z}$ can be evaluated as follows

$$\int_{\Omega} \mathbf{Z} \mathrm{d}\Omega = \sum_{k}^{n_c} \int_{\Omega_k} \mathbf{Z} \mathrm{d}\Omega = \sum_{k}^{n_c} \sum_{k}^{n_g} \hat{w}_i \mathbf{Z}(\mathbf{x}_{Qi}) |\mathbf{J}_{ik}| \tag{3.59}$$

where, n_g is the number of Gauss points in each cell, $\hat{w}_i$ is the Gaussian weighting factor at point $\mathbf{x}_{Qi}$ and $|\mathbf{J}_{ik}^D|$ is the Jacobian matrix for the area integration of the cell k.

The algorithmic implementation of the MATLAB code of elasto-statics is presented in

Algorithm 3.1. It is noted that the elasto-static algorithm does not differ significantly from that of FEM with exception of boundary conditions enforcement step and retrieval of the nodal displacement values. This is mainly since both EFG and FEM are based on the weak forms. The shape function calculations are presented in Algorithm 3.2. The assembly of the shape function and derivatives follows the procedure of Belytschko et al. [124], which improves the efficiency of the algorithm.

Algorithm 3.1: Elasto-statics EFG model

- Input parameters and program controls
- Calculate material properties matrix
- Generate geometry of domain
- Distribute nodes in domain and on boundaries
- Generate background mesh and distribute Gauss points (domain and boundary)
- Calculate and store MLS shape function and its derivatives (Algorithm 3.2)
- Assemble the global stiffness matrix, Equation 3.46.
- Distribute integration points along the traction boundary.
- Calculate the shape function of the traction integration points.
- Integrate the external forces along the traction boundary, Equation 3.48.
- Distribute integration points along the displacement boundary.
- Calculate the shape function of the displacement integration points.
- Apply Penalty (Eqn. 3.49) or Lagrange multiplier (Eqns. 3.53 and 3.54) to enforce boundary conditions.
- Solve the system equations, Equations 3.51 or 3.58.
- Interpolate the solution to obtain the real nodal displacements.
- Calculate the stresses, Equation 3.33.
- Outputs: plot displacements and stresses.

Algorithm 3.2: MLS shape function calculations

- Loop over Gauss integration points.
- Determine the nodes within the DoI of the integration point.
- Calculate the normalised radius of r_I, Equation 3.20.
- Calculate the weight function and its derivatives.
- Calculate the moment matrix A.
- Calculate the $\mathbf{B}$ matrix.
- Assemble the shape function and its derivatives using LU decomposition.

3.5.3 Non-convex Boundaries

Construction of the shape function in non-convex domain is handled by the visibility criteria. It was proposed by Belytschko et al. [48] to deal with internal cracks and other irregularities in the geometry. In constructing the shape function, if the integration point is near a non-convex boundary area, the nodes that are not *visible* (e.g. on the other side of the crack) from that point and lie within the DoI are excluded from the calculations.

The numerical implementation of the visibility criteria involves a lot of geometrical calculations that can be burdensome. In order to improve the efficiency of the simulations, a proposed procedure (shown in Algorithm 3.3) is applied locally near the non-convex boundaries. This assumes that the approximate location of the geometrical irregularities is known a priori; however, it is not essential requirement for the calculations. It was applied in such manner since arbitrary crack propagation problems are not in the scope of this work. Where the approximate location of the cracks is not known, more search could be applied to locate the nodes that need to be excluded from the DoI.

Algorithm 3.3: Implementation of visibility criteria

```
• Input location of non-convex boundaries $d$.
• Find integration points $gp_d$ near $d$.
• Find boundary segments $L_d$ near $d$.
• Loop over $gp_d$
    – Create line segments between the point and its support nodes $L_c = [gp_{di}\ x(gp_d(i))]$
    – Check intersection between every item of $L_c$ with $L_d$.
    – Remove the nodes $m$ from DoI ($gp_d(i)$) where $L_c(m) \cap L_d \neq \emptyset$.
```

3.5.4 Numerical Example: Timoshenko Beam

The aim of this example is to verify some essential aspects of the EFG implementation in MATLAB. Most importantly of which are the shape function calculations, stress calculations and imposition of boundary conditions. The problem has an analytical solution and was proposed by Timoshenko [125]. A schematic is shown in Figure 3.3.

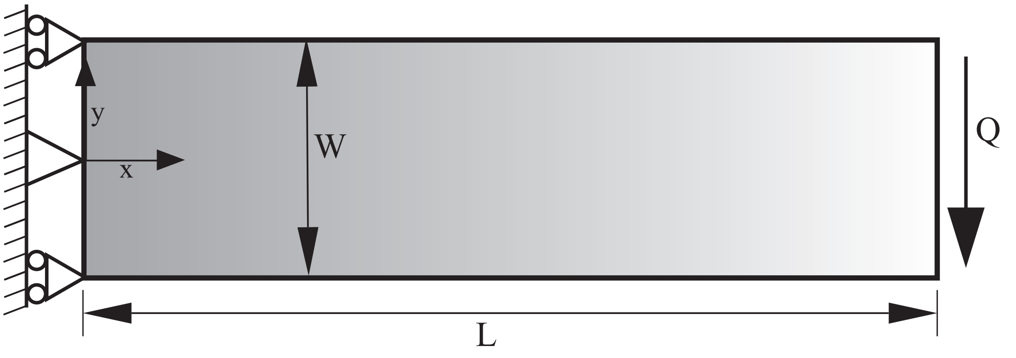

Figure 3.3: Timoshenko beam geometry and loading

The applied external load follows parabolic distribution and the beam is considered in plane stress condition with depth equals to unity. The traction at the free end is given as

$$T = -\frac{Q}{2I_m}(\frac{W^2}{4} - y^2) \tag{3.60}$$

where, $I_m = \frac{W^3}{12}$ is the moment of inertia of the beam. The displacement field is given follows

$$u_x = -\frac{Q}{6EI_m}\left[(6L-3x)x + (2+\nu)\left(y^2 - \frac{W^2}{4}\right)\right] \tag{3.61}$$

$$u_y = \frac{Q}{6EI_m}\left[3\nu y^2(L-x) + (4+5\nu)\frac{W^2 x}{4} + (3L-x)x^2\right] \tag{3.62}$$

Figure 3.4 shows the normal and shear stress fields imposed on the deformed geometry. The deformation was scaled for easy identification.

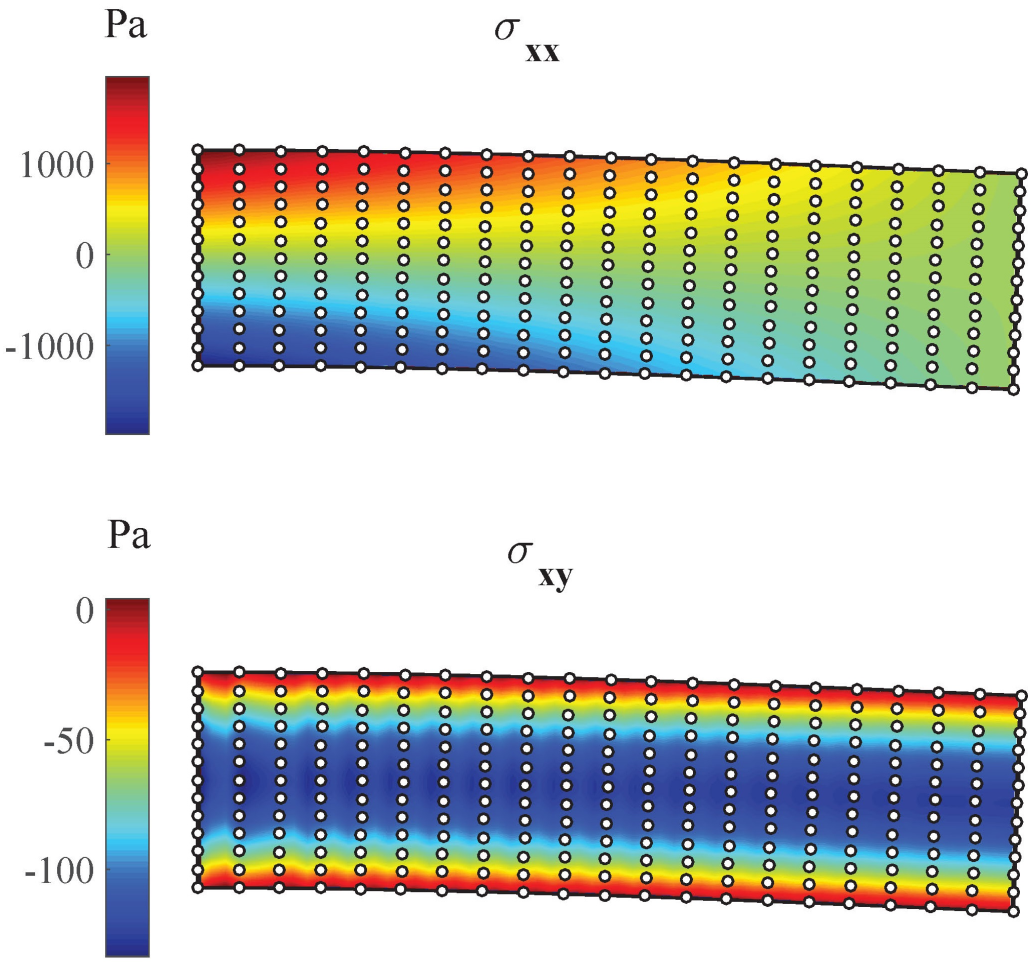

Figure 3.4: Normal and shear stress fields with scaled deformation

Figure 3.5 shows the comparison in deflection at the centre of the beam. Both Lagrange and penalty used Quartic spline weight function, $DoI = 1.3$ and $N = 147$. Penalty method was calculated with $\alpha_u = 3 \times 10^7$. A very good agreement is found between the analytical solution and both methods. However, the approximate imposition of the boundary condition in the case of penalty is clear since the deflection does not start at exactly 0. Lagrange multiplier results are almost identical with the analytical solution. Figure **??** shows the stress distribution across the width of the beam. Good accuracy is achieved using penalty and Lagrange multiplier. The smoothness of the stress field is evident, especially near the free edges. This is achieved without any stress post-processing techniques usually needed in FEM.

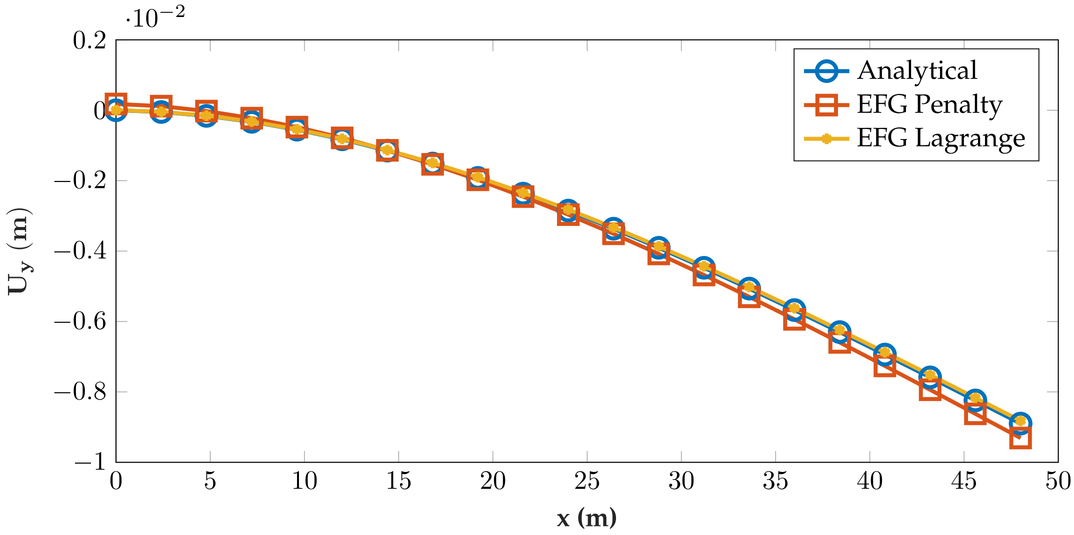

Figure 3.5: Comparison of beam deflection at $y = 0$ between analytical, Lagrange multiplier and penalty method

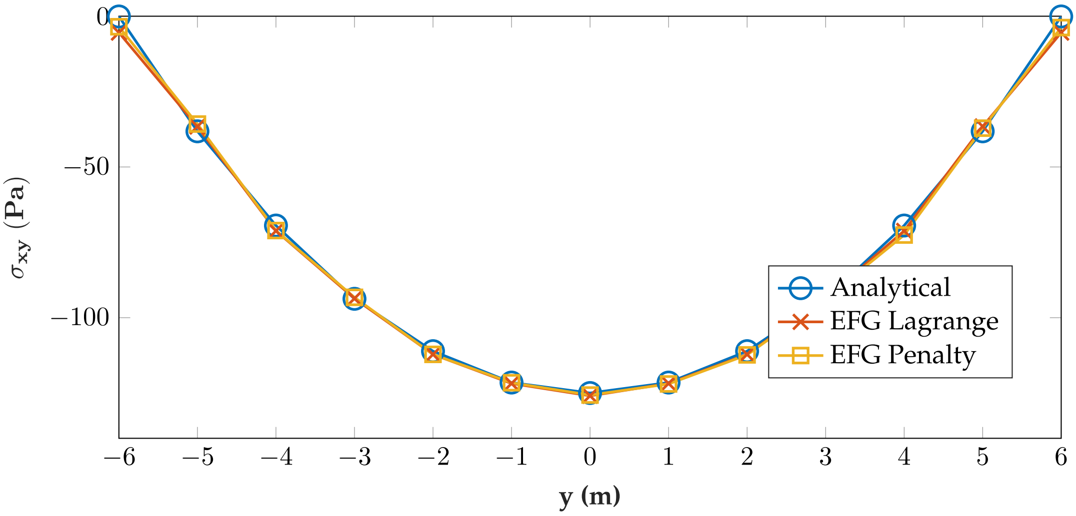

Figure 3.6: Comparison of shear stress at $x = L/2$ between analytical, Lagrange multiplier and penalty method

3.5.5 Numerical Example: Cracked Specimen

The aim of this example is to verify the implementation of the code in terms of dealing with complex geometry and especially the visibility criteria.

The chosen computational domain is part of an infinite plate with a centred crack with length a_0 .The material is considered in plane strain condition. Due to the symmetry of the problem, only square part of the problem around the right edge of the crack is modelled. The analytical solution is given in polar coordinates as follows [52]

$$u_x(r,\Theta) = \frac{2K_f(1+\nu)}{E}\sqrt{\frac{r}{2\pi}}\,cos\left(\frac{\Theta}{2}\right)\left(2-2\nu-cos^2\left(\frac{\Theta}{2}\right)\right) \tag{3.63}$$

$$u_y(r,\Theta) = \frac{2K_f(1+\nu)}{E}\sqrt{\frac{r}{2\pi}}\,sin\left(\frac{\Theta}{2}\right)\left(2-2\nu-cos^2\left(\frac{\Theta}{2}\right)\right) \tag{3.64}$$

where, $K_f = \sigma\sqrt{\pi a}$ is the stress concentration factor. The origin of the polar coordinates is chosen the edge of the crack and the positive angle is measured in (CCW) direction. The model set up is shown in Figure 3.7

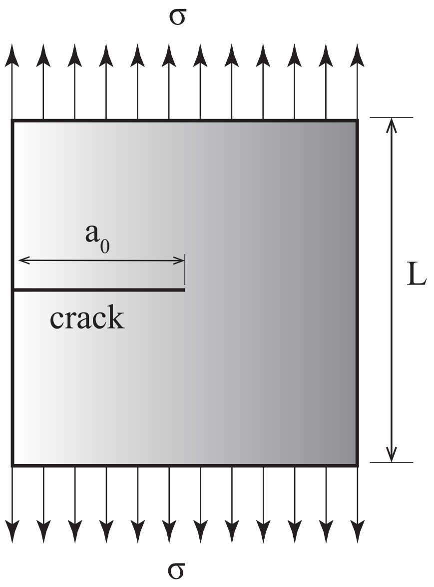

Figure 3.7: Cracked Specimen Model Set up

The numerical values used in obtaining the results are as follows: $\sigma = 10000\,N/mm^2,\ L = 10\,mm,\ a_0 = 5\,mm,\ E = 10^7\ N/mm^2,\ \nu = 0.3,\ \beta = 2.5,\ N = 676.$ The displacement boundary condition is enforced using Lagrange multiplier along the top, right and bottom. Figure 3.8 shows the specimen after deformation and as compared with the analytical solution. Figure 3.9 shows the normal stresses field. A good agreement is obtained by comparison with the analytical solution in both displacement and stress. By applying the visibility criteria, good level of accuracy solution is obtained. Further improvements can be reached using intrinsic or extrinsic enrichments. However, numerical implementation becomes more complicated and the gain in accuracy is relatively small, as described by Nguyen et al. [52].

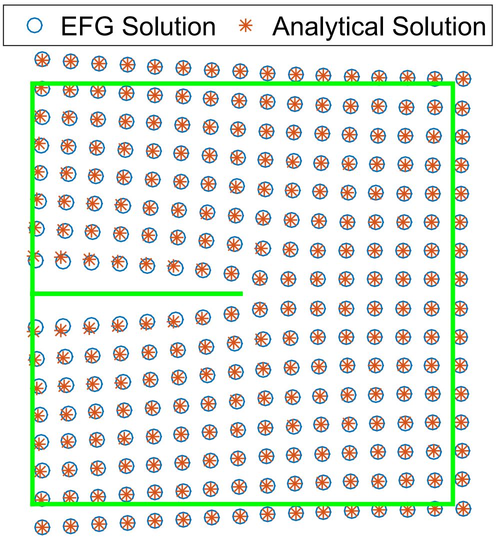

Figure 3.8: Deformed Specimen (scaled)

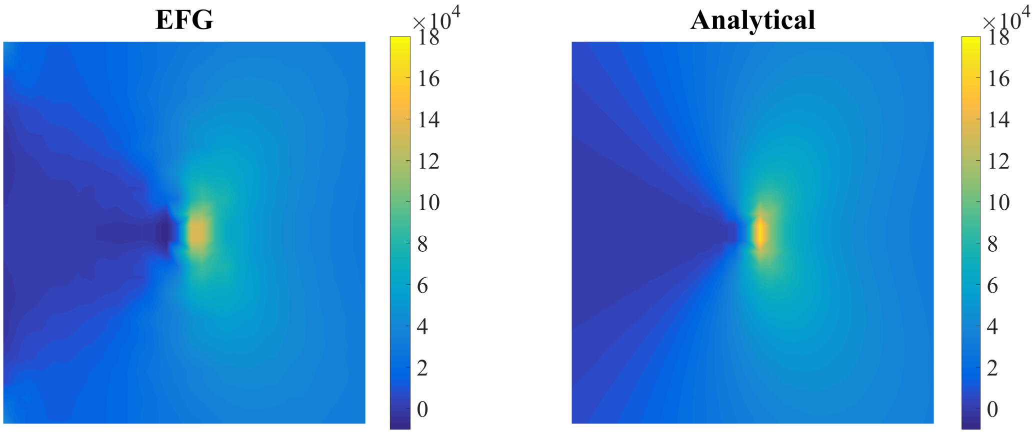

Figure 3.9: σ_y comparison between EFG and Analytical Solutions

3.6 EFG for Elasto-dynamics with Material Non-linearities

In cases where inertial effects cannot be neglected, the dynamic weak form is used instead of the static weak form. In order to make the formulation applicable to situations with geometrical non-linearity, the small-displacement elasticity assumption is dropped. This means that Hooke's Law is not substituted in the weak form. The penalty functional in Equation 3.36 is added to the dynamic weak form in Equation 3.7 to enforce the displacement boundary conditions.

$$\begin{aligned}\int_{\Omega}(\mathbf{L}\,\delta\mathbf{u})^{T}\sigma\,\mathrm{d}\Omega-\int_{\Omega}\delta\mathbf{u}^{T}\mathbf{b}\,\mathrm{d}\Omega-\int_{\Gamma_t}\delta\mathbf{u}^{T}\bar{t}\,\mathrm{d}\Gamma+\int_{\Omega}\rho\delta\mathbf{u}^{T}\ddot{\mathbf{u}}\,\mathrm{d}\Omega\\-\int_{\Gamma_u}\delta(\mathbf{u}-\bar{\mathbf{u}})^{T}\alpha_u\,(\mathbf{u}-\bar{\mathbf{u}})\,\mathrm{d}\Gamma=0\end{aligned}\tag{3.65}$$

3.6.1 Discrete Equations

The second, third and fifth terms of Equation 3.65 are discretised in a similar way to the static case in Section 3.5.1. The first term is discretised as follows

$$\int_{\Omega}(\mathbf{L}\,\delta\mathbf{u})^{T}\sigma\,\mathrm{d}\Omega=\int_{\Omega}\sum_{I}^{N}(\mathbf{L}\mathbf{\Phi}_I\delta\mathbf{u}_I)^{T}\sigma_I\,\mathrm{d}\Omega=\sum_{I}^{N}\delta\mathbf{u}_I^{T}\underbrace{\int_{\Omega}\mathbf{B}_I^{T}\sigma_I\,\mathrm{d}\Omega}_{\mathbf{F}_I^{int}}=\delta\mathbf{U}^{T}\,\mathbf{F}^{int}\tag{3.66}$$

where the stiffness matrix is not used and replaced with an internal force vector, which is a function of the displacement unlike the stiffness matrix in linear analysis. The forth term in Equation 3.65 is discretised in a similar manner

$$\begin{aligned}\int_{\Omega}\delta\mathbf{u}^{T}\rho\ddot{\mathbf{u}}\,\mathrm{d}\Omega&=\int_{\Omega}\sum_{I}^{N}(\mathbf{\Phi}_I\delta\mathbf{u}_I)^{T}\rho\sum_{J}^{N}(\mathbf{\Phi}_J\ddot{\mathbf{u}}_J)\,\mathrm{d}\Omega\\&=\sum_{I}^{N}\sum_{J}^{N}\delta\mathbf{u}_I^{T}\underbrace{\int_{\Omega}\mathbf{\Phi}_I^{T}\rho\mathbf{\Phi}_J\,\mathrm{d}\Omega}_{\mathbf{M}_{IJ}}\,\ddot{\mathbf{u}}_J=\delta\mathbf{U}^{T}\mathbf{M}\ddot{\mathbf{U}}\end{aligned}\tag{3.67}$$

where $\mathbf{M}$ is the mass matrix. After combining all the discrete terms and invoking the arbitrariness of $\delta\mathbf{U}$

$$\mathbf{M}\ddot{\mathbf{U}}=\mathbf{F}^{ext}+\mathbf{F}^{u}-\mathbf{F}^{int}-\mathbf{K}^{u}\mathbf{U}\tag{3.68}$$

Equation 3.68 is called the semi-discrete equation because it is discrete in space but not in time. The central difference method is used to discretise in time. It is commonly used method in nonlinear solid mechanics. The temporal quantities, i.e. velocity and acceleration are calculated based on the central differencing formulae. The equations and procedure presented by Belytschko et al. [121] are adopted in this work. Time increments are divided into half steps. This is done in order to be able to perform energy balance calculations. Hence, the time increment quantities are

$$\Delta t^{n+{}^1/_2} = t^{n+1} = t^n \ , \quad t^{n+{}^1/_2} = 0.5(t^{n+1} + t^n) \ , \quad \Delta t^n = t^{n+{}^1/_2} - t^{n-{}^1/_2} \tag{3.69}$$

The displacement at time $n+1$ can be calculated from the velocity at $n+{}^1/_2$ as follows

$$\mathbf{u}^{n+1} = \mathbf{u}^n + \Delta t^{n+{}^1/_2}\mathbf{v}^{n+{}^1/_2} \tag{3.70}$$

Acceleration can be expressed in terms of displacements for equal time step

$$\ddot{\mathbf{u}}^n = \frac{\mathbf{u}^{n+1} - 2\mathbf{u}^n + \mathbf{u}^{n-1}}{(\Delta t^n)^2} \tag{3.71}$$

3.6.2 Numerical Implementation

Time integration is the major difference between the static and dynamic algorithms. Algorithm 3.4 shows the detailed implementation of the CDM in MATLAB. It is noted that the CDM requires the mass matrix to be diagonal. This avoids solving the system equations and makes the algorithm efficient. The integration of the mass according to Equation 3.67 produces a sparse and banded matrix, similar in structure to that of the stiffness matrix in elasto-statics. This mass matrix is called the consistent mass matrix M^C. Changing it into diagonal (lumped) matrix M^D is achieved using the row-sum lumping technique

$$\mathbf{M}^D_{II} = \sum_J \mathbf{M}^C_{IJ} \tag{3.72}$$

Algorithm 3.4: Dynamic EFG model using central difference time integration

Inputs

- Initialise
- Input parameters and program controls
- Boundary and initial conditions

Pre-processing

- Generate geometry of domain.
- Distribute nodes in domain and on boundaries.
- Calculate material properties matrix.
- Distribute Gauss points in cells (domain and boundary).
- Calculate and store MLS shape function and its derivatives.
- Integrate the external force along the traction boundary (if applicable).
- Calculate the lumped mass matrix.
- Calculate initial nodal forces $\mathbf{F}^0 = \mathbf{F}^0_{ext} - \mathbf{F}^0_{int}$.

Processing

- Loop over time steps.
- First velocity half step update
- Update nodal positions/displacements.
- Apply boundary conditions.
- Calculate the nodal internal forces.
- Enforce other constraints (if applicable).
- Update the total nodal forces $\mathbf{F}^t = \mathbf{F}^t_{ext} - \mathbf{F}^t_{int}$.
- Calculate the new acceleration $\ddot{\mathbf{u}} = \mathbf{M}^{-1}\mathbf{F}^t$.
- Second velocity half step update.
- Check conservation of energy.
- Save interim variables.
- End time loop.

Post-processing

- Display and visualise stresses and displacements.

3.6.3 Numerical Example: Stress Wave in Solid

A numerical example is solved to verify the implementation of the dynamic EFG model presented above. The computational domain is a rectangular of length L and width W in plane strain condition. The block is not supported but subjected to a stress shock at the top edge by applying constant acceleration of $10^8 \frac{m}{sec^2}$ for $0.1\ \mu s$ as shown in Figure 3.10.

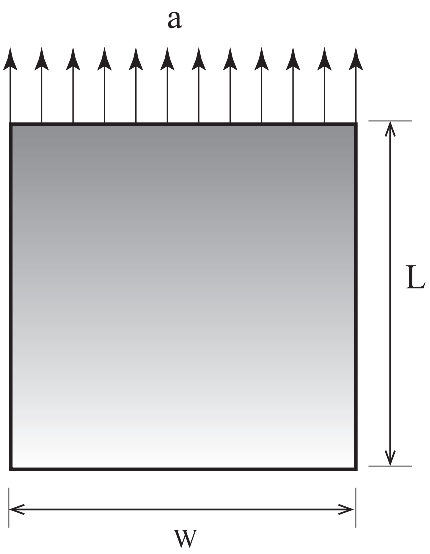

Figure 3.10: Set up for the Stress Wave Example

The results of this example are compared with the FEM results presented by deBorst et al. [126]. The parameters used in this case are as follows: $L = W = 1\ mm, N = 441, \beta = 2.5$. Number of nodes, time step and material constants were set similar to [126] to allow for comparison. The calculated dilatational wave speed is approximately $1950\ m/sec$, which is close to the theoretical value of $2090\ m/sec$. This is slightly slower than FEM solution as shown in the Figure 3.11. The magnitude of the normal stress at the first wave is oscillating around $25MPa$ for both EFG and FEM. The stress field for the EFG solutions is smooth and does not require post processing. The progression of the wave is shown in Figure 3.12.

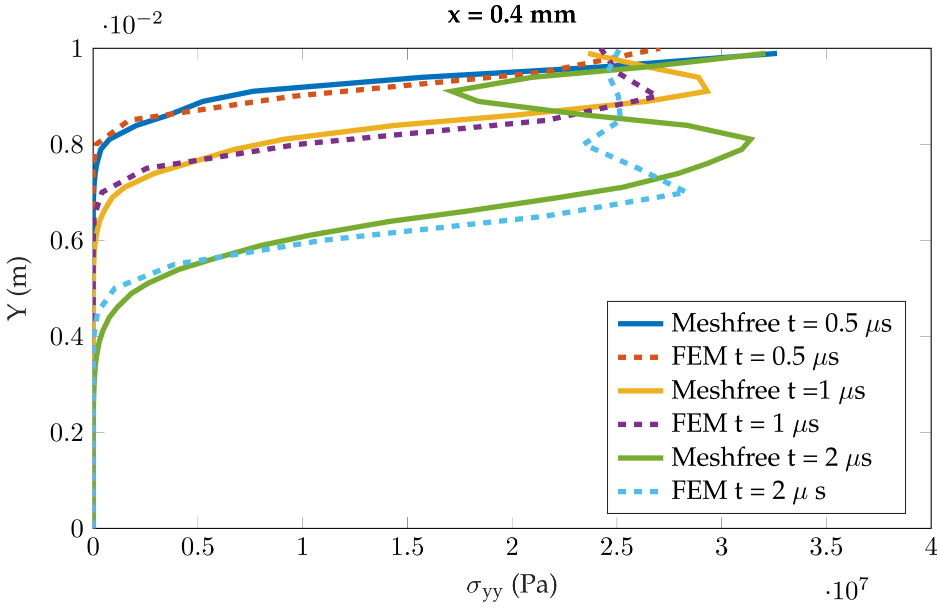

Figure 3.11: Normal stress comparison between EFG and FEM at different times

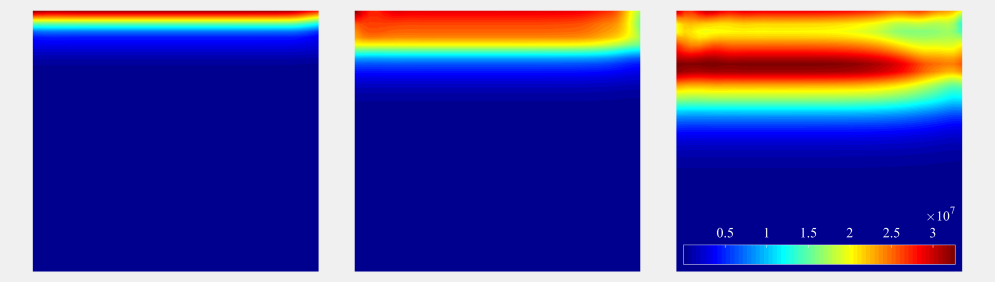

Figure 3.12: Normal stress wave in Pascals at $0.5\ \mu sec$, $1\ \mu sec$ and $2\ \mu sec$

3.7 Numerical Modelling of Contact-Impact

Modelling of the machining process entails modelling the workpiece and cutting tool. Cutting forces result from contact between the tool and workpiece, which is one of the fundamental outcomes of the proposed model. Contact is considered to be one of the most challenging aspects in computational mechanics since it leads to *boundary non-linearity*. This means that the contacting nodes (where forces should be calculated) are not known a priori (they are part of the solution) [127, 128]. From computational point of view, contact can be seen as a constraint on the model, where the displacement field (solution), has to fulfil the contact constraints as well as the boundary and initial conditions. As such, in theory, any method to impose constraints on the model could work in finding out the contact forces. In this study, the penalty method is chosen for the following reasons:

1. Using penalty does not increase the number of unknowns in the system.
2. The system matrices retain the positive definite properties, which makes them easier to solve.
3. The penalty method is easy to incorporate in both static and dynamic analysis.

While the Lagrange multiplier is more accurate, it introduces new unknowns, makes the system equations non-positive definite, and it is difficult to incorporate in the dynamic analysis. This is because in CDM, system equations are not *solved*. This is due to the utilisation of the lumped mass matrix as mentioned in Section 3.6.2. If Lagrange multipliers were to be introduced to the system, the mass matrix will no longer by diagonal and therefore, there will be a need to solve the system equations at each time step. This would make the CDM prohibitively time consuming. In this section, a frictionless penalty formulation for contact between an elastic body and a rigid one is developed. Chapters 4 and 5 will detail more advanced methods for capturing contact forces.

3.7.1 Penalty Formulation for Frictionless Contact

Contact between two solids can be formalised in two main conditions: the mechanical and kinematic contact conditions. The former states that in the absence of boundaries adhesion, tensile tractions are not allowed at the contacting boundaries

$$T_1 \leq 0 \tag{3.73}$$

The kinematic contact condition states that two material points (usually belonging to the contacting bodies) cannot occupy the same spatial position at the same time. This can be described using the normal gap function

$$g_n(X,t) \leq 0 \tag{3.74}$$

This condition is sometimes called the interpenetration condition. A graphical description is shown in Figure 3.13.

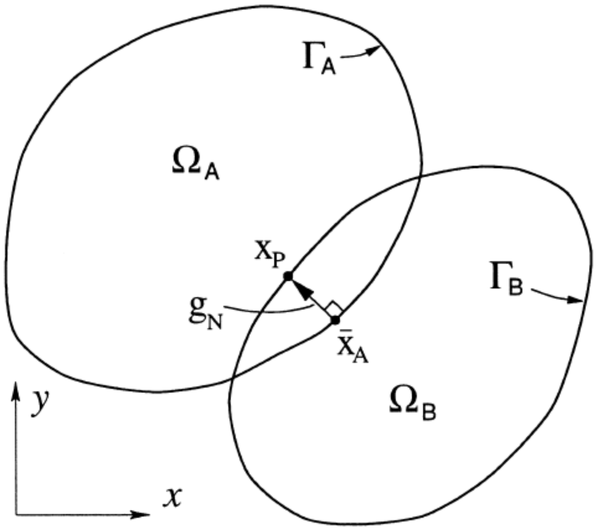

Figure 3.13: Interpenetration of two bodies, [8]

The normal gap can be expressed as follows

$$g_n = \parallel \bar{\mathbf{x}}_A - \mathbf{x}_P \parallel = min_{\mathbf{x}_A \in \Gamma_A} \parallel \mathbf{x}_A - \mathbf{x}_P \parallel \tag{3.75}$$

where, $\bar{\mathbf{x}}_A$ is the minimiser of the distance from point P to Γ_A. A popular approach in handling contact constraints is called the master-slave approach, whereby the master is considered rigid and the kinematic condition is enforced on the slave body. This can be expressed in terms of displacements and in local coordinates as follows

$$g_n = (\mathbf{u}^S - \mathbf{u}^M).\mathbf{n} \leq 0 \tag{3.76}$$

where, $\mathbf{n}$ is the unit normal constructed on one contacting surface. The superscripts M

and S refer to Master and Slave bodies. Using penalty method, a functional is constructed as follows

$$P_c(\mathbf{u}) = \int_{\Gamma_c} g_n^T \alpha_c g_n \mathrm{d}\Gamma \tag{3.77}$$

where, α_c is a penalty parameter. Assuming that the motion of the master body is known, the unknowns are reduced to the displacement of the slave body. The functional in Equation 3.77 is differentiated with respect to displacement and then MLS approximate field is used for the slave body as follows

$$\begin{aligned} \delta P_c &= \int_{\Gamma_c} \delta g_n^T \alpha_c g_n \mathrm{d}\Gamma = \int_{\Gamma_c} \delta(\mathbf{u}^M.\mathbf{n} - \sum_I^{n_c} \mathbf{\Phi}_I \mathbf{u}_I.\mathbf{n})^T \alpha_c (\mathbf{u}^M.\mathbf{n} - \sum_J^{n_c} \mathbf{\Phi}_J \mathbf{u}_J.\mathbf{n}) \mathrm{d}\Gamma \\ &= \int_{\Gamma_c} \sum_I^{n_c} \sum_J^{n_c} \delta \mathbf{u}_I^T (\mathbf{\Phi}_I.\mathbf{n})^T \alpha_c (\mathbf{\Phi}_J.\mathbf{n}) \mathbf{u}_J \mathrm{d}\Gamma - \int_{\Gamma_c} \sum_I^{n_c} \delta \mathbf{u}_I^T (\mathbf{\Phi}_I.\mathbf{n})^T \alpha_c (\mathbf{u}^M.\mathbf{n}) \mathrm{d}\Gamma \\ &= \sum_I^{n_c} \sum_J^{n_c} \delta \mathbf{u}_I^T \underbrace{\int_{\Gamma_c} (\mathbf{\Phi}_I.\mathbf{n})^T \alpha_c (\mathbf{\Phi}_J.\mathbf{n}) \mathrm{d}\Gamma}_{\mathbf{K}_{IJ}^c} \mathbf{u}_J - \sum_I^{n_c} \delta \mathbf{u}_I^T \underbrace{\int_{\Gamma_c} (\mathbf{\Phi}_I.\mathbf{n})^T \alpha_c (\mathbf{u}^M.\mathbf{n}) \mathrm{d}\Gamma}_{\mathbf{F}_I^c} \end{aligned} \tag{3.78}$$

where, n_c is the number of contacting nodes. Subsequently, the stiffness and force contributions of contact are added to the global discrete equations 3.51 and 3.68.

3.7.2 Numerical Implementation

The contact boundaries are part of the solution and therefore, the contacting nodes are not known prior to the solution. Contact detection is an important part of any computational contact implementation. In this work, contact detection is performed based on the built-in functions of MATLAB, which makes the implementation more efficient. The procedure entails defining the master body as a closed polygon and then searching for the nodes of the slave body within the master polygon. This is achieved using the MATLAB function `inpolygon`, and then identifying the contacting nodes within the global nodal matrix. This is equivalent to updating the position of the contacting bodies as if they were not contact and then searching for the contacting nodes and correcting the displacement field according to the updated force and stiffness matrices. Following the detection of the contacting nodes, the contact force calculations and the stiffness are then performed. Algorithm 3.5 shows the implementation of this formulation. Geometric calculations are performed using the natural coordinates since a local coordinate system at each master segment is constructed to calculate the normal gap function. This makes the calculations more efficient and robust.

Algorithm 3.5: Frictionless contact using penalty procedure

```
• Loop over contact points
• Distribute integration points along contacting boundary
• Calculate shape functions at integration points
    - Compute the master segment length
    - Compute the unit normal and tangent at the master segment
    - Compute the normal gap $g_n$
    - Apply the interpenetration condition
    - Compute the contact point in natural coordinates
    - If contact point is out of segment; return
    - Integrate the normal contact force and stiffness (Equation 3.78)
• End loop of contact points
```

3.7.3 Numerical Example: Elastic Bar Impacting Rigid Wall

An elastic bar of length $L = 0.2\ m$ and width $W = 0.01\ m$ travelling at $v_0 = 5\ m/sec$ impacts a rigid wall as shown in Figure 3.14. No prescribed pressure is applied. The bar impacts the rigid wall for a period of time and then bounces back. The analytical solution is obtained from the work of Zhong [127]. The material is assumed to be in plane strain condition with $E = 2 \times 10^{11}\ Pa,\ \nu = 0,\ \rho = 7800\ kg/m^3$ and the initial gap is zero.

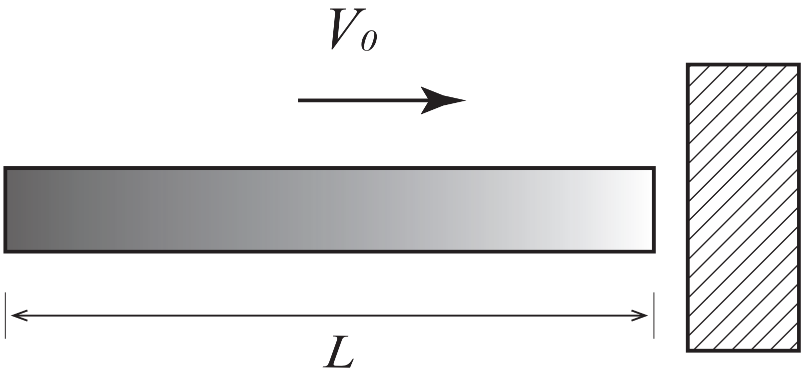

Figure 3.14: Set up of elastic bar impact example

The problem is solved with 40 nodes, 76 integration points, and penalty parameter $\alpha_c = 5 \times 10^{10}$. The MLS shape function was constructed using cubic spline weight function. The CDM algorithm proposed in Section 3.6.2 with a constant $\Delta t = 1 \times 10^{-8}\ sec$ was used. Figure 3.15 shows the comparison between the analytical and EFG solutions. The average contact force is in good agreement with the analytical solution. However, some numerical noise is present in the solution. This is a characteristic of the penalty method and is dependent on the selected penalty parameter. Higher penalty parameter tend to give noisier solutions. However, low values of penalty parameters allow for too much penetration and suffers from response delay (compare the slope of analytical and EFG solution at the end of the contact time). Numerical experiments are needed to determine the best value of the penalty parameter.

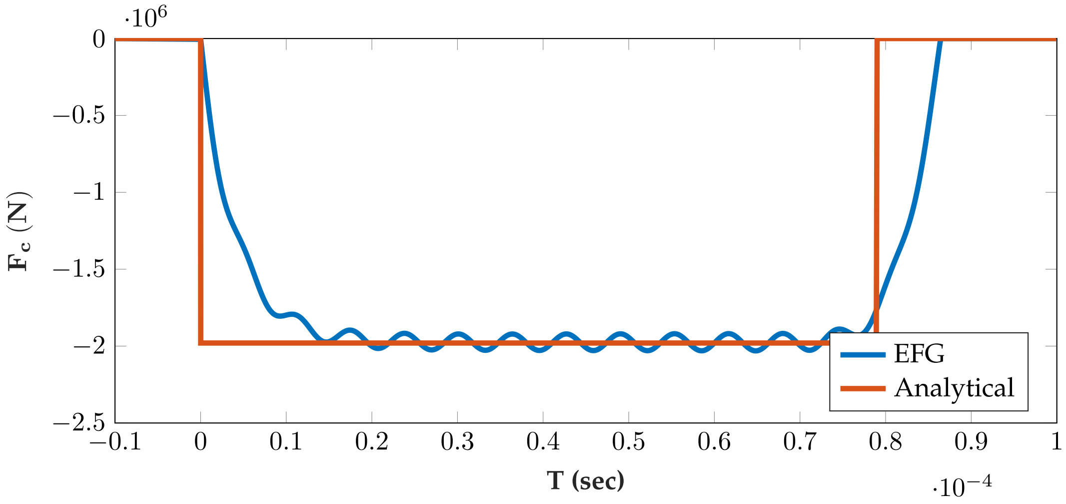

Figure 3.15: Contact force comparison

Figure 3.16 shows the change in components of system energy throughout the simulation. It is clear that the total energy is conserved in the system, which indicate that the algorithm is not generating spurious energy modes. At the end of the contact, energy of the system returns to being totally kinematic as all other forms vanish.

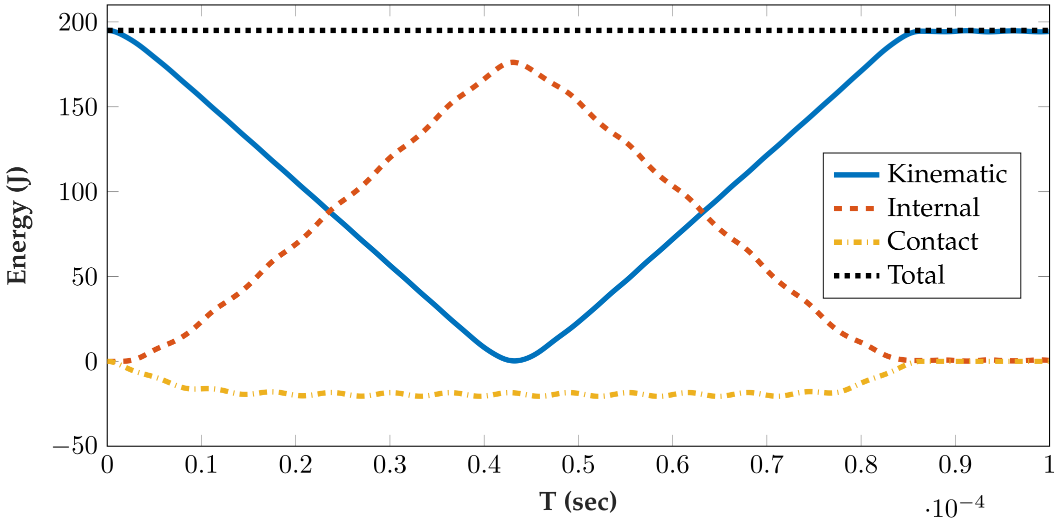

Figure 3.16: Conservation of Energy of the solution

3.8 Composite Materials Failure

The last major component of the orthogonal cutting model to be verified independently is the failure of composites. This is a crucial aspect of the model and links to many other aspects, such as stress calculations, non-linear formulation and method of time integration. The scope is limited in this research to unidirectional composites. In this section, three composites failure theories will be presented first, then their failure envelopes compared against published experimental data.

3.8.1 Failure Theories of Composites Laminates

For calculating failure, material strength parameters are required. Given the non-isotropic nature of composites, they have different strength values in the three principle directions. Furthermore, strength in tension is usually different than strength in compression. For the case of unidirectional laminate in-plane stress conditions, five strength parameters are required: X^t strength in the local x direction in tension; X^c strength in the local x direction in compression; Y^t and Y^c strength in tension and compression in the local y direction and the in-plane shear strength S^l. The failure index FI_j is a useful quantity, it is the normalised value that quantifies the level and type of failure, where j signifies the mode of failure (fibre, matrix or interface). $0 \leq FI_j \leq 1$, indicating no failure to complete failure.

From computational point of view, full description of failure requires two essential components, failure onset and failure progression. The first is governed by failure theory or criteria. The second one is a numerical procedure that determines how failure propagates within the computational domain while reflecting the physical behaviour of the material. Failure onset is presented in this chapter. Progressive failure will be discussed in Chapter 4.

As mentioned in Section 2.3.4, failure theories can be grouped into: (i) non-interactive, (ii) interactive and (iii) failure mode-based. In this study, three failure theories have been utilised, Maximum stress from the first group, and Hashin and LaRC02 from the third. The mathematical relations are presented below:

Maximum Stress

It is given as

$$FI_f = \left(\frac{\sigma_1}{X^k}\right)^2 \leq 1\,; \qquad k = [t, c] \tag{3.79a}$$

$$FI_m = \left(\frac{\sigma_2}{Y^k}\right)^2 \leq 1\,; \qquad k = [t, c] \tag{3.79b}$$

$$FI_i = \left(\frac{\tau_{12}}{S^l}\right)^2 \leq 1 \tag{3.79c}$$

Fibre and matrix criteria include two equations each, one for compression and one for tension, giving a total of 5 equations. As for shear, the sign of the shear stress does not affect the shear strength [22, 23].

Hashin

It is a very important failure theory, which was developed in 1973 and then a variation of it proposed in 1980. The model equations are given below

$$FI_{f,t} = \left(\frac{\sigma_1}{X^t}\right)^2 + \zeta\left(\frac{\tau_{12}}{S^l}\right)^2 \leq 1 \tag{3.80a}$$

$$FI_{f,c} = \left(\frac{\sigma_1}{X^c}\right)^2 \leq 1 \tag{3.80b}$$

$$FI_{m,t} = \left(\frac{\sigma_2}{Y^t}\right)^2 + \left(\frac{\tau_{12}}{S^l}\right)^2 \leq 1 \tag{3.80c}$$

$$FI_{m,c} = \left(\frac{\sigma_2}{2S^l}\right)^2 + \left[\left(\frac{Y^c}{2S^t}\right)^2 - 1\right]\frac{\sigma_2}{Y^c} + \left(\frac{\tau_{12}}{S^l}\right)^2 \leq 1 \tag{3.80d}$$

where, ζ is an interaction factor.

LaRC02

LaRC02 was developed by Davila et al. [129] of NASA and named after Langley Research Centre. It is based on Puck's action plane concept [130] combined with concepts proposed by Hashin [131]. The aim was to develop failure criteria that does not rely on experimental parameters but based on physical understanding of the composite lamina failure. LaRC02 was chosen in this work for the following reasons:

- It can account for the positive effect of transverse compression on the shear strength of unidirectional lamina.
- It corresponds well with the experimental evidence of the World Wide Failure Exercise.
- It does not contain empirical parameters/tuning parameters.
- While newer versions of LaRC02 were later developed (LaRC03 and LaRC04), they require additional material testing and are more complicated to implement.

Summary of the equations are given below

For matrix tension

$$FI_{m,t} = \left(\frac{\sigma_{22}}{Y^t}\right)^2 + \left(\frac{\tau_{12}}{S^l}\right)^2 \leq 1 \tag{3.81}$$

For matrix compression when $\sigma_{22} < 0$ and $\sigma_{11} < Y^c$

$$FI_{m,c} = \left(\frac{\tau_{\mathrm{eff}}^{\mathrm{mT}}}{S^{\mathrm{T}}}\right)^2 + \left(\frac{\tau_{\mathrm{eff}}^{\mathrm{mL}}}{S^{\mathrm{l}}}\right)^2 \leq 1 \tag{3.82}$$

For matrix compression when $\sigma_{22} < 0$ and $\sigma_{11} \leq Y^c$

$$FI_{m,c} = \left(\frac{\tau_{\mathrm{eff}}^{\mathrm{T}}}{S^{\mathrm{T}}}\right)^2 + \left(\frac{\tau_{\mathrm{eff}}^{\mathrm{L}}}{S^{\mathrm{l}}}\right)^2 \leq 1 \tag{3.83}$$

For fibre tension $\sigma_{11} \leq 0$

$$FI_{f,t} = \frac{\varepsilon_{11}}{\varepsilon_1^t} \leq 1 \tag{3.84}$$

For fibre compression when $\sigma_{11} < 0$ and $\sigma_{22}^m < 0$

$$FI_{f,c} = \left\langle \frac{|\tau_{12}^{\mathrm{m}}| + \eta^L \sigma_{22}^m}{S^l} \right\rangle \leq 1 \tag{3.85}$$

where $\langle x \rangle = x$ if $x \geq 0$; otherwise $\langle x \rangle = 0$. For fibre compression when $\sigma_{11} < 0$ and $\sigma_{22}^{m} \leq 0$

$$FI_{f,c} = \left(\frac{\sigma_{22}^{\mathrm{m}}}{Y^{\mathrm{t}}}\right)^2 + \left(\frac{\tau_{12}^{\mathrm{m}}}{S^{\mathrm{l}}}\right)^2 \leq 1 \tag{3.86}$$

The effective stress are calculated as follows

$$\tau_{\mathrm{eff}}^{\mathrm{T}} = \left\langle -\sigma_{22} \cos \Upsilon (\sin \Upsilon - \eta^{T} \cos \Upsilon) \right\rangle \tag{3.87}$$

$$\tau_{\mathrm{eff}}^{\mathrm{L}} = \left\langle \cos \Upsilon (|\tau_{12}| + \eta^{L} \sigma_{22} \cos \Upsilon) \right\rangle \tag{3.88}$$

where, Υ is fracture plane angle and Υ_0 is fracture plane angle in pure transverse compressive loading. The transverse shear strength is

$$S^{T} = Y^{c} \cos \Upsilon_0 \left(\sin \Upsilon_0 + \frac{\cos \Upsilon_0}{\tan 2\Upsilon_0} \right) \tag{3.89}$$

The coefficients of transverse and longitudinal influence are given as

$$\eta^{T} = \frac{-1}{\tan 2\Upsilon_0} \tag{3.90}$$

$$\eta^{L} \approx -\frac{S^{l} \cos 2\Upsilon_0}{Y^{c} \cos^2 \Upsilon_0} \tag{3.91}$$

The stresses in the misalignment frame are

$$\sigma_{11}^{m} = \cos^2 \psi \, \sigma_{11} + \sin^2 \psi \, \sigma_{22} + 2 \sin \psi \cos \psi \, \tau_{12} \tag{3.92}$$

$$\sigma_{22}^{m} = \sin^2 \psi \, \sigma_{11} + \cos^2 \psi \, \sigma_{22} - 2 \sin \psi \cos \psi \, \tau_{12} \tag{3.93}$$

$$\tau_{12}^{m} = -\sin \psi \cos \psi \, \sigma_{11} + \sin \psi \cos \psi \, \sigma_{22} + (\cos^2 \psi - \sin^2 \psi) \, \tau_{12} \tag{3.94}$$

where,

$$\psi = \frac{\tau_{12} + (G_{12} - X^c)\,\psi^c}{G_{12} + \sigma_{11} - \sigma_{22}} \tag{3.95}$$

$$\psi^c = \tan^{-1}\left(\frac{1 - \sqrt{1 - 4\left(\frac{S^l}{X^c} + \eta^L\right)\left(\frac{S^l}{X^c}\right)}}{2\left(\frac{S^L}{X^c} + \eta^L\right)}\right) \tag{3.96}$$

The effective stresses $\tau_{\text{eff}}^{\text{mT}}$ and $\tau_{\text{eff}}^{\text{mL}}$ are calculated by substituting the stresses in the misaligned frame in the effective stress Equations. All three theories use the local coordinates in evaluation of failure, therefore, local stresses have to be retrieved from global stresses before checking for the failure of the composite. Failure envelopes for UD-GFRP based on the three theories are presented in Figures 3.18 and 3.17. This allows verification of the MATLAB code and to show the differences between the presented theories. The calculated values are compared with experimental data provided in the World Wide Failure Exercise [10, 11]. The beneficial effect of compression stress on the shear is captured by LaRC02 as it is clear from the second quadrant of Figure 3.18.

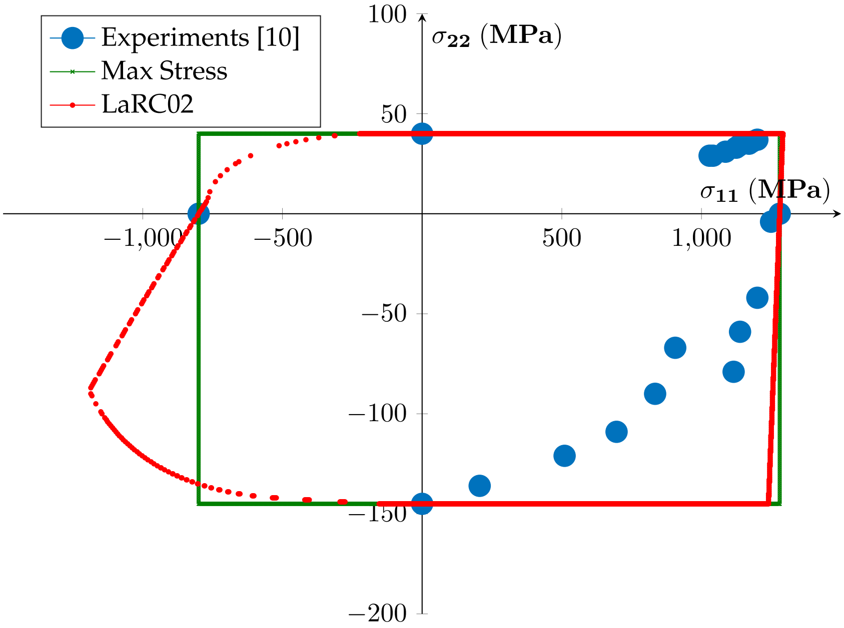

Figure 3.17: Comparison of failure envelopes with experimental data for Eglass/MY750

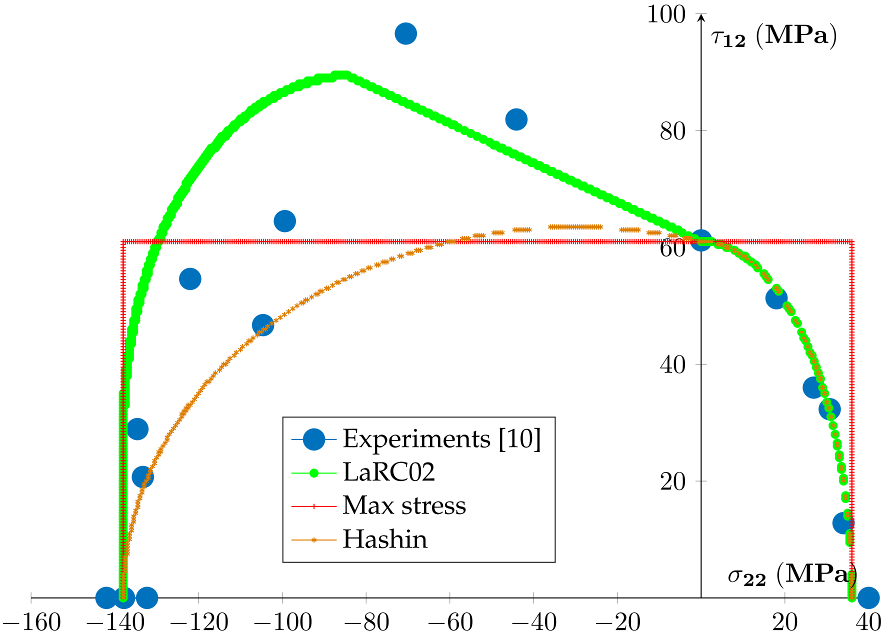

Figure 3.18: Comparison of failure envelopes with experimental data for Eglass/LY556

3.9 Concluding Remarks

This chapter presented a detailed derivation and development of the meshfree model components required in the orthogonal cutting of composites model. Step-by-step process is followed in developing the computer code accompanied by verification examples in order to ensure that each part of model is working as expected. This chapter summarised the results of laborious and iterative process that spanned over one and half years of this project's duration and is considered by the author to be the major learning experience of the PhD project. Some key findings/achievements can be summarised as follows:

- The system equations for static and dynamic models were derived from the weak form of momentum conservation, discretised using the EFG procedure and implemented in a MATLAB code.
- Penalty method and Lagrange multiplier were implemented to impose displacement boundary conditions for static models and penalty for dynamic ones.
- The accuracy of displacement and stress calculations were demonstrated by solving

Timoshenko beam example. Both penalty and Lagrange multiplier were in close agreement with the analytical solution with marginally better accuracy for Lagrange multiplier.

- The centre-cracked specimen example showed the capability of the code to model non-convex boundary using the visibility criteria and achieved good agreement with analytical solution.
- Characteristic of the hyperbolic PDE is studied using the stress wave propagation example. The model showed good agreement with FEM results and the calculated dilatational wave speed was also in good agreement with the theoretical value.
- Multi-body capability was added to the model by means of frictionless contact formulation and demonstrated with example of elastic bar impacting a rigid wall.
- Three different failure theories were added to the code and their envelopes were generated and compared with experimental evidence from the world wide failure exercise.

Chapter 4

Steady State EFG Model for Orthogonal Cutting of Composites

4.1 Introduction

Following the development of the main components of the meshfree model in the previous chapter, the author is now in position to present the first orthogonal cutting model of UD composites. The model will include some novel features that were not presented in Chapter 3, such as frictional contact formulation and progressive failure procedure.

Referring to the framework of machining model presented in Section 2.6, the features of the proposed model are summarised in Table 4.1. The dynamic effects are not included in this model as the objective at this stage of development is to simulate cutting at low speeds in which the steady state assumption is acceptable. Similar trend was noticed in FEM literature, where earlier models adopted steady-state approach and then developed dynamic models (e.g. the work of the same research group started with steady-state [5, 6] and then developed to dynamic [34, 116]). The material is assumed to be linear elastic up to failure, which is acceptable given the lack of plastic deformation during composites machining. Dual failure criteria is used to accurately predict the onset and completion

Table 4.1: Features of the proposed model

Features of machining model	*The proposed model*
Numerical method	Meshfree: EFG
Type of mesh	Lagrangian
Number of Dimensions	2
Dynamic effects	No
Constitutive model	Single phase: Orthotropic linear-elastic up to failure
Failure model	Dual failure criteria with selective stiffness degradation
Tool-workpiece contact	Frictional contact using penalty method
Main outputs	Cutting forces

of chip formation. Friction is added to the contact forces due to its high importance in machining simulations. The focus of this model is to accurately capture the cutting forces as a fundamental output of the cutting process. Analysis of the chip formation is better handled by dynamic models and will be discussed in Chapter 5. The fibre orientations is limited to the range $0 \leq \theta^o \leq 90$ due to the limits of applicability of the used failure model. System equations are solved using Implicit, Newton-Raphson non-linear solver with displacement control. Validation of the proposed model is carried out against experimental evidence found in literature as well as comparison against other FEM models found in literature that used the same validation data.

This chapter is organised as follows: the weak form is first presented followed by the frictional contact formulation. Spatial approximation followed by the discrete system equations are presented. Progressive failure modelling is discussed and then numerical procedure and model set-up are shown. Cutting forces results at different rake angles are compared against numerical and experimental data. Finally convergence studies are conducted and the effect of some meshfree parameters are discussed.

4.2 Governing Equations

The computational domain Ω in 2D is bounded by Γ. The penalty method is adopted to enforce boundary conditions. Since the material is linear elastic, it is possible to start with the weak from as shown in Equation 3.37. This mathematical model should be constrained to by contact conditions.

4.2.1 Frictional Contact Formulation using Penalty Method

Figure 4.1 shows a generic case for two discretised bodies in contact. A common way to approach contact calculations is by assuming one body as master and the other as slave. When the slave body moves from configuration Ω_0 to configuration Ω, then the slave node S penetrates the master body in the segment M_1M_2 and contact is assumed to have taken place. The local coordinates are defined at the first point of the master segment with outward unit normal $\mathbf{n}$ and in plane unit tangent $\mathbf{t}$.

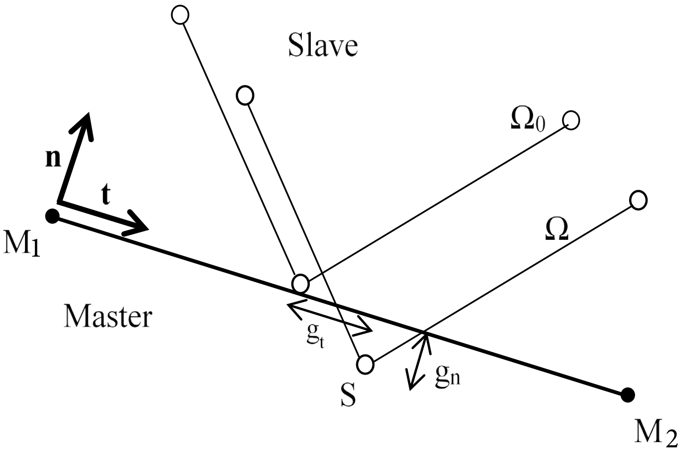

Figure 4.1: Basic Contact Terminology

As a result of the penetration, normal and tangential gap functions are defined as follows

$$g_n = \left(\mathbf{u}^S - \mathbf{u}^{M_1}\right) \cdot \mathbf{n} \tag{4.1a}$$

$$g_t = \left(\mathbf{u}^S - \mathbf{u}^{M_1}\right) \cdot \mathbf{t} \tag{4.1b}$$

where $\mathbf{u}^S$, $\mathbf{u}_1^M$ are the displacement of the slave node and the first master node respectively, $\mathbf{t} = \dfrac{\mathbf{x}_{M_2} - \mathbf{x}_{M_1}}{\parallel \mathbf{x}_{M_2} - \mathbf{x}_{M_1} \parallel}$ and $\mathbf{n} = \mathbf{t_3} \times \mathbf{t}$, $\mathbf{t_3}$ is the out-of-plane unit tangent.

At the contact boundary, the interpenetration condition should be enforced, which states that the two bodies cannot occupy the same space at the same time. When the normal gap $\mathbf{g}_n$ is negative, the impenetrability condition is violated and contact occurs. A contact traction proportional to the normal gap magnitude is used to enforce the condition again. Details of the contact implementation are presented in Section 4.3. The tangential slip expression in Equation 4.1b represents the sliding movement of the slave node on the boundary of the master body. The tangential contact component is calculated using Coulomb friction law

$$\parallel \mathbf{T}_t \parallel - |\mu \mathbf{T}_n| \leq 0 \tag{4.2}$$

where, μ is the friction coefficient and $\mathbf{T}$ is the traction at the contact boundary. The inequality of the law implies two states. The first is when $\parallel \mathbf{T}_t \parallel - |\mu \mathbf{T}_n| < 0$, and is called the stick condition. In this case, tangential traction cannot overcome the frictional one and hence there will be no relative motion between the contact bodies (on the macro scale). When the two terms in the equations are equalised, a relative motion occurs and this condition is called the slip condition. The role of the friction coefficient is clear in changing the threshold of sliding.

In order to include the contact constraints into Equation 3.37, a penalty functional including both terms of contact is constructed [128, 132]

$$P \equiv \int_{\Gamma_c} \alpha_n \frac{g_n^2}{2} \mathrm{d}\Gamma + \int_{\Gamma_c} \alpha_t \frac{g_t^2}{2} \mathrm{d}\Gamma \tag{4.3}$$

where, $\alpha_n,\ \alpha_t$ are penalty parameters. Differentiating with respect to $\mathbf{u}$ gives

$$\delta P_c \equiv \int_{\Gamma_c} \delta g_n(\mathbf{u})^T \ \alpha_n \ g_n(\mathbf{u}) \mathrm{d}\Gamma + \int_{\Gamma_c} \delta g_t(\mathbf{u})^T \ \alpha_t \ g_t(\mathbf{u}) \mathrm{d}\Gamma = 0 \tag{4.4}$$

Using penalty method in imposing constraints has several advantages. The number of unknowns does not increase. The system equations maintain the positive definite property. However, the accuracy of the constraint imposition relies on the choice of a suitable penalty parameter and convergence might slow down. Theoretically, higher penalty parameter improves the accuracy; however, in practice, choosing very large penalty parameter could cause ill-conditioning of the system equations.

The constrained Galerkin weak form is obtained by adding Equation 4.4 to Equation 3.37

$$\begin{aligned}\int_{\Omega}(\mathbf{L}\,\delta\mathbf{u})^T(\mathbf{L}\,\mathbf{D}\,\mathbf{u})\mathrm{d}\Omega - \int_{\Omega}\delta\mathbf{u}^T\mathbf{b}\mathrm{d}\Omega - \int_{\Gamma_t}\delta\mathbf{u}^T\bar{t}\mathrm{d}\Gamma - \int_{\Gamma_u}\delta\left(\mathbf{u}-\bar{\mathbf{u}}\right)^T\alpha_u\left(\mathbf{u}-\bar{\mathbf{u}}\right)\mathrm{d}\Gamma \\ - \int_{\Gamma_c}\delta g_n(\mathbf{u})^T\,\alpha_n\,g_n(\mathbf{u})\mathrm{d}\Gamma - \int_{\Gamma_c}\delta g_t(\mathbf{u})^T\,\alpha_t\,g_t(\mathbf{u})\mathrm{d}\Gamma = 0\end{aligned} \tag{4.5}$$

4.2.2 Discretised Equations

Using the MLS shape functions and their derivatives (Equations 3.18, 3.19) along with the strain-displacement relation (Equation 3.8), Equation 4.5 can be discretised to give

$$\left(\mathbf{K}+\mathbf{K^u}+\mathbf{K^c}\right)\mathbf{U} = \mathbf{F}+\mathbf{F^u}+\mathbf{F^c} \tag{4.6}$$

where,

$$\mathbf{K}_{IJ} = \int_{\Omega}\mathbf{B}_I^T\mathbf{D}\mathbf{B}_J\mathrm{d}\Omega \tag{4.7a}$$

$$\mathbf{F}_I = \int_{\Omega}\mathbf{\Phi}_I^T\,\mathbf{b}\,\mathrm{d}\Omega + \int_{\Gamma}\mathbf{\Phi}_I^T\,\bar{\mathbf{t}}\,\mathrm{d}\Gamma \tag{4.7b}$$

$$\mathbf{K}_{IJ}^u = \int_{\Gamma_u}\mathbf{\Phi}_I^T\alpha_u\mathbf{\Phi}_J\mathrm{d}\Gamma \tag{4.7c}$$

$$\mathbf{F}_I^u = \int_{\Gamma}\mathbf{\Phi}_I^T\alpha_u\,\bar{\mathbf{u}}\,\mathrm{d}\Gamma \tag{4.7d}$$

$$\mathbf{B}_I = \mathbf{L}\,\mathbf{\Phi}_I \tag{4.7e}$$

Using collocation integration, the contact components are given for stick condition

$$\mathbf{K}_{IJ}^c = \alpha_n\left(\mathbf{n}_I\cdot\mathbf{n}_J^T\right) + \alpha_t\left(\mathbf{t}_I\cdot\mathbf{t}_J^T\right) \tag{4.8a}$$

$$\mathbf{F}_I^c = -\left(\alpha_n g_n\cdot\mathbf{n}_I + \alpha_t\cdot\mathbf{t}_I\right) \tag{4.8b}$$

and for slip condition

$$\mathbf{K}^c_{IJ} = \alpha_n \left(\mathbf{n}_I \cdot \mathbf{n}^T_J\right) + \mu\alpha_n \, \text{sign}(g_t) \left(\mathbf{t}_I \cdot \mathbf{n}^T_J\right) \tag{4.9a}$$

$$\mathbf{F}^c_I = -\alpha_n g_n \cdot \mathbf{n}_I + \left(1 + \mu \, \text{sign}\left(g_t\right)\right) \tag{4.9b}$$

Collocation integration (integration at nodes) was chosen instead of Gaussian quadrature as it offers significant simplification in the final equations and avoids distributing guass points at the contacting boundary each iteration. This however, necessitates using fine discretisation along the contact boundary to prevent excessive penetration of slave nodes into the master segments. As can be seen in Figure 4.7, the nodes are distributed so as the maximum nodal density is located at the contacting boundary.

4.2.3 Material Failure Model

Composite failure modelling is essential component of the machining model. Onset, progression and completion of chip formation are mainly governed by this component. In this study, a dual failure criteria is used: primary failure criterion that controls the onset of chip formation and a secondary that controls the progression and completion of chip formation. As mentioned before, the scope of this model is cutting at positive fibre angles; in this range, the chip formation undergoes primary and secondary failure (refer to Section 2.4.2). Earlier studies have utilised this observation and adopted this double failure criteria approach in modelling chip formation [5, 6, 96].

When the tool engages with the workpiece, the primary failure criterion is checked every iteration. The material ahead of the cutting tool is deemed failed if

$$FI \equiv \sqrt{\left(\frac{\sigma_n}{S_\sigma}\right)^2 + \left(\frac{\tau}{S_\tau}\right)^2} \geq 1 \tag{4.10}$$

where, σ_n is the stress normal to the cutting plane in global coordinates, τ is the in-plane shear stress, S_σ is the interface strength in the normal direction and S_τ is the shear interface

Table 4.2: Normal and Shear strength values [5]

θ^o	0	15	30	45	60	75	90
$S_\sigma\ (N/mm^2)$	59	87.13	127.75	379.5	598.25	998.55	1200
$S_\tau\ (N/mm^2)$	25	39.82	59.89	96.96	150	180.62	250

Table 4.3: Stiffness degradation parameters

Failure Mode	E_1	E_2	G_{12}
Longitudinal Failure	0.01	0.01	0.01
Transverse Failure	1	0.01	0.2
In-plane shear failure	1	0.01	0.01

strength. The values of S_σ and S_τ are dependent on fibre orientation and are given in Table 4.2. Maximum stress criteria is used as secondary (progressive) failure criteria. The equations are given in Section 3.8.1.

Progressive failure of materials can be described mathematically by the stiffness degradation concept. Once a material point has failed (usually evaluated at the integration points), the stiffness of that point is *degraded* by multiplying the original values with a small constant number. This loss of stiffness is applied suddenly. Gradual stiffness degradation could be used but it proved to be highly mesh-sensitive and required additional material data. Due to the high directionality in stiffness of the unidirectional composite, some modes of failure do not mean complete loss of load bearing in the composite, such as failure in transverse direction. As such selective stiffness degradation of unidirectional composites has been used in studying composites failure including machining of composites [99, 101, 112]. In this study, the stiffness degradation values were adopted from the work of Zhao et al. [133] and are shown in Table (4.3).

It is generally agreed that fibre failure means a total loss of load carrying capacity, which is why all variables are degraded when longitudinal failure happens. Degradation values of 0.05 were used in the study of Lasri et al. [112], the author conducted simulations using 0.01 and 0.05 and found that the effect on force was less significant.

4.3 Numerical Procedure

Due to the presence of nonlinearities in the model, a direct solution cannot be obtained and an iterative procedure should be utilised. The nonlinearities in the problem are: material non-linearty due to the presence of failure (despite using linear elastic constitutive model) and boundary non-linearity due to the contact between the workpiece and tool. In this work, full Newton-Raphson algorithm is employed to solve the discretised system equations. Since the motion of the cutting tool is prescribed, a displacement-controlled algorithm is adopted instead of load-controlled. In order to improve the robustness of the algorithm, step bisection is utilised in case of divergence[1]. If the maximum number of iterations or maximum allowed residual are reached, last converged solution is retrieved, then the displacement increment is halved and calculations restarted [128].

A condensed flowchart of the numerical procedure is shown in Figure 4.2. Failure and contact calculations are at the heart of the algorithm. The analysis is set to terminate at the completion of the first chip. This is assumed to have happened when the failure has propagated from the cutting point until the free surface of the workpiece. Failure is calculated from local stresses, which are retrieved from global stresses by applying appropriate rotation rules presented in Section 2.3.3. Primary failure (F_p) is evaluated after each converged iteration according to Equation 4.10. If the onset of chip formation is not yet reached, the tool is displaced and another iteration loop starts. Once the chip formation has started, secondary failure is used to calculate progressive failure. Failed points are degraded according to the mode of failure and the degradation values shown in Table 4.3. This process is repeated until the failure has propagated till the free surface of the workpiece.

Contact searching is performed according to Section 3.7.2, after which, contact force and stiffness calculations are performed according to Algorithm 4.1. It is worth noting that setting $\mu = 0$ is equivalent to performing frictionless contact calculations but using the same procedure.

---

[1] Divergence usually happens when the system matrix become positive indefinite. This means that rounding off and other errors amplify and *blow up* the solution

Algorithm 4.1: Frictional contact calculations using penalty method

```
Loop over contact points
    • Compute the master segment length
    • Compute the unit normal and tangent at the master segment
    • Compute the normal gap $g_n$
    • Apply the interpenetration condition
    • Compute the contact point in natural coordinates
    • If contact point is out of segment; return
    • Calculate the normal contact force and stiffness
    • if $\mu > 0$
        – Calculate the tangential gap $g_t$
        – If stick condition = true, use Equations 4.8.
        – If slip condition = true, use Equations 4.9.
    • Add normal and tangential components to the global force and stiffness matrices.
End loop over contact points
```

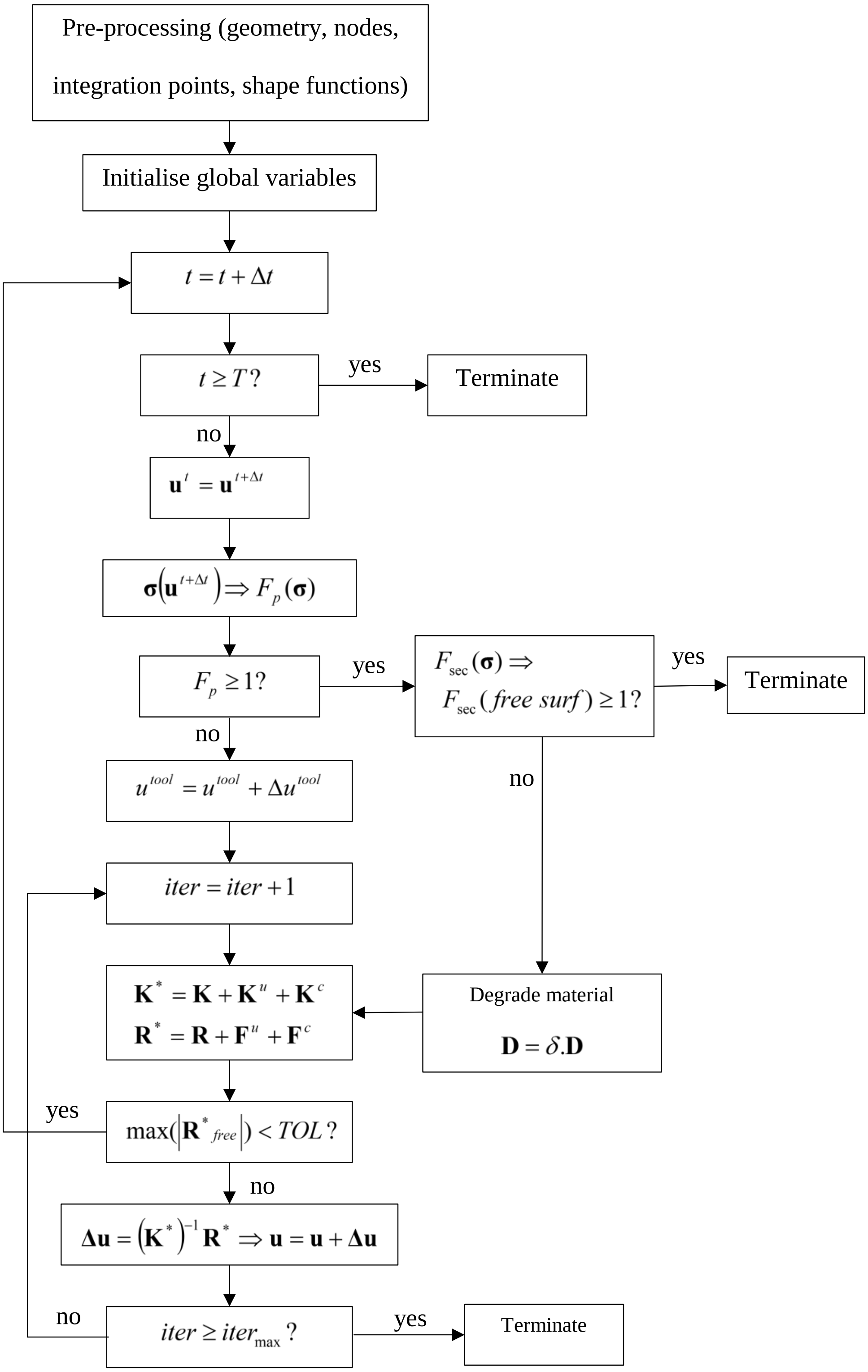

Figure 4.2: Flowchart of the steady state orthogonal cutting model

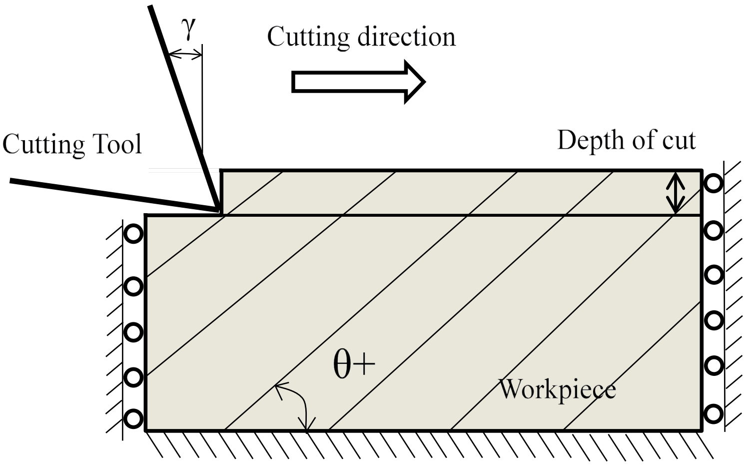

Figure 4.3: Numerical Model Set up

Table 4.4: Model geometrical parameters

Workpiece dimensions (mm)	10×5
Depth of cut (mm)	0.2
rake angle γ^o	0, 5, 10
clearance angle (^{o})	6
Fibre orientation (θ^o)	0,15, 30, 45, 60, 75, 90

4.3.1 Model Set up

The model set up is given in Figure 4.3. The geometrical parameters used to construct the model are given in Table 4.4.The mechanical properties of the workpiece material is given in Table 4.5. The simulation results will be compared against the experimental evidence presented in Bhatnagar et al. [5]. As such the model geometry, cutting conditions and material properties are taken from the same work. 3 rake angles and 7 orientations were simulated giving a total of 21 simulation.

In this study, the tool is considered rigid body and thermal effects are not considered as the cutting speed is chosen to be very low ($0.5\ m/min$) in order to reduce the thermal effects to the extent possible. The friction coefficient is taken as $\mu = 0.5$ after Lasri et al.

Table 4.5: Mechanical properties for UD-GFRP [5]

E_1	E_2	ν_{12}	G_{12}	X^t	X^c	Y^t	Y^c	S^l
GPa	GPa	-	GPa	MPa	MPa	MPa	MPa	MPa
48	12	0.19	6	1200	800	59	128	25

[112]. The effect of the friction coefficient was found minimal in the proposed model. This is supported by the work of Nayak et al. [6], where they determined the friction coefficient as a function of fibre orientation using pin on disk experiments, then ran simulations with and without friction and found that only thrust force magnitude was marginally affected by friction.

4.3.2 Meshfree Set up and Preprocessing

Accurate numerical integration of the weak form is critical in obtaining meaningful results. Numerical integration of meshfree methods takes two main approaches: (i) mesh based and (ii) nodes based. In this study, cell structure mesh with 2×2 integration points were used, which was found to be accurate and easy to implement, although in nonlinear analysis it can be computationally intensive [71]. Nodal density was increased near the cutting edge to improve the accuracy of the calculations. A total of $9,288$ nodes were used in discretisation.

Constructing the domain of influence (DoI) is an important step in calculating the MLS shape functions. The procedure presented in Chapter 3 was mainly for uniform nodal spacing. Since the nodal spacing is non-uniform, in this case a more general procedure is required. The proposed procedure was adopted from Liu and Tu [93] and modified and can be summarised as follows:

1. Construct quadrilateral cells and distribute integration points.

2. Calculate cell areas.

3. Find cells surrounding each node.

4. Find nodes around each integration point with radial distance $r_I \leq \beta \bar{a}_q$.

where, $\beta \geq 1$ is the scaling parameter which controls the size of the domain and $\bar{a}_q$ is the mean area of the cells surrounding point. This method provides a robust approach in calculating the domain of influence at any kind of distribution. Where quadrilateral cells are not suitable, triangular cells could be used in the same manner.

4.4 Results and Discussion

4.4.1 Cutting Forces

Figure 4.4 shows the cutting forces comparison between the proposed model, FEM simulations [101] and experimental evidence for three fibre orientations found in [31]. The general trend of forces between the proposed model and the other sources were in agreement. The minimum force was obtained at $\theta = 15^o$, while the maximum was obtained at $\theta = 90^o$. The values ranged from 21 to 95 N/mm. For $\theta = 30^o \rightarrow 60^o$, comparison with the experimental data showed that the difference between EFG model and experiments was within $\pm 15\%$ or (less than $5\ N/mm$), which is comparable to the FEM results shown. By comparing with FEM model, the EFG model under-estimated the forces at lower angles and overestimated them at higher angles. This could be the case since failure model used in this study is Maximum stress, whereas Soldani et al. [101] used Hashin failure model. Furthermore, at lower θ, shear failure according to the primary failure criteria (Equation 4.10) has relatively small values, refer to Table 4.2. This indicates that the onset of damage starts fairly quickly triggering the secondary failure criteria. Due to the selective stiffness degradation, failure propagates along fibre direction. Matrix and interface failure quickly reach the free surface of the workpiece and thereby chip formation is complete. On the other hand, at higher angles, the onset of damage is delayed due to the higher values of primary failure, which leads to a delay in chip completion process and thereby overestimating the force. It is noted that there is a scarcity in data in literature for simulated thrust force at $\gamma = 0^o$.

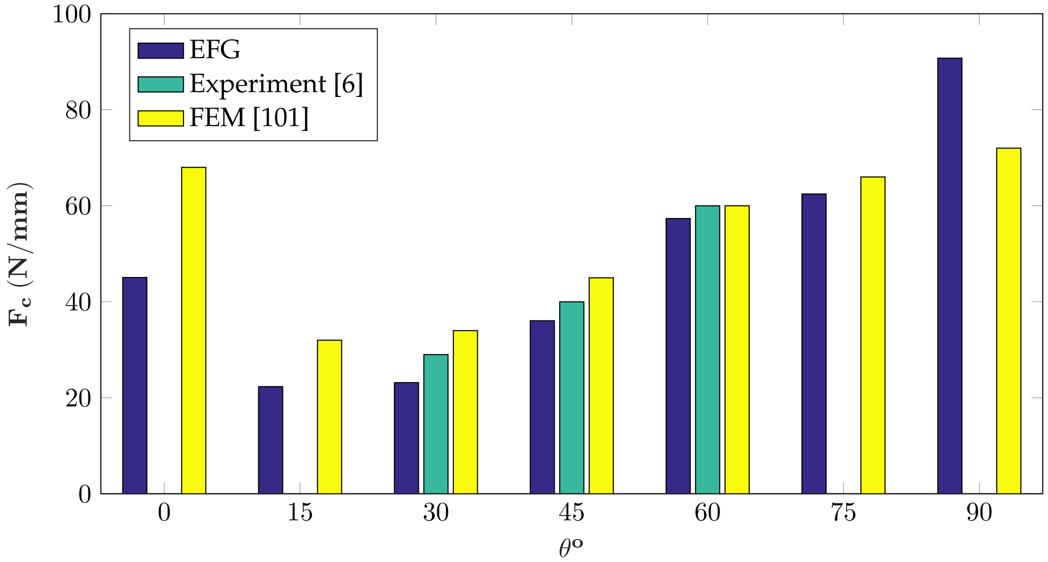

Figure 4.4: Cutting force at $\gamma = 0^o$

Figure 4.5 shows the cutting and thrust forces at $\gamma = 5^o$ for the EFG model, experimental values given by Bhatnagar et al. [5] and FEM results given in the work of Lasri et al. [112]. Regarding the cutting force, (Figure 4.5a), the minimum value of $16\ N/mm$ was observed at $\theta = 15^o$ and maximum of $64\ N/mm$ was observed at $\theta = 90^o$. Generally, the trend for cutting forces (as a function of fibre orientation) matched well between EFG and FEM models with experiments. However, the EFG model results seem to be consistently lower than that of experiments and FEM. This could be attributed to the assumption of sharp tool nose in the proposed EFG model as opposed to $0.05\ mm$ nose radius in experiments and FEM model. Nose radius increases the force due to reduction of effective rake angle at the nose tip. Soldani et al. [101] studied the effect of nose radius numerically and found that nose edge radius increased the cutting force ($10\ N/mm$ increase between $0.05 - 0.15\ mm$). Adding nose radius to the EFG model caused convergence difficulties for the Newton-Raphson solver, therefore it was excluded from this investigation.

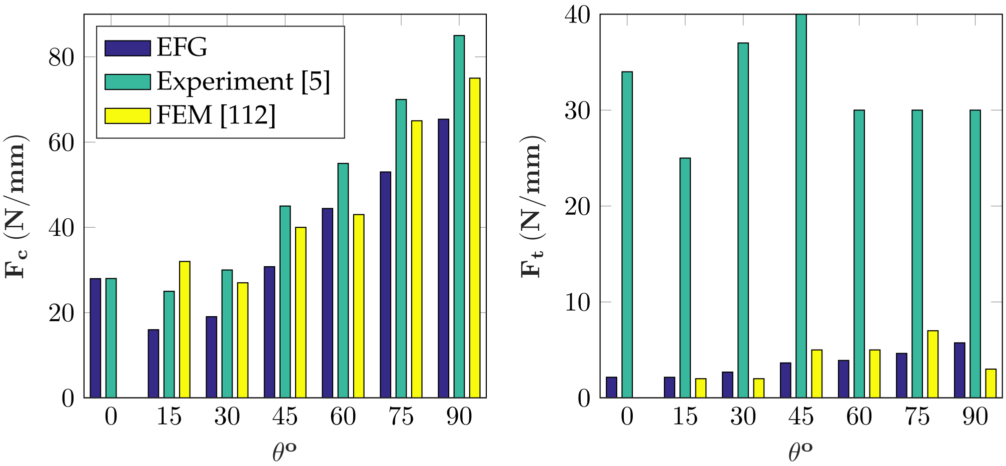

(a)

(b)

Figure 4.5: Comparison of (a) cutting and (b) thrust force at $\gamma = 5^o$

Figure 4.5b shows similar comparison but for thrust forces. It is clear that the models considerably underestimated the force magnitude. Lasri at al. [112] argued that the thrust force relies on the bouncing back effect of the machined surface, which creates an upward force on the clearance face [134]. The nature of the quasi-static model and the termination of the calculation after the completion of the first chip suggest that this kind of models have limited capabilities in capturing the bouncing back effect and subsequently the bulk of the thrust force magnitude. This is further compounded by starting the machining process within the workpiece and not at the free edge, which is used to avoid numerical difficulties [5].

Figure 4.6a shows cutting force comparison between the proposed EFG model, experiments of Nayak et al. [6] and FEM results reported by Soldani et al. [101] for $\gamma = 10^o$. As before, the overall trend is similar although the meshfree model tended to underestimate the force value. This could be attributed to the exclusion of tool nose in the meshfree model as explained earlier. A minimum of $14\ N/mm$ was observed at $\theta = 15^o$ and maximum of $66\ N/mm$ was observed at $\theta = 90^o$ compared with minimum of $20\ N/mm$ and maximum of $67\ N/mm$ for the experiments. Figure 4.6b shows the thrust force comparison, it can be seen that the EFG model predictions is significantly lower than that of the experiments, the same logic applies as in the case of $\gamma = 5^o$. However, by comparison with FEM results, FEM showed better agreement with the trend of the experimental values. This could be attributed to the fact that Soldani et al. [101] have used explicit procedure, which allows for simulation of consecutive chip formation. The convergence problems of the quasi-static solver are not found in the explicit algorithm. In the case of $\gamma = 5^o$, by comparing the results with [112], where similar solver was used, EFG and FEM results in agreement. This indicates that this is not a drawback in meshfree methods but rather in the chosen solving scheme. This could be addressed by using explicit solver like the central difference method.

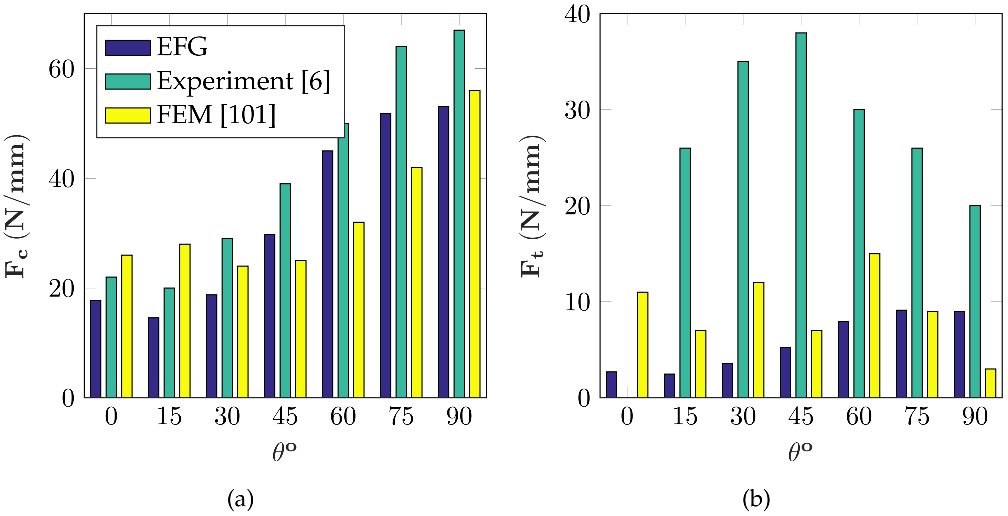

Figure 4.6: Comparison of (a) cutting and (b) thrust forces at $\gamma = 10^o$

4.5 Convergence Studies

In the following section, the effect of discretisation on the forces is studied by changing the nodal density. Then, the effect of the meshfree parameters on the results is examined. Two important parameters are selected, namely, the size of the domain of influence (β) and the weight function used in constructing the MLS approximation. Full factorial design is employed with $\beta \in [1, 1.5, 2]$ and weight function is either cubic or quartic spline.

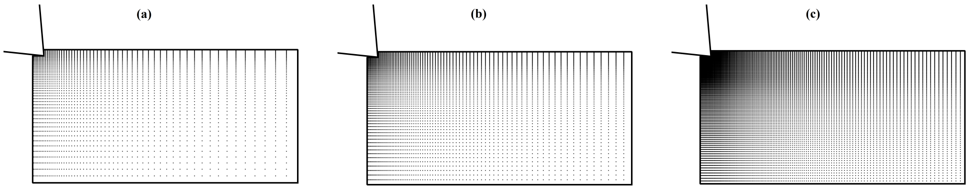

Figure 4.7: Discretised domain using (a) 3385, (b) 9288 and (c) 21621 nodes

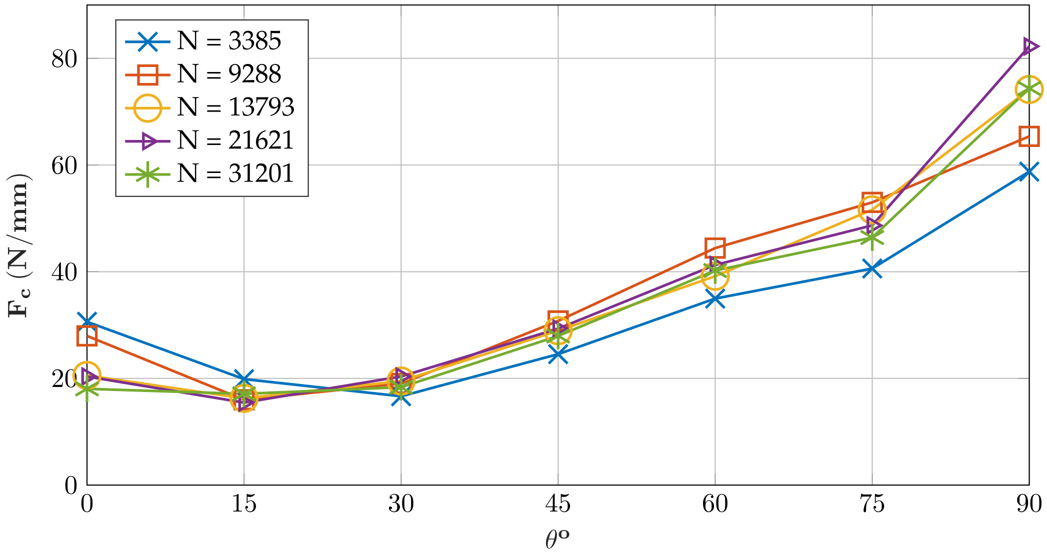

Figure 4.8: Discretisation sensitivity

4.5.1 The Effect of Nodal Distribution on Cutting Forces

Using uniform mesh with the current set up proved infeasible, because of the need for fine mesh at the cutting zone to accurately capture the contact forces. This necessitated using very fine mesh throughout the domain creating out-of-memory errors in the MATLAB code. Instead, non-uniform nodal density distribution is used with highest density near the tool-workpiece interface as shown in Figure 4.7.

Figure 4.8 shows the cutting force results of 5 meshes with increased nodal density for $\gamma = 5^o$. The results are in close agreement although they do not follow the expected convergence behaviour, i.e. approaching the accurate solution from one side. This could be attributed to the following inaccuracies: Using collocation integration of the contact interface meant that small variations in the effective contact length exist among different meshes. This in turn leads to small variations in contact forces. Another possible source of inaccuracy is the triggering of the primary failure criterion. Changes in mesh size leads to change in the energy needed to trigger the primary failure criteria (the damaged area ahead of the cutting tool that would trigger the primary failure decreases with increased nodal density). This can have significant effect at $\theta = 0^o$ and $\theta = 90^o$ since the primary failure is triggered early in the case of 0^o and late in the case of 90^o (refer to Table 4.2) leading to underestimating the force in the former and overestimating it in the latter as the nodal density increases. As such, the mesh with $N = 9288$ nodes is used throughout the study as it provides the best compromise between accuracy (agreement with experimental evidence) and computational time.

4.5.2 The Effect of DoI Size on Cutting Forces

Figure 4.9 shows the effect of β on cutting force at different rake angles. Generally, higher β values yielded lower forces across the different rake angles. This could be explained by the fact that larger domain tends to defuse/smooth high stress gradients. Since the cutting zone is at high stress, the reduced stresses lead to reduced forces. This is further explained by the partition of unity property of the MLS shape function i.e. more nodes in the domain tend to flatten the shape function. β has little effect on the trend of the cutting forces.

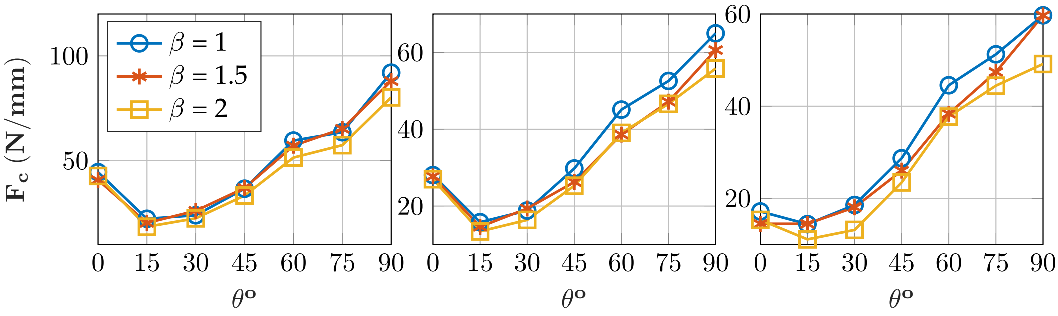

Figure 4.9: Effect of DoI size on cutting force at $\gamma^o =$ (a) 0, (b) 5 and (c) 10

The effect of β on the thrust force is shown in Figure 4.10 As with the cutting force, the thrust force decreased with increased β. Across the range $\beta = 1 - 2$, average thrust force was reduced by 10.8% ($5.3\ N/mm$) for $\gamma = 0^o$, by 7.9% ($2.9\ N/mm$) for $\gamma = 5^o$ and by 17% ($5.7\ N/mm$) for $\gamma = 10^o$. The fluctuations in Figure 10-a are likely to be due to numerical noise combined with the small magnitude of force which amplified the noise contribution.

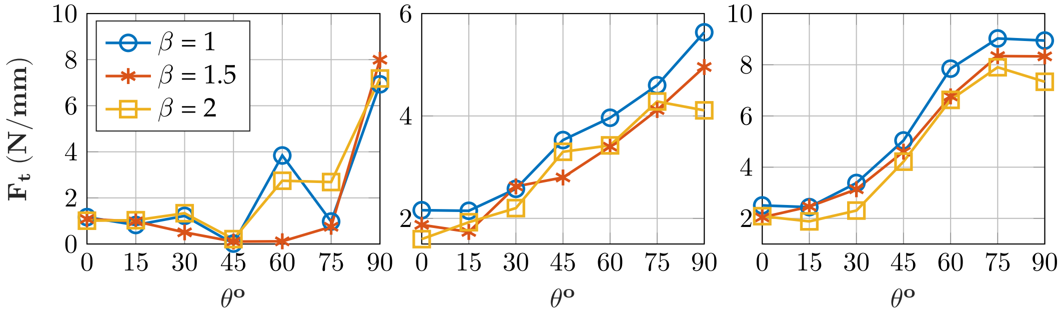

Figure 4.10: Effect of DoI size on thrust force for γ^o = (a) 0, (b) 5 and (c) 10

4.5.3 The Effect of Weight Function on Cutting Forces

The weight functions used in this study had a negligible effect on the cutting forces for all rake angles, with marginally higher values for cubic weight function at $\gamma = 10^o$ as shown in Figure 4.11.

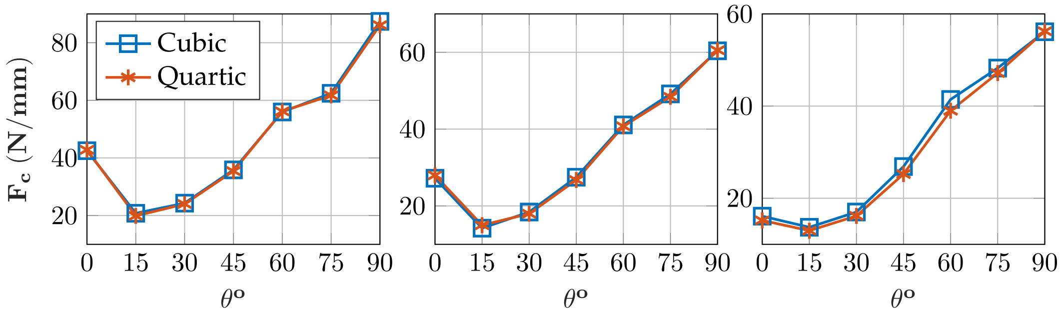

Figure 4.11: Effect of weight function on cutting force for γ^o = (a) 0, (b) 5 and (c) 10

The effect of the weight function on thrust force is more pronounced, this might be attributed to the very small values of force. Generally, cubic spline yielded higher values: 11.6% for $\gamma = 0^o$, 1.4% for $\gamma = 5^o$ and 4.9% for $\gamma = 10^o$. Figure 4.12-a showed similar fluctuations to Figure 4.10-a and for similar reasons. Since higher values of thrust force are more accurate, cubic spline is a better choice for this class of problems.

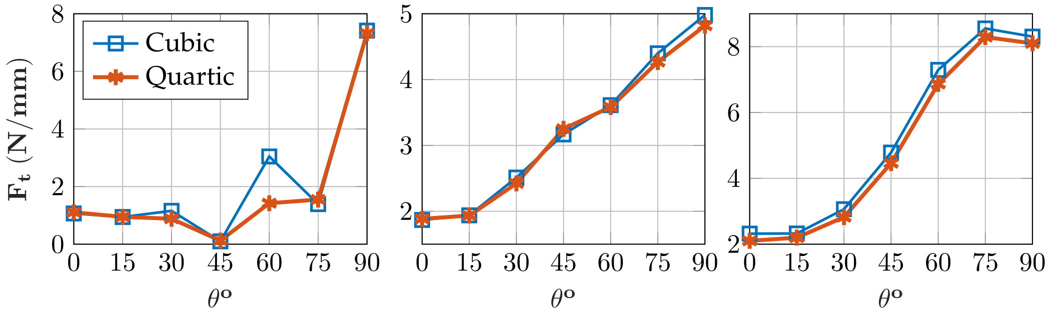

Figure 4.12: Effect of Weight function on thrust force for γ^o = (a) 0, (b) 5 and (c) 10

4.6 Conclusions

In this chapter, the application of the Element-Free Galerkin Method (EFG) was extended to modelling machining of composites. Moving least squares approximation was used to construct the shape functions with cubic or quartic spline weight functions. Full Newton-Raphson solver with bisection capabilities was utilised to solve the system equations. The composites were modelled as Equivalent-homogeneous material in plane stress and with linear elastic behaviour up to failure. Two stress-based failure criteria were used to simulate the onset and progression of chip formation. The cutting forces were calculated using penalty method and regularised Coulomb friction law. The model was validated against experiments and FEM simulations available in literature.

The model was able to capture the strong dependency of the forces on fibre orientations and also the dependency on rake angle. Among the meshfree parameters, the size of DoI was found more significant than the weight function. A good rule of thumb for choosing DoI is to use the minimum value that maintains the invertibility of the moment matrix. An added advantage of smaller DoI is the reduction of the computational cost as fewer nodes are used in stress calculations at each integration point.

The present model has demonstrated the viability of the EFG model for simulating composites cutting. The pre-processing phase was simple since the nodal connectivity was not required for domain discretisation. This facilitates easy changes in the model (e.g.

changing the depth of cut, rake angle, workpiece dimensions) and allows the analyst to concentrate more on analysing the results rather than building the model. One drawback in the model was the need for some trials to choose a suitable penalty parameter. This is not inherent to the meshfree methods but to the penalty method. Other constraint methods could be employed to alleviate this issue, such as Lagrange multiplier and augmented Lagrangian. Future research effort can include: incorporating dynamic effects (explicit time integration), coding more accurate failure models and utilising more sophisticated approach to chip formation modelling.

Chapter 5

Dynamic EFG Model for Orthogonal Cutting of Composites

5.1 Introduction

In this chapter, a dynamic EFG model for orthogonal cutting of composites is developed. Building on the steady-state model, several advanced features are added to improve the predictive capability and efficiency of the dynamic model. This include: a regularised weight function that approximately possess interpolating properties, novel constitutive model, advanced failure criteria, and a contact algorithm based on central differencing.

Referring back to Section 2.6, the features of the dynamic model are summarised in

Table 5.1: Features of the proposed dynamic model

Features of machining model	*The proposed model*
Numerical method	Meshfree: EFG
Type of mesh	Lagrangian
Number of Dimensions	2
Dynamic effects	Yes
Constitutive model	Single phase: Orthotropic nonlinear-elastic up to failure
Failure model	Three failure criteria with selective stiffness degradation
Tool-workpiece contact	Frictional contact using central differencing
Main outputs	Cutting forces and Chip formation

Table 5.1. Inclusion of the dynamic effects makes the model suitable to simulate cutting at higher speeds. Inertial terms are integrated using explicit time integration of the central difference method. The discrete equations are developed using the Updated Lagrangrian formulation of nonlinear solid mechanics. A novel constitutive model is developed based on *Saint Venant-Kirchhoff* formulation of nonlienar elasticity and adapted for orthotropic materials. This model utilises finite-deformation stress and strain measures instead of the small deformation ones. Three different failure theories are coded into the dynamic model; namely, max stress, Hashin and LaRC02. This allows for comparison between the different failures within the context of the machining model (beyond just comparison of failure envelopes). Frictional contact forces are calculated using an algorithm that utilises the central differencing combined with collocation integration at the contact boundary. The formulation is similar to the penalty method with one major difference, that is, the proposed method does not require setting of the penalty parameter as it is calculated from the mass of the contacting node and the timestep. Simulation results are focused on two fundamental outputs; namely, cutting forces and chip formation. The cutting forces are validated against experimental evidence given in Section 6.5.3 for fibre orientations in the range $0 < \theta^o < 90$.

The chapter is organised as follows: The discrete equations are developed from the virtual work principle following updated Lagrangian formulation. Constitutive and failure models are then presented followed by numerical implementation aspects. The cutting forces calculated using different failure criteria are compared against experiments. Chip formation mechanisms using different failure criteria are compared and finally, some numerical investigations are presented and discussed.

5.2 Governing Equations

Consider the solid body shown in Figure 5.1. At time $t = 0$ the body is occupying a reference configuration Ω_0 and is bounded by Γ_0. The body is then subjected to forces, which

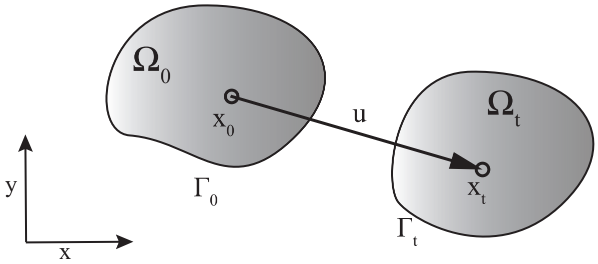

Figure 5.1: Initial and current configuration of solid

create a displacement $\mathbf{u}$. At time t, the current configuration is Ω_t and the boundaries are Γ_t. In order to determine the state of the body at time t, we apply the strong form given in Equation 3.2 along with boundary and initial conditions. The corresponding weak form at time t is given as

$$\int_{\Omega_t} \delta\varepsilon^T \sigma \, \mathrm{d}\Omega - \int_{\Omega_t} \delta\mathbf{u}^T \mathbf{b} \, \mathrm{d}\Omega - \int_{\Gamma_t} \delta\mathbf{u}^T \bar{t} \, \mathrm{d}\Gamma - \int_{\Omega_t} \rho \, \delta\mathbf{u}^T \, \ddot{\mathbf{u}} \, \mathrm{d}\Omega = 0 \tag{5.1}$$

Equation 5.1 cannot be evaluated as it refers to the current (unknown) configuration of the body Ω_t. Integration domain can be changed from Ω_t to a known configuration using appropriate stress and strain measures [126]. To achieve this, two main approaches are used, namely, total Lagrangian formulation or updated Lagrangian formulation. In the former, the integration domain is changed to Ω_0, while in the latter, the integration domain is changed to the last known configuration Ω_{t-1}.

In the proposed model, the Updated Lagrangian formulation is adopted. This is due to the presence of contact forces, which should be calculated with reference to the deformed configuration rather than the un-deformed [121]. As mentioned before, appropriate stress and strain measures should be used to refer back to a known configuration. Here, Second Piola-Kirchhoff stress ($\mathbf{S}$) and Green-Lagrange strain ($\mathbf{E}$) are utilised. These measures are suitable for describing geometrical non-linearity and are widely used in nonlinear solid mechanics problems that involve large deformations. Second Piola-Kirchhoff stress is related to Cauchy (nominal) stress by

$$\mathbf{S} = \det(\mathbf{H})\mathbf{H}^{-1} \cdot \sigma \cdot \mathbf{H}^{-\mathrm{T}} \tag{5.2}$$

where, $\mathbf{H}$ is the deformation gradient. The Green-Lagrange strain vectors is defined as follows

$$\mathbf{E} = \frac{1}{2}(\mathbf{H}^T \cdot \mathbf{H} - \mathbf{I}) \tag{5.3}$$

where, **I** is the identity matrix. Now we can rewrite Equation 5.1 as follows

$$\underbrace{\int_{\Omega_\mathrm{r}} \delta\mathbf{E}^T\,\mathbf{S}\,\mathrm{d}\Omega}_{\delta\mathrm{W}^{\mathrm{int}}} - \underbrace{\int_{\Omega_\mathrm{r}} \delta\mathbf{u}^T\mathbf{b}\,\mathrm{d}\Omega - \int_{\Gamma_\mathrm{r}} \delta\mathbf{u}^T\bar{t}\,\mathrm{d}\Gamma}_{\delta\mathrm{W}^{\mathrm{ext}}} + \underbrace{\int_{\Omega_\mathrm{r}} \rho\,\delta\mathbf{u}^T\ddot{\mathbf{u}}\,\mathrm{d}\Omega}_{\delta\mathrm{W}^{\mathrm{kin}}} = 0 \tag{5.4}$$

where, $\Omega_r \equiv \Omega_0$ for total Lagrangian formulation and $\Omega_r \equiv \Omega_{t-1}$ for updated Lagrangian formulation. Equation 5.4 can be viewed as the principle of virtual work and each of the terms can be given a physical interpretation as follows: δW^{int} is the virtual internal work, δW^{ext} is the virtual external work and δW^{kin} is the virtual kinetic work. In case of linear analysis[1], Equation 5.4 becomes equivalent to the Galerkin weak form presented in Equation 3.7.

5.3 MLS approximation

Discretisation of the virtual work terms is carried out using MLS procedure proposed in Section 3.3. In constructing the shape functions, a regularised weight function proposed by Most et al. [135] is used instead of the ones given in Section 3.3.1. It approximately possesses the Kronecker-delta property, which is then inherited by the shape function. This makes imposing of displacement boundary conditions possible without the need for using constraints methods such as penalty or Lagrange multiplier. The regularised weight

---

[1] In linear analysis $\Omega_0 \approx \Omega_t$, therefore the current configuration can assumed to be known

function is given as

$$w_R(r_I) = \frac{\tilde{w}_R(r_I)}{\sum_{j=1}^{m} \tilde{w}_R(r_I)} \tag{5.5}$$

$$\tilde{w}_R(r) = \frac{\left(\left(\frac{r}{D_m}\right)^2 + \iota\right)^{-2} - (1+\iota)^{-2}}{\iota^{-2} - (1+\iota)^{-2}}; \quad \iota \ll 1 \tag{5.6}$$

The derivative of the weight function is

$$\frac{\partial w}{\partial r} = -\frac{4r_I \left(\left(\frac{r_I}{D_m}\right)^2 + \iota\right)^{-3}}{D_m^2 \iota^{-2} - (1+\iota)^{-2}} \tag{5.7}$$

5.4 Discretisation of the Virtual Work Terms

Spatial discretisation of the virtual work terms is similar to that presented in Section 3.6. The discrete displacement and strain are substituted into each term of the virtual work. The discrete strain matrix $\mathbf{B}_I$ for 2D finite deformation is:

$$\mathbf{B}_I = \begin{bmatrix} H_{11}\frac{\partial \phi_1}{\partial x} & H_{21}\frac{\partial \phi_1}{\partial x} & \dots \\ H_{12}\frac{\partial \phi_1}{\partial y} & H_{22}\frac{\partial \phi_1}{\partial y} & \dots \\ H_{11}\frac{\partial \phi_1}{\partial y} + H_{12}\frac{\partial \phi_1}{\partial x} & H_{21}\frac{\partial \phi_1}{\partial y} + H_{22}\frac{\partial \phi_1}{\partial x} & \dots \end{bmatrix} \tag{5.8}$$

In case of small displacement, $\mathbf{H} \approx \mathbf{I}$ and $\mathbf{B}_I$ becomes equivalent to the strain matrix for small displacements shown in Equation 3.43.

The semi discrete system equation is given as

$$\delta \mathbf{U}^T \left(\mathbf{M}\ddot{\mathbf{U}} - \mathbf{F}^{ext} + \mathbf{F}^{int}\right) = 0 \tag{5.9}$$

Since $\delta \mathbf{U}$ is arbitrary, it follows that

$$\mathbf{M}\ddot{\mathbf{U}} = \mathbf{F}^{ext} - \mathbf{F}^{int} \tag{5.10}$$

where,

$$\mathbf{M} = \sum_{I}^{N} \sum_{J}^{N} \int_{\Omega} \mathbf{\Phi}_I^T \rho \mathbf{\Phi}_J \mathrm{d}\Omega \tag{5.11a}$$

$$\mathbf{F}^{ext} = \sum_{I}^{N} \left(\int_{\Omega} \mathbf{\Phi}_I^T \, \mathbf{b} \, \mathrm{d}\Omega + \int_{\Gamma} \mathbf{\Phi}_I^T \, \bar{\mathbf{t}} \, \mathrm{d}\Gamma \right) \tag{5.11b}$$

$$\mathbf{F}^{int} = \sum_{I}^{N} \int_{\Omega} \mathbf{B}_I^T \mathbf{S}_I \, \mathrm{d}\Omega \tag{5.11c}$$

By comparing Equations 5.4 with Equation 3.68, the simplification of the former equation is evident by the absence of the displacement penalty terms. This is made possible by utilising the regularised weight function, making the shape function almost-interpolating.

Time discretisation is performed using the central difference method as per Equations 3.70 and 3.71. Mass matrix is lumped using row-sum lumping technique and variable time step is used to improve the robustness of the algorithm. Calculation of the critical time step is shown in Section 5.7.1.

5.5 Contact/Impact Formulation for Explicit Algorithms

In this section, contact/impact formulation suitable for explicit algorithms is developed. The starting point of the formulation is similar to that in Section 4.2.1 by utilising the master-slave approach and interpenetration condition. However, penalty method is not used in calculating the contact contributions. Alternatively, the central difference method is used to add the contact contributions to the virtual work principle.

Starting with the definition of the gap function for finite deformation of two discrete bodies

$$g_i = (\mathbf{x}^S - \mathbf{x}^M) \cdot \mathbf{i} \, ; \qquad \mathbf{i} = [\mathbf{n}, \ \mathbf{t}] \tag{5.12}$$

The nodal contact forces are calculated as follows [136,137] The normal force acting on the slave nodes due to penetration of a master segment (frictionless contact) is given as

$$f_{n,j}^{con} = \frac{2M_{(j)}^{s} g_{n,j}}{(\Delta t)^2} \cdot \mathbf{n} \tag{5.13}$$

where, $M_{(j)}^{s}$ is mass of the penetrating slave node and Δt is the time step. By utilising Coulomb friction law, tangential contact force can be calculated in terms of relative contact velocity v_r or in terms of the tangential gap. For stick conditions

$$f_{t,j}^{con} = \frac{M_{(j)}^{s} v_{r(j)}}{\Delta t} \cdot \mathbf{t} = \frac{M_{(j)}^{s} g_{t,j}}{(\Delta t)^2} \tag{5.14}$$

For slip condition

$$f_{t,j}^{con} = \mu f_{n,j}^{con} \tag{5.15}$$

Thus the contact force acting on each slave node j can be summed for stick and slip conditions respectively

$$\mathbf{f}_{j}^{con} = \frac{M_{(j)}^{s}}{(\Delta t)^2} \left(2g_j \cdot \mathbf{n} + g_j \cdot \mathbf{t}\right) \tag{5.16a}$$

$$= \frac{2M_{(j)}^{s}}{(\Delta t)^2}\, g_j \cdot \mathbf{n} \,(1 + \mu) \tag{5.16b}$$

The contact nodal forces calculated in Equations 5.16 should be added to the virtual work in order to obtain the final spatially discretised form of the virtual work equation.

$$\delta W^{con} = \int_{\Gamma_c} \mathbf{f}\; \delta \mathbf{u}^T \mathrm{d}\Gamma = \int_{\Gamma_c} \sum_{j}^{m} f_j \delta \mathbf{u}^T \mathrm{d}\Gamma = \sum_{j}^{m} f_j \sum_{I}^{P} (\mathbf{\Phi}_I \delta \mathbf{u}_I)^T \tag{5.17a}$$

$$= \sum_{I}^{P} \left(\mathbf{\Phi}_I^T \sum_{j}^{m} f_j \right) \delta \mathbf{u}_I^T = \sum_{I}^{P} \bar{f}_j\; \delta \mathbf{u}_I^T = \mathbf{F}^{con}\; \delta \mathbf{U}^T \tag{5.17b}$$

where, m is the total number of contacting nodes and P is the total number of field nodes in the neighbourhood of the contacting nodes that are within the DoI of the contacting nodes. The last term can be added to Equation 5.9 and the contact contribution is then added to global system Equation 5.10.

Practically, distributing the local contact forces into the global contact force vector using the shape function is not required in this case. This is a consequence of the almost-interpolating property of the shape function combined with the force calculations at the nodes (not at quadrature points). However, it is kept to maintain the generality of the algorithm and in the case of using weight functions that do not have interpolating properties.

It is worth noting that the above nodal force calculations given in Equations 5.16, are equivalent to penalty method with variable penalty parameter. The "penalty parameter"is calculated from mass of the node and timestep of the algorithm. This has an advantage from numerical implementation point-of-view, as the same contact algorithm can be used with implicit and explicit solvers and only the "penalty parameter"value would change. In implicit algorithms, mass and time steps are usually not calculated, a constant penalty parameter can be used. Choosing penalty parameter usually requires numerical experiments [42]. However, in the case of explicit algorithm such as the proposed model, choosing the penalty parameter is avoided without adding extra unknowns to the system (e.g. as in Lagrange multiplier).

5.6 Material Modelling

The material behaviour before failure is modelled using *Saint Venant-Kirchhoff* model [121], which is an extension of linear elastic behaviour while taking into account the non-linear components of stress and strain (using Green-Lagrange strain and PK2 stress). The material model is written as follows

$$S_{ij} = D_{k-ijml} E_{ml} \text{ or } \mathbf{S} = \mathbf{D_k}\, \mathbf{E} \tag{5.18}$$

This material model can describe fully anisotropic material [121], so it is capable of dealing with orthotropic materials. Standard rotation matrices apply when calculating local stresses from global ones.

Regarding failure modelling, primary failure is modelled using the same criteria presented in Equation 4.10. For progressive failure, three different failure theories were coded into the model. These are, maximum stress, Hashin and LaRC02. The details of these theories/criteria are provided in Section 3.8.1. It is worth noting that maximum stress and Hashin have been used before in machining simulations while LaRC02 has not been used before and it has the potential to capture some behaviour of composites failure, which the other two cannot. Progression of failure is modelled using stiffness degradation similarly to Section 4.2.3 and using the same degradation values presented in Table 4.3.

5.7 Numerical Implementation

This section describes some aspects of the code implementation including model parameters and settings, critical time step calculations and the general algorithm.

5.7.1 Critical Time Step

The central difference method is only conditionally stable [121, 126, 127]. This means that a robust algorithm should have an automatic time step calculation. The critical time step is related to the stress wave propagation speed. This is a function of the material density and mechanical properties as well as the distance between discretisation nodes. Unlike isotropic material, a composite laminate has several phase velocities. The maximum velocity is used in critical time step calculations [120]

$$c_{max} = \sqrt{D_{11}/\rho}\,; \quad \text{where } D_{11} = \frac{E_{11}}{1-\nu_{12}\,\nu_{21}} \tag{5.19}$$

$$\Delta t_{cr} < \frac{\min(d)}{c_{max}} \tag{5.20}$$

where, d is the distance between nodes. In the code, the time step is calcualted from the critical time step as follows

$$\Delta t = \kappa \Delta t_{cr}; \qquad \kappa \in [0.95\ 0.99] \tag{5.21}$$

This acts as a safety factor to ensure that rounding off errors does not bring the calculation beyond the stability region.

5.7.2 Material Parameters

Material inputs required for the model are shown in Table 5.2. These are the same of the UD-GFRP samples used in the experiments shown in Section 6.5. As such, model validation becomes possible.

Table 5.2: Mechanical properties for UD-GFRP samples

E_1 GPa	E_2 GPa	ν_{12} -	G_{12} GPa	X^t MPa	X^c MPa	Y^t MPa	Y^c MPa	S^l MPa
34.28	11.57	0.24244	2.05	697.8	443.76	89.72	148.33	33.1

Inputs for the primary failure criteria are estimated based on the Merchant model and the experimental data of Section 6.5.3. Using principle force components, shear and normal stress components acting on the shear plane can be calculated as per the following well-known relations

$$F_s = F_c cos(\varphi) - F_t sin(\varphi) \tag{5.22}$$

$$F_{ns} = F_c sin(\varphi) + F_t cos(\varphi) \tag{5.23}$$

where, φ is the shear plane angle, which is given as follows

$$\varphi = \tan^{-1} \frac{r_c \cos\gamma}{1 - r_c \sin\gamma} \tag{5.24}$$

where,γ is the rake angle of the cutting tool and r_c is the cutting ratio, i.e. the ratio of the chip thickness to the depth of cut. Since composites display brittle behaviour, it is reasonable to assume that $r_c \approx 1$ [138]. Using the above equations and knowing the area of the shear plane, we obtain the normal and shear strength values used to evaluate failure in the cutting zone as shown in Table 5.3.

Table 5.3: Interfacial Normal and shear strength values for E-glass FRP

θ^o	*0*	*15*	*30*	*45*	*60*	*75*	*90*
S_σ (N/mm^2)	146.3	103.5	102.9	119.2	143	158.9	183.5
S_τ (N/mm^2)	49.3	26.8	35.2	50.2	71	85.1	113

Generating failure envelopes for the workpiece material helps in better understanding the chip formation and their relation to the different loading modes. Figures 5.2a and 5.2b show the $\sigma_{11} - \sigma_{22}$ and $\sigma_{22} - \tau_{12}$ envelopes respectively for the three failure criteria used in this chapter. The normal stresses envelope for Max stress and Hashin is identical since $\tau_{12} = 0$.

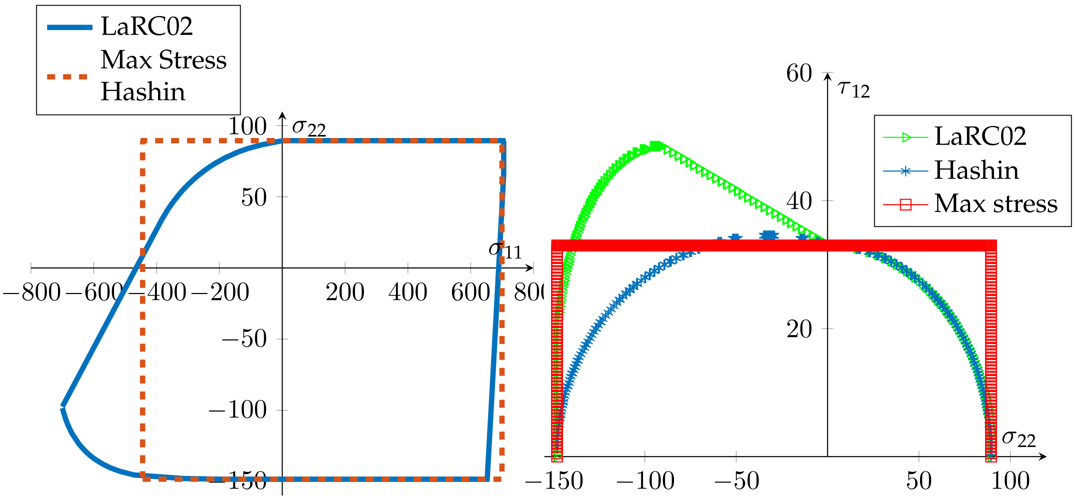

(a) $\sigma_{11} - \sigma_{22}$ at $\tau_{12} = 0$

(b) $\sigma_{22} - \tau_{12}$ at $\sigma_{11} = 0$

Figure 5.2: Failure Envelopes for the GFRP samples used in Experiments

5.7.3 Model Setup and Settings

Model setup is shown in Figure 4.3. Cutting tool is modelled with 50 μm nose radius consistent with the cutting tools used in validation experiments. Friction coefficient is made function of fibre orientation as proposed by Mkaddem et al. [139]. However, the effect of friction coefficient was found to be minimal due to the termination of the simulation at the completion of the first chip. Cutting conditions are set as follows (consistent with experiments): speed $V_c = 3800\ mm/min$, rake angle $\gamma = 0^o$, depth of cut $a_c = 0.25\ mm$. The only process variable is fibre orientation with 5 levels, $\theta^o = [15,\ 30,\ 45,\ 60,\ 75]$. Meshfree model set up is similar to that presented in Section 4.3.2 in terms of numerical integration, DoI construction and nodal distribution. Visibility criteria is used to modify the shape functions near the cutting edge. The analysis is terminated at the completion of the first chip, which is determined according to Section 5.8.4.

5.7.4 Main Algorithm

The MATLAB implementation followed Algorithm 5.1. Time integration procedure is similar to that proposed in Section 3.6.2 with addition of critical timestep calculations as per Section 5.7.1. Mass matrix is calculated only once at the beginning of the simulation given that the discretisation is Lagrangian. Updating the shape function is carried out at every $i \geq 1$ timestep. Strictly speaking, in Updated Lagrangian $i = 1$, however, given the very small timestep, this could be increased without compromising accuracy. Numerical experiments were carried out and found that using $i = 10$ does not affect accuracy but greatly improves runtime.

Algorithm 5.1: Dynamic EFG orthogonal cutting model

```
• Inputs
• Generate geometry, nodes and gauss points.
• Calculate and store shape function and derivatives.
• Calculate lumped mass matrix.
• Initialise global variables.
• Calculate critical time step.
• For every time step
    – First velocity update at half time step.
    – Update displacement for workpiece and cutting tool.
    – Update integration points and shape functions.
    – Calculate contact force.
    – Calculate trial stress in global and local coordinates.
    – Calculate primary failure criteria.
    – If primary failure = true, update damage variables.
    – Calculate internal nodal forces.
    – Calculate acceleration.
    – Second velocity update at time step.
    – Calculate critical time step and check chip formation completion.
    – Write interim outputs.
• Return
```

5.8 Results and Discussion

5.8.1 Effect of Failure Criteria on Cutting Forces

Figure 5.3 shows the comparison of the normalised mean cutting force between the EFG model with different failure criteria and the experiments for the range $15^o \leq \theta \leq 75^o$. The experimental values had a minimum of 32.6 ± 1.6 N/mm at $\theta = 15^o$ and maximum of 61 ± 1.5 N/mm at $\theta = 75^o$. Forces using Maximum stress failure ranged from minimum of 27.5 N/mm at $\theta = 30^o$ to maximum of 56.8 N/mm at $\theta = 75^o$. Force using Hashin failure ranged from minimum of 36.3 N/mm at $\theta = 30^o$ to maximum of 50.1 N/mm at $\theta = 75^o$. Force using LaRC02 failure ranged from minimum of 30.3 N/mm at $\theta = 30^o$ to maximum of $58.5\ N/mm$ at $\theta = 75^o$. Maximum deviation from experimental force range was $3.2\ N/mm$ using LaRC02 at $\theta = 15^o$, while for Hashin it was $9.6\ N/mm$ at $\theta = 75^o$ and for Maximum stress, it was $5.1\ N/mm$ at $\theta = 30^o$. This indicates that LaRC02 generated results closest to experimental data within the studied range.

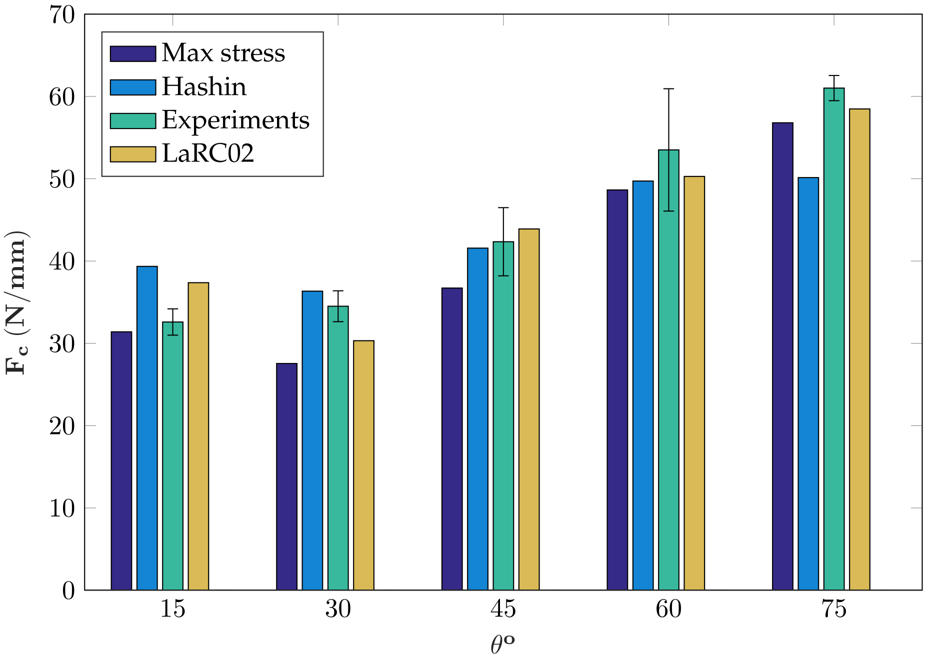

Figure 5.3: Cutting force comparison between model and experiments with different failure criteria

Figure 5.4 shows thrust force comparison. It is clear that the model significantly underestimated the thrust force throughout the studied range. The force values tended to increase with increased orientation angle. This might be due to the combined effect of increasing friction coefficient and cutting force magnitude at higher orientations. The experimental values showed little variation in the thrust force across the studied range (when taking the error bounds into account). The experimental values ranged between 17 to 19.2 N/mm. Force calculated with maximum stress ranged between 0.9 to $5.6\ N/mm$. Force calculated using Hashin were between 1.6 to $4.1\ N/mm$ and using LaRC02 ranged between 2.1 to $5.5\ N/mm$. This significant under-estimation of the thrust force is seen throughout modelling of machining composite literature, across different numerical methods e.g. [99,101,108,112].

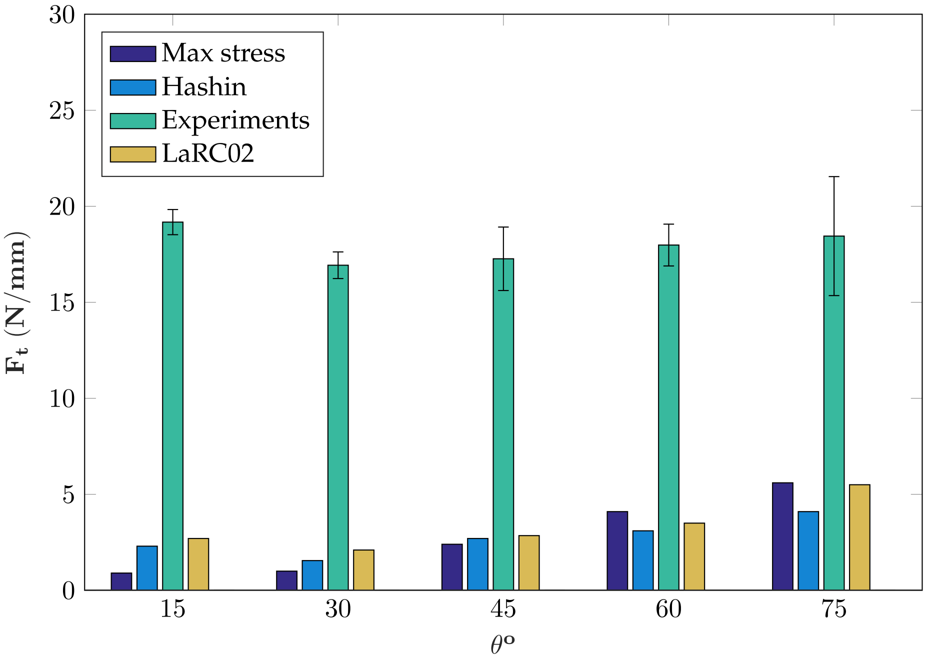

Figure 5.4: Thrust force comparison between model and experiments with different failure criteria

This indicates that it is not related to the choice of meshfree methods, rather it is more related to the difficulties in accurately modelling the composites behaviour under machining conditions. In the current study, two reasons may have contributed to the low thrust force values. Firstly, starting the machining process within the workpiece rather than the free edge. This set up was chosen for numerical stability reasons. Secondly, terminating the simulation after the completion of the first chip. This reduced the bouncing back effect (bouncing back of the machined surface and exerting vertical reaction force on the clearance face of the cutting tool), which was identified as important contributor to the thrust force magnitude in composites machining [99, 112, 138]. Clearly this is an area where significant improvement is required by implementing better constitutive models and material separation criteria.

5.8.2 Mechanisms of Chip formation

The study of chip formation is essential in shedding light on the mechanisms of cutting. Machining models provide a valuable tool in analysing the chip formation process that is difficult to conduct experimentally such as obtaining the failure stresses and failure modes. Figures 5.5 - 5.7 and Figures 5.6 - 5.8 show the progression of the fibre and matrix failure at $\theta = 30^o$ and 75^o respectively. The figures show beginning of cutting (left figures), halfway (middle figures) and near the end of the chip formation (right figures). Top row shows simulations using maximum stress, the middle row using Hashin and bottom using LaRC02. It is worth noting that the chip formation was complete at slightly different intervals among the different failure criteria but time was normalised for each individual case for ease of comparison.

Fibre failure at $\theta = 30^o$ is shown in Figure 5.5. It is noted that the maximum stress did not predict any significant fibre damage. This is due to the uncoupling of the shear effects, which plays an important role in reducing the failure stress of the material. Hashin failure predicts moderate fibre failure along a narrow band of the chip boundaries. This due to the effect of shear stress on the failure stress as the location of fibre failure coincides with high shear stresses. This means that the completion of chip formation in Hashin is due to fibre failure since matrix failure has already been completed (refer to Figure 5.6f). As for LaRC02, a substantial fibre damage is predicted in the chip. This is mainly due to the different way of calculating fibre failure under compression. LaRC02 predicts fibre fails under compression due to formation of kink bands resulting from shear deformation. The kink generates misalignment in the fibres and leads to damage in the fibre and the nearby supporting matrix. This is expected to be dominant failure at lower fibre orientations and 0^o rake angle as the rake face directly engages with the workpiece causing severe compressive load on the fibres. Naturally, this loading will propagate along the fibre direction and will cause the observed severe damage.

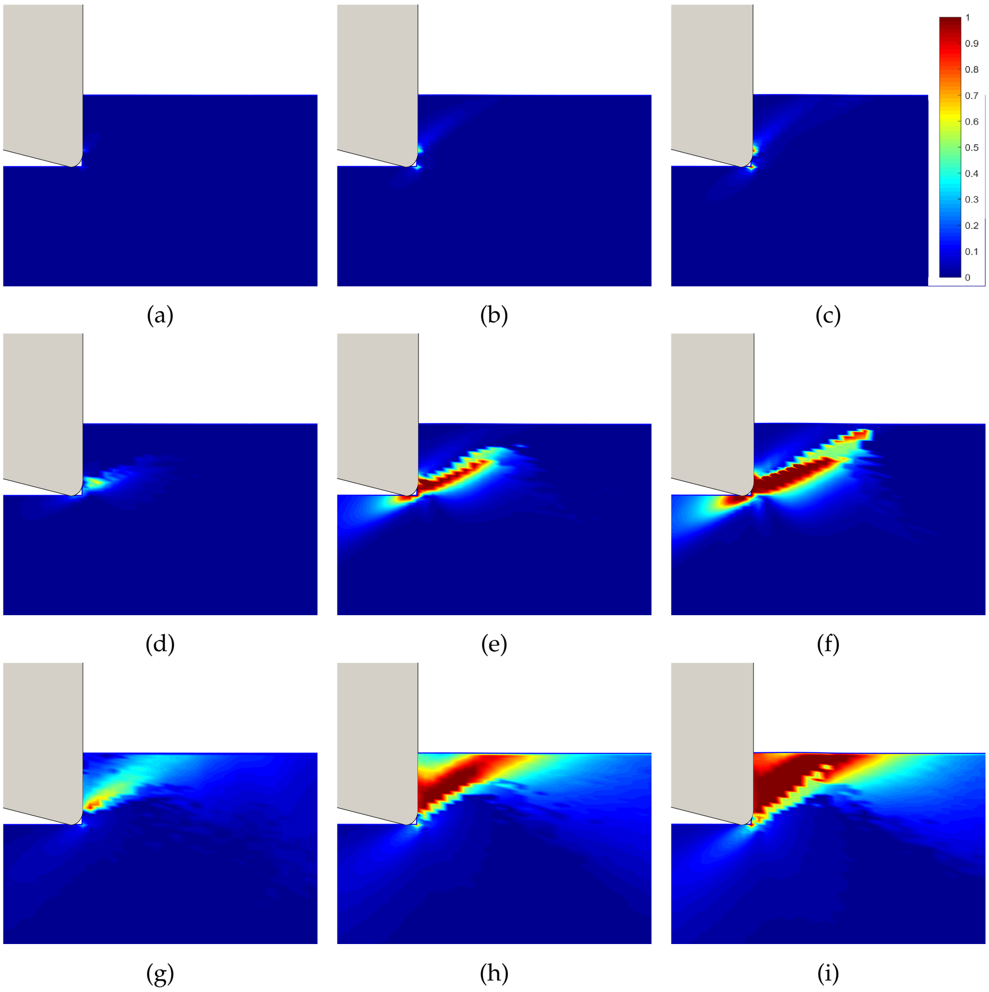

(a) (b) (c)

(d) (e) (f)

(g) (h) (i)

Figure 5.5: Fibre damage progression at $\theta = 30^o$ using maximum stress (a, b, c), Hashin (d, e, f) and LaRC02 (g, h, i)

Figure 5.6 shows the progression of matrix failure at $\theta = 30^o$. The matrix failure starts early near the end of the tool nose and quickly propagates along the fibre directions towards the free surface. A wide band of failure emanating from the rake face towards the free surface is observed due to the high compressive stresses exerted by the 0^o rake tool. The completion of the chip formation is characterised by almost complete damage in the chipped area. Furthermore, the damage is extended in the machined surface along the fibre direction to a small depth. This is consistent with experimental evidence that cutting at small angles produces good finished surface of the uni-directional composites [30]. The chip formation is qualitatively similar for all the failure criteria. However, LaRC02 predicted less matrix damage in the chip. This is due to the increased shear strength at high compressive load in the matrix direction. (Compare the failure envelopes at the second quadrant in Figure 5.2b).

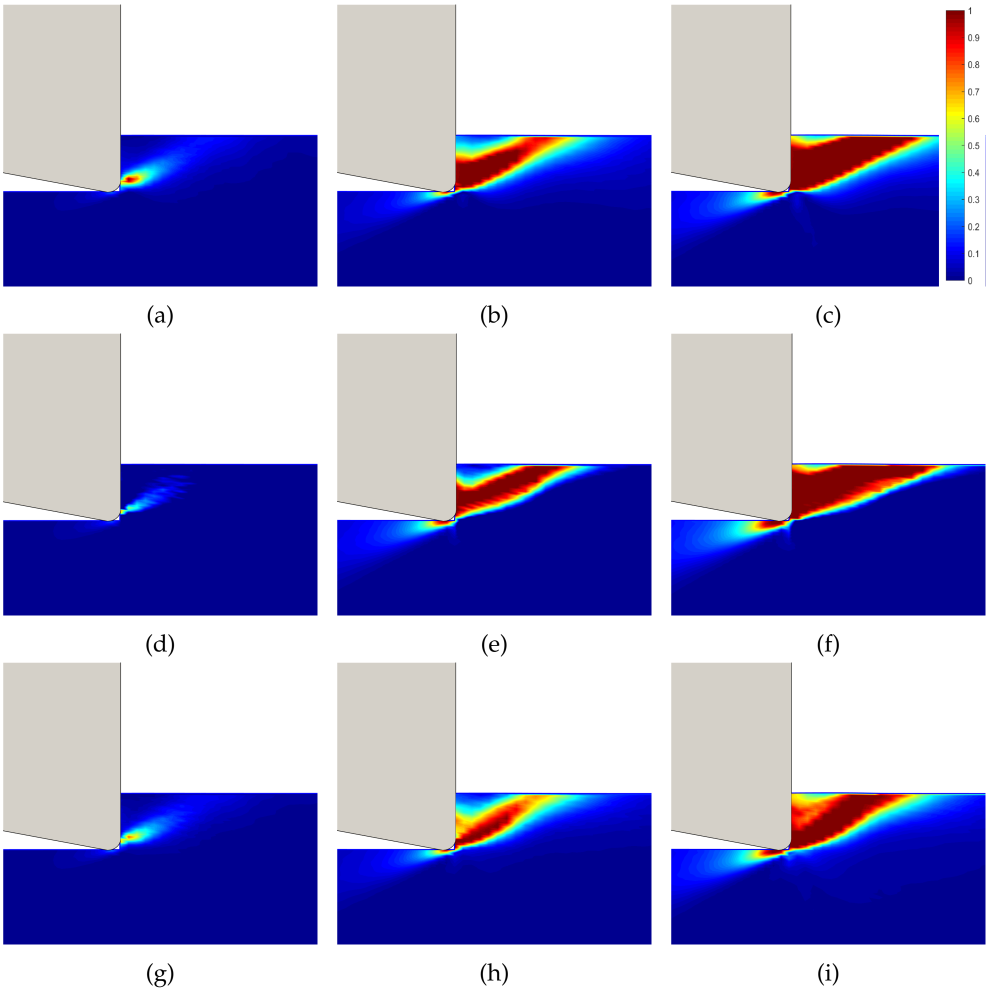

(a) (b) (c)

(d) (e) (f)

(g) (h) (i)

Figure 5.6: Matrix Damage at $\theta = 30^o$ for different failure criteria

Figure 5.7 shows the fibre failure at $\theta = 75^o$. Similarly to Figure 5.5, maximum stress failure criteria predicted negligible failure at the chip root. Hashin and LaRC02 predicted limited failure of the fibre perpendicular to the fibre orientation. This is confirmed experimentally in the work of Arola et al. [35].

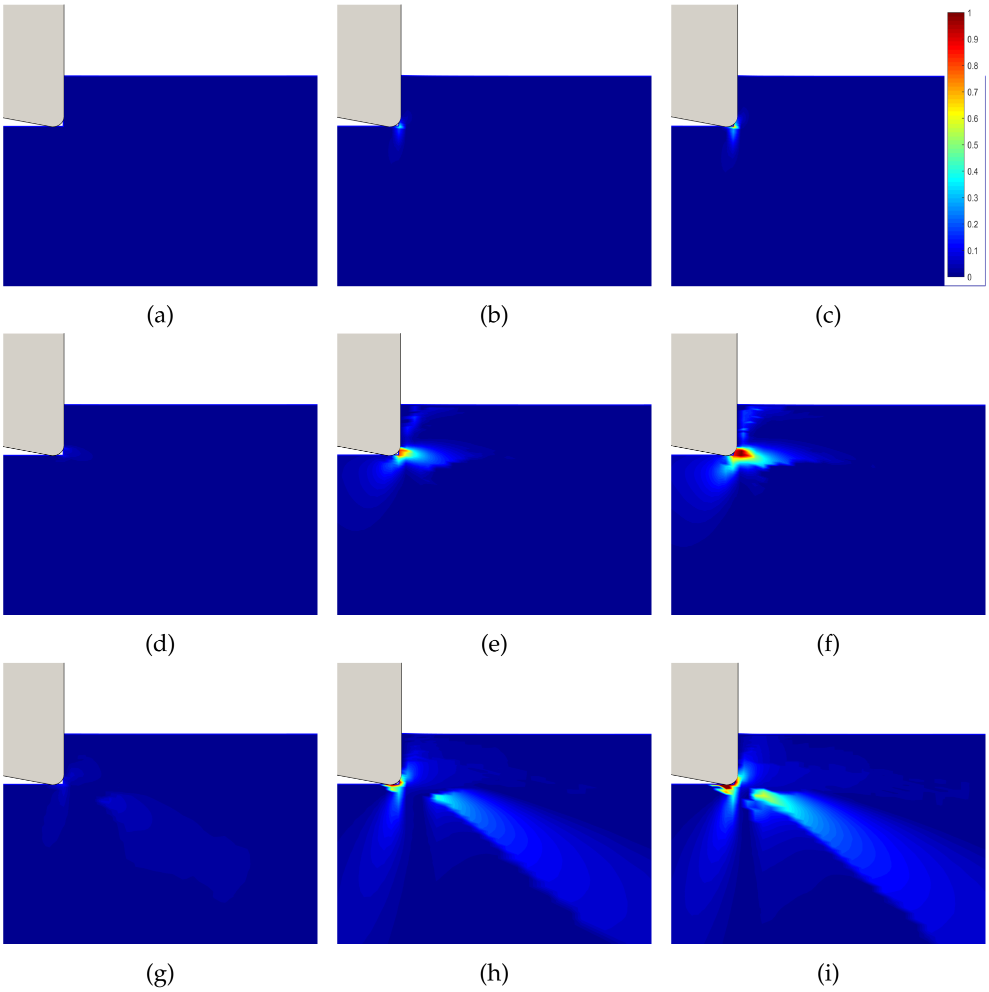

(a) (b) (c)

(d) (e) (f)

(g) (h) (i)

Figure 5.7: Fibre Damage at $\theta = 75^o$ for different failure criteria

The matrix damage is shown in Figure 5.8. The chip is smaller than in the case of $\theta = 30^o$. This is noted experimentally by Nayak et al. [31] and explained by the change in the main failure mechanisms from bending of the fibres to brittle crushing. The damage extends to the entire chip in this case due to the non-positive rake angle. Ahead of the complete chip, a large area of damaged workpiece is observed. Damage to the machined surface is also larger than in the case of $\theta = 30^o$. It is noted that the damaged area is similar using the different failure criteria. This can be explained with the help of Figure 5.2b by noting that at high fibre orientations, the ratio $\frac{-\sigma_{22}}{\tau_{12}}$ increases. This will cause the stress evolution to follow a path closer to the negative σ_{22} axis. At this region the three failure envelopes are close to each other.

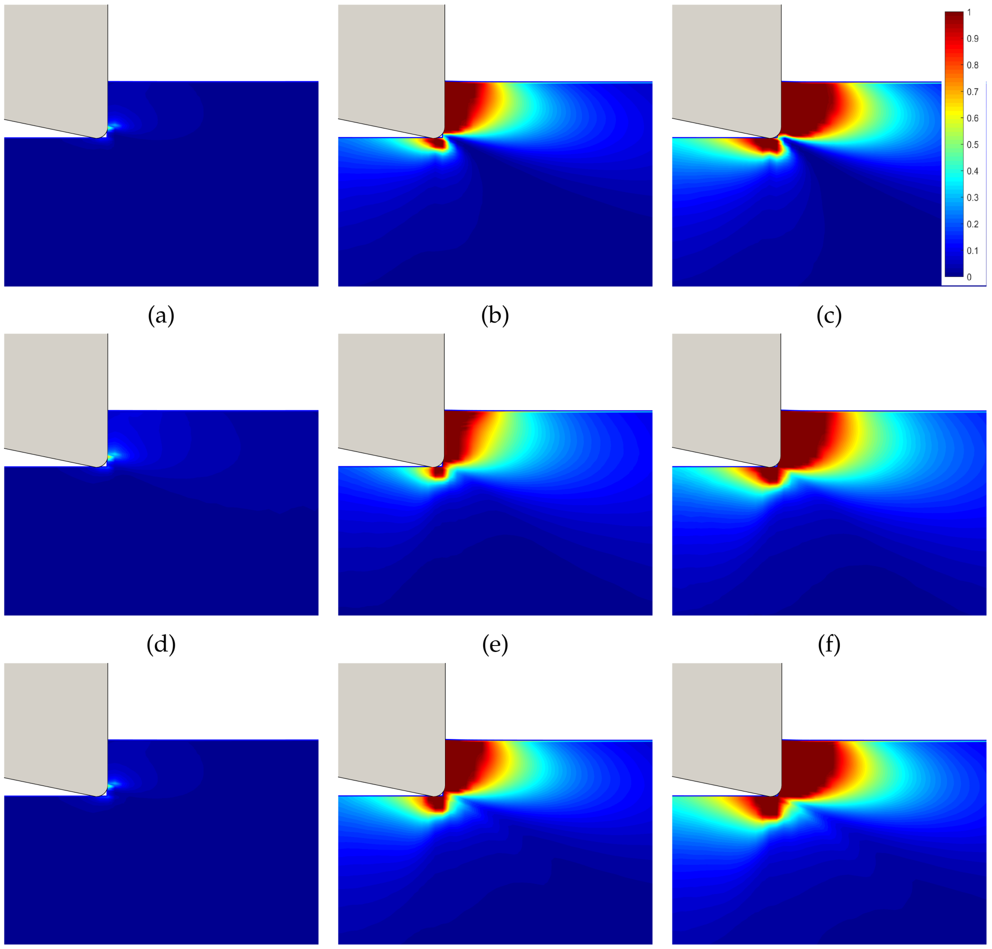

(a) (b) (c)

(d) (e) (f)

(g) (h) (i)

Figure 5.8: Matrix Damage at $\theta = 75^o$ for different failure criteria

5.8.3 Effect of Nodal Density on Cutting Forces

A study of the nodal density effect on the cutting forces is carried out in order to determine the minimum number of nodes that would give a satisfactory results. Figure 5.9 shows the trend of the cutting force convergence against the number of nodes.

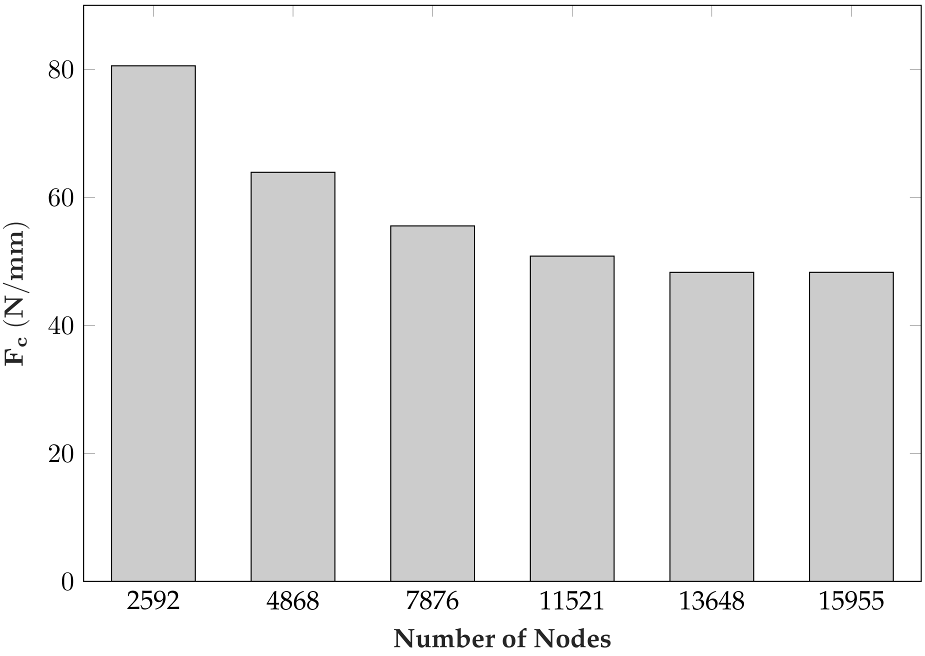

Figure 5.9: Cutting force convergence against the number of nodes

As it is clear from the figure, the convergence approaches the accurate force value from the top since the model is usually stiffer when it contains lesser number of nodes. $N = 13,648$ nodes is chosen for the simulations throughout the study.

5.8.4 Termination Criteria

Completion of the chip formation in orthogonal cutting is usually characterised by material damage propagating from the cutting point (in 2D) to the free surface. Detection of completion of chip formation is somewhat complicated and requires intensive geometrical calculations that add to the computational cost of the code. In this study, a numerical approach utilising the critical time step is devised to predict the completion of the chip without resorting to burdensome geometrical calculations. It was noted that the completion of the chip is detectable from a sudden drop in the critical time step. This is due to the loss of stiffness in the chip as it becomes completely damaged. This in turn will induce sudden large displacement causing the nodes along the chipping plane to get closer and thereby causing significant drop in the time step (refer to Eqn 5.20). This effect is shown in

Figure 5.10, where the timestep remains nearly constant until the chip completion where the force diverges due to high displacements of the contact surface between the tool and workpiece. In the algorithm 5.1, the gradient of the critical time step is calculated at every time step, when the sudden drop is detected, the code terminates.

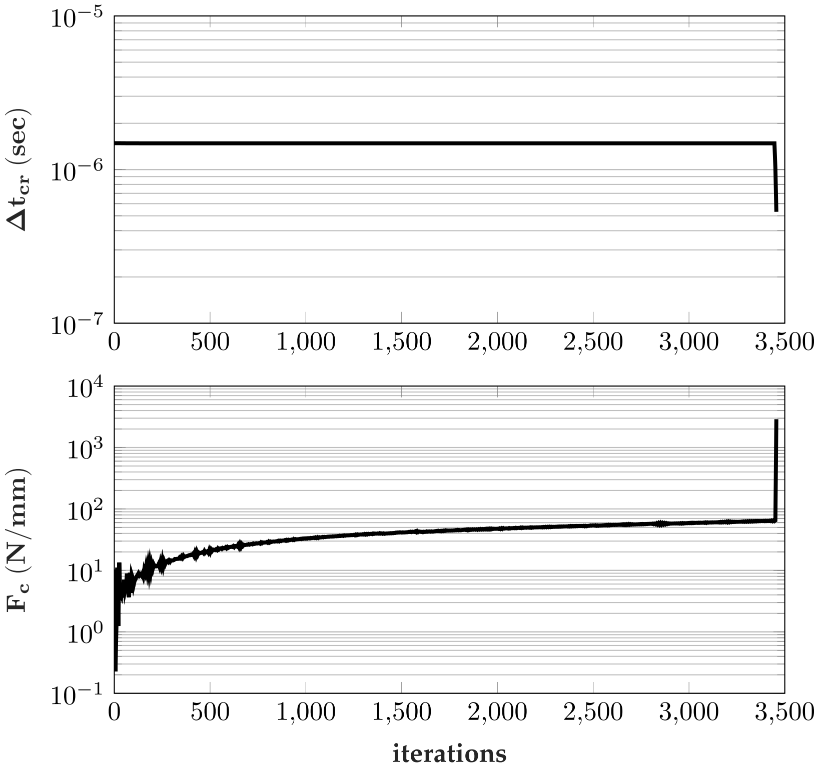

Figure 5.10: Detection of chip formation completion from gradient of critical time step

5.9 Conclusions

This chapter presented a novel explicit Element-Free Galerkin Model to simulate the dynamic orthogonal cutting of unidirectional composites. The discrete system equations were derived from the virtual work principle and non-linear analysis was handled using Updated Lagrangian formulation. An orthotropic Kirchhoff material model combined with option of three different failure criteria were used to model the material behaviour. LaRC02 failure criteria, which has not been used before in composite machining simulations, was found to give a better accuracy in cutting force prediction as well as to capture important fibre failure modes that were not predicted by Hashin or Maximum stress criteria. Frictional contact calculations were handled by a novel algorithm using central differencing at the contact nodes. The proposed method avoided the selection of numerical parameters as in the penalty method while not increasing the unknowns as in Lagrange multiplier. Another advantage is that the same algorithm reduces to penalty formulation that can be used in implicit numerical analysis.

The model results were compared with experimental evidence of orthogonal cutting at 0^o rake angle and fibre orientations $15^o \leq \theta \leq 75^o$. It was found that the cutting force was predicted with good accuracy for all the failure models; however, thrust force was significantly under-estimated by the model. This maybe due to the inability to capture the bouncing back effect and terminating the analysis at the completion of the first chip. Chip formation analysis confirmed that the chip separation occurred along the direction of fibres. This means that the cutting plane coincides with fibre directions in the studied range. The model can be extended to study other operating and material parameters such as rake angles, fibre orientations, cutting speeds. The range of study was limited here by the availability of reliable experimental data for validation.

Comparison between the steady-state machining model of Chapter 4 and the current dynamic model highlights several differences: The dynamic model is capable of modelling high speed machining by taking the inertial effects into account. This extends the applicability of the model to realistic speeds while maintaining accuracy. Furthermore, chip formation is better studied with the dynamic model rather than the steady-state model. The dynamic model is equipped with more advanced material modelling and more efficient meshfree algorithm with direct imposition of boundary conditions. On the other hand, the steady-state model is less computationally intensive. This can be attributed to the very small time step required to maintain the numerical stability of the dynamic model. The advantages of using meshfree methods is clear in both models, such as easy and automatic pre-processing and high quality approximation of field variables.

Chapter 6

Experimental Work: Orthogonal Cutting of Composite Materials

6.1 Introduction

This chapter presents the experimental work conducted as part of this research. The aim of these experiments is threefold: Firstly, to gain a better understanding of the fundamental cutting process and the effect of different material and machining parameters on fundamental outputs of the process. Secondly, to investigate the effect of fibre content on the cutting process, something which has been rarely looked at systematically in literature. Thirdly, to generate necessary cutting and thrust forces values for validating the developed orthogonal cutting model in Chapter 5. Three phases of orthogonal cutting experiments on UD-GFRP were carried out to fulfil each aim of this chapter.

This chapter starts by describing the measurements of the mechanical properties of UD-GFRP samples that will be used in cutting experiments. A description of experimental set-up, results and discussions for each phase is then presented sequentially. Finally, overall conclusions and gained insights are presented.

6.2 Workpiece Material Characterisation

Material characterisation was carried out on the UD-GFRP laminates used in the cutting experiments of Phases I and III. Without the necessary mechanical properties of the workpiece, the validation of the meshfree model would not be possible. To this end, a series of mechanical tests were carried out to determine stiffness and strength properties of the composite laminate. The testing was conducted by Applied Polymer Development Ltd. (APD). Two unidirectional sheets and one cross-ply sheet were supplied by Heathcoates Co. of dimensions $300 \times 300 \times 2\ mm$. Test samples were prepared by APD from these sheets. Where necessary, tabs were bonded on samples using cold cure epoxy adhesive. The specimens were machined using a wet diamond saw to ensure clean cuts. The laminates were tested using the following standards: Tensile Strength and modulus following ISO 527-4. Compression strength and modulus following ISO 14126. In-plane shear following ISO 14129. The mechanical testing was performed using an Instron 5982, 100kN load frame and analysed using Instron Bluehill 3 (v3.33) software. In order to ensure accuracy, 5-7 repetitions of each test were carried out.

In tensile testing, clip-on extensometers were used for strain measurement at 0^o to obtain the modulus and at 90^o to obtain the Poisson Ratio. The compression testing was conducted using the ASTM modified 695 test fixture. Tabbed specimens were used for the strength tests and untabbed specimens were used for the modulus tests. An extensometer was used to obtain the strain at 0^o in the compressive modulus tests. Micro cracking was determined by attaching a transducer onto the specimen and noting the strain at which the micro cracking started. A summary of the mechanical properties is given in Table 6.1. The complete sets of test results are shown in Appendix A.

Table 6.1: Mechanical properties of UD-GFRP samples

Property	*Unit*	*Mean*	*std.*
E_1*(tension)*	GPa	34.28	2.257
X^t	MPa	697.8	36.576
ν_{12}	-	0.24244	0.037
ε_{1-max}	%	2.15	0.164
E_2	GPa	11.57	0.496
Y^t	MPa	89.7216	7.251
ν_{21}	-	0.0932	0.007
ε_{2-max}	%	1.817	0.121
E_1 *(compression)*	GPa	34.91	0.75
E_2 *(compression)*	GPa	12.53	0.91
X^c	MPa	443.76	66.09
Y^c	MPa	148.33	4.13
G_{12}	GPa	2.05	0.207
S^l	MPa	33.1	2.238

6.3 Phase I Experiments

6.3.1 Introduction

As mentioned in Chapter 2, the orthogonal cutting process lends itself well to research in cutting, since it is a 2D process with minimum geometrical complexity. Furthermore, using unidirectional composites as workpiece material has an advantage of isolating the effect of the composites' anisotropy on the cutting process. This is despite the fact that most commercially used composites are multi-directional.

The first phase of experiments is conducted with the aim of improving the author's understanding of the process of cutting UD composites. Therefore, a wide range of process variables and levels are studied with a total of 54 cutting experiments. Cutting speed, rake angle, fibre orientation and depth of cut are selected as process variables. Cutting forces, chip formation and surface integrity are selected as process outputs. Furthermore, advanced statistical treatment of the results is presented. This include main effects and statistical significance calculation.

6.3.2 Experimental Work of Phase I

Orthogonal cutting experiments were performed on Royal 10" shaping machine. Single-point, high speed steel (HSS) cutting tools with dimensions of $6 \times 6 \times 63$ mm were used. The width of the cutting tools was chosen to be larger than the panel thickness in order to better-approximate the orthogonal cutting conditions as shown schematically in Figure 6.1. The tools were ground with 0^o, 5^o and 10^o rake angles and 15^o clearance angle.

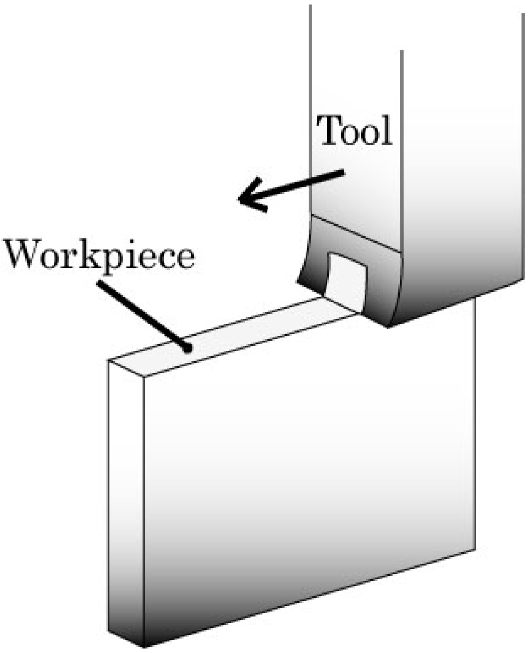

Figure 6.1: Orthogonal Cutting Schematic

Workpiece material was chosen to be unidirectional GFRP panels supplied by Heathcotes Co. Ltd. Fibres were E-glass and matrix was epoxy with $\approx 70\%$ fibre volume. Each panel was made up of 5 lamina of ≈ 0.42 mm thickness each. The workpiece material was cut into $80 \times 80 \times 2.1$ mm. Small fraction (6%) of the fibres were laid in the transverse direction in order to hold the fibre bundles in place and improve the uniformity of fibre distribution. The workpiece was mounted using bespoke jig that was designed for these experiments. The workpiece was held in a vertical position in order to investigate the effect of fibre orientation. The jig is shown in Figure 6.2.

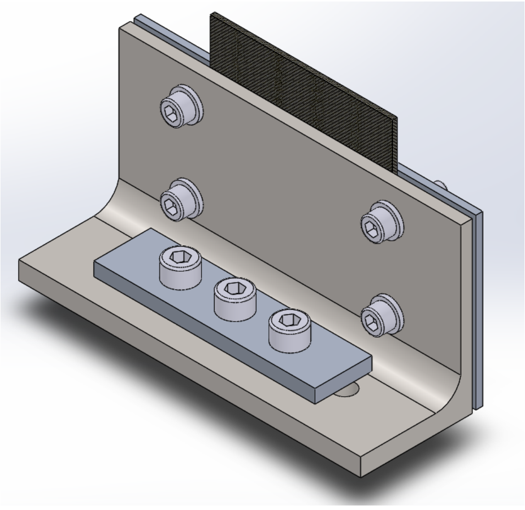

Figure 6.2: Bespoke jig design

The jig was mounted on Kistler 9257B tri-axial dynamometer, which was used to measure cutting forces. The cutting force measurement system comprised of the dynamometer, a channel amplifier, a data acquisition card and a PC. The cutting forces were displayed on the PC using Dynoware software version 2.6.4.15. In-situ chip formation was analysed with the help of Hotshot CC1024 High speed camera connected to PC with Hotshot link software to operate and process the captured videos. The camera was equipped with Sigma Macro $105mm$ $F2.8$ EX-DG lens that has high optical performance up to 1:1 magnification, which enabled detailed view of the action at the cutting edge. Videos were taken at 700 and 1000 frames per second (fps). Four sources of LED lights were used to provide proper illumination. A schematic of the experimental set up is shown in Figure 6.3.

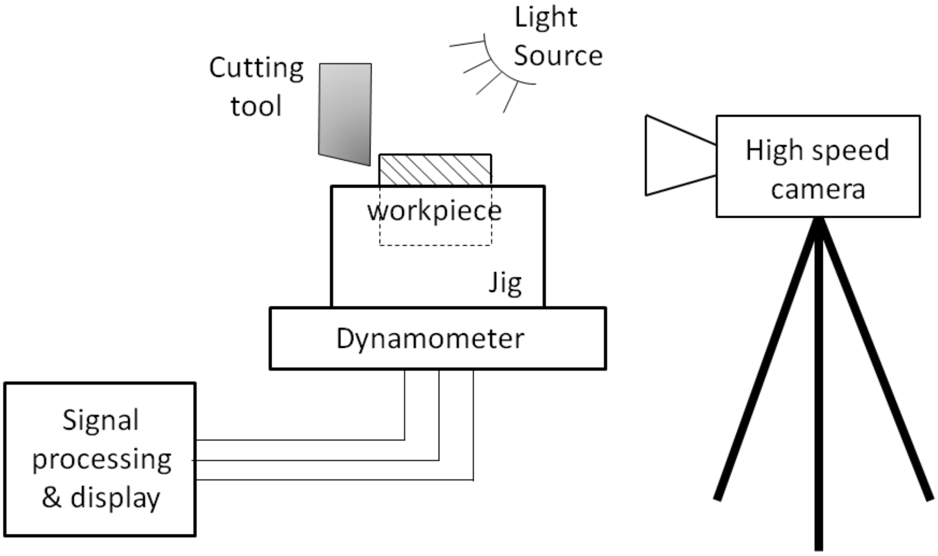

Figure 6.3: Experimental setup for Phase I

3D surface topography assessment was carried out using an Alicona Infinite Focus G4 optical scanner, having a resolution down to 10 nm. The scanning area was 3.9 $mm \times$ 2.1 mm in the X and Y directions respectively. Scanning directions are shown in Figure 6.4. Scans were obtained using 2.4 μm and 7.8 μm vertical (Z direction) and lateral (X and Y) resolutions respectively. Average surface roughness was then measured from the 3D scans in the cutting direction (along the x axis) in accordance in with Figure 6.4.

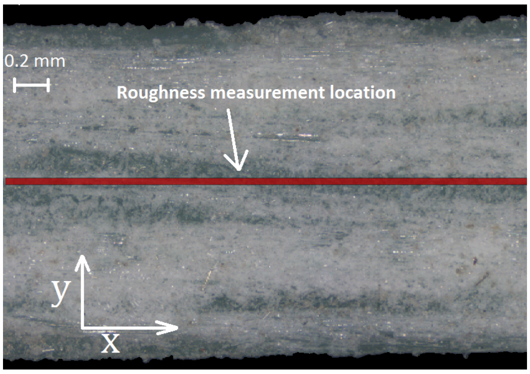

Figure 6.4: Location of surface roughness measurements

All measurements conformed to ISO4287 using 0.8 mm cut-off and 4 mm evaluation length. The roughness measurements were taken at three locations on the machined surface, one at the centre and two at 0.5 mm from the edges and an average was then computed. Chip morphology was also assessed using a stereoscope (Leica EZ4D) in conjunction with Leica LAS EZ software. Data processing was performed on MATLAB R2015-A. The experiments followed full factorial design. The process variables were chosen to be fibre orientation (θ), rake angle (γ), cutting speed (V_c) and depth of cut (a_c). Their levels are shown in Table 6.2. The total number of experiments conducted was 54. The cutting speed levels were dictated by the available speeds on the shaping machine.

Table 6.2: Process control variables and their levels

Control Variables	*Units*	*Levels*		
Speed	m/sec	14	19	-
Fibre Orientation	Deg	0	90	135
Rake Angle	Deg	0	5	10
Depth of Cut	mm	0.5	1	2

6.3.3 Results and Discussion of Phase I

Cutting Forces

Average cutting and thrust forces collected from the dynamometer are shown in Table 6.3. The cutting force ranged between $90\ N$ and $637\ N$ and with an overall average of $381\ N$. The thrust force ranged between $-8\ N$ and $69\ N$ with an overall average of $30\ N$. Figure 6.5 shows sample cutting force measurement for three different fibre orientations. The largest fluctuation in force signal was observed when cutting samples having 90^o fibre orientation. This agrees with the observations by Wang et al. [3] and is likely caused by the tool cutting through layers of fibres and matrix in sequence across the depth of cut. However, in this study the ratio of cutting to thrust force was higher than that presented in [3]. This might be due to the large values of depth of cut used in this study. In Wang et al. [3], maximum depth of cut was $0.381\ mm$ whereas in this study the maximum depth was $2\ mm$.

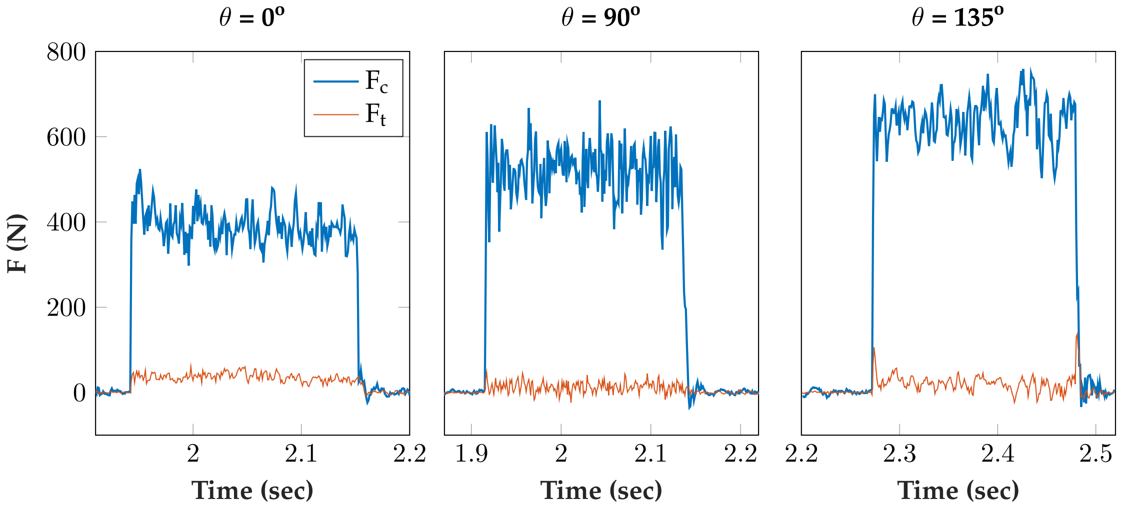

Figure 6.5: Sample cutting and thrust forces with $V_c = 19m/min$, $a_c = 1mm$ and $\gamma = 5^o$

Table 6.3: Mean cutting and thrust forces of Phase I

$Test\ no.$	γ^o	$V_c\ m/min$	θ^o	$a_c\ mm$	$F_c\ N$	$F_t\ N$
1	0	19	0	0.5	140.1	55.5
2	0	19	0	1	278.1	64.9
3	0	19	0	2	305.5	51.2
4	0	19	90	0.5	420.9	36.2
5	0	19	90	1	374.9	32.3
6	0	19	90	2	534.5	35.9
7	0	19	135	0.5	289.4	42.4
8	0	19	135	1	390.2	40.6
9	0	19	135	2	589.7	43.7
10	0	14	0	0.5	93.2	44.2
11	0	14	0	1	268.2	66.6
12	0	14	0	2	442.9	67.4
13	0	14	90	0.5	265.1	36.7
14	0	14	90	1	348.3	37.9
15	0	14	90	2	573.8	40.7
16	0	14	135	0.5	348.5	39.8
17	0	14	135	1	386.5	40.8
18	0	14	135	2	407.9	39.9
19	5	19	0	0.5	89.4	34.7
20	5	19	0	1	318.5	54.3
21	5	19	0	2	390.2	36.2
22	5	19	90	0.5	337.4	21.3
23	5	19	90	1	435.3	19.5
24	5	19	90	2	517.6	12.9
25	5	19	135	0.5	348.5	23.8
26	5	19	135	1	439.9	25.3
27	5	19	135	2	636.9	21.2
28	5	14	0	0.5	147.2	30.2

Table 6.3 – continued

Test no.	γ^o	$V_c\ m/min$	θ^o	$a_c\ mm$	$F_c\ N$	$F_t\ N$
29	5	14	0	1	182.6	35.8
30	5	14	0	2	483.8	49.7
31	5	14	90	0.5	254.7	24.0
32	5	14	90	1	410.9	24.1
33	5	14	90	2	527.7	13.7
34	5	14	135	0.5	293.8	23.2
35	5	14	135	1	382.8	26.4
36	5	14	135	2	551.3	26.2
37	10	19	0	0.5	187.2	42.4
38	10	19	0	1	301.8	29.4
39	10	19	0	2	556.7	33.3
40	10	19	90	0.5	313.2	12.4
41	10	19	90	1	548.5	-8.4
42	10	19	90	2	568.0	14.1
43	10	19	135	0.5	450.1	7.0
44	10	19	135	1	481.3	11.1
45	10	19	135	2	591.9	13.0
46	10	14	0	0.5	193.4	33.1
47	10	14	0	1	249.4	31.5
48	10	14	0	2	344.7	32.6
49	10	14	90	0.5	395.5	7.0
50	10	14	90	1	454.2	-0.2
51	10	14	90	2	524.8	-6.3
52	10	14	135	0.5	325.3	12.6
53	10	14	135	1	453.0	12.1
54	10	14	135	2	427.0	11.1

Figure 6.6 shows the main effects plot for the cutting force. Average cutting force measured when cutting workpieces had 135^o and 90^o fibre orientations differed significantly from 0^o fibre orientation. Lower cutting forces were obtained when cutting using 0^o rake angle, lower cutting speed, 0^o fibre orientation and low depth of cut. Clearly, fibre orientation and depth of cut were found to have substantial influence on cutting force. Contrary to previous literature [29, 31], average cutting force was found to increase with the rake angle. This may be attributed to the differences in cutting conditions and laminate properties. Rake angle and cutting speed had lower contribution on the cutting force results.

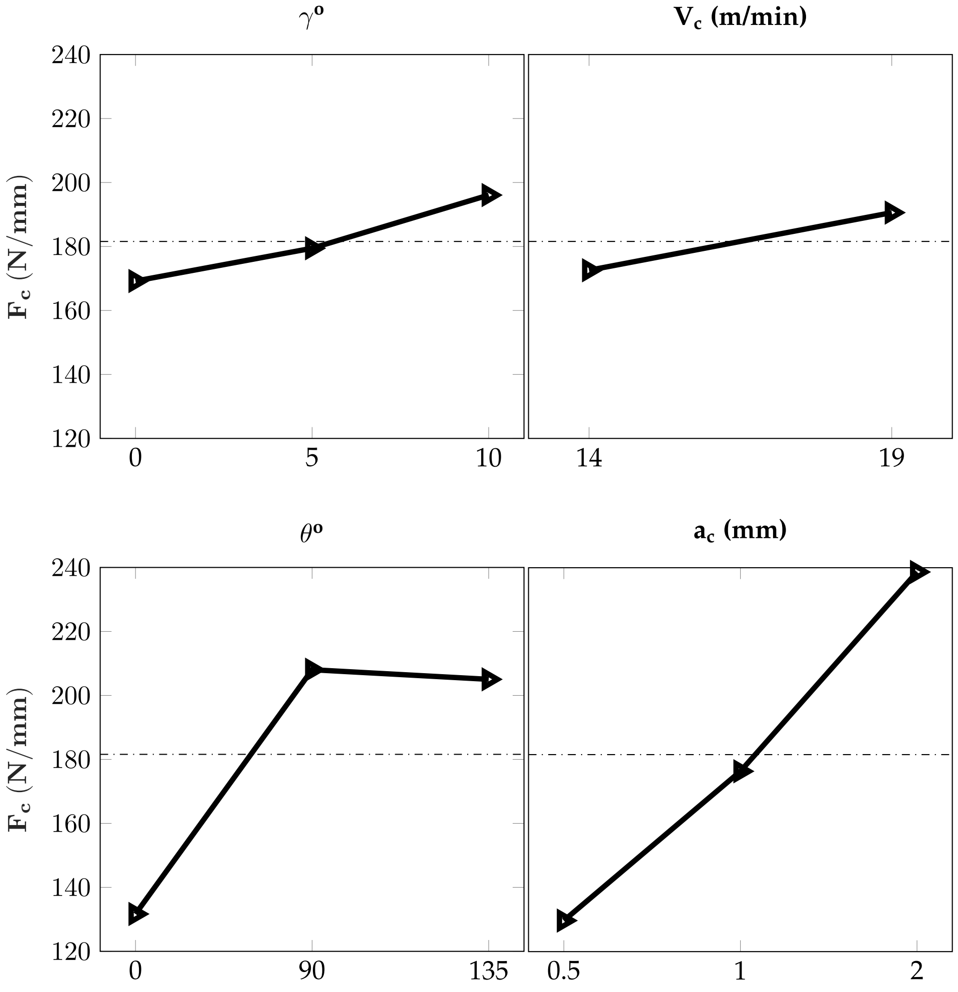

Figure 6.6: Main effects plot for cutting force

Analysis of Variance (ANOVA) for the main cutting force is performed and shown in Table 6.4. All factors were found statistically significant at the 5% level but the depth of cut had the highest Percentage Contribution Ratio (PCR) of 48% followed by fibre orientation with 30% PCR. The error associated with the main cutting force evaluation was marginally higher than the accepted level (15%) which could be ascribed to possible unconsidered interactions between some of the control factors.

Table 6.4: ANOVA results for the cutting force

Source	*DF*	*SS*	*MSS*	*SSe*	*F*	*P*	*PCR* (%)
γ^o	2	29203	14601	25731	4.21	0.021*	2.63
$V_c\ m/min$	1	19331	19331	15859	5.57	0.023*	1.62
θ^o	2	296835	148418	293363	42.75	0*	29.95
$a_c\ mm$	2	474517	237259	471045	68.34	0*	48.09
Error	46	159689	3472	-	-	-	17.72
Total	53	979575					

DF = Degrees of Freedom
SS = Sum of Squares
MSS = Mean Sum of Squares
SSe = Expected Sum of Squares
F = F-test value
P = probablity
PCR = Precent Contribution Ratio
*Significant at the 5% level

The average thrust force for the tests performed was $30\ N$, which is 11% of the average main cutting force. It can be seen from the main effects plot in Figure 6.7 that the rake angle and the fibre orientation are the most significant factors affecting the thrust force. Thrust force decreased with increased rake angle. This is in agreement with the findings reported in the work of Caprino et al. [29] but differs from the conclusions drawn by Wang et al. [3]. Cutting speed and depth of cut had negligible effect. Lower thrust force has been obtained with increased rake angle and when cutting at 90^o fibre orientation samples.

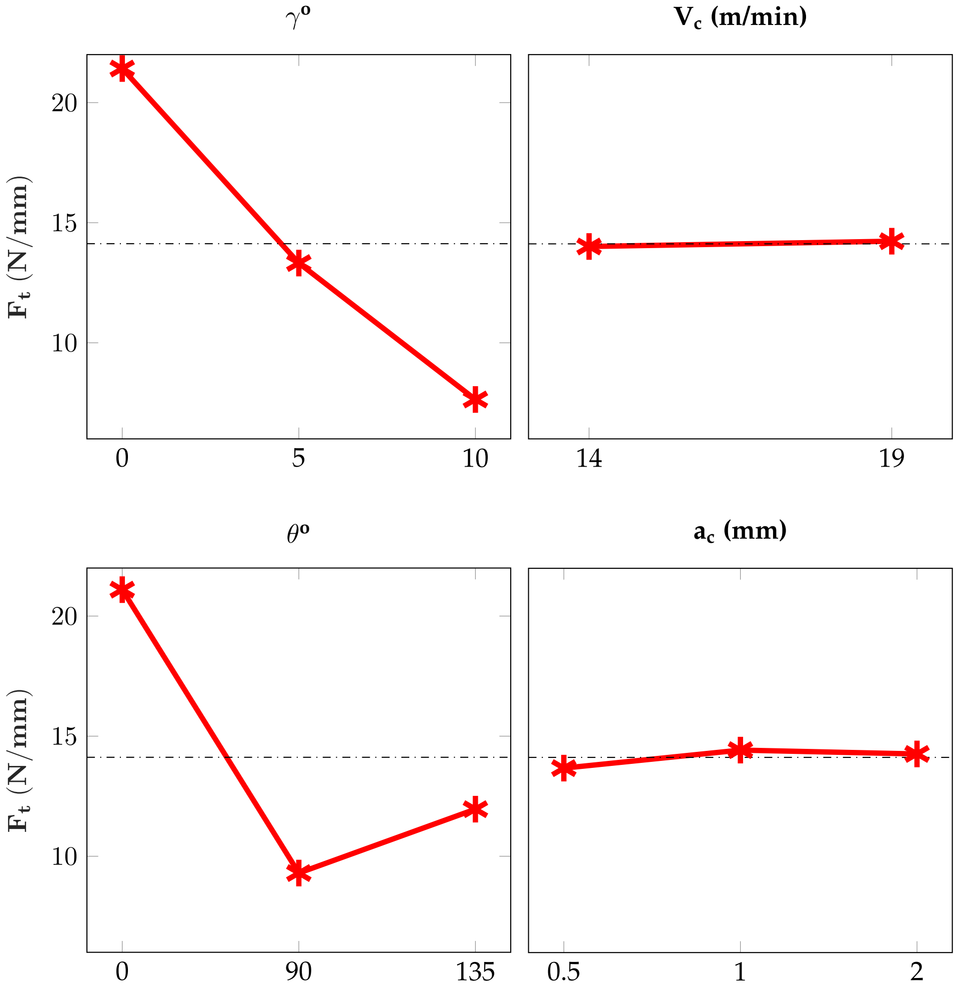

Figure 6.7: Main effects plot for thrust force

ANOVA was also performed for thrust force results and is shown in Table 6.5. Rake angle and fibre orientation were found to be statistically significant at the 5% level with a relatively higher PCR of 48 and 38% respectively. The small error level (13%) associated with the thrust force evaluation was within the acceptable levels (up to 15%), suggesting that all important variables had been considered and measurements accurately performed [140].

Table 6.5: ANOVA results for thrust force

Source	*DF*	*SS*	*MSS*	*SSe*	*F*	*P*	*PCR* (%)
γ^o	2	7619.7	3809.85	7576.893	89	0*	48.26
$V_c\ m/min$	1	2.9	2.9	0	0.07	0.794	0.00
θ^o	2	6085.4	3042.7	6042.593	71.08	0*	38.48
$a_c\ mm$	2	24.2	12.1	0	0.28	0.755	0.00
Error	46	1969.1	42.80652	-	-	-	13.26
Total	53	15701.2					

Chip Formation

High speed videos showed strong dependency of the chip formation on the fibre orientation. This is evident in Figure 6.8, which shows distinct chip formations at 0^o, 90^o and 135^oangles. At 0^o fibre orientation, long and continuous chips were observed with crushed area ahead of the cutting tool. Cutting 135^o samples resulted in fragmented chips flowing on the rake face. Sustainable cutting took place mainly in the centre of the workpiece while workpiece sides (fibre/matrix) deflected under the tool cutting edge and bounced back once the tool has advanced. This is evident by the recorded high speed videos which clearly showed that the side fibres/matrix were subjected to bending, buckling and out of plane forces. In other words, the fibres along the unsupported edges (sides) were deflected outwards under the tool nose and bounced back after tool progression, which resulted in valley-shaped cuts across the width of the workpiece. Cutting samples with 90^o orientation resulted in small and dust-like chips ejected at high speeds. Material failure was governed by shear due to bending exerted by the tool on the workpiece. Fibre bouncing and pull out along the unsupported edges was also observed leading to high subsurface damage and edge delamination although to less extent than the 135^o cuts. Depth of cut affected the chip formation in all three cases. In 90^o and 135^o, a substantial subsurface damage was observed accompanied with uncut material on the unsupported edges. The extent of the damage correlated to the depth of cut, i.e. higher damage with increased depth of cut. Rake angle had little effect on chip formation, which agrees with the findings in literature (Refer to Section 2.4.2). Also cutting speed had a minimum effect on the chip formation. This might be due to the relatively small range of cutting speed levels.

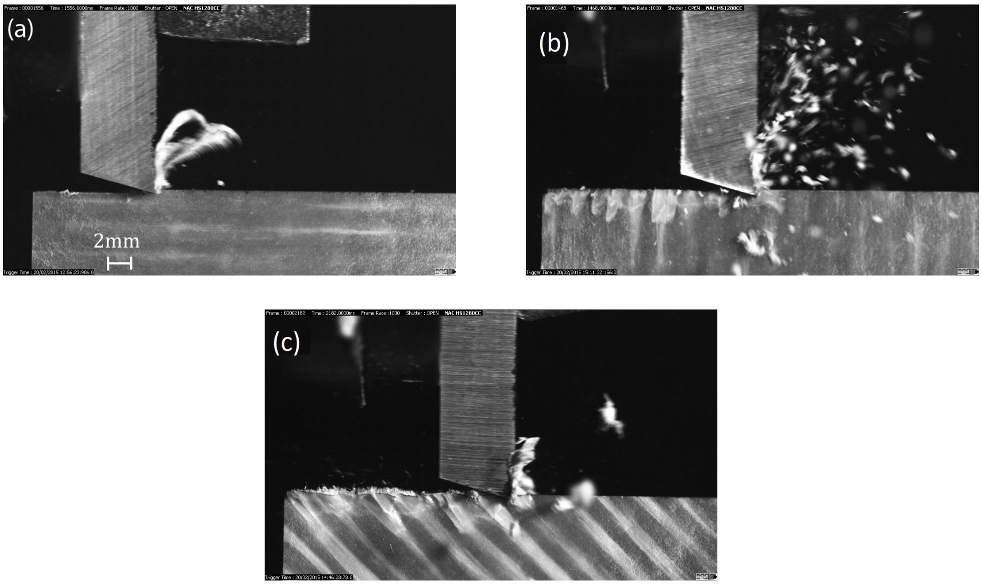

Figure 6.8: Chip formation at (a) 0^o, (b) 90^o and (c) 135^o

Surface Roughness

Table 6.6 shows the average roughness and waviness values for all conducted tests (average of three readings per workpiece).

Table 6.6: Average Surface roughness and waviness results

Test no.	γ^o	$V_c\ m/min$	θ^o	$a_c\ mm$	$R_a\ \mu m$	$R_t\ \mu m$	$W_a\ \mu m$	$W_t\ \mu m$
1	0	19	0	0.5	3.2	25.0	3.2	19.6
2	0	19	0	1	4.2	38.0	6.6	40.3
3	0	19	0	2	4.7	43.4	12.1	55.8
4	0	19	90	0.5	6.2	95.0	22.6	158.5
5	0	19	90	1	4.1	39.8	13.2	65.2
6	0	19	90	2	9.3	104.9	30.1	167.0
7	0	19	135	0.5	17.2	184.0	49.2	165.7
8	0	19	135	1	16.2	109.9	60.9	271.7
9	0	19	135	2	53.3	514.7	79.2	410.1
10	0	14	0	0.5	2.3	22.2	3.8	20.3
11	0	14	0	1	6.1	56.7	10.4	57.0
12	0	14	0	2	5.6	48.8	7.9	40.8
13	0	14	90	0.5	3.5	29.2	5.0	26.5
14	0	14	90	1	4.0	36.6	7.2	45.5
15	0	14	90	2	10.7	94.8	25.2	137.4
16	0	14	135	0.5	14.6	196.9	47.3	258.9
17	0	14	135	1	18.1	163.6	49.5	220.4
18	0	14	135	2	18.0	136.2	43.7	233.6
19	5	19	0	0.5	2.6	37.8	3.2	16.9
20	5	19	0	1	4.1	45.8	7.9	48.2

Table 6.6 – continued

Test no.	γ^o	$V_c\ m/min$	θ^o	$a_c\ mm$	$R_a\ \mu m$	$R_t\ \mu m$	$W_a\ \mu m$	$W_t\ \mu m$
21	5	19	0	2	2.6	27.9	4.3	21.1
22	5	19	90	0.5	4.0	45.8	10.6	70.8
23	5	19	90	1	4.6	40.6	12.7	63.0
24	5	19	90	2	15.6	288.3	36.2	327.0
25	5	19	135	0.5	13.0	173.0	57.4	288.6
26	5	19	135	1	19.7	156.0	52.4	263.1
27	5	19	135	2	26.4	290.5	96.6	455.0
28	5	14	0	0.5	2.7	42.0	4.4	39.0
29	5	14	0	1	3.5	32.0	4.1	27.1
30	5	14	0	2	5.8	53.9	10.6	51.5
31	5	14	90	0.5	3.4	31.0	5.9	32.4
32	5	14	90	1	4.8	47.6	11.4	55.1
33	5	14	90	2	4.7	48.2	22.8	116.7
34	5	14	135	0.5	11.0	136.1	23.3	109.1
35	5	14	135	1	12.8	112.5	37.3	200.8
36	5	14	135	2	31.2	392.1	113.6	593.2
37	10	19	0	0.5	4.4	41.2	6.3	37.7
38	10	19	0	1	5.0	62.7	8.5	59.8
39	10	19	0	2	3.6	31.3	7.6	50.8
40	10	19	90	0.5	3.1	27.0	4.8	25.6
41	10	19	90	1	4.1	43.5	13.6	66.7
42	10	19	90	2	5.7	55.9	21.6	104.6
43	10	19	135	0.5	19.9	210.3	67.1	310.0
44	10	19	135	1	14.8	154.5	45.0	264.6
45	10	19	135	2	56.9	943.3	183.9	708.0
46	10	14	0	0.5	3.3	31.0	5.5	28.2
47	10	14	0	1	3.4	41.0	7.1	38.5
48	10	14	0	2	3.7	28.8	5.1	29.8
49	10	14	90	0.5	3.3	30.9	6.4	30.5
50	10	14	90	1	3.9	31.0	9.5	44.0
51	10	14	90	2	4.2	36.8	13.9	66.8
52	10	14	135	0.5	21.4	237.1	33.6	174.2
53	10	14	135	1	16.7	181.9	66.2	271.4
54	10	14	135	2	13.4	161.2	41.5	212.7

The longitudinal roughness calculations were taken at the centre of the workpiece because of the severe damage at the edges caused by out-of-plane deformation of the fibres in 90^o and 135^o samples as shown in Figure 6.9. Generally, 0^o cuts generated the best transverse profile and the cleanest surfaces with overall average of $3.9\ \mu m$ as compared with $5.5\ \mu m$ and $21.9\ \mu m$ for 90^o and 135^o respectively. In Figure 6.9(c) fibre pullout is evident on the unsupported sides with a v-shaped transverse profile. Figure 6.9(b) shows uncut fibres as well but with U transverse shape.

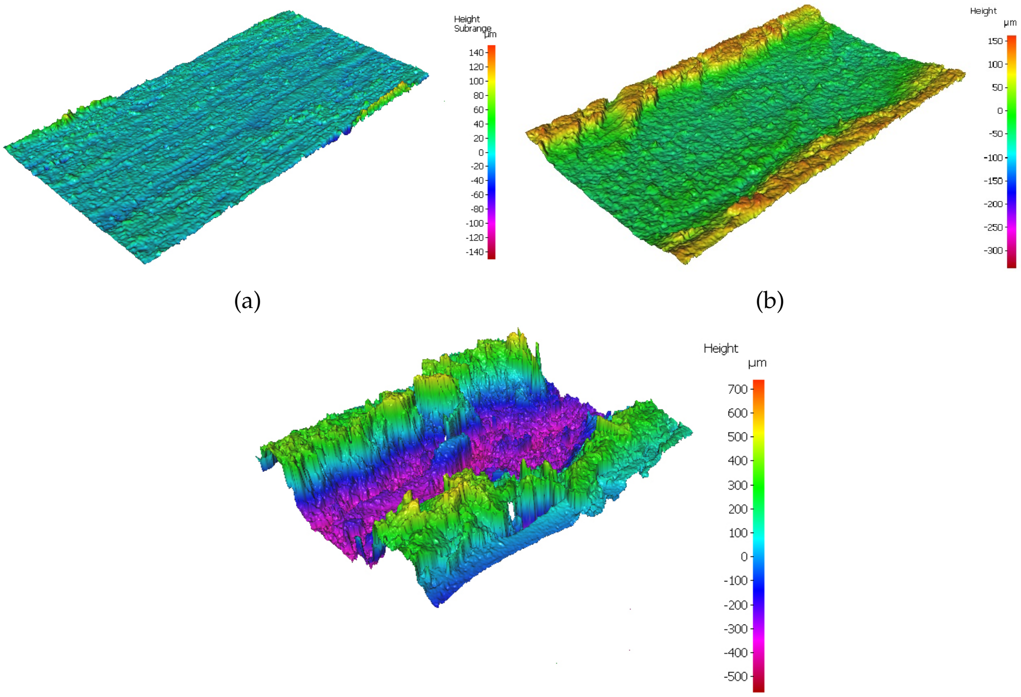

(a) (b) (c)

Figure 6.9: Sample surface profiles at $\theta =$ (a) 0^o, (b) 90^o and (c) 135^o

Table 6.7 shows a summary of results for the average surface roughness (R_a) as a function of the fibre orientation. The 0^o results are comparable to previous literature e.g. average $R_a = 2\ \mu m$ to $3\ \mu m$ was reported by Wang et al. [3] whereas roughness measurements beyond 60^o were not reported due to the severe surface damage. Palanikumar [141] investigated the surface roughness while turning GFRP, although 0^o orientation was not investigated, it was noted that increased fibre orientation caused increase in roughness. While their findings cannot be mapped directly to this study, it shows that the general trend in both studies were similar.

Table 6.7: R_a statistics as a function of fibre orientation

θ^o	*Mean*	*Min*	*Max*
0	3.9	2.3	6.1
90	5.5	3.1	15.6
135	21.9	11	56.9

Figure 6.10 and Table 6.8 show the main effects plot and ANOVA results for R_a. Fibre

orientation and depth of cut were the statistically significant factors at the 5% level. The fibre orientation contribution was found to be dominant with 4 times increase in roughness at 135^o as compared to 0^o and 90^o fibre orientations. Increased depth of cut also resulted in rise in the average roughness. Cutting speed and rake angle had lower effects on R_a.

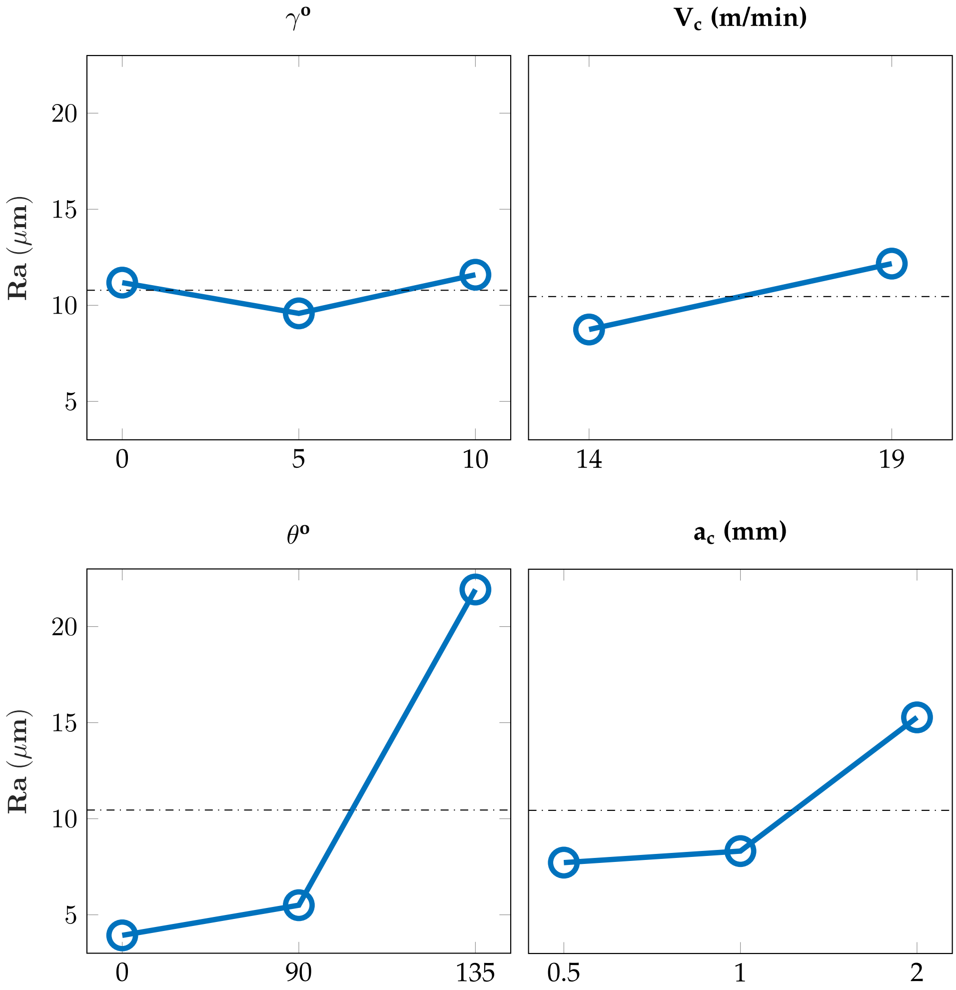

Figure 6.10: Main effects plot for R_a

ANOVA results showed that fibre orientation and depth of cut were found statistically significant affecting the average surface roughness with a corresponding PCR of 53% and 9% respectively. For fibre orientation, these results were in agreement with the visual observations where poor surface quality was produced from cutting 135^o fibre orientation laminates.

Table 6.8: ANOVA results for R_a

Source	*DF*	*SS*	*MSS*	*SSe*	*F*	*P*	*PCR* (%)
γ^o	2	23.78	11.89	0	0.24	0.787	0.00
$V_c\ m/min$	1	158.48	158.48	109.06	3.21	0.08	1.64
θ^o	2	3577.41	1788.7	3527.99	36.19	0*	52.90
$a_c\ mm$	2	636.07	318.03	586.65	6.43	0.003*	8.80
Error	46	2273.51	49.42	-	-	-	36.67
Total	53	6669.25					

The average waviness of the surface (W_a) showed similar trends to R_a (shown in Figure 6.11), with the fibre orientation as the dominant factor followed by the depth of cut while rake angle and cutting speed were found to have limited impact on surface waviness. The overall average of the waviness was $28.5\ \mu m$ and it varied from $3.2\ \mu m$ to $183.9\ \mu m$.

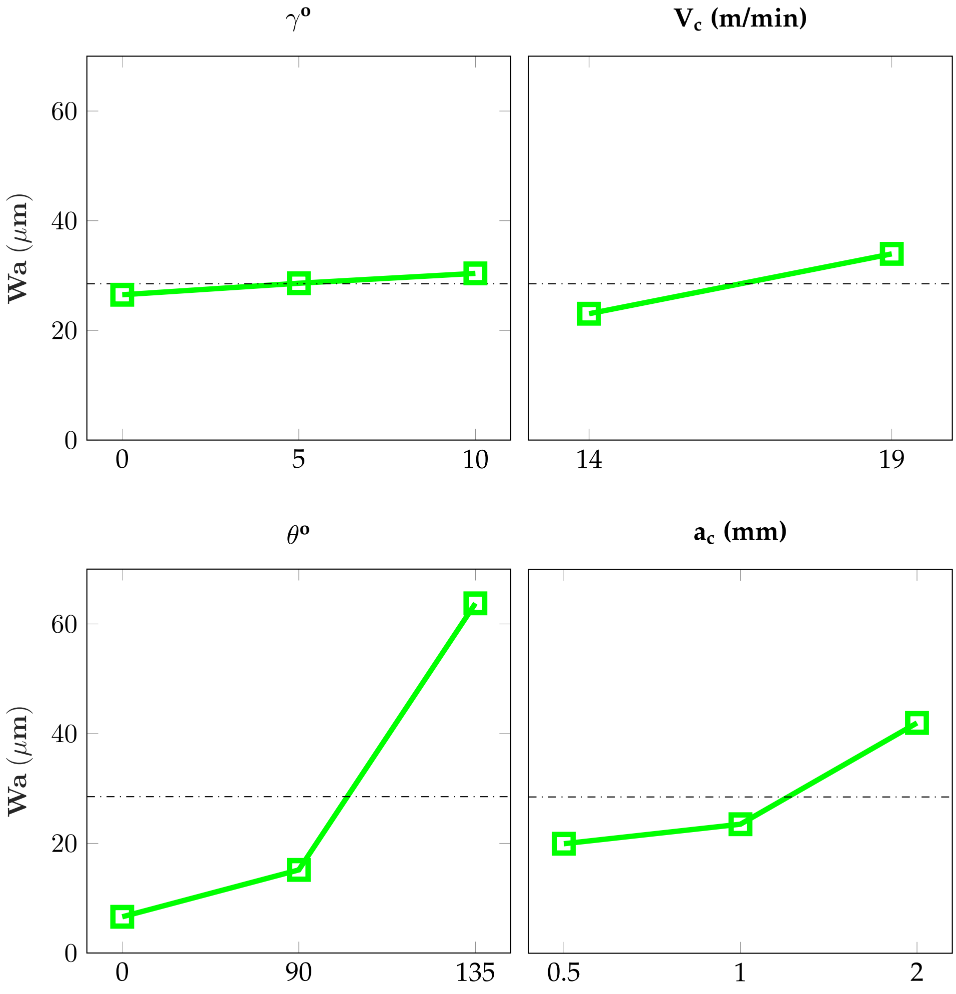

Figure 6.11: Main effects plot for W_a

6.3.4 Concluding Remarks on Phase I

This section summarised the experimental work carried out in Phase I. Cutting forces, chip formation and surface integrity showed a strong dependency on fibre orientation. The main cutting force was mainly dependent on fibre orientation and depth of cut and averaged $381.3\ N$, whereas thrust force was mainly affected by the fibre orientation and the rake angle and had a mean of $30\ N$. Three distinct chip modes were observed at the three levels of fibre orientation. Long continuous chips resulted at the 0^o, dust like particles at the 90^o and segmented chips at 135^o. These different sizes reflect different cutting mechanisms. Average roughness ($R_a = 10.5\ \mu m$) and waviness ($W_a = 28.5\ \mu m$) of the machined surface were affected mainly by the fibre orientation and depth of cut. Out-of-plane deformation of unsupported fibres at the edges caused large damaged surface at 90^o and 135^o orientations with substantially higher roughness at 135^o. By choosing wide range of depth of cut up to $2\ mm$, it was found that it is statistically more significant than fibre orientation, which was thought of previously as the most influential factor affecting the main cutting force. To summarise, cutting at 0^o and small depth of cut resulted in better surface quality and lower cutting forces. Rake angle and cutting speed were found to be less significant factors. Cutting at 135^o with single point tools should be avoided in practical applications and cutting of unsupported edges is also undesirable since it generates out-of-plane fibre deformation and subsequently lower surface quality.

6.4 Phase II Experiments

6.4.1 Introduction

The content of fibres in composites is usually quantified by the volume ratio of the fibres to the cured composite and is called fibre volume fraction V_f. The fibres have high stiffness and strength while the matrix has low stiffness and strength; the resulting lamina properties fall in between these two extremes [22]. The extent to which the lamina properties approach those of fibres or matrix primarily depends on the V_f. The effect of fibre volume fraction was rarely studied in the literature of composites machining and should be investigated more in depth [28]. The V_f is expected to have an effect on cutting forces and machinability in general due to its effect on the mechanical properties of the composite. Phase II experiments aim at exploring the combined effect of fibre volume fraction as well as fibre orientation on cutting forces when orthogonal cutting of UD-GFRP. The effect shall be formulated as an empirical model to predict cutting force as a function of fibre orientation and fibre volume fraction. Phase II experiments build on phase I in many aspects. The experimental set up is similar. In addition, some of the factors which were found less significant were not included as process variables (e.g. rake angle and cutting speed). Finally, the outputs of interests were narrowed down to cutting forces as chip formation mechanisms are expected to be qualitatively similar with variation of V_f.

6.4.2 Experimental Work of Phase II

The test rig and cutting tools were the same as Phase I. The tools were ground with 0^o rake angles and 15^o clearance angle. The effect of tool wear was eliminated from the experiments by using new tool at the beginning of each test. A sample cutting tool is shown in Figure 6.12. Each tool has two cutting sides

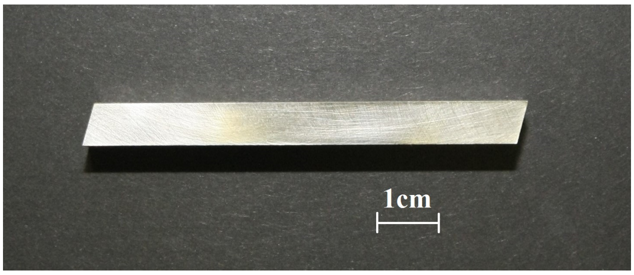

Figure 6.12: Sample cutting tool used in experiments

The workpiece material was unidirectional GFRP plates produced by hand layup from E-glass fibres and Impreg 22 epoxy resin. The plates were manufactured to request by PE Composites Co. with varying fibre content. The samples were cut at different fibre orientations into $80 \times 80 \times 2\ mm$ plates. The fibre content of the samples was verified using images obtained with Scanning Electron Microscope MIRA3 TESCAN available at Northumbria University labs. The imaging samples were cut into $8 \times 8 \times 2\ mm$ and ground on the sides perpendicular to the fibre direction. The samples were then coated with $5nm$ coating of platinum using sputter coater. Three images at different locations were taken for each sample. Image analysis was carried out using ImageJ software Version 1.50b. Force calculations were collected similarly to Phase I experiments. Dynamometer signal measurement frequency was set at 1000 Hz. Phase I of the experiments established the limited effect of rake angle and cutting speed on cutting forces, as such they were fixed at $\gamma = 0^o$ and $V_c = 14\ m/min$. A depth of cut of $0.5\ mm$ and dry cutting were used in all tests. The chosen process variables are fibre orientation θ and fibre volume fraction V_f. Five levels for θ and three for V_f were chosen, giving a total of 15 experiments. The process variables and their levels are shown in Table 6.9. The three levels of the V_f were chosen to cover the range of most of the practical applications from 45% to 65%. The five different fibre orientations were chosen due to the considerable influence on the cutting forces which would enable to capture detailed variations on cutting forces. Furthermore, the range of orientations were chosen to complement the range of orientations in Phase I.

Table 6.9: Experimental factors and their levels

process variables	*levels*				
$V_f(\%)$	45	55	65		
$\theta(^o)$	0	30	60	90	120

6.4.3 Results and Discussion of Phase II

The variation between the nominal and average measured fibre content is shown in Table 6.10. The variation ranged between 1.8% and 2.6%. This is acceptable given that the samples were custom-made by hand layup.

Table 6.10: Variation of nominal and measured fibre content

V_f level	*Nominal (%)*	*Measured (%)*	*Variation (%)*
1	45	43.2	1.8
2	55	57.1	2.1
3	65	62.4	2.6

Sample images are shown in Figure 6.13. Some defects in the surface are visible but were excluded during the image analysis. The distribution of the fibres is not uniform on a microscopic level.

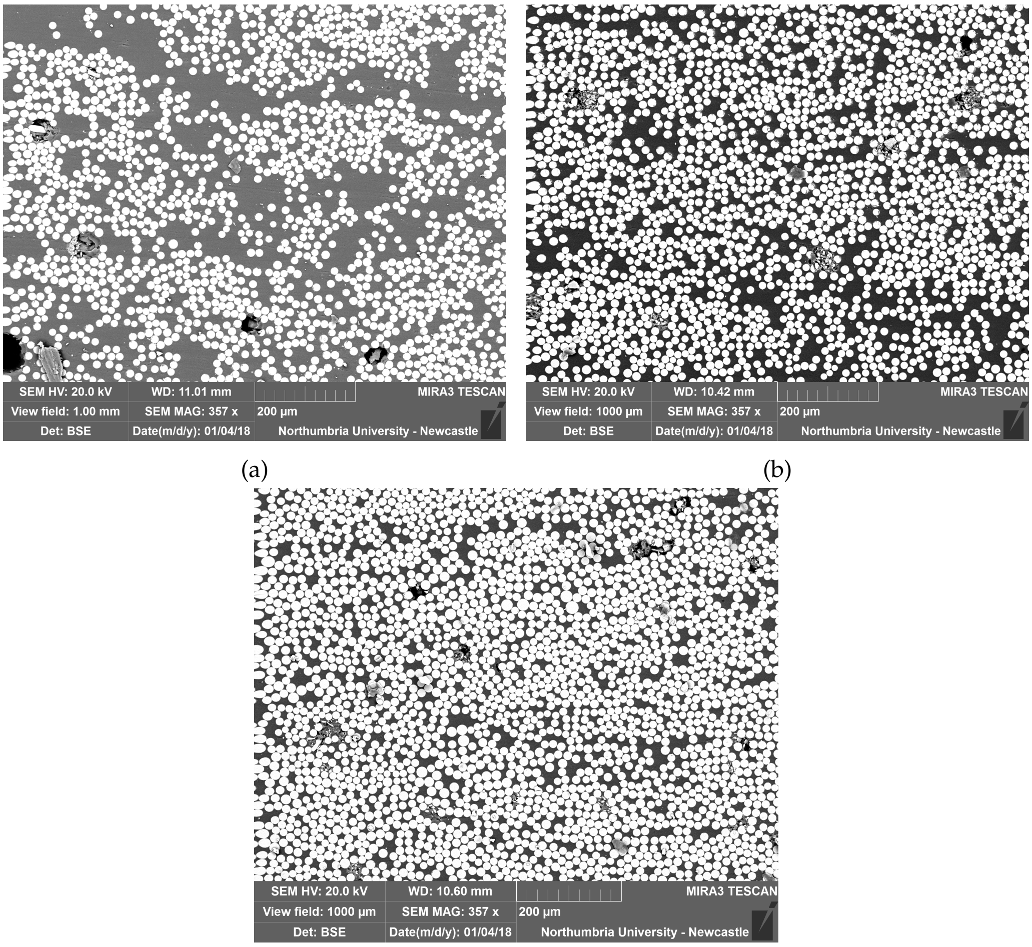

(a) (b)

(c)

Figure 6.13: Sample SEM images at 357 magnification for (a) $V_f = 45\%$, (b) $V_f = 55\%$ and (c) $V_f = 65\%$

Figure 6.14 and Table 6.11 detail the average cutting and thrust forces as function of θ^o and V_f. The minimum cutting force was recorded at 30^o whereas the maximum at 90^o and generally ranged between $150\ N$ to $550\ N$. This was in line with force trends reported by Caprino and Langella [28] and could be explained by different cutting mechanisms. Low forces at low orientations corresponded with compression-induced shear crack propagating along the fibre direction to form the chip, whereas at higher orientations, fibre failure under bending becomes more dominant with damage extending below cutting surface [3,28].

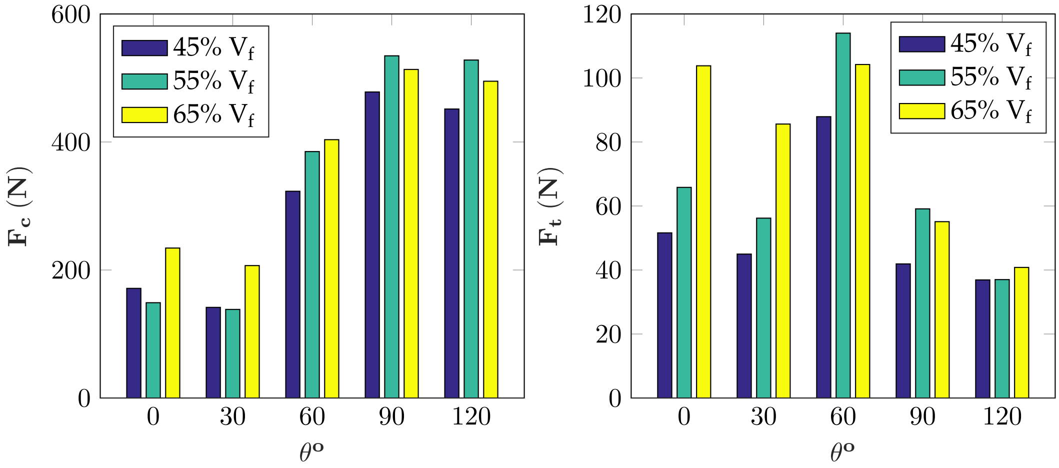

(a) (b)

Figure 6.14: Cutting (a) and thrust force (b) as function of fibre orientation

Similar force trend was observed regardless of the V_f of the material. V_f did not cause considerable variation in the cutting force whereas a maximum variation of $\approx 90\ N$ was observed at 30^o fibre orientation angle. The maximum thrust force of $115\ N$ was observed at 60^o while the minimum of $38\ N$ was recorded at 120^o, with values ranging from $115\ N$ to $40\ N$; these trends were in agreement with the findings of Ramulu [36].

Table 6.11: Mean cutting and thrust force results for Phase II experiments

V_f (%)	$\theta(^o)$	F_c (N)	F_t (N)
45	0	171.30	51.60
45	30	141.60	44.97
45	60	323	87.90
45	90	478.10	41.90
45	120	451.50	36.90
55	0	148.90	65.81
55	30	138.40	56.20
55	60	385	114
55	90	534.60	59.10
55	120	528	37
65	0	234.30	103.80

Table 6.11 – continued

V_f (%)	$\theta(^o)$	F_c (N)	F_t (N)
65	30	206.90	85.60
65	60	403.60	104.20
65	90	513.30	55.10
65	120	494.90	40.80

Figures 6.15 and 6.16 show the main effects plots for cutting and thrust forces. Average cutting force values increased by 29 N/mm between 45% and 65% of V_f whereas thrust force increased by 13 N/mm in the same range. Both force components showed clear linear dependency on V_f, probably as a result of increased strength of the workpiece with increased fibre content. Larger effect of V_f was seen on the thrust force, which could be attributed to the smaller magnitude of thrust force. The effect of fibre orientation on cutting force was characterised by a local minimum at 30^o and local maximum at 90^o. The effect of fibre orientation on thrust force was maximum at 60^o and minimum at 120^o.

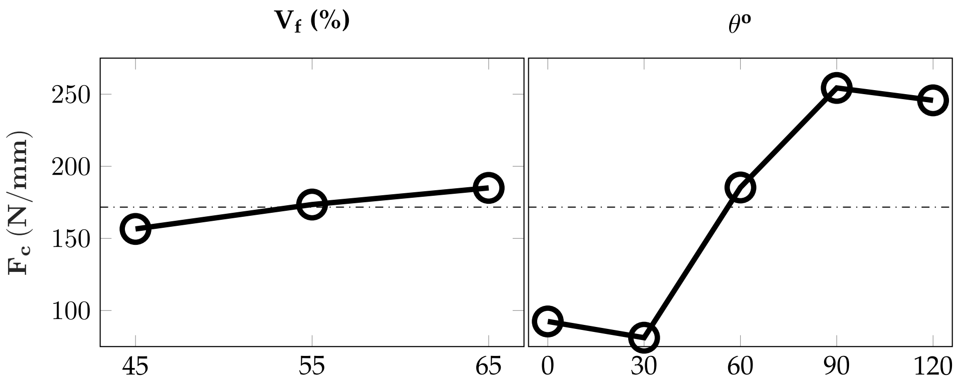

Figure 6.15: Main effects plots for cutting force of Phase II

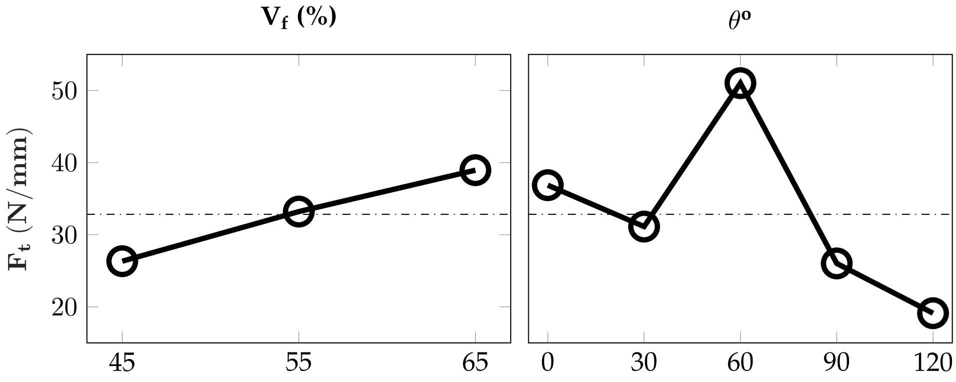

Figure 6.16: Main effects plots for thrust force of Phase II

Table 6.12 and 6.13 show ANOVA results for cutting and thrust forces respectively. Relatively high PCR for the fibre orientation (95.31%) was observed as compared to 2.22% for V_f, though both factors were statistically significant on the cutting force. Larger effect of V_f was seen on the thrust force with PCR =14.59%, however, fibre orientation was still found to be the most significant factor with PCR = 69.46%.

Table 6.12: ANOVA results for cutting force of Phase II

Source	*DF*	*SS*	*MSS*	*SSe*	*F*	*P*	*PCR* (%)
θ^o	2	323740	80935	322903.6	96.77	0*	95.31
V_f %	2	8353	4176.5	7516.625	4.99	0.039*	2.22
Error	8	6691	836.375	-	-	-	2.47
Total	14	338785					

DF = Degrees of Freedom
SS = Sum of Squares
MSS = Mean Sum of Squares
SSe = Expected Sum of Squares
F = F-test value
P = probablity
PCR = Precent Contribution Ratio
*Significant at the 5% level

Table 6.13: ANOVA results for thrust force of Phase II

Source	*DF*	*SS*	*MSS*	*SSe*	*F*	*P*	*PCR* (%)
θ^o	2	7013	1753.3	6855.838	11.14	0.002*	69.46
V_f %	2	1597.8	798.9	1440.38	5.08	0.038*	14.59
Error	8	1258.9	157.36	-	-	-	15.94
Total	14	9869.9					

Figure 6.17 shows the ratio between the cutting and thrust force (F_c/F_t) as a function of the fibre orientation for different V_f. The ratio increased with fibre orientation from 2 at $\theta = 0^o$ to 14 at $\theta = 120^o$. This increase was gradual between $\theta = 0^o$ and $\theta = 60^o$ whereas a

sharp rise could be seen between $\theta = 60^o$ and $\theta = 120^o$. This ratio was significantly higher than what was reported in some literature, e.g. the results reported by Wang et al. [32] who indicated that this ratio was always less than 1. This could be ascribed to the different cutting conditions between the two studies. In the work of Wang et al. [32], depth of cut was 0.01 mm and speed 1 m/min; as compared to 0.5 mm depth and 14 m/min speed for this work. This indicates that this ratio depends on depth of cut and cutting speed which can be investigated in further investigations.

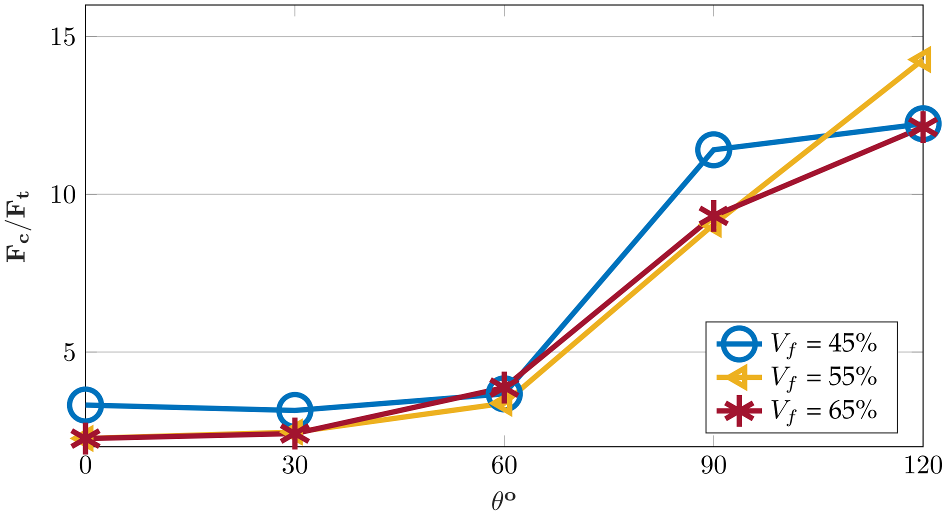

Figure 6.17: Force ratio for different V_f

The experimental results were formulated into an empirical model, which predicted the magnitude of the cutting force as a function of fibre orientation and fibre volume fraction. A multivariate regression technique was deployed using polynomial fitting. Guidance about required polynomial order that achieved the best fit could be found in the main effects plots (Figure 6.15) which showed that first order is suitable for the linear V_f effect; as for θ, due to the existence of local maxima and minima, a third order polynomial is preferred. The resulting model is shown in Equation 6.1 and force surface is shown in Figure 6.18. Black dots are experimental values and the surface represents the predicted values. The goodness of fit indicators were $SSE = 8446; R^2 = 0.9751;$ adjusted$R^2 = 0.9564; RMSE = 32.49$. As for thrust force, similar model was not feasible as goodness of fit was not adequate.

$$F_c(\theta, V_f) = 352.1 + 300.6\,\theta + 27.25\,V_f - 9.1\,\theta^2 - 4.28\,\theta V_f - 1000.9\,\theta^3 - 3.16\,\theta^2\,V_f \quad (6.1)$$

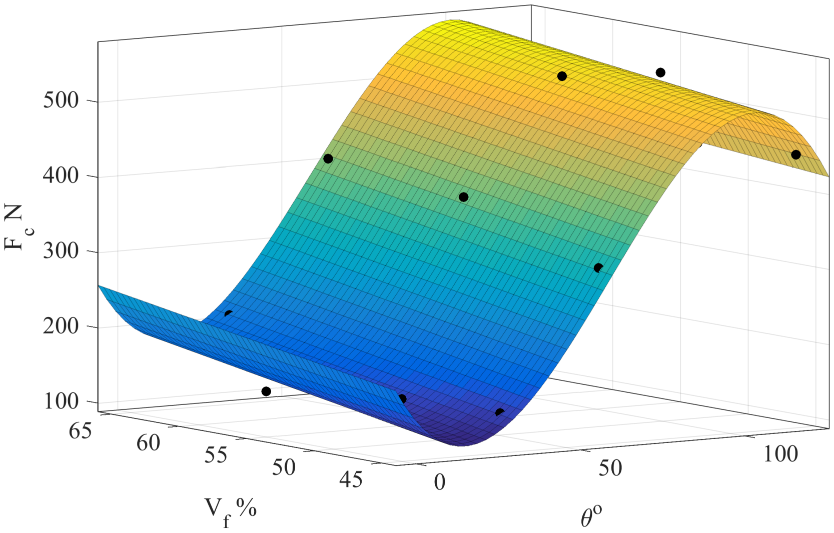

Figure 6.18: Cutting force fit surface

6.4.4 Concluding Remarks on Phase II

This section presented the experimental investigations of the effect of fibre volume fraction and fibre orientation on cutting and thrust forces when orthogonal cutting of UD-GFRP. The fibre volume fraction had nearly linear effect on both force components within the studied range (45% to 65%). The variation with V_f was around 25% for the main cutting force and 45% for thrust force, which may indicate that increasing fibre content (within the studied levels) did not change the fundamental cutting mechanisms. It merely amplified the stiffness of the plates and increased the forces required to perform the cutting. The fibre orientation had significant effect on the cutting forces with relatively high PCR (95.31% and 69.46%). Cutting with low positive fibre orientation angles was found to give the best results in terms of reducing cutting forces due to favourable cutting mechanisms.

6.5 Phase III Experiments

6.5.1 Introduction

Producing validation force data for the meshfree model is the aim of Phase III. The main effort was directed towards obtaining high accuracy data and ensuring the cutting conditions are reproducible in the meshfree model. To this end, the test rig was changed from the shaping machine used in Phases I and II to a vertical milling CNC centre that was set up to carry out orthogonal cutting tests. This ensured higher control over the cutting conditions. Having previously established the high significance of the depth of cut on cutting forces, special measures were carried out to ensure accurate and consistent depth of cut across the workpiece. Furthermore, each test was repeated three times to reduce uncertainty related to the variability in material properties. The experiments were conducted on the same composite that was characterised in Section 6.2. Finally, supplementary in-situ chip formation analysis was carried out. Benefiting from the improved cutting conditions (especially lower cutting speed), high resolution images were obtained and discussed.

6.5.2 Experimental Work of Phase III

Orthogonal cutting experiments were conducted using 3 axis DENFORD vertical CNC machine (VMC 1300 PRO). It has variable feed rate up to $5000\ mm/min$. The spindle was locked to prevent rotational movement during cutting. The cutting speed was controlled by the table feed speed. Single point HSS cutting tools with 0^o rake angle and 15^o clearance angle were used. The dimensions of the tool were $6 \times 6 \times 63\ mm$. The squared-profile tool was fixed inside the circular tool holder using a specially designed and fabricated fitting, which is shown in Figure 6.19.

Figure 6.19: Tool holder for squared section cutting tool

Workpiece materials was UD-GFRP, similar to that used in Phase I experiments. The workpiece was fixed in vertical position in order to investigate the effect of fibre orientation. This was achieved using bespoke clamp. The clamp was fixed on top of a triaxial force piezo-electric dynamo-meter (Kistler 9257B). The dynamometer was connected through charge amplifier to a data acquisition device and a PC to collect and analyse the force signals. The experimental set up is shown in Figure 6.20. The only process variable was fibre orientation. Seven levels were tested between 0^o and 90^o with 15^o increments. Cutting speed was set at 3.8 m/min and depth of cut was set at 0.25 mm.

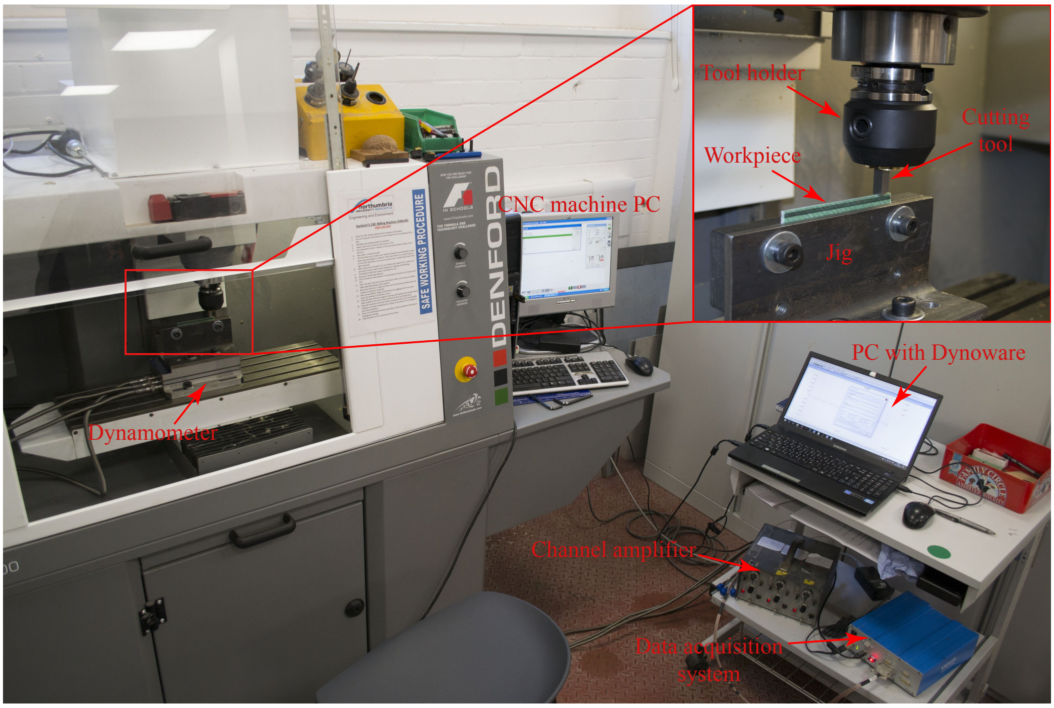

Figure 6.20: Experimental set up of Phase III

Accurate depth of cut throughout the cut was ensured as follows: A magnetic base, metric dial gauge was used to ensure the cut surface is flat within acceptable range of tolerance (±20 μm). The dial gauge was fixed on the ceiling of the machine, then made contact with the top of the workpiece, zeroed and then the workpiece moved slowly while taking readings of the dial. Adjustments to the workpiece position were made iteratively until the workpiece was appropriately levelled within the acceptable tolerance range. A snapshot of this process is shown in Figure 6.21.

Figure 6.21: Dial gauge set up

The supplementary high speed videos were obtained with Hotshot CC1024 High speed camera connected to PC with Hotshot link software to operate and process the captured videos. The camera was equipped with Sigma Macro $105\ mm$, $F2.8$ EX-DG lens that has high optical performance up to 1:1 magnification. LED lighting sources were used to illuminate the scene. When recording, cutting was carried out at low speed (0.5m/min). This allowed using lower fps than that used in Phase I (300-500) and resulted in images with higher resolution. Four fibre orientations were filmed, namely $[0^o,\ 30^o,\ 60^o,\ 90^o]$. Depth of cut was fixed at $0.25\ mm$.

6.5.3 Results and Discussion of Phase III

Table 6.14 shows cutting and thrust forces results of the experiments and Figures 6.22 and 6.23 show a plot with average values and standard error for each studied level. The standard error formula is as follows $err = \frac{std}{\sqrt{n}}$, where std is the standard deviation and n is the number of test repetitions. The normalised cutting forces were obtained by dividing the raw force values (shown in Table 6.14) by the width of the sample.

Table 6.14: Mean cutting and thrust forces of phase III

θ^o	*Test 1*	*Test 2*	*Test 3*
	Fc		
0	100.5	86	100.7
15	73.92	62.27	70.81
30	70.48	73	82.02
45	76.91	87.9	106.5
60	110.7	147.2	91.18
75	124.1	134.1	129.8
90	130.1	158.7	147
	Ft		
0	46.3	42.27	53.97
15	43.43	39.02	39.32
30	35.97	35.31	39.38
45	31.5	35.83	43.29
60	37.4	43.9	35.96
75	35.67	29.83	51.85
90	27.3	31.41	45.14

In order to improve accuracy in normalising data, the width of each sample was measured before the test. The average cutting force ranged between at minimum $32.6\ N/mm$ at $\theta = 15^o$ and a maximum $74.1\ N/mm$ at $\theta = 90^o$. The trend of forces show steady increase of force magnitude with fibre orientations (except at 0^o). This can be explained by the progressive reduction in compression-induced shear failure mode and increase in bending-dominated fibre failure mode. Thrust force values showed less variation in magnitude (if the error bounds are included). Maximum thrust force was at $\theta = 0^o$. This could be attributed to the distinct failure mechanism that dominate at this fibre orientation in which mode II failure is the main material removal mechanism.

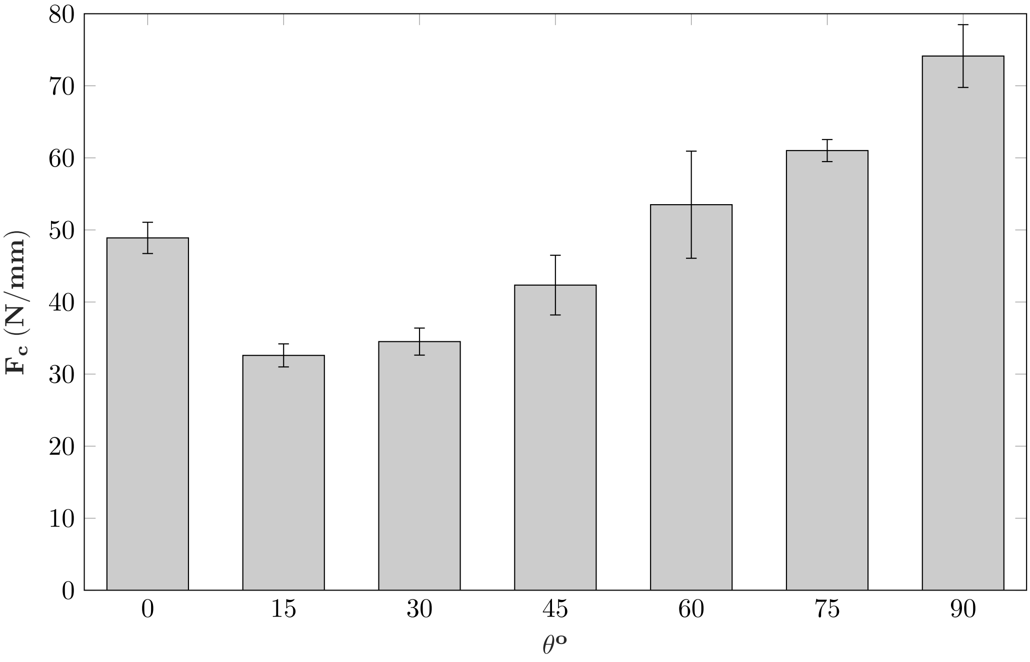

Figure 6.22: Mean cutting force of Phase III

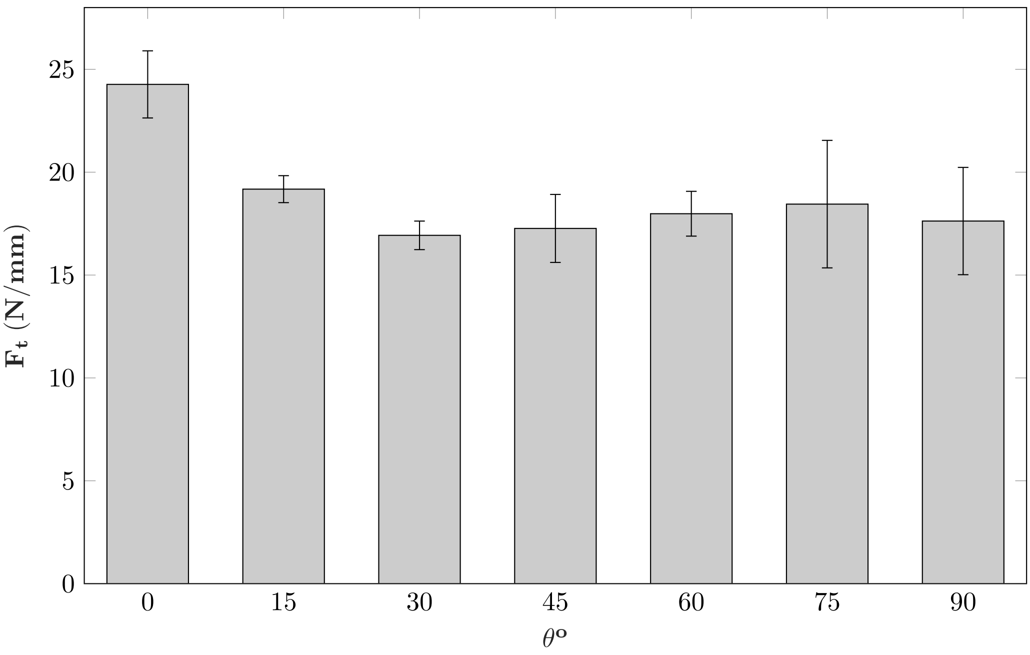

Figure 6.23: Mean thrust force of Phase III

6.5.4 Supplementary Chip Formation Observations

Figure 6.24 shows 4 images taken from high speed videos at each of the studied fibre orientations. At $\theta = 0^o$ (Figure 6.24a), the chips were formed by compression ahead of the cutting tool. Separation happened at the fibre-matrix interface and then delamination occurred. This caused multiple strands of long chips to flow on the rake face of the tool and then move out-of-plane.

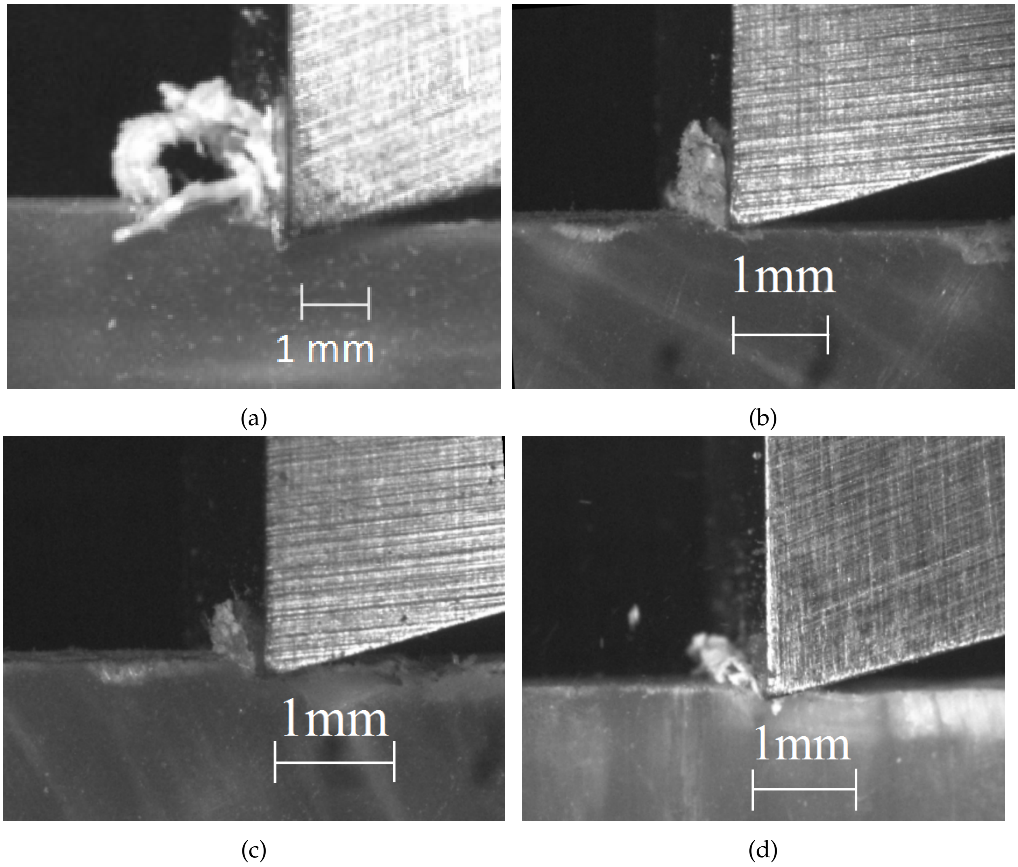

(a) (b)

(c) (d)

Figure 6.24: Chip formation at θ (a) 0^o, (b) 30^o, (c) 60^o and (d) 90^o

Figures 6.24b and 6.24c show the chip forming at 30^o and 60^o respectively. It is clear that the chips were formed by initial separation due to compression at the cutting edge, then subsequent separation happened at the matrix-fibre interface. In these orientations, the “shear angle”seems to be coinciding with fibre orientation. This is supported by earlier experimental studies [3,31].

Chip formation at 90^o is shown in Figure 6.24d. Small, discontinuous chips were formed from bending of fibres ahead of the rake face and then ejected at high speed from the workpiece. With the advancement of the tool, an area of subsurface damage is formed ahead of the tool for about $0.5\ mm$. Unsupported edges were bent and bounced back rubbing against the clearance face. This effect however, was noticed to be less pronounced than that observed in Phase I, which could be attributed to the high dependency of this phenomenon on the depth of cut.

6.5.5 Concluding Remarks on Phase III

Phase III of the experiments was concerned with generating the validation data for the dynamic meshfree model. Reliable cutting and thrust force values were obtained by utilising more accurate experimental set up/procedure than the previous phases. Cutting force showed steady increase between a minimum of 32.6 N/mm at $\theta = 15^o$ to a maximum of 74.1 N/mm at $\theta = 90^o$. Thrust forces were roughly constant ranging between $17 - 19$ N/mm with exception of 0^o which showed higher forces. These force values were used in Chapter 5 to validate the dynamic meshfree model. Supplementary chip formation analysis was also carried out. Most interesting observation was at 30^o and 60^o where the “shear plane”was observed at the fibre-matrix interface. The chips were separated from the workpiece by fracture emanating near the cutting edge towards the free surface following the fibre orientation.

6.6 Conclusions

This chapter presented the experimental work of this research project. Three phases of orthogonal cutting experiments of UD-GFRP were carried out. The first phase was a broad study that included four process variables and three outputs. The second phase was focused on the effect of material parameters such as fibre volume fraction and fibre orientation on cutting and thrust force. An empirical model to predict cutting force as a function of orientation and fibre volume fraction was proposed. The third phase was concerned with generating data to validate the meshfree model.

Experiments of Phase I were not replicated, which was mainly due to its exploratory nature. The main objective was to establish which process parameters were significant on three important outputs. The findings of Phase I guided the selection of process parameters and studied responses in Phases II and III. Furthermore, the main findings were generally in agreement with literature, thus there was little incentive to replicate. Regarding Phase II, resource constraint was the main factor of not replicating the experiments. The GFRP panels were hand-laid by composite supplier, which requires a lot of man-hours. Furthermore, the need to use new tool for every experiment added to the cost. In Phase III, in which high fidelity data was required, experiments were replicated three times.

As a result, insights about composites cutting were gained and can be summarised as follow:

- Depth of cut, fibre orientation, rake angle and cutting speed have statistically significant effects on cutting force.
- Fibre orientation and rake angle have statistically significant effects on thrust force.
- Fibre orientation and depth of cut have statistically significant effects on mean surface roughness and waviness.
- Nearly linear correlation was found between fibre volume fraction and cutting forces. It is also found to be statistically significant factor.
- High fidelity cutting and thrust force data were generated to validate the dynamic meshfree model.
- Chip formation was studied using high speed camera. Different chipping mechanisms are dominant at different fibre orientations.
- Chip separation in the range $0^o < \theta < 90^o$ occurs parallel to fibre orientations, giving an impression of having a “shear plane”similar to that noted in metal cutting.
- Favourable cutting conditions were found to be at low fibre orientations (less than 60^o), low depth of cut and positive rake angle.

Chapter 7

Conclusion

7.1 Introduction

Cutting of FRPs poses a challenge due to their inhomogeneous and abrasive nature. Insufficiently clean cuts could result in performance degradation and parts rejection. Given the relatively high cost of these materials, optimising cutting parameters using trial and error approach could significantly increase the product development cost. Using numerical modelling can be an attractive tool to reduce the reliance on trial and error and speed up product development cycles. However, modelling of cutting composites is challenging due to the existence of material, geometrical and boundary nonlinearities. In fact, to the author's best knowledge, direct prediction of the most relevant outputs to industry, such as tool life and surface roughness is not yet attainable directly from continuum-based numerical modelling. Instead, fundamental outputs such as cutting forces, chip geometry and temperatures can be predicted using these numerical models. Subsequently, these fundamental outputs can be used to predict industry-relevant outputs using other techniques (mainly through empirical models). Improving the predictive capabilities of numerical models can be improved by (i) improving the numerical solution technique (e.g. using novel numerical methods) and (ii) improving the approximation of the process (e.g.

advanced material models, chip/tool contact). This research project presented an effort in both directions. Addressing the first point was done by using meshfree methods (EFG) as a numerical solution technique, while addressing the second point was done by developing/integrating several algorithms in material, failure and contact modelling.

7.2 Summary

Chapter 2 presented the necessary background for the research undertaken in subsequent chapters. The chapter began by detailing background of the disciplines related to this research; namely, machining processes and composite materials. State of the art in orthogonal cutting of composites was presented with emphasis on cutting forces and chip formation. Finally, numerical modelling and meshfree methods were presented followed by modelling of machining composites. A comprehensive comparison of cutting forces predictions was compiled and presented graphically.

Chapter 3 presented the development of the EFG model components. Initially, the mathematical formulation of the problem was presented followed by the EFG approximation procedure and constraint enforcement methods. An iterative and progressive approach in developing model components was adopted. Elasto-statics models were used to verify accurate shape function and stress calculations. Timoshenko beam example was used to verify the EFG solution. Non-convex boundaries were handled using the visibility criterion. Cracked specimen example was used to verify the accuracy of the MATLAB implementation of the visibility. Elasto-dynamic model was then presented and verified with an example of a solid subjected to shock loading. Stress wave propagation was compared with FEM solution available in literature. Frictionless contact formulation using penalty method was then presented and verified with an example of bar impacting a rigid wall. Penalty method was found to give good accuracy provided a suitable penalty parameter was chosen. Finally, three composite failure theories/criteria were presented; namely, Maximum stress, Hashin, and LaRC02. Failure envelopes were calculated for UD-GFRP found in literature. This ensured accurate failure calculations across different loading scenarios.

Chapter 4 presented the development and validation of steady-state orthogonal cutting model of unidirectional composites: The variational principle was used to derive the system equations. A novel frictional contact calculations based on penalty method was presented. Workpiece material was modelled using single-phase, orthotropic linear elastic model and failure was calculated based on dual stress-based criteria. Progressive failure was modelled using selective stiffness degradation. The resulting nonlinear system equations were solved using Full Newton-Raphson algorithm with displacement control and step bisection. The model was set to compare against experimental work of Bhatnagar et al. [5] and other FEM simulations found in literature. Cutting and thrust forces were compared for fibre orientations $0 \leq \theta^o \leq 90$ and for three rake angles$\gamma^o = [0,\ 5,\ 10]$. Finally, numerical investigations were carried out to check the convergence of the model and effect of DoI size and weight functions on the results.

In Chapter 5, a dynamic model for orthogonal cutting was developed. Several enhancements over the steady-state model were incorporated. The mathematical model was developed from the virtual work principle and Updated Lagrangian formulation. MLS shape functions were constructed using a regularised weight function that approximately possesses interpolation property. This was inherited by the shape function and therefore direct imposition of the displacement boundary conditions was possible. Composites were modelled using a novel Saint Venant-Kirchhoff model. It is a finite strain formulation of nonlinear elasticity and therefore presents a more general approach to composite response under machining. Furthermore, composite failure was calculated using three failure theories that were described in Chapter 3. A novel frictional contact algorithm was presented. It was based on central differencing of contacting nodes. The discrete force components were similar to that of penalty formulation but avoided the need for choosing penalty parameter. Temporal integration was performed using explicit, CDM algorithm combined with diagonal mass matrix to avoid coefficients matrix inversion. The model was set-up to compare against experiments shown in Chapter 6 for orientations $0 < \theta^o < 90$ and $\gamma = 0^o$.

In Chapter 6, orthogonal cutting experiments on UD-GFRP were carried out over three phases. In Phase I, orthogonal cutting experiments were carried out using shaping machine to study cutting forces, surface integrity and chip formation. Process variables were fibre orientation angle, rake angle, depth of cut and cutting speed. In Phase II, the effect of fibre volume fraction on cutting forces was investigated and empirical model was proposed using multivariate polynomial regression . Phase III aimed at generating validation data for the dynamic model. Test was carried out on vertical milling CNC centre. Seven orientations in the range $0 \leq \theta^o \leq 90$ were investigated and each test was repeated three times to ensure accuracy of the results. Furthermore, high speed videos of the chip formation were obtained and analysed.

7.3 Conclusions

Some conclusions that can be drawn from this research are summarised below:

Modelling

- The viability of the EFG to simulate orthogonal cutting of unidirectional composites was established in steady state and dynamic cases as shown in Chapters 4 and 5 respectively. The effectiveness of the model resided in the simple and automated pre-processing. The method was not susceptible to approximation errors in locations of large deformations when shape functions were updated during time integration.

- The predictive capability of the dynamic model was better than steady-state model; however, runtime of the dynamic model was an order of magnitude higher than steady-state model. This was mainly due to the very small time step required to maintain stability of the CDM algorithm.

- The steady-state and dynamic models were capable of predicting the cutting forces accurately. The strong dependency of the force on fibre orientation was predicted and validated in the range $0 \leq \theta^o \leq 90$.

- Thrust force was significantly underestimated in both steady state and dynamic models; however, this was also observed in FEM literature, which indicate that this limitation is not related to the EFG. The inability to capture the bouncing-back effect in continuum-based models is probably a significant factor contributing to this issue.

- Chip formation in the studied range mainly consisted of two modes of failure: compression failure ahead of the cutting edge extending along the cutting plane and shear-dominated failure propagating towards the free edge along the direction of the fibres. LaRC02 failure theory was found to predict compression-induced failure that Maximum stress and Hashin theories did not predict.

- Size of DoI was the most influential meshfree parameter on cutting forces. It should be chosen as small as possible while maintaining the invertibility of the moment matrix during shape functions construction. Weight function was less influential parameter.

Experiments

- Fibre orientation and depth of cut were generally the most significant factors affecting cutting forces and surface integrity in orthogonal cutting experiments of UD-FRPs.

- Fibre volume fraction was found to be statistically significant material parameter affecting cutting forces. Nearly linear increase of cutting forces was observed with increased fibre content in the studied range $45\% \leq V_f \leq 65\%$.

- Obtaining an acceptable quality of machined surface using single point, orthogonal cutting process seems limited to a narrow range of fibre orientations $0 \leq \theta^o \leq 60$ in the studied range of parameters. Using tools with positive rake angles and reducing depth of cut can improve the quality of the machined surface.

- Ensuring accurate force data requires test repetition due to the large variability of material properties.

7.4 Contribution, Achievements and Impact

The major accomplishments of this research work can be divided into two components: contribution in numerical modelling and in experimental work

- *Numerically:* Extension of the EFG to modelling of machining composites. To the author's best knowledge, EFG has not been used in modelling of machining of any material. It proved to be a viable tool for modelling of machining composites. Simulations were carried out using steady-state and dynamic models with several advanced and novel features, especially in material and contact modelling.
- *Experimentally:* Generating sizeable amount of orthogonal cutting data that could be used for model validation and to guide parameters selection in other experiments. Furthermore, the dependency of cutting forces on fibre volume fraction was established and put into an empirical model.

Contributions in modelling were possible due to the extensive development of the inhouse MATLAB code. Great improvements in efficiency were possible since the code was specifically built and optimised for cutting composites. Furthermore, the code was built in a modular way, which allows for easy addition of new features/functions. The major achievements in coding can be summarised as follows:

- Building a computational template for orthogonal cutting process. This greatly improved the flexibility of the code. Changing of cutting conditions and the geometry of the tool and workpiece was achieved by changing entries in the input file without resorting to case-specific coding.
- The nonlinear solver was developed to be compatible with Updated and Total Lagrangian formulations, allowing for greater flexibility in choosing the suitable for-

mulation. Furthermore, updating the shape functions during time integration can be done at arbitrary intervals. This reduced the computational burden of updating the shape functions every time step in the dynamic model.

- The distribution of nodes in the domain, construction of background cells and Gauss quadrature points was coded for uniform and non-uniform distributions.
- Coding a robust procedure to construct the DoI. This procedure is suitable for uniform and arbitrary nodal distribution alike and guarantees that the minimum number of support nodes exist for each integration point in the domain. Furthermore, this procedure is readily usable in h-adaptive codes.
- Utilising vectorisation techniques and assembling the system equations using sparse matrices. These features greatly improved the computational efficiency of the code.
- Using of variable time step, this meant that the maximum stable time step is used throughout the simulations.
- Development of visibility criteria algorithm suitable for the cutting problem, where the approximate location of discontinuities is known a priori. This avoided brute force procedure and greatly improved the efficiency of the algorithm.
- Development of two displacement-based contact algorithms. The first is based on penalty formulation and is suitable for steady state modelling and the second is based on finite differencing at the contact interface and is suitable for dynamic models. It was noted that the finite difference formulation reduces to penalty with a calculated penalty parameter. This circumnavigated the need for choosing a penalty parameter as in the steady state model without increasing the unknowns in the system. The contact calculations code was re-written so as to reflect this equivalence and now the same function can be used in explicit or implicit solvers.
- The development of a novel nonlinear elastic material model based on Kirchhoff model suitable for orthotropic materials. This model enhanced the accuracy and

stability of the calculations in the dynamic case.

- Although this study was focused on GFRP panels, the code is readily capable of modelling other brittle or quasi-brittle orthotropic materials such as other FRPs, masonry and some kinds of rocks.
- Significant effort was devoted to modelling progressive failure of composites. Three failure criteria were coded, including LaRC02, which was not used before in studying machining of composites and proved to have better predictive capabilities in chip formation than Hashin or Maximum stress criteria. Computationally, all three models were integrated into a progressive failure algorithm that permits adding new failure criteria in the future.

The impact of this research can be categorised into scholarly and practical impact. In the former, the results and insights gained from this research were disseminated through several scholarly publications that are listed in Page (iv). Practically, the potential impact of developing this meshfree model is to bring the ability of modelling of machining to the shop-floor. Constructing the mesh for machining simulations usually requires significant experience and man-hours, which limits the utility of such models. The proposed model (with some enhancements discussed in the future work section) could be utilised to investigate cutting parameters by engineers that have limited experience in numerical modelling. Generally, EFG is more computationally expensive than FEM. However, the engineer's time is more important than machine time, which give a good justification for the adoption of EFG despite the need for more computational resources.

7.5 Critical Appraisal and Future Work

Finally, some limitations of this research are discussed along with recommendations for future work based on addressing these limitations.

The model was limited to 2D analysis. This is advantageous in research work; however, given that machining processes are mostly 3D, extending the model in the third dimension is essential to gain practical utility. This requires adding capabilities for constructing DoI and calculating shape functions in 3D, modelling of multidirectional FRPs and addition of 3D failure theories to predict out-of-plane damage modes such as delamination.

Thermal effects were not included in the model. This is justified since the composite chips are discontinuous and therefore temperature rise would not be severe as in cutting of ductile materials with continuous chips. However, reaching glass transition temperature of matrix material could cause damage in the machined surface. Glass transition temperature for epoxy resin is $180\ C^o$. Santiuste et al. reported [142] that machined surface suffered from mechanical and thermal damage. In addition, in certain cases, depth of thermal damage could exceed mechanical damage, which indicate the importance of including thermal effects.

Single-phase material models were used throughout this work. As discussed in Chapter 2, multi-phase material models have advantage in revealing more failure mechanisms than is possible with single-phase models. However, multi-phase modelling requires significantly more pre-processing time, input data and computational resources. Even using hybrid models addresses only the computational cost aspect. As such, the choice of single vs multiphase models should be guided by the required outputs and available resources. For example, as was demonstrated in Chapters 4 and 5, acceptable prediction of cutting forces can be obtained using single phase models. The pre-processing of these models was simple and automated, which might be advantageous in practical applications.

Finally, some considerations relating to numerical implementation are presented:

- The code was developed for serial processing. Re-writing the code for parallel processing is a priority future work for the author, especially the dynamic model. However, parallelisation of meshfree domains is more challenging due to the diffuse nature of approximation.

- The integration was performed using Gaussian background cells. This is simple to implement but expensive and requires a construction of background mesh. Alternatively, other integration methods could be used in future work such as stress point integration, nodal integration or stabilised conforming nodal integration.

- Accuracy of calculations and simplification of nodal distribution could be achieved using adaptive procedure. This requires implementing error estimation and nodal refinement strategies. EFG is suitable for adaptivity since remeshing is not required after adding or deleting nodes from the domain.

- Improvement in computational runtime could be achieved by utilising the Total Lagrangian (TL) formulation. This minimises shape function update during time integration. However, contact calculations should be performed using Updated Lagrangian procedure. One possibility to resolve this might be using UL formulation near the contacting boundaries and TL for the rest of the domain.

References

[1] J. Y. Sheikh-Ahmad, *Machining of polymer composites*. Springer, 2009.

[2] D. Gay, *Composite materials: design and applications*. CRC press, 3 ed., 2015.

[3] D. Wang, M. Ramulu, and D. Arola, "Orthogonal cutting mechanisms of graphite/epoxy composite. part i: unidirectional laminate," *International Journal of Machine Tools and Manufacture*, vol. 35, no. 12, pp. 1623–1638, 1995.

[4] G.-R. Liu and Y.-T. Gu, *An introduction to meshfree methods and their programming*. Springer, 2005.

[5] N. Bhatnagar, D. Nayak, I. Singh, H. Chouhan, and P. Mahajan, "Determination of machining-induced damage characteristics of fiber reinforced plastic composite laminates," *Materials and Manufacturing Processes*, vol. 19, no. 6, pp. 1009–1023, 2004.

[6] D. Nayak, N. Bhatnagar, and P. Mahajan, "Machining studies of ud-frp composites part 2: finite element analysis," *Machining Science and Technology*, vol. 9, no. 4, pp. 503–528, 2005.

[7] K. A. Calzada, S. G. Kapoor, R. E. DeVor, J. Samuel, and A. K. Srivastava, "Modeling and interpretation of fiber orientation-based failure mechanisms in machining of carbon fiber-reinforced polymer composites," *Journal of Manufacturing Processes*, vol. 14, no. 2, pp. 141–149, 2012.

[8] T. Belytschko and M. Fleming, "Smoothing, enrichment and contact in the element-free galerkin method," *Computers & Structures*, vol. 71, no. 2, pp. 173–195, 1999.

[9] P. Soden, M. Hinton, and A. Kaddour, "A comparison of the predictive capabilities of current failure theories for composite laminates," *Composites Science and Technology*, vol. 58, no. 7, pp. 1225–1254, 1998.

[10] P. Soden, M. Hinton, and A. Kaddour, "Biaxial test results for strength and deformation of a range of e-glass and carbon fibre reinforced composite laminates: failure exercise benchmark data," *Composites Science and Technology*, vol. 62, no. 12, pp. 1489–1514, 2002.

[11] P. Soden, M. Hinton, and A. Kaddour, "Lamina properties, lay-up configurations and loading conditions for a range of fibre-reinforced composite laminates," *Composites Science and Technology*, vol. 58, no. 7, pp. 1011–1022, 1998.

[12] M. Hinton, A. Kaddour, and P. Soden, "A comparison of the predictive capabilities of current failure theories for composite laminates, judged against experimental evidence," *Composites Science and Technology*, vol. 62, no. 12, pp. 1725–1797, 2002.

[13] M. Hinton and A. Kaddour, "The background to the second world-wide failure exercise," *Journal of composite materials*, vol. 46, no. 19-20, pp. 2283–2294, 2012.

[14] A. Kaddour and M. Hinton, "Benchmarking of triaxial failure criteria for composite laminates: comparison between models of 'part (a)'of 'wwfe-ii'," *Journal of Composite Materials*, vol. 46, no. 19-20, pp. 2595–2634, 2012.

[15] A. Kaddour, M. Hinton, P. Smith, and S. Li, "The background to the third world-wide failure exercise," *Journal of Composite Materials*, vol. 47, no. 20-21, pp. 2417–2426, 2013.

[16] A. Kaddour, M. Hinton, P. Smith, and S. Li, "A comparison between the predictive capability of matrix cracking, damage and failure criteria for fibre reinforced composite laminates: Part a of the third world-wide failure exercise," *Journal of Composite Materials*, vol. 47, no. 20-21, pp. 2749–2779, 2013.

[17] M. C. Shaw and J. Cookson, *Metal cutting principles*, vol. 2. Oxford university press New York, 2005.

[18] J. R. Davis, "Asm handbook, volume 16: Machining," *ASM International Handbook Committee, ASM International, Electronic*, 1989.

[19] A. P. Markopoulos, *Finite element method in machining processes*. Springer Science & Business Media, 2012.

[20] M. E. Merchant, "Mechanics of the metal cutting process. i. orthogonal cutting and a type 2 chip," *Journal of applied physics*, vol. 16, no. 5, pp. 267–275, 1945.

[21] R. Teti, "Machining of composite materials," *CIRP Annals-Manufacturing Technology*, vol. 51, no. 2, pp. 611–634, 2002.

[22] R. M. Jones, *Mechanics of composite materials*. CRC press, 1998.

[23] A. K. Kaw, *Mechanics of composite materials*. CRC press, 2005.

[24] M. Holmes, "Global carbon fibre market remains on upward trend," *Reinforced Plastics*, vol. 58, no. 6, pp. 38–45, 2014.

[25] M. Holmes, "Continued growth for european grp market," *Reinforced Plastics*, vol. 58, no. 6, pp. 28–30, 2014.

[26] R. Talreja, "Assessment of the fundamentals of failure theories for composite materials," *Composites Science and Technology*, vol. 105, pp. 190–201, 2014.

[27] I. Daniel, "Failure of composite materials," *Strain*, vol. 43, no. 1, pp. 4–12, 2007.

[28] G. Caprino and A. Langella, "Analysing cutting forces in machining processes for polymer-based composites," *Machining Technology for Composite Materials: Principles and Practice*, p. 75, 2012.

[29] G. Caprino and L. Nele, "Cutting forces in orthogonal cutting of unidirectional gfrp composites," *Journal of engineering materials and technology*, vol. 118, no. 3, pp. 419–425, 1996.

[30] N. Bhatnagar, N. Ramakrishnan, N. Naik, and R. Komanduri, “On the machining of fiber reinforced plastic (frp) composite laminates,” *International Journal of Machine Tools and Manufacture*, vol. 35, no. 5, pp. 701–716, 1995.

[31] D. Nayak, N. Bhatnagar, and P. Mahajan, “Machining studies of uni-directional glass fiber reinforced plastic (ud-gfrp) composites part 1: effect of geometrical and process parameters,” *Machining science and technology*, vol. 9, no. 4, pp. 481–501, 2005.

[32] X. Wang and L. Zhang, “An experimental investigation into the orthogonal cutting of unidirectional fibre reinforced plastics,” *International journal of machine tools and manufacture*, vol. 43, no. 10, pp. 1015–1022, 2003.

[33] H. Agarwal, A. Amaranath, Y. Jamthe, and S. Gururaja, “An investigation of cutting mechanisms and strain fields during orthogonal cutting in cfrps,” *Machining Science and Technology*, vol. 19, no. 3, pp. 416–439, 2015.

[34] G. Rao, P. Mahajan, and N. Bhatnagar, “Micro-mechanical modeling of machining of frp composites–cutting force analysis,” *Composites science and technology*, vol. 67, no. 3, pp. 579–593, 2007.

[35] D. Arola, M. Ramulu, and D. Wang, “Chip formation in orthogonal trimming of graphite/epoxy composite,” *Composites Part A: applied science and manufacturing*, vol. 27, no. 2, pp. 121–133, 1996.

[36] M. Ramulu, “Machining and surface integrity of fibre-reinforced plastic composites,” *Sadhana*, vol. 22, no. 3, pp. 449–472, 1997.

[37] V. Madhavan, G. Lipczynski, B. Lane, and E. Whitenton, “Fiber orientation angle effects in machining of unidirectional cfrp laminated composites,” *Journal of Manufacturing Processes*, vol. 20, pp. 431–442, 2015.

[38] H. Li, X. Qin, G. He, Y. Jin, D. Sun, and M. Price, “Investigation of chip formation and fracture toughness in orthogonal cutting of ud-cfrp,” *The International Journal of Advanced Manufacturing Technology*, vol. 82, no. 5-8, pp. 1079–1088, 2016.

[39] V. Lopresto, L. Santo, G. Caprino, and I. De Iorio, "Mechanism of chip generation in orthogonal machining of unidirectional carbon fibre reinforced plastics," in *Prime 2001 Conference, Sestri Levante (Ge), Italy*, pp. 19–22, 2001.

[40] J. Peiro and S. Sherwin, "Handbook of materials modeling. volume i: Methods and models," *Department of Aeronautics, Imperial College, London, UK*, pp. 1–32, 2005.

[41] K.-J. Bathe, *Finite element procedures*. Klaus-Jurgen Bathe, 2006.

[42] G.-R. Liu, *Meshfree methods: moving beyond the finite element method*. CRC press, 2010.

[43] P. Arrazola, T. Özel, D. Umbrello, M. Davies, and I. Jawahir, "Recent advances in modelling of metal machining processes," *CIRP Annals-Manufacturing Technology*, vol. 62, no. 2, pp. 695–718, 2013.

[44] A. Huerta, T. Belytschko, S. Fernández-Méndez, and T. Rabczuk, "Meshfree methods," 2004.

[45] T. Belytschko, Y. Krongauz, D. Organ, M. Fleming, and P. Krysl, "Meshless methods: an overview and recent developments," *Computer methods in applied mechanics and engineering*, vol. 139, no. 1, pp. 3–47, 1996.

[46] G. Liu, "An overview on meshfree methods: for computational solid mechanics," *International Journal of Computational Methods*, vol. 13, no. 05, p. 1630001, 2016.

[47] S. Li and W. K. Liu, "Meshfree and particle methods and their applications," *Applied Mechanics Reviews*, vol. 55, no. 1, pp. 1–34, 2002.

[48] T. Belytschko, Y. Y. Lu, and L. Gu, "Element-free galerkin methods," *International journal for numerical methods in engineering*, vol. 37, no. 2, pp. 229–256, 1994.

[49] C. Duarte, O. Hamzeh, T. Liszka, and W. Tworzydlo, "A generalized finite element method for the simulation of three-dimensional dynamic crack propagation," *Computer Methods in Applied Mechanics and Engineering*, vol. 190, no. 15, pp. 2227–2262, 2001.

[50] S. R. Idelsohn and E. Onate, "To mesh or not to mesh. that is the question…," *Computer methods in applied mechanics and engineering*, vol. 195, no. 37, pp. 4681–4696, 2006.

[51] K. Liew, T. Ng, and Y. Wu, "Meshfree method for large deformation analysis–a reproducing kernel particle approach," *Engineering Structures*, vol. 24, no. 5, pp. 543–551, 2002.

[52] V. P. Nguyen, T. Rabczuk, S. Bordas, and M. Duflot, "Meshless methods: a review and computer implementation aspects," *Mathematics and computers in simulation*, vol. 79, no. 3, pp. 763–813, 2008.

[53] A. Zahedi, S. Li, A. Roy, V. Babitsky, and V. V. Silberschmidt, "Application of smooth-particle hydrodynamics in metal machining," in *Journal of Physics: Conference Series*, vol. 382, p. 012017, IOP Publishing, 2012.

[54] J. Limido, C. Espinosa, M. Salaün, and J.-L. Lacome, "Sph method applied to high speed cutting modelling," *International journal of mechanical sciences*, vol. 49, no. 7, pp. 898–908, 2007.

[55] M. F. Villumsen and T. G. Fauerholdt, "Simulation of metal cutting using smooth particle hydrodynamics," *Tagungsberichtsband zum LS-DYNA Anwenderforum, Bamberg*, vol. 30, no. 01.10, p. 2008, 2008.

[56] E. Bagci, "3-d numerical analysis of orthogonal cutting process via mesh-free method," *Int J Phys Sci*, vol. 6, no. 6, pp. 1267–1282, 2011.

[57] U. Heisel, W. Zaloga, D. Krivoruchko, M. Storchak, and L. Goloborodko, "Modelling of orthogonal cutting processes with the method of smoothed particle hydrodynamics," *Production Engineering*, vol. 7, no. 6, pp. 639–645, 2013.

[58] M. Madaj and M. Píška, "On the sph orthogonal cutting simulation of a2024-t351 alloy," *Procedia CIRP*, vol. 8, pp. 151–156, 2013.

[59] P. Eberhard and T. Gaugele, “Simulation of cutting processes using mesh-free lagrangian particle methods,” *Computational Mechanics*, vol. 51, no. 3, pp. 261–278, 2013.

[60] P. Cleary, M. Prakash, and J. Ha, “Novel applications of smoothed particle hydrodynamics (sph) in metal forming,” *Journal of materials processing technology*, vol. 177, no. 1, pp. 41–48, 2006.

[61] E. Barbieri and M. Meo, “A meshfree penalty-based approach to delamination in composites,” *Composites Science and Technology*, vol. 69, no. 13, pp. 2169–2177, 2009.

[62] E. Barbieri, *Meshfree and Partition of Unity Methods for the Analysis of Composite Materials*. PhD thesis, University of Bath, 2010.

[63] E. Barbieri and M. Meo, “A meshless cohesive segments method for crack initiation and propagation in composites,” *Applied Composite Materials*, vol. 18, no. 1, pp. 45–63, 2011.

[64] B. Nayroles, G. Touzot, and P. Villon, “Generalizing the finite element method: diffuse approximation and diffuse elements,” *Computational mechanics*, vol. 10, no. 5, pp. 307–318, 1992.

[65] T. Belytschko, Y. Lu, L. Gu, and M. Tabbara, “Element-free galerkin methods for static and dynamic fracture,” *International Journal of Solids and Structures*, vol. 32, no. 17, pp. 2547–2570, 1995.

[66] T. Belytschko, Y. Y. Lu, and L. Gu, “Crack propagation by element-free Galerkin methods,” *Engineering Fracture Mechanics*, vol. 51, no. 2, pp. 295–315, 1995.

[67] T. Belytschko and M. Tabbara, “Dynamic fracture using element-free galerkin methods,” *International Journal for Numerical Methods in Engineering*, vol. 39, no. 6, pp. 923–938, 1996.

[68] T. Belytschko, Y. Y. Lu, L. Gu, and M. Tabbara, "Element-free galerkin methods for static and dynamic fracture," *International Journal of Solids and Structures*, vol. 32, pp. 2547–2570, sep 1995.

[69] S. Beissel and T. Belytschko, "Nodal integration of the element-free Galerkin method," *Computer Methods in Applied Mechanics and Engineering*, vol. 139, no. 1, pp. 49–74, 1996.

[70] T. Belytschko, P. Krysl, and Y. Krongauz, "A three dimensional explicit element free galerkin method," *International Journal for Numerical Methods in Fluids*, vol. 24, no. 12, pp. 1253–1270, 1997.

[71] G. Li and T. Belytschko, "Element-free galerkin method for contact problems in metal forming analysis," *Engineering Computations*, vol. 18, no. 1/2, pp. 62–78, 2001.

[72] J.-P. Ponthot and T. Belytschko, "Arbitrary lagrangian-eulerian formulation for element-free galerkin method," *Computer methods in applied mechanics and engineering*, vol. 152, no. 1, pp. 19–46, 1998.

[73] T. Belytschko, Y. Krongauz, M. Fleming, D. Organ, and W. K. Snm Liu, "Smoothing and accelerated computations in the element free Galerkin method," *Journal of Computational and Applied Mathematics*, vol. 74, no. 1–2, pp. 111–126, 1996.

[74] J. Belinha and L. Dinis, "Analysis of plates and laminates using the element-free galerkin method," *Computers & structures*, vol. 84, no. 22, pp. 1547–1559, 2006.

[75] Most and Bucher, "MLS-Weighting Function For EFG Method Which Almost Fulfills Essential Boundary Conditions," *Structural Engineering and Mechanics*, 2005.

[76] H. Askes, R. de Borst, and O. Heeres, "Conditions for locking-free elasto-plastic analyses in the Element-Free Galerkin method," *Computer Methods in Applied Mechanics and Engineering*, vol. 173, pp. 99–109, apr 1999.

[77] K. Liew, Y. Cheng, and S. Kitipornchai, "Boundary element-free method (befm) for two-dimensional elastodynamic analysis using laplace transform," *International journal for numerical methods in engineering*, vol. 64, no. 12, pp. 1610–1627, 2005.

[78] X. Zhang, P. Zhang, and L. Zhang, "An improved meshless method with almost interpolation property for isotropic heat conduction problems," *Engineering Analysis with Boundary Elements*, vol. 37, no. 5, pp. 850–859, 2013.

[79] R. Cheng and K. Liew, "Analyzing modified equal width (MEW) wave equation using the improved element-free Galerkin method," *Engineering Analysis with Boundary Elements*, vol. 36, no. 9, pp. 1322–1330, 2012.

[80] M. J. Peng, R. X. Li, and Y. M. Cheng, "Analyzing three-dimensional viscoelasticity problems via the improved element-free Galerkin (IEFG) method," *Engineering Analysis with Boundary Elements*, vol. 40, pp. 104–113, 2014.

[81] Z. Zhang, P. Zhao, and K. M. Liew, "Improved element-free Galerkin method for two-dimensional potential problems," *Engineering Analysis with Boundary Elements*, vol. 33, pp. 547–554, apr 2009.

[82] Z. Zhang, S. Y. Hao, K. M. Liew, and Y. M. Cheng, "The improved element-free Galerkin method for two-dimensional elastodynamics problems," *Engineering Analysis with Boundary Elements*, vol. 37, pp. 1576–1584, dec 2013.

[83] H. Ren and Y. Cheng, "The interpolating element-free Galerkin (IEFG) method for two-dimensional potential problems," *Engineering Analysis with Boundary Elements*, vol. 36, no. 5, pp. 873–880, 2012.

[84] M. Abbaszadeh and M. Dehghan, "A meshless numerical procedure for solving fractional reaction subdiffusion model via a new combination of alternating direction implicit (ADI) approach and interpolating element free Galerkin (EFG) method," *Computers & Mathematics with Applications*, vol. 70, pp. 2493–2512, nov 2015.

[85] Y. M. Cheng, F. N. Bai, and M. J. Peng, "A novel interpolating element-free Galerkin (IEFG) method for two-dimensional elastoplasticity," *Applied Mathematical Modelling*, vol. 38, pp. 5187–5197, nov 2014.

[86] M. Dehghan, M. Abbaszadeh, and A. Mohebbi, "The use of interpolating element-free Galerkin technique for solving 2D generalized Benjamin–Bona–Mahony–Burgers and regularized long-wave equations on non-rectangular domains with error estimate," *Journal of Computational and Applied Mathematics*, vol. 286, pp. 211–231, oct 2015.

[87] Z. Ullah, W. M. Coombs, and C. E. Augarde, "An adaptive finite element/meshless coupled method based on local maximum entropy shape functions for linear and nonlinear problems," *Computer Methods in Applied Mechanics and Engineering*, vol. 267, no. 0, pp. 111–132, 2013.

[88] H.-J. Chung and T. Belytschko, "An error estimate in the efg method," *Computational mechanics*, vol. 21, no. 2, pp. 91–100, 1998.

[89] M. Puso, J. Chen, E. Zywicz, and W. Elmer, "Meshfree and finite element nodal integration methods," *International Journal for Numerical Methods in Engineering*, vol. 74, no. 3, pp. 416–446, 2008.

[90] Y. Liu and T. Belytschko, "A new support integration scheme for the weakform in mesh-free methods," *International Journal for Numerical Methods in Engineering*, vol. 82, no. 6, pp. 699–715, 2010.

[91] Y. Liu and T. Belytschko, "A new support integration scheme for the weakform in mesh-free methods," *International journal for numerical methods in engineering*, vol. 82, no. 6, pp. 699–715, 2010.

[92] D. Racz and T. Q. Bui, "Novel adaptive meshfree integration techniques in meshless methods," *International Journal for Numerical Methods in Engineering*, vol. 90, no. 11, pp. 1414–1434, 2012.

[93] G. Liu and Z. Tu, "An adaptive procedure based on background cells for meshless methods," *Computer Methods in Applied Mechanics and Engineering*, vol. 191, no. 17, pp. 1923–1943, 2002.

[94] M. Griebel and M. A. Schweitzer, "A particle-partition of unity method–part ii: Efficient cover construction and reliable integration," *SIAM Journal on Scientific Computing*, vol. 23, no. 5, pp. 1655–1682, 2002.

[95] D. Arola and M. Ramulu, "Orthogonal cutting of fiber-reinforced composites: a finite element analysis," *International journal of mechanical sciences*, vol. 39, no. 5, pp. 597–613, 1997.

[96] D. Arola, M. Sultan, and M. Ramulu, "Finite element modeling of edge trimming fiber reinforced plastics," *Journal of manufacturing science and engineering*, vol. 124, no. 1, pp. 32–41, 2002.

[97] G. Rao, P. Mahajan, and N. Bhatnagar, "Three-dimensional macro-mechanical finite element model for machining of unidirectional-fiber reinforced polymer composites," *Materials Science and Engineering: A*, vol. 498, no. 1, pp. 142–149, 2008.

[98] C. R. Dandekar and Y. C. Shin, "Multiphase finite element modeling of machining unidirectional composites: prediction of debonding and fiber damage," *Journal of Manufacturing Science and Engineering*, vol. 130, no. 5, p. 051016, 2008.

[99] C. Santiuste, X. Soldani, and M. H. Miguélez, "Machining fem model of long fiber composites for aeronautical components," *Composite structures*, vol. 92, no. 3, pp. 691–698, 2010.

[100] C. Santiuste, H. Miguélez, and X. Soldani, "Out-of-plane failure mechanisms in lfrp composite cutting," *Composite Structures*, vol. 93, no. 11, pp. 2706–2713, 2011.

[101] X. Soldani, C. Santiuste, A. Muñoz-Sánchez, and M. Miguélez, "Influence of tool geometry and numerical parameters when modeling orthogonal cutting of lfrp

composites," *Composites Part A: Applied Science and Manufacturing*, vol. 42, no. 9, pp. 1205–1216, 2011.

[102] S. Zenia, L. B. Ayed, M. Nouari, and A. Delamézière, "An elastoplastic constitutive damage model to simulate the chip formation process and workpiece subsurface defects when machining cfrp composites," *Procedia CIRP*, vol. 31, pp. 100–105, 2015.

[103] A. Abena, S. L. Soo, and K. Essa, "Modelling the orthogonal cutting of ud-cfrp composites: Development of a novel cohesive zone model," *Composite Structures*, vol. 168, pp. 65–83, 2017.

[104] D. Wang, X. He, Z. Xu, W. Jiao, F. Yang, L. Jiang, L. Li, W. Liu, and R. Wang, "Study on damage evaluation and machinability of ud-cfrp for the orthogonal cutting operation using scanning acoustic microscopy and the finite element method," *Materials*, vol. 10, no. 2, p. 204, 2017.

[105] C. Gao, J. Xiao, J. Xu, and Y. Ke, "Factor analysis of machining parameters of fiber-reinforced polymer composites based on finite element simulation with experimental investigation," *The International Journal of Advanced Manufacturing Technology*, vol. 83, no. 5-8, pp. 1113–1125, 2016.

[106] D. Iliescu, D. Gehin, I. Iordanoff, F. Girot, and M. Gutiérrez, "A discrete element method for the simulation of cfrp cutting," *Composites Science and Technology*, vol. 70, no. 1, pp. 73–80, 2010.

[107] I. Shchurov, A. Nikonov, I. Boldyrev, and D. Ardashev, "Sph modeling of chip formation in cutting unidirectional fiber-reinforced composite," *Russian Engineering Research*, vol. 36, no. 10, pp. 883–887, 2016.

[108] F. Kahwash, I. Shyha, and A. Maheri, "Meshfree formulation for modelling of orthogonal cutting of composites," *Composite Structures*, vol. 166, pp. 193–201, 2017.

[109] M. Mahdi and L. Zhang, “An adaptive three-dimensional finite element algorithm for the orthogonal cutting of composite materials,” *Journal of Materials Processing Technology*, vol. 113, no. 1, pp. 368–372, 2001.

[110] A. Mkaddem, I. Demirci, and M. E. Mansori, “A micro–macro combined approach using fem for modelling of machining of frp composites: cutting forces analysis,” *Composites science and technology*, vol. 68, no. 15, pp. 3123–3127, 2008.

[111] A. Mkaddem and M. El Mansori, “Finite element analysis when machining ugf-reinforced pmcs plates: Chip formation, crack propagation and induced-damage,” *Materials & Design*, vol. 30, no. 8, pp. 3295–3302, 2009.

[112] L. Lasri, M. Nouari, and M. El Mansori, “Modelling of chip separation in machining unidirectional frp composites by stiffness degradation concept,” *Composites Science and Technology*, vol. 69, no. 5, pp. 684–692, 2009.

[113] S. Usui, J. Wadell, and T. Marusich, “Finite element modeling of carbon fiber composite orthogonal cutting and drilling,” *Procedia CIRP*, vol. 14, pp. 211–216, 2014.

[114] S. Zenia, L. B. Ayed, M. Nouari, and A. Delamézière, “Numerical analysis of the interaction between the cutting forces, induced cutting damage, and machining parameters of cfrp composites,” *The International Journal of Advanced Manufacturing Technology*, vol. 78, no. 1-4, pp. 465–480, 2015.

[115] C. R. Dandekar and Y. C. Shin, “Modeling of machining of composite materials: a review,” *International Journal of Machine tools and manufacture*, vol. 57, pp. 102–121, 2012.

[116] G. Venu Gopala Rao, P. Mahajan, and N. Bhatnagar, “Machining of ud-gfrp composites chip formation mechanism,” *Composites science and technology*, vol. 67, no. 11, pp. 2271–2281, 2007.

[117] A. Abena, S. L. Soo, and K. Essa, “A finite element simulation for orthogonal cutting of ud-cfrp incorporating a novel fibre-matrix interface model,” *Procedia CIRP*, vol. 31, pp. 539–544, 2015.

[118] R. Rentsch, O. Pecat, and E. Brinksmeier, “Macro and micro process modeling of the cutting of carbon fiber reinforced plastics using fem,” *Procedia engineering*, vol. 10, pp. 1823–1828, 2011.

[119] T. J. Hughes, J. A. Cottrell, and Y. Bazilevs, “Isogeometric analysis: Cad, finite elements, nurbs, exact geometry and mesh refinement,” *Computer methods in applied mechanics and engineering*, vol. 194, no. 39-41, pp. 4135–4195, 2005.

[120] V. Laš and R. Zemčík, “Progressive damage of unidirectional composite panels,” *Journal of Composite Materials*, vol. 42, no. 1, pp. 25–44, 2008.

[121] T. Belytschko, W. K. Liu, B. Moran, and K. Elkhodary, *Nonlinear finite elements for continua and structures*. John Wiley & Sons, 2013.

[122] J. Dolbow and T. Belytschko, “An introduction to programming the meshless element f reegalerkin method,” *Archives of Computational Methods in Engineering*, vol. 5, no. 3, pp. 207–241, 1998.

[123] G.-R. Liu, *Meshfree methods: moving beyond the finite element method*. Taylor & Francis, 2009.

[124] T. Belytschko, Y. Krongauz, M. Fleming, D. Organ, and W. K. S. Liu, “Smoothing and accelerated computations in the element free galerkin method,” *Journal of Computational and Applied Mathematics*, vol. 74, no. 1-2, pp. 111–126, 1996.

[125] S. Timoshenko, S. Timoshenko, and J. Goodier, *Theory of Elasticity, by S. Timoshenko and JN Goodier,...* McGraw-Hill book Company, 1951.

[126] R. De Borst, M. A. Crisfield, J. J. Remmers, and C. V. Verhoosel, *Nonlinear finite element analysis of solids and structures*. John Wiley & Sons, 2012.

[127] Z.-H. Zhong, *Finite element procedures for contact-impact problems*, vol. 7. Oxford university press Oxford, 1993.

[128] N.-H. Kim, *Introduction to nonlinear finite element analysis*. Springer, 2012.

[129] C. G. Dávila and P. P. Camanho, “Failure criteria for frp laminates in plane stress,” *NASA TM*, vol. 212663, no. 613, 2003.

[130] A. Puck and H. Schürmann, “Failure analysis of frp laminates by means of physically based phenomenological models,” *Composites Science and Technology*, vol. 58, no. 7, pp. 1045–1067, 1998.

[131] Z. Hashin, “Failure criteria for unidirectional fiber composites,” *Journal of applied mechanics*, vol. 47, no. 2, pp. 329–334, 1980.

[132] P. Wriggers, T. V. Van, and E. Stein, “Finite element formulation of large deformation impact-contact problems with friction,” *Computers & Structures*, vol. 37, no. 3, pp. 319–331, 1990.

[133] L. Zhao, N. Warrior, and A. Long, “Finite element modelling of damage progression in non-crimp fabric reinforced composites,” *Composites Science and Technology*, vol. 66, no. 1, pp. 36–50, 2006.

[134] L. Zhang, “Cutting composites: A discussion on mechanics modelling,” *Journal of Materials Processing Technology*, vol. 209, no. 9, pp. 4548–4552, 2009.

[135] T. Most and C. Bucher, “A moving least squares weighting function for the element-free galerkin method which almost fulfills essential boundary conditions,” *Structural Engineering and Mechanics*, vol. 21, no. 3, pp. 315–332, 2005.

[136] S. Li, D. Qian, W. K. Liu, and T. Belytschko, “A meshfree contact-detection algorithm,” *Computer methods in applied mechanics and engineering*, vol. 190, no. 24, pp. 3271–3292, 2001.

[137] G. T. Camacho and M. Ortiz, "Computational modelling of impact damage in brittle materials," *International Journal of solids and structures*, vol. 33, no. 20-22, pp. 2899–2938, 1996.

[138] L. Zhang, H. Zhang, and X. Wang, "A force prediction model for cutting unidirectional fibre-reinforced plastics," 2001.

[139] A. Mkaddem and M. El Mansori, "Finite element analysis when machining ugf-reinforced pmcs plates: Chip formation, crack propagation and induced-damage," *Materials & Design*, vol. 30, no. 8, pp. 3295–3302, 2009.

[140] I. Shyha, D. Aspinwall, S. L. Soo, and S. Bradley, "Drill geometry and operating effects when cutting small diameter holes in cfrp," *International journal of machine tools and manufacture*, vol. 49, no. 12, pp. 1008–1014, 2009.

[141] K. Palanikumar, "Modeling and analysis for surface roughness in machining glass fibre reinforced plastics using response surface methodology," *Materials & design*, vol. 28, no. 10, pp. 2611–2618, 2007.

[142] C. Santiuste, J. Díaz-Álvarez, X. Soldani, and H. Miguélez, "Modelling thermal effects in machining of carbon fiber reinforced polymer composites," *Journal of Reinforced Plastics and Composites*, vol. 33, no. 8, pp. 758–766, 2014.

Appendix A

Mechanical Tests Results for GFRP Samples

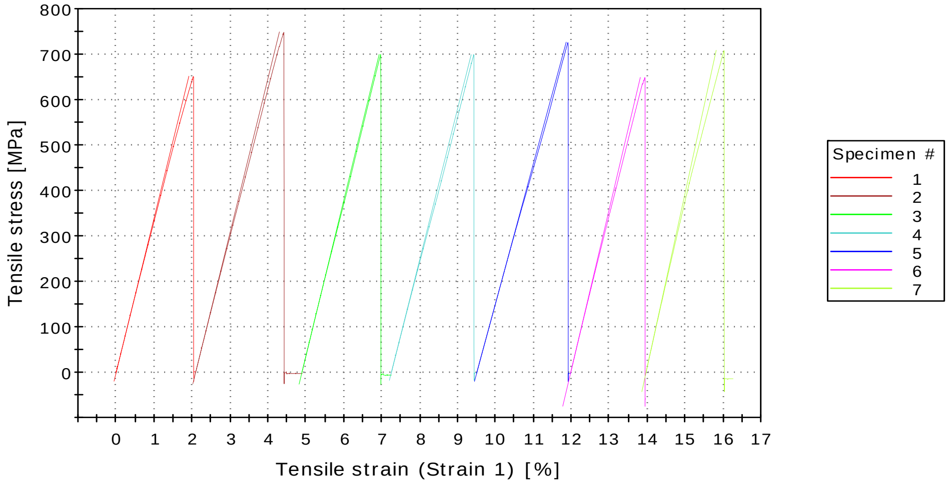

Figure A.1: Tensile test results at $\theta = 0^o$

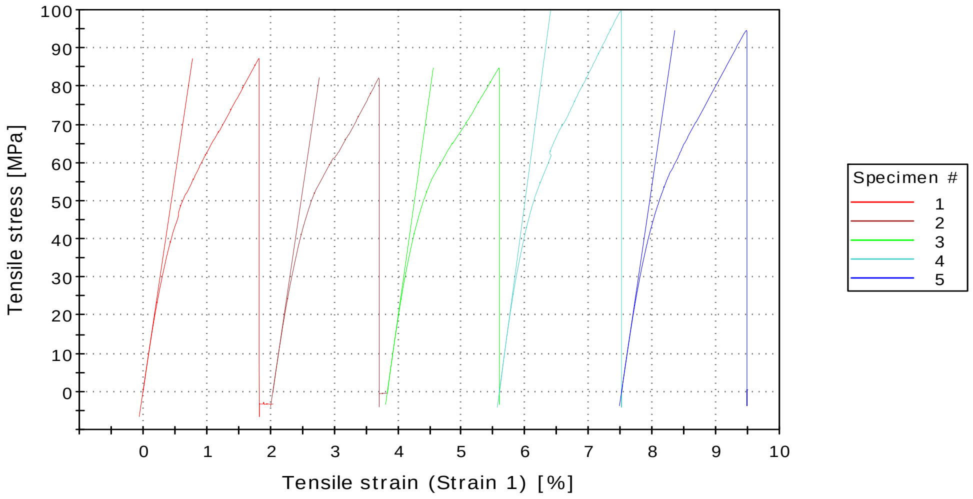

Figure A.2: Tensile test results at $\theta = 90^o$

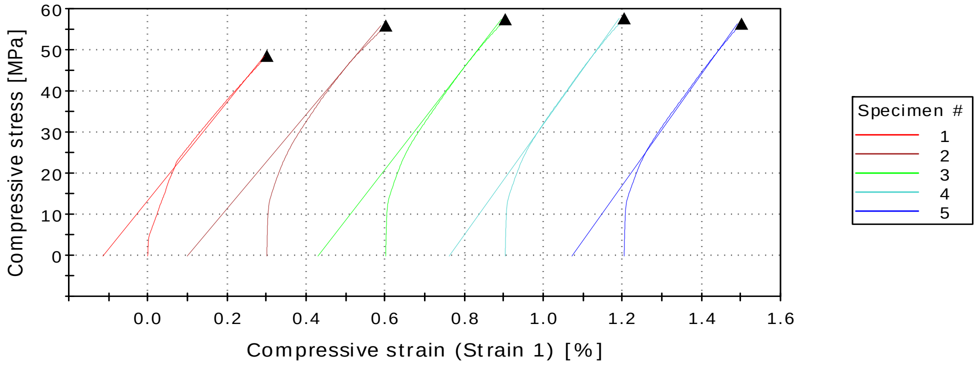

Figure A.3: Compressive Modulus at $\theta = 90^o$

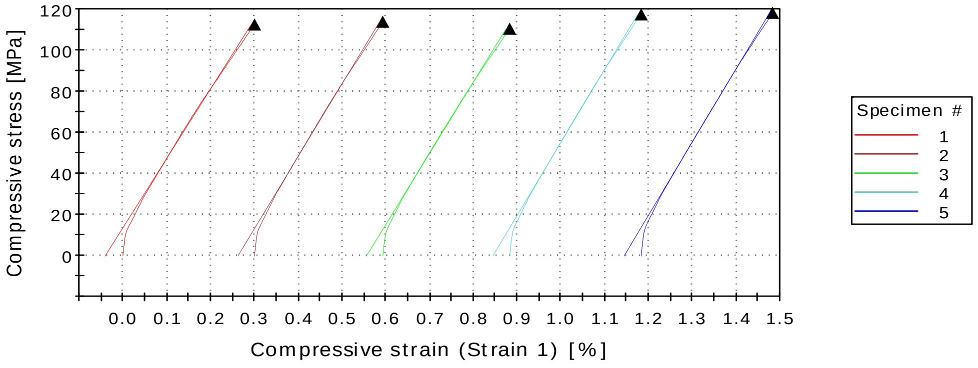

Figure A.4: Compressive Modulus at $\theta = 0^o$

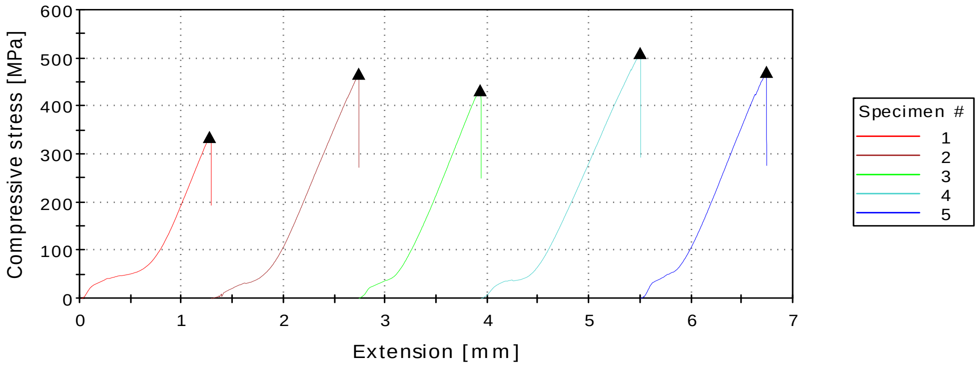

Figure A.5: Compressive Strength at $\theta = 0^o$

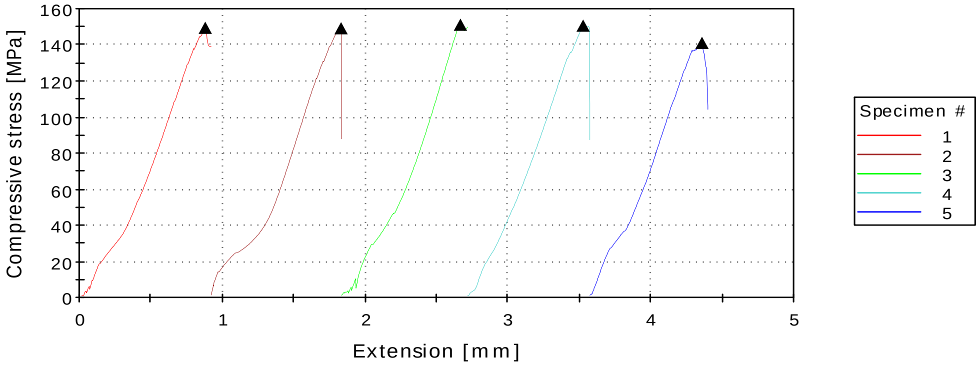

Figure A.6: Compressive Strength at $\theta = 90^o$

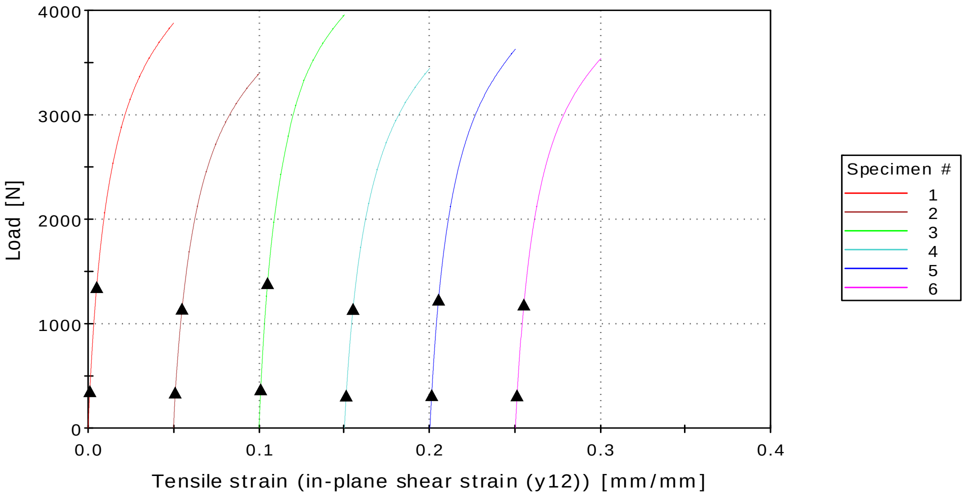

Figure A.7: In-plane shear strength and modulus

Appendix B

EFG Techniques and Applications

B.1 Element Free Galerkin Method Techniques

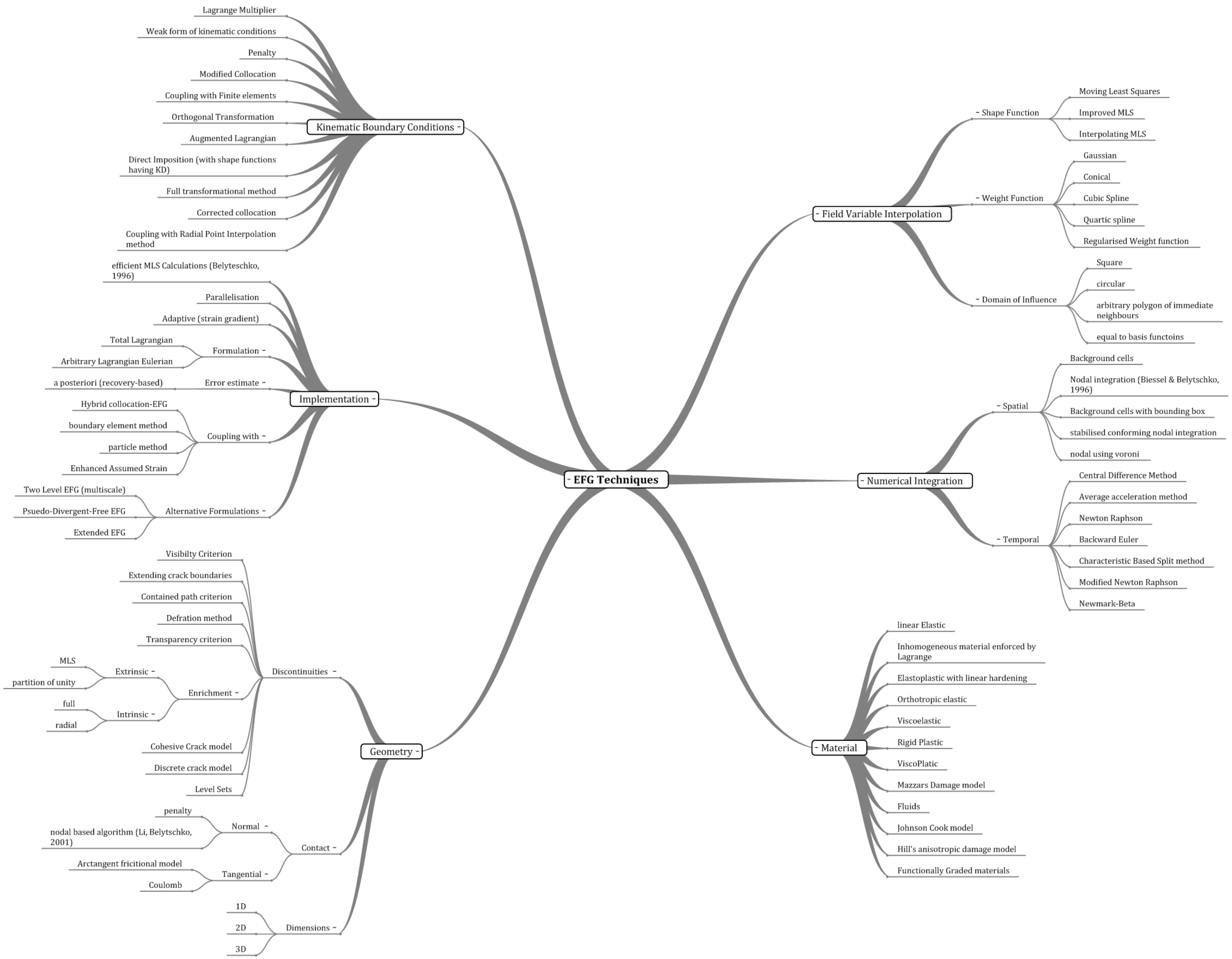

B.2 Element Free Galerkin Method Applications